

A Search for Time Dependent $B_s^0 - \bar{B}_s^0$ Oscillations Using Exclusively Reconstructed D_s^+ at SLD*

Cheng-Ju Stephen Lin

Stanford Linear Accelerator Center
Stanford University
Stanford, CA 94309

SLAC-Report-584
September 2001

Prepared for the Department of Energy
under contract number DE-AC03-76SF00515

Printed in the United States of America. Available from the National Technical Information Service, U.S. Department of Commerce, 5285 Port Royal Road, Springfield, VA 22161.

*Ph.D. thesis, University of Massachusetts, Amherst, Massachusetts.

A SEARCH FOR TIME DEPENDENT $B_S^0 - \bar{B}_S^0$ OSCILLATIONS
USING EXCLUSIVELY RECONSTRUCTED D_S^+ AT SLD

A Dissertation Presented

by

CHENG-JU STEPHEN LIN

Submitted to the Graduate School of the
University of Massachusetts Amherst in partial fulfillment
of the requirements for the degree of

DOCTOR OF PHILOSOPHY

September 2001

Department of Physics

A SEARCH FOR TIME DEPENDENT $B_S^0 - \bar{B}_S^0$ OSCILLATIONS
USING EXCLUSIVELY RECONSTRUCTED D_S^+ AT SLD

A Dissertation Presented

by

CHENG-JU STEPHEN LIN

Approved as to style and content by:

Guy T. Blaylock, Chair

Barry R. Holstein, Member

Richard R. Kofler, Member

Michael F. Skrutskie, Member

Stéphane Y. Willocq, Member

John F. Donoghue, Department Head
Physics

ACKNOWLEDGEMENTS

There are many people to whom I would like to say thank you. My thesis advisor Guy Blaylock has been a key figure in my development as a physicist. I am very fortunate to have him as a mentor and a friend. I have learned a great deal from him over the years. My other physics mentor is Stéphane Willocq. He has taught me almost everything that I know about B_s^0 mixing. It has been a pleasure working along the sides of first-rate physicists. I would also like to express my sincere gratitude to Richard Kofler and Stan Hertzbach. I had a wonderful time working with them on the BaBar calorimeter. They have always shown keen interests in my work and have done everything in their ability to make my time as a graduate student as smooth as possible. Dick and Stan are model group leaders. Although not really a member of the UMass group, Howard Nicholson has certainly made important contributions to the group. On the personal front, I would like to thank Howard for all the sage advices he has given me over the years. He is truly an educator at heart.

This dissertation would not have been possible without the help of many people from the SLD collaboration, in particular, members of the B mixing/lifetime analysis group. They have given me, time and time again, valuable suggestions and assistance. I give my heartfelt thanks to you all (without listing the individual names to save some trees and avoid the risk of missing a few). I agree with Marty that the SLD collaboration is the most congenial collaboration around. My experi-

ence working on the SLD experiment has been very pleasant and memorable. Once again, thank you all for the fond memories.

I would like to take this opportunity to dedicate this dissertation to my father (Cheng-Yeh) and mother (Meiyu). They have stood by my side and provided the greatest source of inspiration and support during all these years. My parents and sister (Chia-Ching) are always there when I needed them. Finally, I would like to tell my dear wife Yih-Chih (Bernice) how much I appreciate her. I appreciate everything that you have done for me, the big and the small. I look forward to sharing the rest of my life, through the good time and the bad time, with you.

ABSTRACT

A SEARCH FOR TIME DEPENDENT $B_s^0 - \bar{B}_s^0$ OSCILLATIONS
USING EXCLUSIVELY RECONSTRUCTED D_s^+ AT SLD

SEPTEMBER 2001

CHENG-JU STEPHEN LIN, B.S., BOSTON UNIVERSITY

B.A., BOSTON UNIVERSITY

Ph.D., UNIVERSITY OF MASSACHUSETTS AMHERST

Directed by: Professor Guy T. Blaylock

We set a preliminary 95% C.L. exclusion on the oscillation frequency of $B_s^0 - \bar{B}_s^0$ mixing using a sample of 400,000 hadronic Z^0 decays collected by the SLD experiment at the SLC during the 1996-98 run. In this analysis, B_s^0 mesons are partially reconstructed by combining a fully reconstructed D_s with other B_s^0 decay products. The D_s decays are reconstructed via the $\phi\pi$ and K^*K channels. The b -hadron flavor at production is determined by exploiting the large forward-backward asymmetry of polarized $Z^0 \rightarrow b\bar{b}$ decays as well as information from the hemisphere opposite to the reconstructed B decay. The flavor of the B_s^0 at the decay vertex is determined by the charge of the D_s . A total of 361 candidates passed the final event selection cuts. This analysis excludes the following values of the $B_s^0 - \bar{B}_s^0$ mixing oscillation frequency: $\Delta m_s < 1.4 \text{ psec}^{-1}$ and $2.5 < \Delta m_s < 5.3 \text{ psec}^{-1}$ at the 95% confidence level.

TABLE OF CONTENTS

	Page
ACKNOWLEDGEMENTS	iv
ABSTRACT	vi
LIST OF TABLES	x
LIST OF FIGURES	xi
CHAPTER	
1. INTRODUCTION	1
2. THEORETICAL MOTIVATION	4
2.1 Overview of the Standard Model	8
2.1.1 Electroweak Interaction	8
2.1.2 Strong Interaction	15
2.2 CP Violation in the Standard Model	17
2.2.1 CKM Matrix	20
2.2.2 Phenomenology of B^0 - \bar{B}^0 Oscillations	22
2.2.3 Experimental Constraints on $\rho - \eta$	26
2.3 Polarized $Z^0 \rightarrow f\bar{f}$ Decays	30
3. EXPERIMENTAL APPARATUS	33
3.1 SLAC Linear Collider	34
3.1.1 SLC Machine Cycle	36
3.1.2 Beam Energy Spectrometer	40
3.1.3 Compton Polarimeter	41
3.2 SLD Detector	43
3.2.1 Vertex Detector	44
3.2.2 Central Drift Chamber	47
3.2.3 Cherenkov Ring Imaging Detector	50
3.2.4 Liquid Argon Calorimeter	52
3.2.5 Magnet	54
3.2.6 Warm Iron Calorimeter	55
3.2.7 Luminosity Monitor	56
3.3 Data Acquisition and Trigger	57

4. MONTE CARLO SIMULATION	59
4.1 Physics Modeling	59
4.2 Detector Modelling	63
4.3 Monte Carlo Tuning	64
5. DATA REDUCTION	67
5.1 Physics Event Filter	67
5.2 Hadronic Event Selection and $b\bar{b}$ Tagging	68
5.2.1 Interaction Point Determination	69
5.2.2 Hadronic Event Selection	70
5.2.3 $b\bar{b}$ Event Selection	71
5.2.3.1 Topological Vertex Reconstruction	71
5.2.3.2 Identifying B Vertices	75
6. EVENT RECONSTRUCTION	78
6.1 Flavor Tagging	79
6.1.1 Polarized Forward-Backward Asymmetry	80
6.1.2 Jet Charge	82
6.1.3 Opposite Hemisphere Topological Tags	82
6.1.3.1 Vertex Charge	83
6.1.3.2 Dipole Charge	83
6.1.3.3 High p_t Leptons/Secondary Kaons	84
6.1.4 Combination Using Neural Networks	84
6.2 B_s^0 Candidate Selection	85
6.2.1 D_s Reconstruction	86
6.2.2 B Decay Length Reconstruction	94
6.2.3 B Boost Reconstruction	95
6.2.3.1 Fragmentation Method	98
6.2.3.2 Mass Method	100
6.2.3.3 Maximum Missing Mass Method	101
6.2.3.4 Thrust Angle Method	102
6.2.3.5 Averaging the Boost Algorithms	104
6.2.4 B_s^0 Proper Time	104
6.2.5 B Vertex Charge Reconstruction	107
7. B_s^0 OSCILLATION STUDIES	110
7.1 Likelihood Function	110
7.2 Likelihood Function Parameterizations	116
7.2.1 Data Composition	117
7.2.2 Final State Mistag	120
7.2.3 Vertex Reconstruction Efficiency	120
7.2.4 Proper Time Resolution Functions	121

7.2.4.1	Event by Event Decay Length Resolution . .	123
7.2.4.2	Event by Event Relative Boost Resolution . .	124
7.2.4.3	Proper Time Offsets	125
7.2.5	Normalizations	128
7.3	Likelihood Fit	128
7.4	Amplitude Fit	132
8.	RESULTS AND CONCLUSIONS	136
8.1	$D_s + Tracks$ Result	136
8.2	Systematic Uncertainties	137
8.2.1	B Hadron Lifetimes and Δm_d	140
8.2.2	Sample Composition	140
8.2.3	Flavor Tagging	142
8.2.4	Proper Time Resolution and Offsets	143
8.2.5	Systematic Error Table	144
8.3	SLD Average	144
8.4	World Scene	146
8.5	Outlook	148
APPENDICES		
A.	THE CHERENKOV RING IMAGING DETECTOR	153
A.1	Maximum Likelihood Method	154
A.2	Liquid Tray Alignment	156
B.	VIRTUAL D_s TRACK RECONSTRUCTION	165
B.1	Parent Track Calculations	166
B.1.1	Parent Track Parameters	166
B.1.2	Parent Track Error Matrix	167
B.1.2.1	Directional Error Matrix	167
B.1.2.2	Spatial Error Matrix	171
B.2	Performance	172
C.	PROPER TIME DISTRIBUTION FUNCTIONS	173
D.	COMBOS INPUT DATA FILE	175
E.	SLD COLLABORATION	180
BIBLIOGRAPHY		183

LIST OF TABLES

Table	Page
1. Electroweak interaction multiplets	10
2. Standard Model vector (v_f) and axial-vector (a_f) couplings for up-type and down-type fermions	15
3. Liquid Argon Calorimeter parameters	55
4. D_s Neural net inputs	88
5. Number of $D_s \rightarrow \phi\pi$ candidates within ± 40 MeV of the nominal D_s mass and the estimated average combinatorial background fractions	90
6. Number of $D_s \rightarrow K^{*0}K$ candidates within ± 40 MeV of the nominal mass and the estimated average combinatorial background fractions	90
7. Decay length resolutions for various decay topologies	95
8. Relative boost resolutions for various decay topologies	104
9. B hadron fractions for the D_s combinatorial events within ± 40 MeV of the nominal D_s mass	115
10. Fit results for the D_s signal peak	118
11. Fit results for the background shape	118
12. Data composition in the D_s mass peak (within ± 40 MeV)	119
13. Effective final state mistag rates	120
14. Decay length resolution correction factors	124
15. The event by event relative boost resolution parameterizations for the various categories	127
16. World average values of B lifetimes and Δm_d	140
17. B production fractions and various branching ratios assumed in the amplitude fit	141
18. Table of statistical and systematic uncertainties for several Δm_s values	145

LIST OF FIGURES

Figure	Page
1. Feynman diagrams of electromagnetic interactions	5
2. Feynman diagrams of charged weak interactions	9
3. The Feynman diagram shows the coupling of quark to gluon	16
4. Two different paths of $A \rightarrow f$ with amplitudes M_1 and M_2	18
5. Feynman diagrams of b decay	19
6. The decay of B^0 to CP eigenstate ($\pi^+\pi^-$) with and without mixing .	19
7. The Unitarity Triangle	22
8. The box diagrams for B_d^0 and B_s^0 oscillations	23
9. Probability distribution functions for mixed and unmixed events with generated Δm_s of 10 psec^{-1} and B_s^0 lifetime of 1.57 psec	25
10. An illustration of the various constraints on the apex of the Unitarity Triangle	27
11. The Feynman diagrams for $e^+e^- \rightarrow$ (a) $\gamma \rightarrow f\bar{f}$ and (b) $Z^0 \rightarrow f\bar{f}$ decays	30
12. The plot shows the differential b quark production cross section as a function of $\cos \theta$ for three polarization values ($P_e = 75\%$, -75% and 0)	32
13. Schematic of the SLC complex showing the various components and transport lines	35
14. Luminosity history of SLC recorded by the SLD detector	37
15. The schematic of the polarized electron source	38
16. The energy levels of bulk GaAs (left) and strained GaAs (right) . . .	39
17. Schematic layout of the energy spectrometer, WISRD	40
18. The layout of the Compton polarimeter	42

19. The schematic of the SLD detector	44
20. A quadrant view of the SLD detector listing the various subdetectors	45
21. A comparison of VXD2 and VXD3	46
22. The layout of a CCD ladder	47
23. The cell structure for the CDC	48
24. A schematic of the axial and stereo wire assignments for the CDC . .	49
25. A sectional view of the SLD barrel CRID	51
26. The figure shows a portion of the cell structure of a LAC module . .	53
27. Schematic of LAC modules	54
28. The schematic of the WIC and the layout of the Iarocci tubes	56
29. Luminosity monitor	57
30. The figure shows the different stages of the underlying physics process	60
31. The figure shows the evolution of quark pair production in the string fragmentation model	62
32. The track Z impact parameter distributions in different VXD3 ϕ re- gions for data	65
33. Track xy impact parameter means (cm) in 4 regions of $\cos\theta$ and 40 regions of ϕ	65
34. Track z impact parameter means (cm) in 4 regions of $\cos\theta$ and 40 regions of ϕ	66
35. A $Z^0 \rightarrow b\bar{b}$ event from the 1996 data	72
36. The Gaussian probability tube for a track	73
37. (a)Plot of Gaussian probability density tubes projected on the x-y plane	74
38. This diagram defines the track attachment parameters L , D and T .	76
39. The p_t corrected vertex mass distributions	77
40. The Feynman diagrams for B_s^0 and B_d^0 decays	79
41. The Feynman diagram for the wrong-sign B_s^0 decay	80
42. The drawing gives an overview of the initial state tags	81

43. Momentum-weighted jet charge distributions for data and Monte Carlo	83
44. The initial state b quark probability distribution for data and Monte Carlo using the combined neural net tag	86
45. $B_s^0 \rightarrow D_s^- X$ event topology	87
46. D_s neural net output distributions for (a) $\phi\pi$ and (b) K^*K^0 modes .	89
47. Distributions of the $KK\pi$ invariant mass for the $\phi\pi$ mode	91
48. Distributions of $KK\pi$ invariant mass for the K^*K^0 mode	92
49. Candidate B_s^0 semileptonic decay event	93
50. Decay length distributions for data and Monte Carlo	96
51. Decay length residual ($L_{reconstructed} - L_{true}$) plots for (a) B_s^0 inclusive, (b) B_s^0 right-sign, (c) B_s^0 wrong-sign, (d) B_d^0 , (e) B^+ and (f) b -baryons events	97
52. Functional dependence between the average un-associated electromagnetic energy and the average neutral fragmentation energy	100
53. Schematic diagram showing the variables used in the thrust angle method	103
54. Reconstructed boost distributions for (a) $\phi\pi$ mode, (b) $K^{*0}K$ mode and (c) combined	105
55. Relative boost residuals for (a) B_s^0 inclusive, (b) B_s^0 right-sign, (c) B_s^0 wrong-sign, (d) B_d^0 , (e) B^+ and (f) b -baryon events	106
56. Reconstructed proper decay time distributions for (a) $\phi\pi$ mode, (b) $K^{*0}K$ mode and (c) combined	108
57. Reconstructed B vertex charge distribution for data (dots), M.C. neutral B events (open histogram), and M.C. charged B events (solid histogram)	109
58. The proper time distribution of the combinatorial D_s events in the data sidebands	116
59. B vertex efficiency functions for (a) B_s^0 , (b) B_d^0 , (c) B^+ and (d) b -baryon events	122
60. σ_τ distributions for $B_s^0 \rightarrow D_s^- X$ events	123
61. Plots (a1)-(a6) are the relative boost residuals in various bins of charged B energy for the right-sign B_s^0 ($Q=0$) events	126

62. Proper time residual distributions (dots) in bins of true proper time for the right-sign B_s^0 ($Q=0$) events	129
63. Mixed fraction distributions (dots) for (a) $B_s^0 \rightarrow D_s^\pm X$, (b) $B_d^0 \rightarrow D_s^\pm X$, (c) $B^+ \rightarrow D_s^\pm X$ and (d) all events	130
64. Mixed fraction distribution (dots) and likelihood function (histogram) for data	131
65. Distribution of $-\log(\text{likelihood})$ versus Δm_s for data	132
66. Amplitude fit plot for Monte Carlo B_s^0 events	134
67. Amplitude fit result using full Monte Carlo simulation including back- ground events with input Δm_s of (a) 4, (b) 10, (c) 17 and (d) 270 $psec^{-1}$	135
68. Amplitude plot for D_s +Tracks	138
69. Exclusion probability for the D_s +Tracks analysis	139
70. SLD average amplitude plot including the final D_s +Tracks result . .	147
71. World amplitude plot including the latest D_s +Tracks result	149
72. The plot shows the amplitudes and errors at Δm_s of 15 $psec^{-1}$	150
73. The allowed regions for $\bar{\rho}$ and $\bar{\eta}$ (contours at 68%, 95%) and the various experimental constraints	151
74. Projections of B_s^0 mixing reach as a function of X_s ($X_s = \Delta m_s/\Gamma_B$) at CDF RUN II	152
75. Partitions of the liquid radiator tray	157
76. Distribution of $\Delta\theta_c$ ($\theta_c(z=0) - \theta_c(z=1.3m.)$) as a function of liquid tray number for the forward Cherenkov photons	158
77. Distribution of $\Delta\theta_c$ ($\theta_c(x=0) - \theta_c(x=33cm.)$) as a function of liquid tray number for the forward Cherenkov photons	159
78. Distribution of the difference between forward and backward inclusive Cherenkov angles for the first z slice nearest to the detector mid- plane as a function of liquid tray number	160
79. Distribution of the average inclusive Cherenkov angles for (a) forward, (b) backward, (c) right-side, (d) left-side and (e) combined photons as a function of liquid tray number before global radial alignment .	161
80. Distribution of the average inclusive Cherenkov angles for (a) forward, (b) backward, (c) right-side, (d) left-side and (e) combined photons as a function of liquid tray number after global radial alignment . .	162

81.	Distributions of liquid Cherenkov resolution as a function of track dip angle before and after liquid tray alignments for (a) forward and (b) backward photons	163
82.	Distributions of liquid Cherenkov resolution as a function of track dip angle before and after liquid tray alignments for (a) right-side and (b) left-side photons	164

C H A P T E R 1

INTRODUCTION

In this dissertation, we present the result of a search for $B_s^0 - \bar{B}_s^0$ oscillations. B_s^0 oscillation is a quantum mechanical phenomenon in which the particle converts to its antiparticle, and vice versa ($B_s^0 \Leftrightarrow \bar{B}_s^0$). The frequency of oscillation is characterized by the mass difference, Δm_s , between the two mass eigenstates, B_H and B_L , and is directly related to fundamental but poorly measured parameters in the current theory of particle physics, the Standard Model. The B_s^0 oscillation frequency is expected to be large. As of today, no direct measurement has been claimed, only lower limits have been established.

A measurement of B_s^0 oscillations could shed light on some of the important questions in particle physics, in particular, the phenomenon of Charge Parity (CP) violation. It was assumed that the laws of physics were invariant under the combined operation of Charge conjugation (particle to antiparticle) and Parity reversal (mirror reflection). It was a startling discovery when Christenson et al. [1] confirmed in 1964 that CP operation is not a perfect symmetry in nature and it is violated in the neutral kaon system. The origin of the CP violation remained a great mystery in particle physics until the birth of the Standard Model. As we will discuss in the next chapter, with 3 generations of quarks, the Standard Model naturally accommodates CP violation. Now the key question is whether the Standard

Model's description of CP violation is correct and complete. To address this question, we will need to know the Standard Model effects accurately. A measurement of B_s^0 mixing will provide an important input to pin down the Standard Model contributions and possibly to establish the presence of new physics.

The search for the rapid oscillations of the B_s^0 meson has proven to be a challenge for all aspects of experimental physics. It is a challenge for the particle accelerator physicists to push the machine to produce the necessary high luminosity, for the detector folks to achieve the best possible detector resolution and for people involved in the analysis to come up with ever more clever ideas to extract the signal from the data. The search has been truly a collaborative venture involving experiments in Europe and in the U.S. The combined efforts over the years from experiments at CERN, Fermi National Accelerator Lab (Fermilab) and the Stanford Linear Accelerator Center (SLAC) have steadily increased the limit on Δm_s . Based on indirect evidence, we believe the experimental sensitivity is now near where the signal lies. In fact, we may already have the first hint of a signal.

In this dissertation, we will discuss the efforts at the SLD (SLC Large Detector) experiment at SLAC to search for B_s^0 oscillations. Although the emphasis is on the “ D_s +Tracks” analysis, most of the issues discussed apply equally well to other mixing analyses at SLD. All B_s^0 mixing analyses require the same three basic ingredients: 1.) a data sample enriched in B_s^0 events, 2.) a means to determine the B_s^0 flavor at production and decay and 3.) an algorithm to reconstruct the B_s^0 proper decay time. Optimizing the three ingredients is the key to achieving good sensitivity to B_s^0 mixing. The discussion in the coming chapters is divided into three main sections: theory, experimental apparatus and analysis. In the theory section, we will introduce the Standard Model with an emphasis on the physics relevant to Z^0 pole and B_s^0 mixing. We will discuss the Cabibbo-Kobayashi-Maskawa ma-

trix (CKM matrix) and the various experimental constraints on the CKM matrix parameters. After the theory discussion, we will move on to describe the experimental apparatus that produced the data used in this dissertation. The remaining chapters are devoted to the analysis of B_s^0 oscillations.

C H A P T E R 2

THEORETICAL MOTIVATION

The fundamental theory of particle physics describes the basic constituents of matter and the interactions between them. Based on our present understanding, there are two categories of point-like particles in nature: fermions and bosons. Fermions come in two distinct classes: quarks and leptons. The six quark flavors have been given whimsical names: up, down, charm, strange, top and bottom. The six leptons are: electron (e), muon (μ), tau (τ) and the three neutrinos (ν_e , ν_μ and ν_τ). For each particle that exists in nature, there is a corresponding partner, the antiparticle. For example, the electron has its partner the anti-electron (or positron).

In our current view, particle interactions are mediated by the exchange of force carrying particles. These force carrying particles are collectively referred to as intermediate vector bosons or as gauge bosons. The photon is the mediator of the electromagnetic interactions. Figure 1 shows the Feynman diagrams that depict examples of electromagnetic interactions. Gluons, on the other hand, participate in the strong interaction and they are responsible for holding the nucleus together. The weak force, mediated by a neutral and two charged bosons, Z^0 and W^\pm , is the culprit behind the decay of heavy particles. Lastly, the gravitational force is presumably transmitted by the undiscovered graviton.

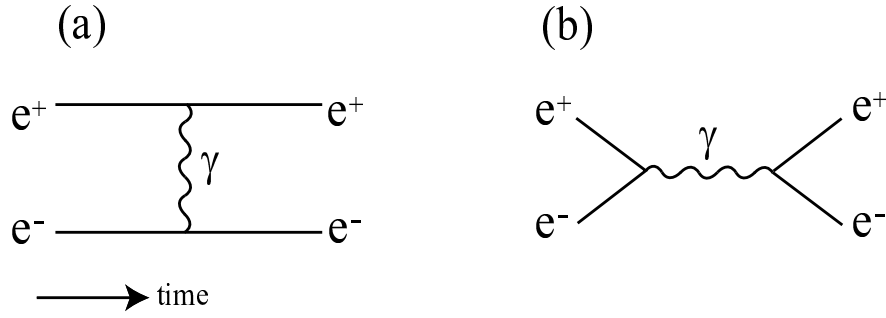


Figure 1: Feynman diagrams of electromagnetic interactions. Diagram (a) shows electron (e^-) positron(e^+) scattering via exchange of a virtual photon. Diagram (b) shows electron and positron annihilating into a photon and the photon later produces an electron-positron pair. These two diagrams are examples of Bhabha scattering.

An important goal, if not the holy grail of particle physics, is to explain all four interactions in the most elegant and simple way. This has inspired physicists on a long journey to unify all forces. Just as electricity and magnetism were shown to be two different manifestations of the same electromagnetic force, Glashow, Salam and Weinberg (GSW) [2] demonstrated that electromagnetic and weak interactions are manifestations of a single electroweak interaction. The electroweak unification required the existence of three gauge bosons, W^\pm and Z^0 . It was a great triumph for the GSW theory when W^\pm and Z^0 particles were later discovered [3]. With the success of the electroweak unification, the next logical step is to incorporate the strong with the electroweak force. The strong interaction is so far described by a stand-alone theory, the Quantum Chromodynamics (QCD). Attempts to combine QCD and GSW theories into a Grand Unified Theory (GUT) are showing great promise. There are some indications that the unification occurs at the high energy scale of about 10^{15} GeV. The last force, gravity, is perhaps the most familiar force to us. After all, gravitational attraction is responsible for keeping us on the earth and the planets in orbits. Ironically, theoretical treatment of gravity has been the

most difficult among the four forces. There is not yet a consistent formulation of renormalizable quantum field theory for gravity due to the fact that graviton is a spin-2 particle. A renormalizable theory is one where the divergences in the theory can be mathematically removed in order to obtain finite physical results. Fortunately, gravity is far weaker than the strong and the electroweak forces at the energy scale pertinent to experimental particle physics. Thus, the effect of gravity could be ignored in our subsequent discussion. Nevertheless, to have a completely unified theory, whether it comes in the form of supergravity, superstring or other theories, gravity would have to be incorporated into the overall scheme.

The Standard Model is our current theory of particle physics. The theory has been extremely successful at describing the electroweak and the strong interactions. It has survived a battery of experimental tests with ever more precision for over two decades. However, the Standard Model is believed to be only an “effective” theory [4], a theory that is a low energy approximation to the more fundamental theory of particle physics. This belief is based on conceptual as well as experimental grounds. As mentioned earlier, the electroweak and the strong interactions are expected to manifest as a single force at the GUT scale. It is conceivable that the unification could also include gravity at higher energy, perhaps near the Planck scale of 10^{19} GeV. At this energy, it is unlikely that the Standard Model in the present form would still be valid without introducing new physics.

On the experimental side, new results are beginning to reveal hints of phenomenon beyond the Standard Model. The recent result released by the g-2 experiment [5], which performed a precision measurement on the anomalous magnetic moment of muon, shows inconsistency with the predicted value from the Standard Model. If the result is verified, this would be a direct confirmation that the Standard Model is incomplete. In the neutrino sector, results from SuperKamiokande [6]

and SNO [7] experiments are suggesting that the atmospheric and solar neutrino deficit anomalies are due to neutrino oscillations. The consequence of the findings is that the neutrinos have to be massive. It is improbable at this point that all the evidence of oscillations will disappear, and thus the Standard Model would have to be modified to include neutrino mass. A more subtle hint of new physics comes from astrophysical observations. There is mounting evidence that most of the matter in the universe is composed of particles outside the Standard Model, the so called non-baryonic cold dark matter [8]. The neutralino, the lightest particle in Supersymmetry (SUSY) is a prime candidate for the mysterious dark matter in the universe. If SUSY is confirmed experimentally, it would open up a new chapter in particle physics as well as solving the cold dark matter problem. It would also double the known list of particles since SUSY rests on the premise that for every particle in nature there is a corresponding SUSY partner.

There are numerous other experimental hints of new physics. The last example that we will discuss concerns baryogenesis. As Sakharov pointed out in his 1967 paper, one of the necessary conditions for the formation of baryon and antibaryon asymmetry in the universe is that CP invariance must be violated [9]. Although the Standard Model accommodates CP violation, it has been suggested that the level of CP violation is insufficient to account for the large asymmetry observed between matter and antimatter [10]. This might be an indication that there are new sources of CP violation beyond the Standard Model. The phenomenon of CP violation is one of the least tested aspects of the Standard Model. At the present time, we still do not have conclusive experimental evidence to demonstrate that the Cabibbo-Kobayashi-Maskawa matrix (to be discussed in section 2.2.1) in the Standard Model correctly describes the CP violation effects in nature. Therefore it is imperative that we thoroughly test the Standard Model's description of CP

violation. As we will discuss later, the study of CP violation is the subject of this thesis analysis.

We will devote the remaining sections of this chapter to aspects of the Standard Model that are important to CP violation. A thorough treatment of the Standard Model is beyond the scope of this dissertation and therefore we will only focus on some of the basic principles. Interested readers could consult reference [11] for more details or clarifications.

2.1 Overview of the Standard Model

The Standard Model is a quantum field theory based on local gauge symmetries. The theory, more specifically the Lagrangian, is constructed in a way that it remains invariant under local gauge transformations. The Standard Model gauge symmetry group is:

$$SU(3)_C \otimes SU(2)_L \otimes U(1)_Y, \quad (2.1)$$

where subscript C denotes the color, L for left-handed helicity, and Y for hypercharge. In particular, $SU(3)_C$ is the symmetry group for the strong interactions and $SU(2)_L \otimes U(1)_Y$ is the group for the electroweak unification. The Standard Model is composed of two distinct parts: the GSW theory that describes the electroweak interaction and the QCD theory that describes the strong interaction.

2.1.1 Electroweak Interaction

The GSW theory is based on the $SU(2)_L \otimes U(1)_Y$ gauge group. The requirement of gauge invariance generates interaction terms. The $SU(2)$ group has three

generators that give rise to three gauge bosons while the $U(1)$ group has one associated gauge field. A new quantum number, the weak isospin (\mathbf{I}) is introduced in the electroweak theory. The left-handed leptons and quarks are arranged in three families or generations of doublets with the weak isospin assignment $\mathbf{I} = 1/2$ and the third component $\mathbf{I}_3 = \pm 1/2$. As illustrated in figure 2, each left-handed quark or lepton in the same family can convert into each other via the charged current interaction involving the W^\pm . The right-handed fermions and the left-handed an-

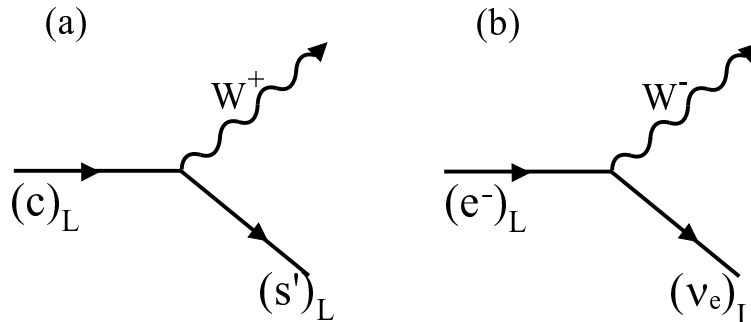


Figure 2: Feynman diagrams of charged weak interactions. Diagram (a) involves the quark sector and (b) involves the lepton sector.

tifermions, however, are weak isospin singlets ($\mathbf{I} = 0$) and do not couple to W^\pm bosons. Thus, the electroweak theory violates Parity (left-right symmetry). In addition to weak isospin, there is another quantum number, the weak hypercharge (Y), that is related to the charge and the third component of weak isospin by the Gell-Mann-Nishijima formula:

$$Q = \mathbf{I}_3 + \frac{1}{2}Y. \quad (2.2)$$

Table 1 summarizes the electroweak multiplets and the associated quantum numbers. There are no right-handed neutrinos and left-handed antineutrinos in the Standard Model (assuming neutrinos are massless). The down-type quarks (d' , s' ,

b') in weak isospin doublets are the rotated states of the flavor eigenstates (see section 2.2.1).

	Fermion Multiplets			I	I₃	Q
Leptons	$\begin{pmatrix} \nu_e \\ e \end{pmatrix}_L$	$\begin{pmatrix} \nu_\mu \\ \mu \end{pmatrix}_L$	$\begin{pmatrix} \nu_\tau \\ \tau \end{pmatrix}_L$	1/2	$\begin{pmatrix} +1/2 \\ -1/2 \end{pmatrix}$	$\begin{pmatrix} 0 \\ -1 \end{pmatrix}$
	e_R	μ_R	τ_R	0	0	-1
Quarks	$\begin{pmatrix} u \\ d' \end{pmatrix}_L$	$\begin{pmatrix} c \\ s' \end{pmatrix}_L$	$\begin{pmatrix} t \\ b' \end{pmatrix}_L$	1/2	$\begin{pmatrix} +1/2 \\ -1/2 \end{pmatrix}$	$\begin{pmatrix} +2/3 \\ -1/3 \end{pmatrix}$
	u_R	c_R	t_R	0	0	+2/3
	d_R	s_R	b_R	0	0	-1/3

Table 1: Electroweak interaction multiplets. The columns under **I** and **I₃** list the weak isospin and the third component of the weak isospin assignments for the fermions. The column under Q lists the electric charge.

The two fundamental interaction terms in the GSW formalism are: a weak isotriplet current \mathbf{J}_μ that couples to the three vector bosons \mathbf{W}^μ with the coupling strength g ,

$$-ig\mathbf{J}_\mu \cdot \mathbf{W}^\mu = -ig(J_\mu^1 W^{\mu 1} + J_\mu^2 W^{\mu 2} + J_\mu^3 W^{\mu 3}), \quad (2.3)$$

and a weak hypercharge current that couples to the vector boson B^μ with the coupling strength $g'/2$,

$$-i\frac{g'}{2}j_\mu^Y B^\mu. \quad (2.4)$$

The wavefunctions of the physical charged bosons W^\pm can be expressed as:

$$|W^\pm\rangle = \frac{1}{\sqrt{2}}(W_\mu^1 \mp iW_\mu^2). \quad (2.5)$$

The two neutral gauge bosons, photon and Z^0 , are mutually orthogonal linear combinations of the fields W_μ^3 and B_μ . More specifically the physical states are:

$$\begin{aligned} |A_\mu\rangle &= B_\mu \cos \theta_w + W_\mu^3 \sin \theta_w \\ |Z_\mu\rangle &= -B_\mu \sin \theta_w + W_\mu^3 \cos \theta_w, \end{aligned} \quad (2.6)$$

where A_μ is the photon field, Z_μ is the Z^0 field and θ_w is the electroweak mixing angle. The electroweak mixing angle tells us the strength of the mixing between the weak and the electromagnetic interactions. For $\theta_w=0$, the two interactions are completely decoupled. This scenario has been ruled out by experiments. The current measured value of the angle is $\sin^2 \theta_w = 0.23146 \pm 0.00017$ [12]. The couplings g and g' are related to the electroweak mixing angle,

$$\sin \theta_w = \frac{g'}{\sqrt{g^2 + g'^2}}, \quad (2.7)$$

and to the electric charge,

$$e = g \sin \theta_w = g' \cos \theta_w. \quad (2.8)$$

The electromagnetic and weak couplings are therefore not independent and are related to more fundamental parameters. This is the essence of electroweak unification.

The above formalism describes beautifully the relationship between electromagnetic and weak interactions. However, it does not elucidate how particles acquire mass. The naive method of introducing mass terms to the Lagrangian spoils the gauge symmetry and leads to problems with renormalization. A possible solution to the issue of mass generation is the Higgs mechanism [13]. In this theoretical model, four scalar fields (Higgs fields) are required, one for each gauge boson. Three of the Higgs bosons, the quanta of the Higgs fields, are absorbed by W^\pm and Z^0 during the electroweak phase transition. This process breaks the $SU(2)_L \otimes U(1)_Y$ symmetry and generates the masses for the three gauge bosons. The fourth Higgs boson remains free since the photon is massless. The search for the Higgs boson is another important area of experimental particle physics. The discovery of the Higgs boson could explain the origin of the electroweak symmetry breaking. The

predicted masses of the gauge bosons are based on three parameters, the coupling constants g and g' , and the vacuum expectation value of the Higgs fields v :

$$\begin{aligned} m_{W^\pm} &= \frac{1}{2}gv = \frac{1}{2}v \frac{e}{\sin \theta_w} \\ m_{Z^0} &= \frac{1}{2}v\sqrt{g^2 + g'^2} = \frac{m_{W^\pm}}{\cos \theta_w} \end{aligned} \quad (2.9)$$

The same Higgs mechanism also gives masses to the fermions (except neutrinos, which are assumed to be massless). The masses of the fermions are introduced via Yukawa couplings between the Higgs boson and the fermions. For the quark sector, the most general Yukawa interaction term can be expressed as [14]:

$$\mathcal{L} = - \sum_{i=1}^3 \sum_{j=1}^3 \left[\tilde{G}_{ij} \overline{u_{iR}} \left(\tilde{\Phi}^\dagger D_{jL} \right) + G_{ij} \overline{d_{iR}} \left(\Phi^\dagger D_{jL} \right) \right] + h.c., \quad (2.10)$$

where the weak eigenstates of the unbroken gauge theory are

$$D_{jL} \equiv \begin{pmatrix} u_j \\ d_j \end{pmatrix}_L, \quad u_{jR}, \quad d_{jR}. \quad (2.11)$$

The matrix, D_{jL} , is the $SU(2)_L$ doublet and u_{jR} , d_{jR} are the right-handed $SU(2)$ singlets for up-type (u , c , t) and down-type (d , s , b) quarks, respectively. The indices, i and j , run from 1 to 3 for three generation of quarks. The 3×3 matrices, G_{ij} and \tilde{G}_{ij} , each contains 9 complex constants that describe the inter-generation quark couplings. The $SU(2)$ Higgs doublets are

$$\Phi = \begin{pmatrix} \Phi^+ \\ \Phi^0 \end{pmatrix}, \quad \tilde{\Phi} = i\tau_2 \Phi^*, \quad (2.12)$$

where $\Phi^+ \equiv (\phi_1 + i\phi_2)/\sqrt{2}$, $\Phi^0 \equiv (\phi_3 + i\phi_4)/\sqrt{2}$ and τ_2 is the second Pauli matrix. The scalar fields ϕ_1 , ϕ_2 , ϕ_3 and ϕ_4 are the four postulated scalar Higgs fields. The mass terms for the up-type and down-type quarks can be obtained from the vacuum

expectation values of Φ and $\tilde{\Phi}$:

$$\begin{aligned} & \overline{(u_1, u_2, u_3)_R} \mathcal{M}^u \begin{pmatrix} u_1 \\ u_2 \\ u_3 \end{pmatrix}_L + h.c., \\ & \overline{(d_1, d_2, d_3)_R} \mathcal{M}^d \begin{pmatrix} d_1 \\ d_2 \\ d_3 \end{pmatrix}_L + h.c., \end{aligned} \quad (2.13)$$

where $\mathcal{M}_{i,j}^u = \frac{v}{\sqrt{2}} \tilde{G}_{i,j}$ and $\mathcal{M}_{i,j}^d = \frac{v}{\sqrt{2}} G_{i,j}$. The parameter $v/\sqrt{2}$ is the vacuum expectation value of Φ . The off-diagonal terms of the mass matrices couple weak eigenstates of different generations. The quark mass eigenstates can be obtained by diagonalizing the mass matrices. The diagonalization is accomplished by multiplying the mass matrices with appropriate unitary matrices on the left and right,

$$\begin{aligned} U_R^{-1} \mathcal{M}^u U_L &= \begin{pmatrix} m_u & 0 & 0 \\ 0 & m_c & 0 \\ 0 & 0 & m_t \end{pmatrix}, \\ D_R^{-1} \mathcal{M}^d D_L &= \begin{pmatrix} m_d & 0 & 0 \\ 0 & m_s & 0 \\ 0 & 0 & m_b \end{pmatrix}, \end{aligned} \quad (2.14)$$

where U_R , U_L , D_R and D_L are the unitary transformation matrices. The diagonal terms on the right are the physical quark masses. The mass eigenstates u , c and t are linear combinations of the weak eigenstates u_1 , u_2 and u_3 and likewise for the down-type quarks. In the charged-current weak interactions involving the W^\pm bosons, the bilinear terms $\bar{u}_{1L} \gamma^\mu d_{1L}$, $\bar{u}_{2L} \gamma^\mu d_{2L}$ and $\bar{u}_{3L} \gamma^\mu d_{3L}$ terms appear in the

Lagrangians. The sum can be expressed as an inner product of vectors:

$$\overline{(u_1, u_2, u_3)_L} \gamma^\mu \begin{pmatrix} d_1 \\ d_2 \\ d_3 \end{pmatrix}_L = \overline{(u, c, t)_L} U_L^\dagger D_L \gamma^\mu \begin{pmatrix} d \\ s \\ b \end{pmatrix}_L. \quad (2.15)$$

Therefore, in the charged current interactions, generation mixing of the mass eigenstates occurs and can be characterized by a mixing matrix

$$V \equiv U_L^\dagger D_L. \quad (2.16)$$

To complete the discussion on the GSW theory, we now show the Lagrangians for electroweak interactions. The Lagrangian for the neutral current interaction involving the photon and the Z^0 has the form:

$$\begin{aligned} \mathcal{L}^{\gamma Z^0} &= \bar{f} \left\{ e \gamma^\mu Q_f A_\mu + \frac{e}{\sin \theta_w \cos \theta_w} \gamma^\mu Z_\mu [\mathbf{I}_{3f}(1 - \gamma^5) - 2Q_f \sin^2 \theta_w] \right\} f \\ &= \bar{f} \left\{ e \gamma^\mu Q_f A_\mu + \frac{e}{\sin \theta_w \cos \theta_w} \gamma^\mu Z_\mu (v_f - a_f \gamma^5) \right\} f, \end{aligned} \quad (2.17)$$

where γ^μ are the Dirac matrices, Q_f is the charge of the fermion, A_μ is the photon field, Z_μ is the Z^0 boson field, \mathbf{I}_{3f} is the third component of the weak isospin, and f is the fermion field. The vector (v_f) and axial-vector (a_f) coupling constants are defined as:

$$\begin{aligned} v_f &= \mathbf{I}_{3f} - 2Q_f \sin^2 \theta_w, \\ a_f &= \mathbf{I}_{3f}. \end{aligned} \quad (2.18)$$

The vector and axial-vector couplings for the Standard Model Fermions are listed in table 2. Unlike the neutral current interaction, the charged current interaction involving W^\pm does not conserve flavor. This behavior is reflected in the charged weak interaction Lagrangian. In particular, the Lagrangian for the quark sector is:

$$\mathcal{L}^{W^\pm} = \frac{e}{\sqrt{2} \sin \theta_w} \left[\bar{\mathbf{u}} \gamma^\mu (1 - \gamma^5) W_\mu^+ (V_{CKM}) \mathbf{d} + \bar{\mathbf{d}} \gamma^\mu (1 - \gamma^5) W_\mu^- (V_{CKM})^\dagger \mathbf{u} \right], \quad (2.19)$$

Fermion (f)	Q	v_f	a_f
ν_e, ν_μ, ν_τ	0	$\frac{1}{2}$	$+\frac{1}{2}$
e, μ, τ	$-\frac{1}{2}$	$-\frac{1}{2} + 2\sin^2\theta_w$	$-\frac{1}{2}$
u, c, t	$+\frac{2}{3}$	$+\frac{1}{2} - \frac{4}{3}\sin^2\theta_w$	$+\frac{1}{2}$
d, s, b	$-\frac{1}{3}$	$-\frac{1}{2} + \frac{2}{3}\sin^2\theta_w$	$-\frac{1}{2}$

Table 2: Standard Model vector (v_f) and axial-vector (a_f) couplings for up-type and down-type fermions.

where W_μ^\pm are the W^\pm boson fields, V_{CKM} is the 3×3 Cabibbo-Kobayashi-Maskawa matrix that describes quark mixing (see equation 2.16), \mathbf{u} represents the up-type quarks (u, c, t) and \mathbf{d} the down-type quarks (d, s, b). The determination of the elements of the CKM matrix is the prime focus of this dissertation. We will return to this topic after completing the survey on the Standard Model.

2.1.2 Strong Interaction

The theory of the strong interaction, QCD, is based on the $SU(3)_C$ gauge symmetry group. The requirement of gauge invariance generates eight interacting terms, gluon fields, that mediate the strong force. The $SU(3)_C$ symmetry is exact and unbroken in QCD and therefore the gluons are massless. In electromagnetic interactions, the photon couples to the electric charge. In a similar fashion, gluons couple to the color charge in strong interactions. There are three types of color charges: red (r), green (g) and blue (b), and the corresponding anticolors. Since leptons do not carry color charge, they do not participate in strong interactions. A consequence of the non-Abelian nature of the $SU(3)_C$ symmetry group is that the gluons themselves carry color charges (color and anticolor). This allows the gluons to couple to other gluons. Color charge, like electric charge, is conserved

in all strong interactions. Figure 3 shows an example of quark-gluon coupling and conservation of color charge.

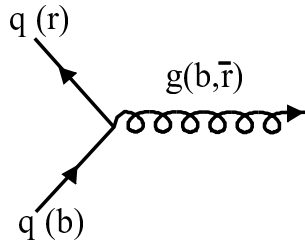


Figure 3: The Feynman diagram shows the coupling of quark to gluon. In this diagram, the quark changes from blue to red and the gluon carries away one unit of blueness to conserve color.

Experimentally, particles appear to come in colorless bound states. That is, quarks in $q\bar{q}$ states (mesons) always come in color-anticolor pairs. For baryons with three quarks, the quarks each carry a different color to form a color singlet state. The fact that no isolated quark with bare color has ever been observed in nature gives rise to the confinement concept. Although confinement is not explicitly demonstrated in QCD, a plausible explanation is that the potential energy between quarks increases with separation so that the quarks can never break free. Therefore, it is more energetically favorable to produce an extra $q\bar{q}$ pair than an isolated quark.

A unique feature of QCD is asymptotic freedom. It is found that the coupling constants in particle interactions are not really constants, they are “running constants”. In particular, the strength of the strong coupling constant α_s decreases as a function of energy due to the presence of self-interactions among gluons. The coupling α_s has the following first order dependence on Q^2 , the four-momentum transfer:

$$\alpha_s(Q^2) = \frac{4\pi}{(11 - \frac{2}{3}n_f)\log(\frac{Q^2}{\Lambda^2})}, \quad (2.20)$$

where n_f is the number of quark flavors involved and Λ is the fundamental QCD

scale ($\Lambda_{QCD} \approx 200$ MeV). For Q^2 approaching the fundamental QCD scale, the strong coupling constant becomes large. For an energy scale of about 1 GeV, the typical hadron mass, α_s is greater than one. This is in the region where the QCD calculations based on perturbation theory fail. One of the few available tools to make calculations in the non-perturbative region is the numerical technique called Lattice Gauge theory [15]. This technique has made tremendous progress in recent years but the application is still very limited. In cases where Lattice QCD has made predictions, the results are often hindered by a large uncertainty. At the energy scale near the Z^0 mass of 91 GeV, the strong coupling constant α_s is approximately equal to 0.12, which is sufficiently small that perturbation theory may be applied to hard processes with $Q^2 \gg \Lambda_{QCD}$.

The success of QCD rests not only on solid theoretical foundation of gauge symmetry but also on experimental verifications. However, to fully exploit the framework, progress in computational technique, especially for soft processes, is needed. This is a challenge for the theoretical community.

2.2 CP Violation in the Standard Model

A process is said to violate CP symmetry if its rate and the rate of the CP-conjugate process are different,

$$\begin{aligned}
 A \rightarrow f & \stackrel{CP}{\rightleftharpoons} \bar{A} \rightarrow \bar{f} \\
 \Gamma(A \rightarrow f) & \neq \Gamma(\bar{A} \rightarrow \bar{f}).
 \end{aligned}
 \tag{2.21}$$

This can occur if there exists a relative complex phase between two amplitudes leading to the same final state (for a pedagogical discussion see [16]). The matrix element for the process illustrated in figure 4 can be written as $M = M_1 + e^{-i\phi}M_2$,

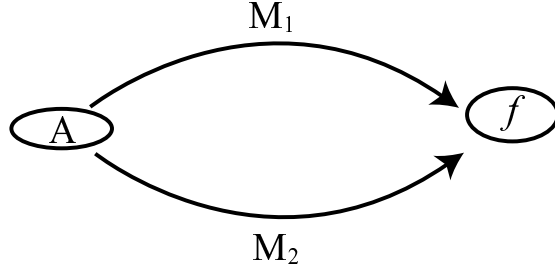


Figure 4: Two different paths of $A \rightarrow f$ with amplitudes M_1 and M_2 .

where ϕ is the relative complex phase between amplitudes M_1 and M_2 . The rate of the process is given by the square of the total amplitude M ,

$$R = MM^* = M_1M_1^* + M_2M_2^* + M_1M_2^*e^{-i\phi} + M_1^*M_2e^{+i\phi}. \quad (2.22)$$

For the amplitude of the CP-conjugate process, the complex phase changes sign,

$$M \xrightarrow{CP} \bar{M} = M_1 + e^{+i\phi}M_2, \quad (2.23)$$

and the transition rate is

$$\bar{R} = \bar{M}\bar{M}^* = M_1M_1^* + M_2M_2^* + M_1M_2^*e^{+i\phi} + M_1^*M_2e^{-i\phi}. \quad (2.24)$$

Now it is clear that there are three conditions for CP violation to occur in a given process:

- there has to be more than one way to go from the initial state to the final state to generate the interference term,
- the amplitudes M_1 and M_2 are complex (CP conserving phases) and
- there is a relative CP violating phase ϕ between the two amplitudes.

There are generally higher order processes that result in the same final states as the tree level decay and therefore the first condition is readily satisfied. An example of

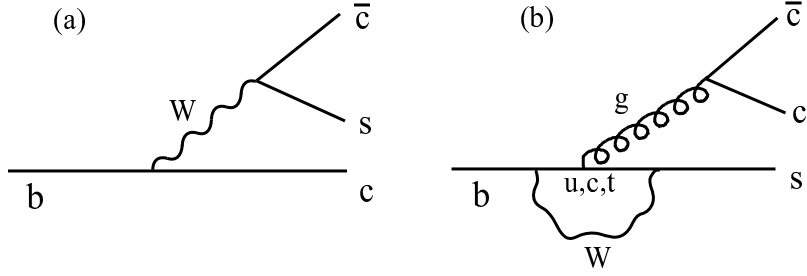


Figure 5: Feynman diagrams of b decay. Diagram (a) shows the tree level decay of b quark to $c\bar{c}s$. Diagram (b) shows the electroweak penguin decay of b quark to the same final states.

this type of decay is illustrated in figure 5. The second condition can be satisfied by strong interaction phases which are invariant under CP. We will discuss in the next section that the final requirement may be fulfilled by the complex phase in the quark mixing matrix for three generations of quarks.

There is another method to generate the required CP violating interference term. Instead of relying on the decay amplitudes, interference can occur through mixing. Figure 6 shows the decay of B^0 to the CP eigenstate of $\pi^+\pi^-$. The same final state is also accessible to \bar{B}^0 . This type of process could potentially generate CP violation if the two amplitudes have a non-vanishing relative phase. Similar to the previous example, the latter condition could be met by the complex phase in the CKM matrix.

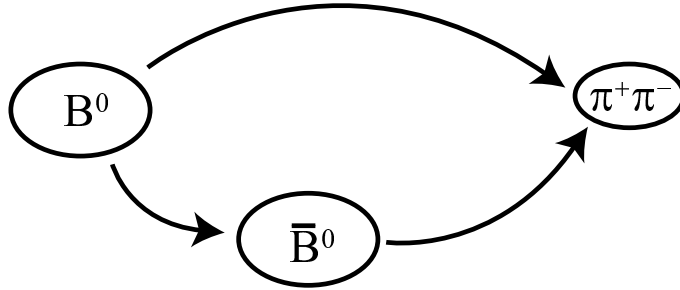


Figure 6: The decay of B^0 to CP eigenstate ($\pi^+\pi^-$) with and without mixing.

2.2.1 CKM Matrix

A consequence of the Higgs mechanism is that the quark weak eigenstates are not the same as the physical mass eigenstates. Instead of coupling to the physical mass eigenstates (u, d, c, s, t, b) , the charged weak currents couple to the weak eigenstates (u, d', c, s', t, b') . This induces mixing in the quark sector and allows transition between generations to occur. By convention, we rotate the down-type quarks and express the weak eigenstates as orthogonal combinations of the physical quark eigenstates:

$$|d'\rangle = V_{CKM} \cdot |d\rangle \Rightarrow \begin{pmatrix} d' \\ s' \\ b' \end{pmatrix} = \begin{pmatrix} V_{ud} & V_{us} & V_{ub} \\ V_{cd} & V_{cs} & V_{cb} \\ V_{td} & V_{ts} & V_{tb} \end{pmatrix} \begin{pmatrix} d \\ s \\ b \end{pmatrix}. \quad (2.25)$$

The CKM matrix is a unitary matrix whose elements describe the strength of the couplings between up-type and down-type quarks. In principle, there are 18 parameters: 9 magnitudes and 9 phases. After applying the unitarity constraint and removing arbitrary phases, the number of independent parameters is reduced to four: three rotation angles and one phase. This phase, if non-zero, could explain the existence of CP violation in the Standard Model. This was the original motivation for Kobayashi and Maskawa to propose the third generation of quarks before the bottom quark was discovered [17]. They recognized that the phase could only occur in the mixing matrix if there are three or more generations of quark (for 2 generations of quarks the matrix elements are all real).

A popular approximation of the CKM matrix is the Wolfenstein parameterization [18]:

$$V_{CKM} \approx \begin{pmatrix} 1 - \lambda^2/2 & \lambda & A\lambda^3(\rho - i\eta) \\ -\lambda & 1 - \lambda^2/2 & A\lambda^2 \\ A\lambda^3(1 - \rho - i\eta) & -A\lambda^2 & 1 \end{pmatrix} + \mathcal{O}(\lambda^4). \quad (2.26)$$

In this parameterization, the 3 real parameters are A , ρ , λ , and the complex term is η . The CKM elements are expressed explicitly in powers of λ ($\lambda = \sin \theta_{Cabibbo} \approx 0.23$), thus the relative magnitudes between the various elements are quite apparent (the other parameters are of order 1).

The Standard Model does not offer any insight on the values of the matrix elements. They all have to be determined experimentally. The values obtained from current experiments are shown below. The range of values corresponds to 90% confidence limits [19]:

$$V_{CKM} = \begin{pmatrix} 0.9742 - 0.9757 & 0.219 - 0.226 & 0.002 - 0.005 \\ 0.219 - 0.225 & 0.9734 - 0.9749 & 0.037 - 0.043 \\ 0.004 - 0.014 & 0.035 - 0.043 & 0.9990 - 0.9993 \end{pmatrix} \quad (2.27)$$

The diagonal elements are for transitions within the same generation. As expected, the values are of order unity. The off-diagonal elements describe transitions across generations. The two least known elements are V_{ub} and V_{td} . These two elements also harbor the most significant imaginary parts. To resolve the CP violation question, V_{ub} and V_{td} will have to be determined to a much better precision.

The elements V_{ub} and V_{td} are related by one of the unitarity constraint equations:

$$V_{ub}^* V_{ud} + V_{cb}^* V_{cd} + V_{tb}^* V_{td} = 0. \quad (2.28)$$

This relation can be expressed as a triangle on the complex plane as shown in figure 7. This triangle is the least degenerate and contains the largest complex term among the six triangle relations. It is often referred to as the Unitarity Triangle. The apex of the normalized triangle is denoted by the Wolfenstein parameters ρ and η , with η being the imaginary term. The Unitarity Triangle provides a natural arena to test the Standard Model. If the Standard Model is to stand on firm footing, two conditions have to be satisfied: 1.) the Unitarity Triangle is closed,

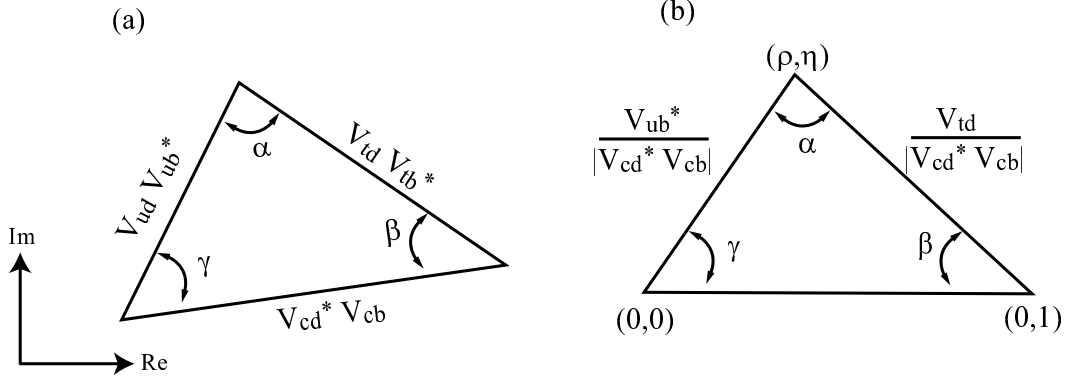


Figure 7: The Unitarity Triangle. Triangle (a) illustrates the unitarity constraints. Triangle (b) is normalized to $|V_{cd}^* V_{cb}|$ so that the base is real and with a unit length.

i.e. $\alpha + \beta + \gamma = 180^\circ$ and 2.) $\eta \neq 0$. The first condition comes from the unitarity constraint of the CKM matrix. If it is found otherwise, it may imply that there is an additional generation of quarks or other interactions. The second condition is needed for CP violation to occur. If η is found to be zero, then the Standard Model in the current form cannot accommodate CP violation. The observed CP violation would have to come from sources beyond the Standard Model.

2.2.2 Phenomenology of $B^0 - \bar{B}^0$ Oscillations

We have discussed in the previous section the importance of measuring CKM matrix elements. We now turn our attention to the phenomenology of B^0 mixing. Our discussion here applies to both B_d^0 and B_s^0 oscillations. We will show that measuring both B_s^0 and B_d^0 mixing is the most promising approach to extract the matrix element $|V_{td}|$.

The oscillation of B^0 mesons comes about due to the fact that the mass eigenstates have different time evolution and the states are not the same as the weak

eigenstates. The time evolution of the system is described by the time dependent Schrödinger equation:

$$\begin{aligned}
i \frac{\partial}{\partial t} \begin{pmatrix} B^0 \\ \bar{B}^0 \end{pmatrix} &= \begin{bmatrix} H_{11} & H_{12} \\ H_{21} & H_{22} \end{bmatrix} \begin{pmatrix} B^0 \\ \bar{B}^0 \end{pmatrix} \\
&= \begin{bmatrix} M - \frac{i}{2}\Gamma & M_{12} - \frac{i}{2}\Gamma_{12} \\ M_{12}^* - \frac{i}{2}\Gamma_{12}^* & M - \frac{i}{2}\Gamma \end{bmatrix} \begin{pmatrix} B^0 \\ \bar{B}^0 \end{pmatrix},
\end{aligned} \tag{2.29}$$

where the diagonal elements M and Γ correspond to the mass and the decay width of the B^0 and \bar{B}^0 , respectively. Invariance under the combined operations of Charge, Parity and Time Reversal (CPT) requires H_{11} and H_{22} to be the same. The off-diagonal term M_{12} corresponds to virtual B^0 - \bar{B}^0 transitions and Γ_{12} corresponds to on-shell transitions. An example of on-shell transition is $B^0 \rightarrow \pi^+ \pi^- \rightarrow \bar{B}^0$. In the Standard Model, M_{12} is expected to be large compared to Γ_{12} [20]. Therefore, unlike the $K^0 - \bar{K}^0$ system where mixing is driven by on-shell transitions, B^0 mixing is dominated by virtual transitions via box diagrams (see figure 8).

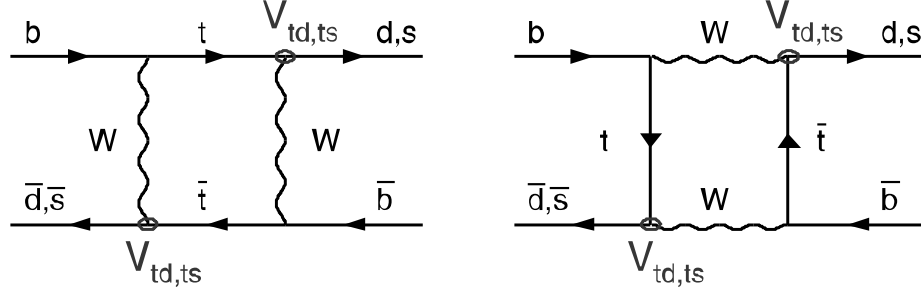


Figure 8: The box diagrams for B_d^0 and B_s^0 oscillations. The diagrams with virtual top quarks in the intermediate loop are the dominant contributions to M_{12} .

To obtain the weak eigenstates, we diagonalize the Hamiltonian in equation 2.29.

We obtain,

$$|B_L\rangle = \frac{1}{\sqrt{p^2 + q^2}} (p|B^0\rangle + q|\bar{B}^0\rangle), \tag{2.30}$$

$$|B_H\rangle = \frac{1}{\sqrt{p^2 + q^2}} (p|B^0\rangle - q|\bar{B}^0\rangle),$$

where $|B_L\rangle$ is the light mass eigenstate, $|B_H\rangle$ is the heavy mass eigenstate, $p^2 = iH_{12}$ and $q^2 = iH_{21}$. Ignoring the effect of CP violation in mixing (assuming $|p/q| = 1$), which is expected to be small in the $B^0 - \bar{B}^0$ system, the weak eigenstates also become CP eigenstates (B_1 and B_2):

$$\begin{aligned} |B_L\rangle \rightarrow |B_1\rangle &= \frac{1}{\sqrt{2}} (|B^0\rangle + |\bar{B}^0\rangle), \\ |B_H\rangle \rightarrow |B_2\rangle &= \frac{1}{\sqrt{2}} (|B^0\rangle - |\bar{B}^0\rangle). \end{aligned} \quad (2.31)$$

The eigenvalues of the Hamiltonian are $m_{1,2} - i\frac{\Gamma_{1,2}}{2}$ where,

$$\begin{aligned} m_{1,2} &= M \pm \frac{\Delta m}{2}, \\ \Gamma_{1,2} &= \Gamma \pm \frac{\Delta \Gamma}{2}. \end{aligned} \quad (2.32)$$

The mass and the decay rate differences between the eigenstates are:

$$\begin{aligned} \Delta m &= m_2 - m_1 = 2 \operatorname{Re} \sqrt{\left(M_{12} - \frac{\Gamma_{12}}{2}\right) \left(M_{12}^* - \frac{\Gamma_{12}^*}{2}\right)}, \\ \Delta \Gamma &= \Gamma_2 - \Gamma_1 = -4 \operatorname{Im} \sqrt{\left(M_{12} - \frac{\Gamma_{12}}{2}\right) \left(M_{12}^* - \frac{\Gamma_{12}^*}{2}\right)}. \end{aligned} \quad (2.33)$$

To obtain the time evolution of the B^0 state, we first invert equations 2.31 to express B^0 as a linear combination of $B_{1,2}$ and then apply the time evolution operator to the $|B^0(t=0)\rangle$ state. The resulting expression is:

$$|B^0(t)\rangle = \frac{1}{\sqrt{2}} e^{(-im_1 t - \Gamma_1 t/2)} |B_1(t=0)\rangle + \frac{1}{\sqrt{2}} e^{(-im_2 t - \Gamma_2 t/2)} |B_2(t=0)\rangle. \quad (2.34)$$

Finally, we can derive the probability for B^0 to decay as B^0 (unmixed) or \bar{B}^0 (mixed) as a function of time. The probability distributions are:

$$\begin{aligned} P_{unmixed}(t) &= |\langle B^0 | B^0 \rangle|^2 = \frac{1}{4} \left(e^{-\Gamma_1 t} + e^{-\Gamma_2 t} + 2e^{-\Gamma t} \cos \Delta m t \right) \\ P_{mixed}(t) &= |\langle \bar{B}^0 | B^0 \rangle|^2 = \frac{1}{4} \left(e^{-\Gamma_1 t} + e^{-\Gamma_2 t} - 2e^{-\Gamma t} \cos \Delta m t \right), \end{aligned} \quad (2.35)$$

where Γ is the average decay rate ($\frac{\Gamma_1+\Gamma_2}{2}$). In the limit of $\Delta\Gamma \ll \Delta m$, equations 2.35 are reduced to:

$$\begin{aligned} P_{unmixed}(t) &= \frac{1}{2}e^{-\Gamma t}(1 + \cos \Delta m t), \\ P_{mixed}(t) &= \frac{1}{2}e^{-\Gamma t}(1 - \cos \Delta m t). \end{aligned} \quad (2.36)$$

The probability distributions for mixed and unmixed events are shown in figure 9.

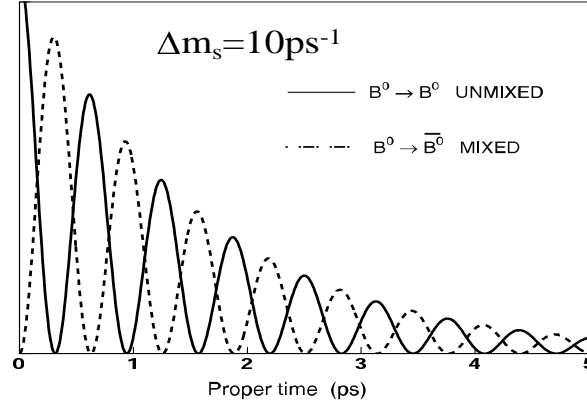


Figure 9: Probability distribution functions for mixed and unmixed events with generated Δm_s of 10 psec^{-1} and B_s^0 lifetime of 1.57 psec .

The frequency of oscillations for the B^0 meson is the mass difference between the mass eigenstates. For the B_d^0 system, the mass difference is denoted by Δm_d and for the B_s^0 system, the chosen notation is Δm_s .

The mass difference, Δm , can be calculated from the box diagrams (figure 8). For Δm_d , the expression is [21],

$$\Delta m_d = \frac{G_F^2}{6\pi^2} \eta_B m_{B_d} m_W^2 f_{B_d}^2 B_{B_d} S_0\left(\frac{m_t^2}{m_W^2}\right) |V_{td} V_{tb}^*|^2, \quad (2.37)$$

where G_f is the Fermi constant, η_B is the QCD correction factor that accounts for the strong interaction at short distances, m_{B_d} is the mass of B_d^0 , m_W is the mass of the W boson, f_{B_d} is the B_d^0 decay constant, B_{B_d} is the bag parameter that

corrects for the vacuum insertion approximation, and S_0 is a kinematic function.

The kinematic function has the form,

$$S_0(z) = \frac{1}{4} + \frac{9}{4(1-z)} - \frac{3}{2(1-z)^2} - \frac{3z^2 \ln(z)}{2(1-z)^3}. \quad (2.38)$$

The mass difference, Δm_d , has been measured to about 2%. The recent world average on Δm_d is $0.484 \pm 0.010 \text{ psec}^{-1}$ [72]. It may appear that with a measurement of Δm_d , equation 2.37 can be used to extract the CKM matrix element $|V_{td}|$. However, there are large theoretical uncertainties associated with the non-perturbative QCD factors, in particular, the value $f_{B_d} \sqrt{B_{B_d}}$ obtained from the Lattice calculation has an uncertainty on the order of 20%. Without further improvement on the theoretical inputs, the extraction of $|V_{td}|$ from Δm_d is severely limited. The problem can be circumvented if one measures the ratio of Δm_d and Δm_s . As shown below, in the ratio, many theoretical uncertainties cancel and that allows one to extract $|V_{td}|$ to about 5%.

$$\frac{\Delta m_s}{\Delta m_d} = \frac{m_{B_s} f_{B_s}^2 B_{B_s}}{m_{B_d} f_{B_d}^2 B_{B_d}} \left| \frac{V_{ts}}{V_{td}} \right|^2 = (1.14 \pm 0.06) \left| \frac{V_{ts}}{V_{td}} \right|^2. \quad (2.39)$$

The B_s^0 oscillation frequency is expected to be large in the Standard Model. In the Wolfenstein parameterization, Δm_d is proportional to λ^6 and Δm_s is proportional to λ^4 ($\lambda \approx 0.23$). Therefore, based on naive coupling analysis (ignoring QCD effects and assuming $|1 - \rho - i\eta| \approx 1$), Δm_s is about 20 times larger than Δm_d .

2.2.3 Experimental Constraints on $\rho - \eta$

The major challenge in B physics for the coming decade is to perform precision measurements of the CKM matrix elements. The experimental goal is to over-constrain the Unitarity Triangle by measuring all three sides and all three internal

angles. Any detected inconsistency in the triangle relation may be a hint of new physics.

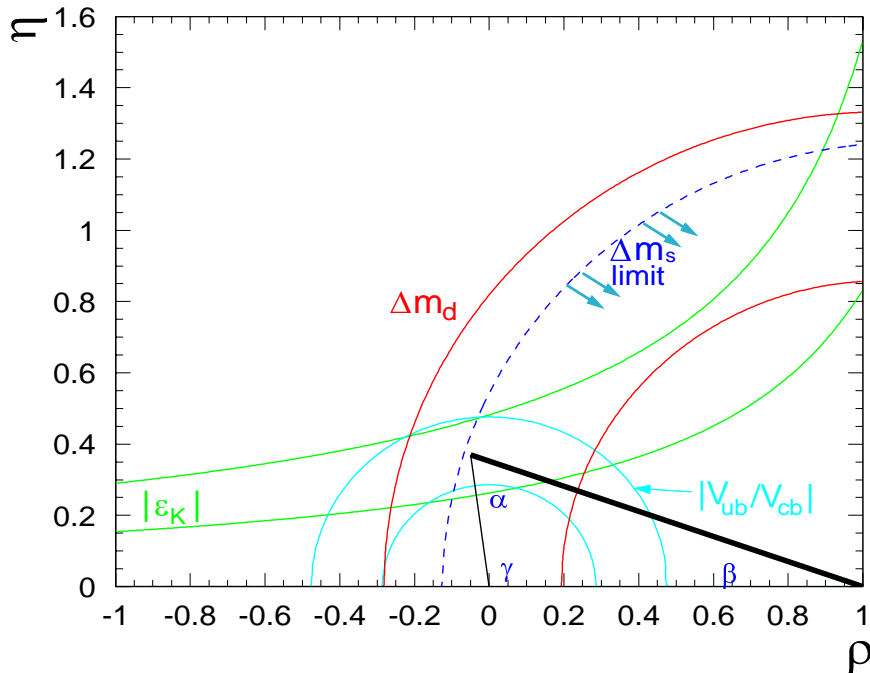


Figure 10: An illustration of the various constraints on the apex of the Unitarity Triangle.

Figure 10 illustrates the various experimental constraints on the apex of the Unitarity Triangle (ρ, η) . The angle β is currently the only internal angle of the Unitarity Triangle that is directly accessible by experiments. In fact, the BaBar experiment at SLAC and the Belle experiment at KEK in Japan have recently reported $\sin(2\beta)$ values of 0.59 ± 0.14 and 0.99 ± 0.15 , respectively [22]. The results are of particular importance since they not only establish for the first time the presence of CP violation in the B system, they also constrain the η parameter in the non-zero region. The $\sin(2\beta)$ value is obtained from measuring the rate asymmetry between the decays of $B^0 \rightarrow J/\psi K_s^0$ and $\bar{B}^0 \rightarrow J/\psi K_s^0$. The time

dependent asymmetry is given by [23],

$$\frac{\Gamma(B^0 \rightarrow J/\psi K_s^0) - \Gamma(\bar{B}^0 \rightarrow J/\psi K_s^0)}{\Gamma(B^0 \rightarrow J/\psi K_s^0) + \Gamma(\bar{B}^0 \rightarrow J/\psi K_s^0)} \propto \sin(2\beta) \sin(\Delta m_d t). \quad (2.40)$$

The ratio of $|V_{ub}|$ and $|V_{cb}|$ is proportional to $\sqrt{\rho^2 + \eta^2}$. Therefore it defines the circular band on the $\rho - \eta$ plot centered at the origin with a width that is given by the uncertainty on the ratio. There are two approaches to measure V_{cb} : inclusive and exclusive [62]. For the inclusive method, the partial width for semileptonic B decay to charm mesons is related to $|V_{cb}|$ using the expression obtained from the heavy quark expansion:

$$|V_{cb}| = 0.044 \times \sqrt{\frac{(Br(b \rightarrow cl\nu) \times 1.55ps)}{(0.105 \times \tau_b)}}. \quad (2.41)$$

In the exclusive method, the value of $|V_{cb}|$ is extracted by measuring the differential decay rate for $B_d^0 \rightarrow D^{*-} l^+ \nu$ as a function of ω , where ω is the four-momentum product of D^{*-} and B_d^0 . The differential decay rate for the decay is given by:

$$\frac{d\Gamma}{d\omega} = K(\omega) F^2(\omega) |V_{cb}|^2, \quad (2.42)$$

where K is the kinematic phase space term and F is the hadronic form factor of the decay. The unknown term in the expression is the form factor. However, it can be calculated in the heavy quark limit at $\omega=1$, which corresponds to the scenario where the D^{*-} is at rest in the B_d^0 rest frame. Experimentally, one measures the differential decay rate near the kinematic endpoint and extrapolates to $\omega=1$ to obtain the value of $|V_{cb}|$.

Similar to the inclusive $|V_{cb}|$ analyses, the element $|V_{ub}|$ can be extracted by measuring the rate of charmless B decays. One could either measure the inclusive $b \rightarrow u$ or exclusive (e.g. $B^0 \rightarrow \rho l \nu$) decay rates [23]. The inclusive approach has the advantage of larger statistics and less model dependence compared to the exclusive analyses.

CP violation in K^0 - \bar{K}^0 mixing can also contribute to the overall determination of the Unitarity Triangle. The parameter ϵ_K describes the CP violating effect in the kaon system. It is given as,

$$\epsilon_K = \frac{e^{i\pi/4}}{\sqrt{2}} \frac{\text{Im } M_{12}}{\Delta m_K}, \quad (2.43)$$

where Δm_K is the mass difference between K_L^0 and K_S^0 , and M_{12} is related to the box diagram for K^0 mixing. By evaluating the matrix element M_{12} and substituting the result into equation 2.43, one could obtain the expression [23]:

$$\eta(1 - \rho) + \eta\xi_1 = \xi_2, \quad (2.44)$$

where $\xi_{1,2}$ are parameters derived from experimental and theoretical inputs. Equation 2.44 specifies the hyperbola on the ρ - η plane (figure 10). The width of the hyperbola band is defined by the uncertainties in ξ_1 and ξ_2 .

As discussed in the previous section, Δm_d is proportional to the matrix element $|V_{td}|$, or in the Wolfenstein parameterization, $\sqrt{(1 - \rho)^2 + \eta^2}$. This defines a circle on the $\rho - \eta$ plane centered at (1,0). The Δm_d input effectively constrains the magnitude of the right side of the Unitarity Triangle. In the absence of a direct Δm_s measurement, the limit on the ratio $\Delta m_s/\Delta m_d$ translates to a tight upper bound on the right side of the Unitarity Triangle.

The constraints from $|V_{td}|$ and the angle β on the apex of the Unitarity Triangle are mutually orthogonal. These two parameters are likely to be the first two well-measured parameters on the triangle relation and could provide strong constraints on the values of ρ and η . The result of the global fit on the apex of the Unitarity Triangle using recent experimental and theoretical inputs is given in the conclusion chapter.

2.3 Polarized $Z^0 \rightarrow f\bar{f}$ Decays

We conclude this chapter with a discussion on the physics of $e^+e^- \rightarrow Z^0 \rightarrow f\bar{f}$ decays. This discussion will naturally lead us to the next chapter on experimental apparatus.

There are two processes that could occur at the e^+e^- collision point. These processes are shown in figure 11. At the Z^0 pole, the cross section is dominated

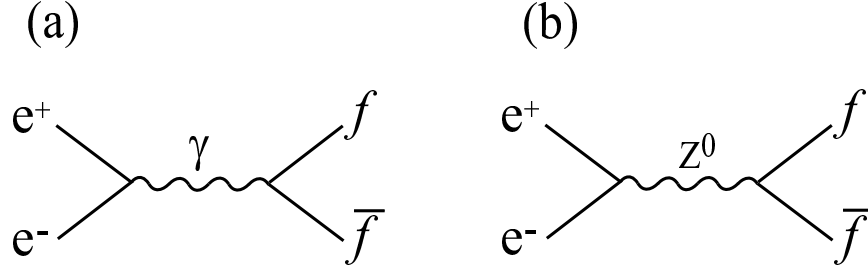


Figure 11: The Feynman diagrams for $e^+e^- \rightarrow$ (a) $\gamma \rightarrow f\bar{f}$ and (b) $Z^0 \rightarrow f\bar{f}$ decays.

by the Z^0 production diagram and therefore the photon exchange term may be neglected. The differential cross section at the Z^0 in the center of mass frame is given by (ignoring γ and $\gamma - Z^0$ interference contributions) [11]:

$$\frac{d\sigma}{d\Omega} = \frac{1}{64\pi^2 s} \frac{p_f}{p_i} |\mathcal{M}_Z|^2, \quad (2.45)$$

where \sqrt{s} equals the total energy in the center of mass frame, p_i (p_f) is the momentum of the incoming (outgoing) particle and \mathcal{M}_Z is the scattering amplitude for the process shown in figure 11b. The scattering amplitude is given by:

$$\mathcal{M}_Z = -\frac{g^2}{4\cos^2\theta_w} [\bar{f}\gamma^\mu(v_f - a_f\gamma^5)f] \left(\frac{g_{\mu\nu} - k_\mu k_\nu / M_Z^2}{k^2 - M_Z^2} \right) [\bar{e}\gamma^\nu(v_e - a_e\gamma^5)e], \quad (2.46)$$

where f (e) is the fermion (electron) field, $g_{\mu\nu}$ is the metric tensor, k is the four-momentum of the Z^0 and M_Z is the mass of the Z^0 . The differential cross section

evaluated for the case of polarized electron beams is then,

$$\frac{d\sigma}{d\cos\theta} \propto (1 - A_e P_e)(1 + \cos^2\theta) + 2A_f(A_e + P_e)\cos\theta, \quad (2.47)$$

where $A_f = 2a_f v_f(a_f^2 + v_f^2)$ and θ is defined as the angle between the outgoing fermion and the electron direction. The electron polarization P_e is defined as:

$$P_e = \frac{N(R) - N(L)}{N(R) + N(L)}, \quad (2.48)$$

where $N(R)$ ($N(L)$) is the number of right-handed (left-handed) electrons in a beam bunch.

An important feature of the differential cross section given in equation 2.47 is that the total cross section is larger for left-handed polarized beams, i.e. the Z^0 boson preferentially couples to the left-handed fermions. This is due to the parity violating nature of the weak interactions. The difference between right-handed and left-handed cross sections is known as A_{LR} and it is related to the fundamental parameter $\sin^2\theta_w$, the weak mixing angle,

$$A_{LR} = \frac{\sigma_L - \sigma_R}{\sigma_L + \sigma_R} \quad (2.49)$$

$$= \frac{2(1 - 4\sin^2\theta_w)}{1 + (4\sin^2\theta_w)^2}. \quad (2.50)$$

Experimentally, the measured quantity is,

$$A_{LR}^{measured} = \frac{n_L - n_R}{n_L + n_R} \quad (2.51)$$

$$= |P_e|A_{LR}, \quad (2.52)$$

where n_L and n_R are the number of Z^0 produced for left-handed and right-handed polarized electron beam, and $|P_e|$ is the average polarization of the electron beam. The measurement of A_{LR} is the most direct and clean method to extract the weak mixing angle. Using this technique, the SLD experiment has produced the best single measurement of $\sin^2\theta_w$.

Another important feature to note is that the differential cross section is asymmetric between forward ($\theta > 0$) and backward ($\theta < 0$) scattering events. This is due to the second term in expression 2.47 which has a linear dependence on $\cos \theta$. Consequently, for left-handed polarized electron beams ($P_e < 0$), the outgoing fermion from the Z^0 decay is more likely to decay along the same direction as the outgoing electron beam (fermion decay direction is reversed for right-handed beam polarization). Figure 12 shows the differential cross section for b quark versus $\cos \theta$ for three different polarization values. The strong dependence of the cross

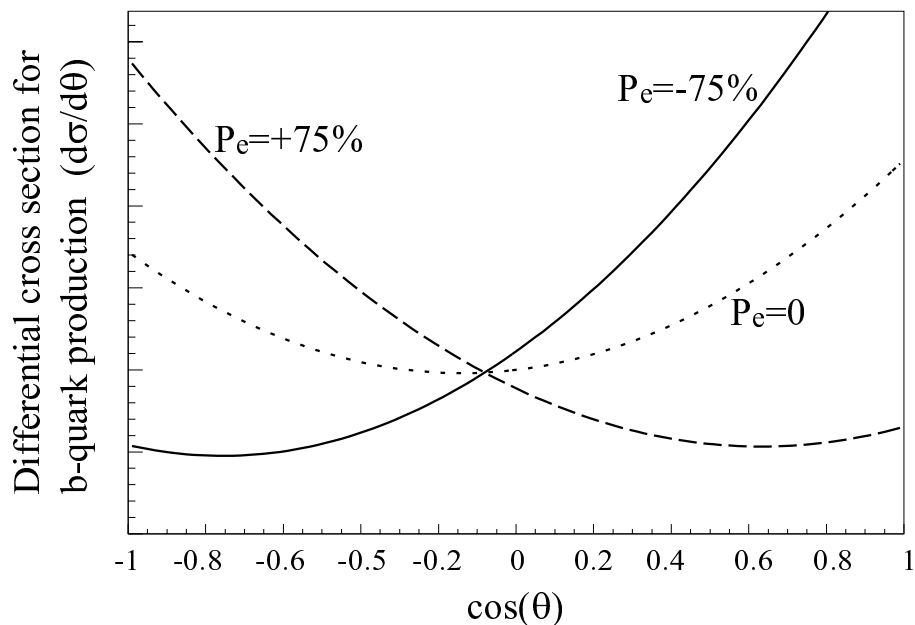


Figure 12: The plot shows the differential b quark production cross section as a function of $\cos \theta$ for three polarization values ($P_e = 75\%$, -75% and 0). The angle θ is defined as the angle between the b quark momentum and the outgoing electron beam direction.

section on the beam polarization can be clearly seen. This behavior, referred to as the polarized forward-backward asymmetry, is exploited at SLD to determine the flavor of the initial quark. This initial state tag is extremely powerful (average correct tag probability of about 72%) and it is unique to SLD.

CHAPTER 3

EXPERIMENTAL APPARATUS

The Stanford Linear Accelerator Center (SLAC) is the home of the largest linear accelerator in the world. The research program began at SLAC in 1966 with the completion of the two-mile long linear accelerator (LINAC). The initial LINAC was designed to accelerate electron beams to 20 GeV and was used in a series of fixed target experiments. In 1983, shortly after the discovery of Z^0 boson at CERN, SLAC embarked on an ambitious project of converting the LINAC to an unique single-pass collider dedicated to the production of Z^0 bosons. The project involved upgrading the LINAC to accelerate electron and positron beams to ~ 45 GeV and constructing a pair of semi-circular arcs at the end of the LINAC to transport the beams to a head-on collision. The collider was named the SLAC Linear Collider (SLC). A corresponding state-of-the-art detector, the SLC Large Detector (SLD) was constructed and placed at the beam collision point to study the detailed properties of the Z^0 boson. The physics data collection began at SLD in 1992 and continued for the next six years. By the end of the run in 1998, over half a million $Z^0 \rightarrow q\bar{q}$ events were recorded by the detector with electron polarization as high as 78%.

In this chapter, we will give a broad overview of the SLC and the SLD detector. A detailed description of the collider can be found in [25] and the detector in [26].

3.1 SLAC Linear Collider

The SLC is a prototype of a new class of machines (linear colliders) that accelerate particles in a straight path as opposed to the traditional storage ring colliders, which maintain particles in a circular orbit. In a storage ring, particles lose energy by emitting synchrotron radiation with an energy loss per turn [27],

$$E_{loss} = \frac{4\pi}{3} \frac{e^2}{R_{ring}} \beta^3 \gamma^4 \propto \frac{E_b^4}{R_{ring}}, \quad (3.1)$$

where E_b is the energy of the beam and R_{ring} is the radius of the storage ring. Therefore, to go to higher beam energy, the radius of the ring would have to be increased by a factor equal to the fourth power of the energy ratio ($E_b^{new}/E_b^{nominal}$) to keep the synchrotron radiation loss at a constant level. Synchrotron radiation loss at a linear collider is negligible in comparison, thus it is the only available type of collider that can realistically push e^+e^- experiments to the TeV energy frontier. Since particles have only one chance to collide (single-pass) at a linear collider, the major challenge for the linear collider instead, is to achieve a high rate of collision.

The SLC is a variant of the linear collider. As shown in figure 13, the same LINAC is used to accelerate the electron and positron bunches. A true linear collider, similar to the current design of potential future machines (NLC, TESLA, and JLC [28]), would have two linear accelerators facing directly at each other. This would eliminate the need to build a pair of transport arcs and avoid the problem of synchrotron radiation loss in the arcs. The SLC, nominally completed in 1987, had a prolonged and difficult commissioning period. The principle challenge was to achieve the desired luminosity. The luminosity L for a linear collider is

$$L \propto \frac{N^+ N^- f_c}{(\beta_x \beta_y \epsilon_x \epsilon_y)^{1/2}}, \quad (3.2)$$

where N^+ and N^- are the number of positrons and electrons in a colliding bunch

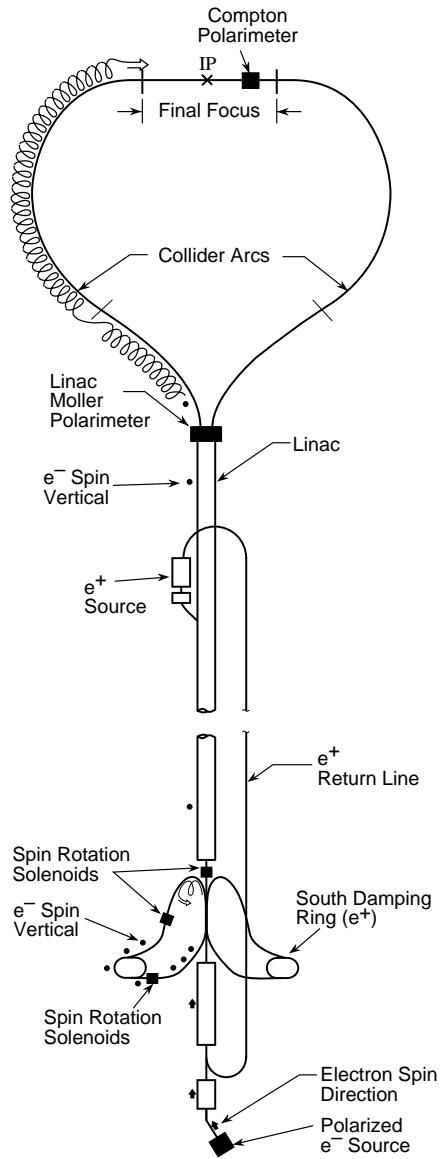


Figure 13: Schematic of the SLC complex showing the various components and transport lines. The orientation of the electron spin along the SLC path is shown in arrows.

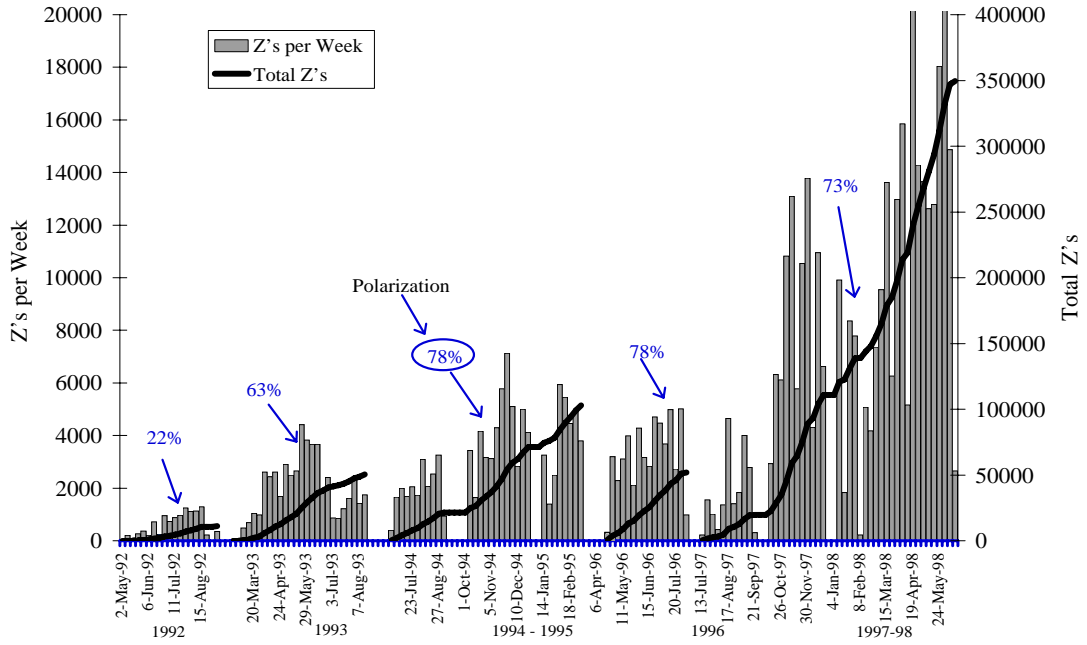
and f_c is the beam crossing frequency. The parameters $\beta_{x,y}^*$ are the beta functions and $\epsilon_{x,y}^*$ are the beam emittances. These four parameters in the denominator of equation 3.2 essentially define the size of the beam spot (in x and y) at the collision point. Many approaches were employed to improve the luminosity of the machine over the years. The efforts included raising the beam currents (higher N^+ and N^-), reducing the beam emittances (smaller beam size) and adding complex beam-control feedback systems to improve machine stability [29]. With better understanding of the complexity of the machine, the luminosity rose steadily over the years. The results can be seen in the luminosity history plot shown in figure 14. The peak luminosity achieved in 1992 was $30 Z^0/\text{hour}$ and by the end of the run in 1998, the peak luminosity surpassed $300 Z^0/\text{hour}$, a factor of ten improvement.

3.1.1 SLC Machine Cycle

The SLC operates at 120 Hz cycle. This frequency is fixed by the AC power distribution to the LINAC klystrons. At the start of each machine cycle, two polarized electron bunches are produced by photoemission from a GaAs photocathode [30]. The photoemissions are induced by shining circularly polarized light from two Nd:YAG-pumped Ti:sapphire lasers firing about 60 *nsec* apart at every cycle (see figure 15). From 1993 onward, a strained-lattice GaAs photocathode (figure 16) is used instead of the bulk GaAs. The strained GaAs photocathode has a maximum theoretical polarization of 100%, but in practice, the maximum polarization obtained is about 80%.

The two bunches of longitudinally polarized electrons from the photocathode (each bunch contains $\approx 7 \times 10^{10}$ particles) are accelerated to 1.2 GeV in the main LINAC before injecting into the north damping ring. To preserve the electron

1992 - 1998 SLD Polarized Beam Running



Vanda 6/22/98

Figure 14: Luminosity history of SLC recorded by the SLD detector. The histograms show the total number of Z^0 produced per week from 1992 to 1998. The solid black line shows the total integrated Z^0 count for the particular run period. The average electron beam polarization values are also indicated on the plot.

polarization, the spin of the electrons are rotated from longitudinal to vertical direction before entering the damping ring. The two electron bunches are stored in the ring for one full machine cycle (1/120 sec) to reduce the beam emittance through emission of synchrotron radiation. The two electron bunches are then re-injected back into the main LINAC along with a positron bunch from the south damping ring produced in the previous machine cycle. The three bunches, with the positron leading the two electron bunches, are accelerated to about 33 GeV (2/3 way down the LINAC) at which point the trailing electron bunch, the scavenger bunch, is

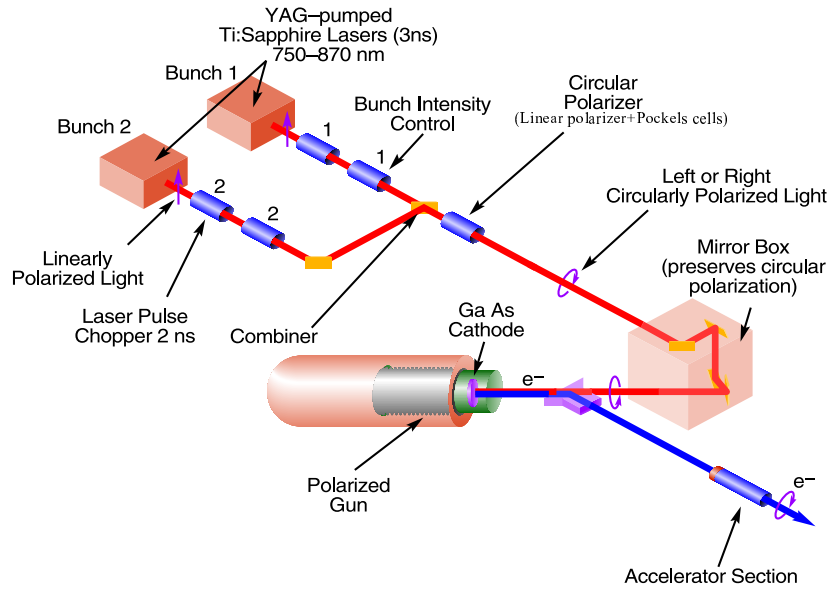


Figure 15: The schematic of the polarized electron source. The two laser pulses from the Ti:Sapphire lasers (2 *nsec* long pulses) are circularly polarized with a linear polarizer and two Pockels cells (CP and PS). The helicity of the laser light is determined by the sign of the voltage applied to the CP Pockels cell. The resulting circular polarized laser pulses are directed onto the GaAs photocathode.

extracted from the LINAC and directed onto a water cooled tungsten-rhenium (W-26Re) target [31] to produce positrons. The resulting positrons from the electromagnetic showers are collected and accelerated to 200 MeV before transported to the south damping ring via the positron return line. The positrons are cooled in the damping ring for two machine cycles (1/60 sec). In the mean while, the two leading bunches continue down the LINAC and acquire the full energy of 46.7 GeV (≈ 1 GeV is later lost in the arc to synchrotron radiation). The 2-mile long LINAC is powered by 244 65-MW peak power S-band (2,856 GHz) klystrons [32] producing an acceleration gradient of 17 MeV/m. At the end of the LINAC, the electron and positron bunches are split apart at the Beam Switchyard by a dipole magnet and diverted into the 1-kilometer long north and south arcs respectively. At this

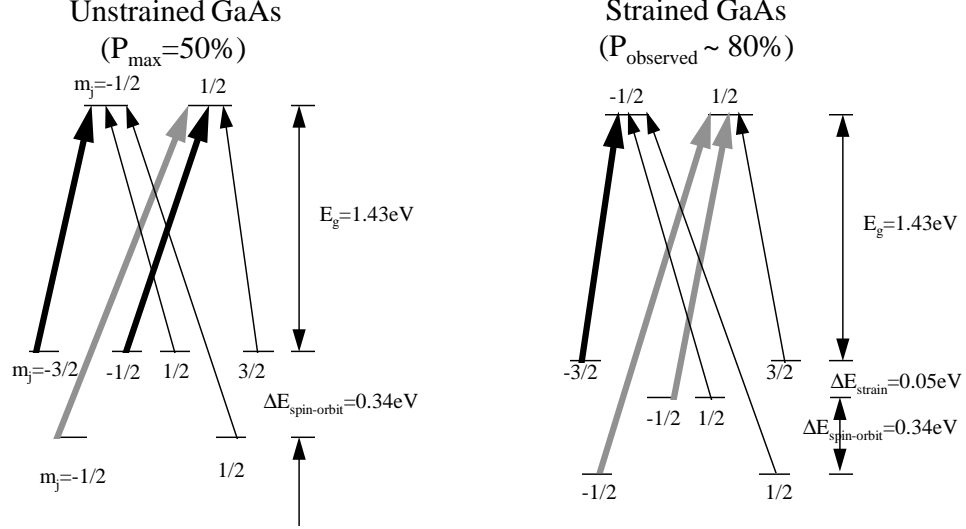


Figure 16: The energy levels of bulk GaAs (left) and strained GaAs (right). For the strained GaAs, the degeneracy between $m_j = \pm 3/2$ and $m_j = \pm 1/2$ valence levels are split by about 0.05 eV, thus allowing a maximum theoretical polarization of 100%.

point, the electron polarization is still aligned in the vertical direction. To steer the polarization back to the longitudinal direction, “spin bumps” are introduced in the north transport arc [33]. The fact that the betatron oscillation of the transport arc is close to the spin-precession frequency of the electron, is exploited to manipulate the spin of the electron. This is accomplished by introducing a perturbation in the electron orbit to cause the spin to precess into the longitudinal direction. The perturbation is optimized to maximize the polarization observed at the interaction point. Prior to reaching the interaction region, a series of magnets focus the beam size to micron level ($\approx 0.6\mu m \times 2.1\mu m$) to increase the luminosity. After passing the interaction point, the electron and positron bunches are steered into their respective beam dumps downstream of the SLD detector. The machine cycle now repeats with two new electron bunches emitted from the photocathode at the head of the LINAC.

3.1.2 Beam Energy Spectrometer

The energy of the positron and electron beams are measured using the Wire Imaging Synchrotron Radiation Detector (WISRD) [34] on every beam crossing. The WISRDs are located immediately before the beam dumps. The schematic of the WISRD is given in figure 17. The energy measurement is performed by first

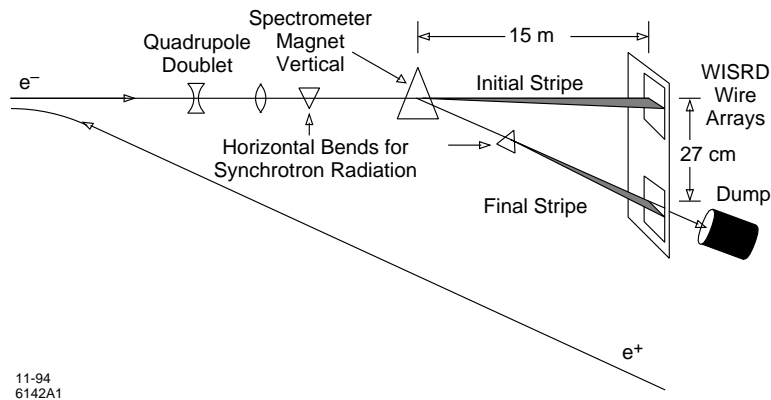


Figure 17: Schematic layout of the energy spectrometer, WISRD.

deflecting the beam in the horizontal direction then vertically by a well calibrated spectrometer magnet and then horizontally again. The horizontal deflections produce two swaths of synchrotron radiation that are imaged by a multiwire chamber. The vertical separation between the two horizontal radiation stripes depends on the deflection angle of the beam through the spectrometer magnet. Having measured the deflection angle and knowing the precise field map in the spectrometer magnet, the energy of the beam can be calculated.

An absolute energy calibration was performed during the 1998 run by measuring the well-known Z^0 line shape. The Z^0 production cross section was measured at three energy points (on, below and above the Z^0 peak) and results indicated that

the energy reported by the WISRD was lower than the true beam energy by about 46 MeV [35]. The cause of the systematic bias is unclear. However, corrections are made to measurements that are sensitive to the absolute energy scale, in particular the A_{LR} measurement.

3.1.3 Compton Polarimeter

The knowledge of the electron beam polarization is important to all electroweak and many B physics measurements. The polarization is measured by a Compton polarimeter located 33 meters downstream of the interaction point [36]. The basic principle of the Compton polarimeter is to use the difference in the Compton scattering of $J_z = 3/2$ and $J_z = 1/2$ states of circularly polarized photons off the longitudinally polarized electron to determine the electron polarization [37]. Experimentally, one simply counts the number of scattered electrons for the two photon helicities as a function of scattered electron energy. The measured asymmetry function is defined as

$$A_{measured} = \frac{N^{obs}(J_z = \frac{3}{2}) - N^{obs}(J_z = \frac{1}{2})}{N^{obs}(J_z = \frac{3}{2}) + N^{obs}(J_z = \frac{1}{2})} = a_d P_e P_\gamma A_c(E), \quad (3.3)$$

where N^{obs} is the number of observed events for the particular photon spin state, a_d is the calculated analyzing power of the detector that determines the scattering asymmetry, P_e is the unknown electron polarization and P_γ is the photon polarization. The parameter $A_c(E)$ is the Compton scattering asymmetry, which is a function of the scattered electron energy only, and it can be calculated from theory.

The schematic of the Compton polarimeter is given in figure 18. The circularly polarized photons at 532 nm (2.33 eV) are produced by a frequency doubled Nd:YAG laser at a repetition rate of 17 Hz. The helicity of the photon is selected

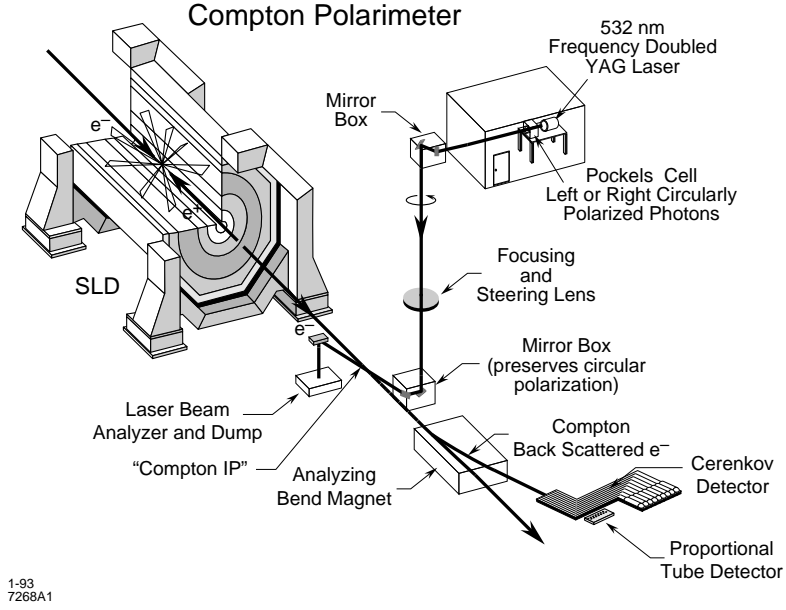


Figure 18: The layout of the Compton polarimeter.

using a series of Pockels cells similar to the laser pulse for the polarized electron source. The photons are guided with a network of mirrors and lenses down to the SLC South final focus tunnel and brought in to collision with the outgoing electron beams at the Compton interaction point with a crossing angle of 10 mrad. The unscattered photons continue in a straight path and enter an analysis box where the polarization of the photons is analyzed using a series of photodiodes. The resulting back-scattered electrons of different energies are separated out by an analyzing bend magnet. The energy distributions of the scattered electrons are measured by a 9 channel Cherenkov detector (CKV). The nine CKV channels each provides an independent P_e measurement. However, only the channel that measures the asymmetry for 180° back scattered electrons is used for the polarization determination. The remaining eight channels are used for cross check purposes.

3.2 SLD Detector

The SLD detector is a general purpose detector for studying the detailed properties of the Z^0 boson production and decay. The detector was completed and moved into the SLC interaction region in 1991 where it recorded data continuously until the end of the SLC program. The detector has undergone a major upgrade in 1996 to install a new CCD vertex detector. The new vertex detector (VXD3) dramatically enhanced the performance of the SLD detector, in particular, in measuring the decay vertices near the e^+e^- interaction point where most of the particle decays occur. The SLD is the only existing colliding beam detector to utilize CCD technology for precision tracking. The technology has given SLD a unique advantage in many areas of physics analysis.

The SLD detector, similar to other modern collider beam detectors, is comprised of cylindrical shells of subdetectors; each measures a specific aspect of Z^0 decay. Figures 19 and 20 show the SLD detector from different perspectives. The inner most layer is the CCD vertex detector. The function of the vertex detector (VXD) is to detect the passage of charged particles by ionization of the silicon pixels, thereby providing tracking/vertexing near the interaction point. Immediately outside the vertex detector is the Central Drift Chamber (CDC), which measures the momentum of the charged particles. The next layer is the dedicated particle identification system, the Cherenkov Ring Imaging Detector (CRID). Moving further outward in radius is the Liquid Argon Calorimeter (LAC), which is primarily used for measuring energy deposition of charged and neutral particles. The four inner detectors are surrounded by a solenoidal magnet that provides 0.6 Tesla of axial magnetic field. The outermost detector is the Warm Iron Calorimeter (WIC), which is used for muon identification as well as a flux return for the magnetic fields.

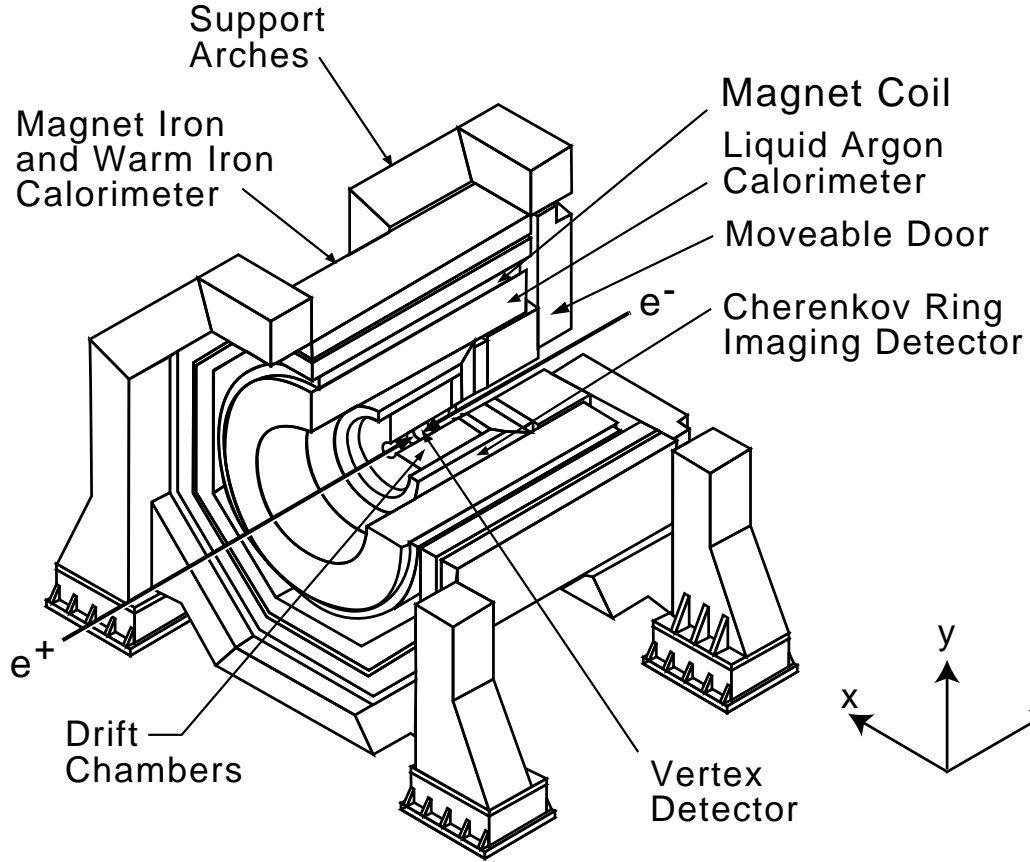


Figure 19: The schematic of the SLD detector. The SLD coordinate system is also shown on the plot. The positive z axis points along the positron direction with the origin $z=0$ at the center of the detector, \vec{x} is defined parallel to the surface and \vec{y} axis points upwards.

The details of the individual subsystems are provided in the following sections. The emphasis is on the detectors in the barrel region since the endcap detectors are not used in this analysis.

3.2.1 Vertex Detector

At the heart of the SLD detector is the pixel-based CCD vertex detector. This device is capable of making precise determination of particle tracks near the inter-

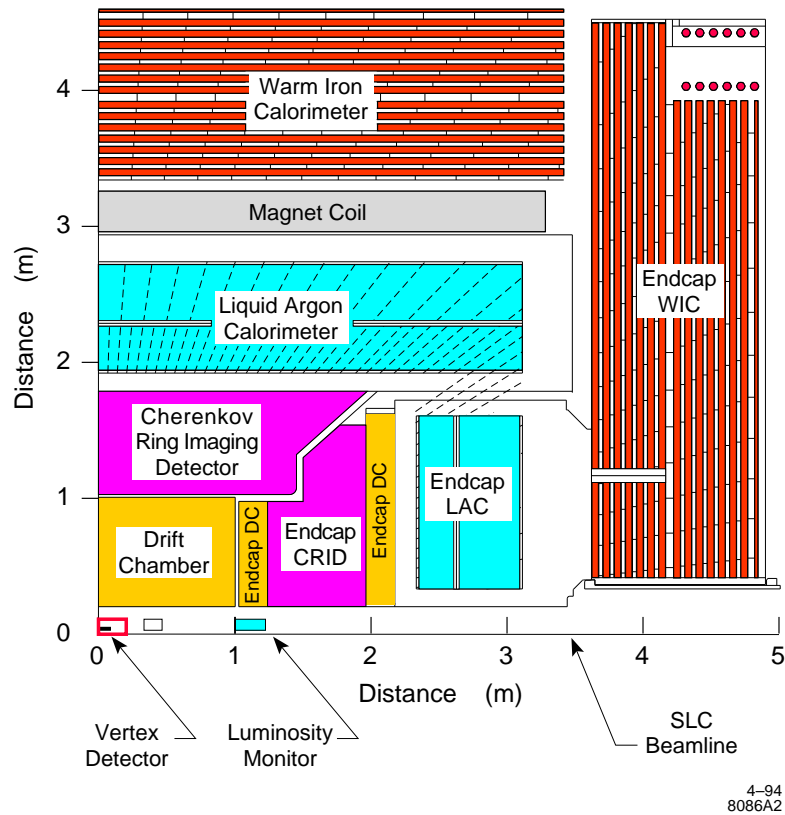


Figure 20: A quadrant view of the SLD detector listing the various subdetectors.

action point. In early 1996, a new vertex detector was installed at SLD [38]. A comparison plot of the geometries of the old (VXD2) and the new (VXD3) detectors is given in figure 21. The VXD3 consists of 96 CCD's arranged on three cylindrical barrel layers with the inner layer at the radius of 28.0 mm and outer layer at 48.3 mm. The radius of the first layer is constrained by the radius of the beampipe. The radius of layer three is chosen to maximize $\cos\theta$ coverage and track impact parameter resolution. The impact parameter resolution is further improved with VXD3 because the detector has less material ($\approx 0.40\%X_0$), therefore less multiple scattering. There are 48 ladders (12, 16 and 20 for layers 1,2 and 3 respectively) and each ladder has two CCD's bonded on opposite sides (see figure 22).

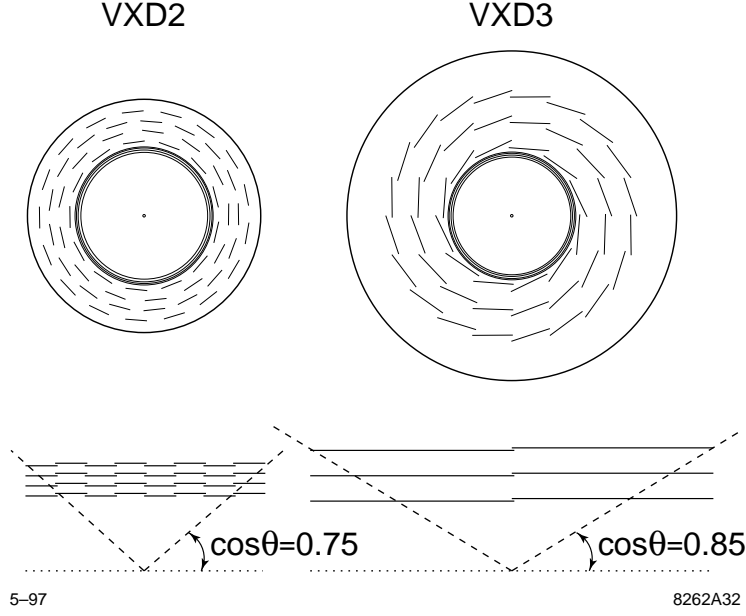


Figure 21: A comparison of VXD2 and VXD3. The $\cos \theta$ coverage of VXD3 is increased to 0.85. The ladder spacings are also increased to provide more leverage arm for track reconstruction.

Each CCD has an active area of $8.0\text{cm} \times 1.6\text{cm}$ and a pixel size of $20 \times 20 \mu\text{m}$. This translates to $4000 \times 800 = 3.2$ million pixels per CCD or 307 million pixels for the entire VXD3. The CCD's are divided into four regions with a readout node located at each corner of each CCD. The pixel charges are transferred to the output nodes at a rate of 5 MHz, which results in a readout time of 0.2 sec or 26 beam crossings.

A bench-top optical survey on the CCD's was performed to parameterize the surface distortions [39]. The optical survey data were later used as the starting point for a more detailed internal alignment using Z^0 decay tracks. Gravity sag, thermal contractions and other geometric distortions that may degrade the resolution of the CCD are corrected for in the internal alignment. The single hit resolution of the CCD, obtained from the sagitta of tracks with hits in all three layers of the vertex detector, is about $4\mu\text{m}$ in both axial and azimuthal directions.

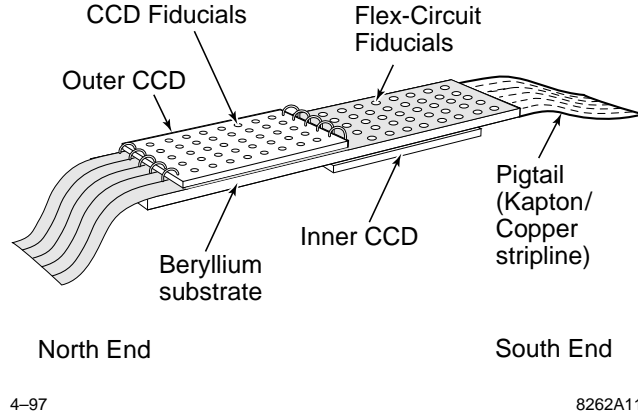


Figure 22: The layout of a CCD ladder. The ladder is made of beryllium substrate. The two CCD's are bonded on opposite sides of the ladder.

3.2.2 Central Drift Chamber

The CDC is the primary detector to measure the charge and momentum of charged particles [40]. The chamber extends from a radius of 20 cm to 100 cm. The CDC contains 5121 $25\mu\text{m}$ diameter of gold-plated tungsten sense wires. Electrons liberated from the drift gas by a charged particle traversing the chamber drift towards the adjacent sense wire and induce an avalanche near the wire. The particle trajectory can be reconstructed from a pattern of hits on the sense wires.

The primary gas in the chamber is CO_2 (75% by volume), which is chosen for its slow electron drift property. The slow drift time is needed to give sufficient time for the CDC electronics to accurately sample the charge waveform induced on the sense wire. The remaining gas compositions are 21% Ar, 4% isobutane and 0.2% H_2O . The Ar gas is used to increase the avalanche gain, isobutane is added as a quencher and the small quantity of water is included to reduce wire aging [41].

The drift cell structure is shown in figure 23. A single cell occupies an area of about 5 cm by 6 cm. It consists of 8 sense wires aligned in the radial direction

and a dummy sense wire at either end. The sense wires are surrounded by 25 field shaping wires and 18 guard wires. The field wires define the electric fields in the cell and the guard wires help to keep the gas gain constant by maintaining the fields near the sense wire. The voltage on the field wires varies depending on the position, with an average value of 5.3 KV. The guard wires are maintained at 3.027 KV.

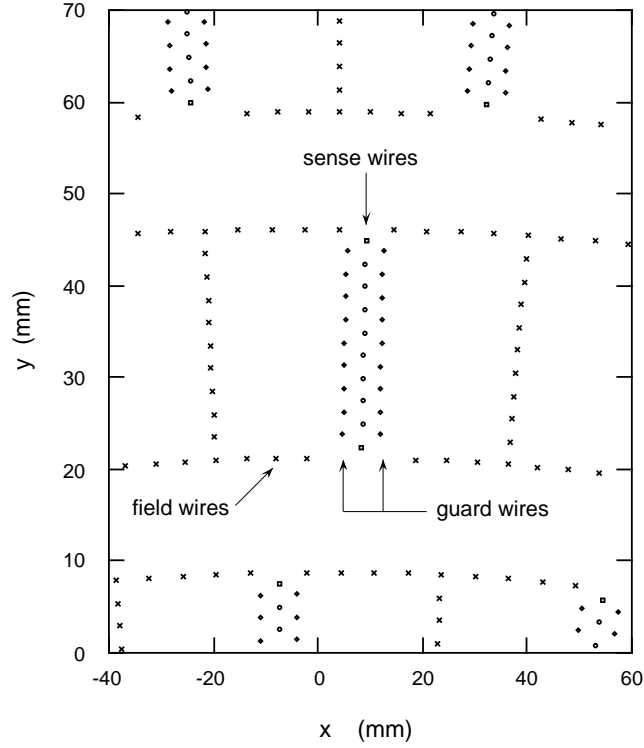


Figure 23: The cell structure for the CDC.

The cells are grouped into 10 superlayers (see figure 24). The wires in a given superlayer are either aligned parallel to the beam or at a crossing angle of ≈ 42 mrad. The pattern, from inner to outermost superlayer, is: AUVAUVAUVA, where A is axial orientation, U is $+42$ mrad crossing angle and V is -42 mrad crossing angle. The stereo angle arrangement allows the possibility of extracting the z coordinate of the particle.

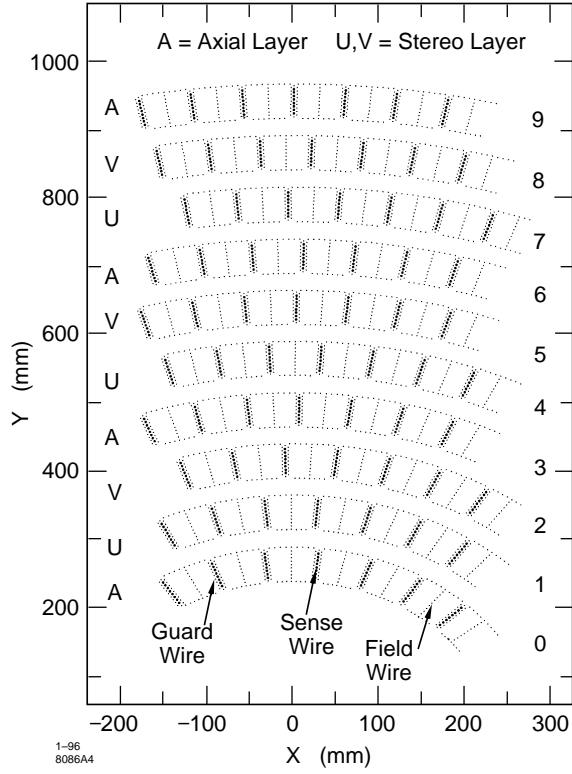


Figure 24: A schematic of the axial and stereo wire assignments for the CDC.

For a track found in the CDC, an attempt is made to link the track to the vertex detector hits. This is done by extrapolating the track back to the vertex detector and then searching for hits near the path of the track. A CDC track is linked only if two or more vertex detector hits are associated with the track. A linked track is then refitted with the vertex detector hits included. The measured momentum resolution for tracks with CDC hits only is

$$\left(\frac{\sigma_{p_{\perp}}}{p_{\perp}^2} \right)^2 = 0.0049^2 + \frac{0.0095^2}{p_{\perp}^2}, \quad (3.4)$$

and with VXD3 hits is

$$\left(\frac{\sigma_{p_{\perp}}}{p_{\perp}^2} \right)^2 = 0.0026^2 + \frac{0.0095^2}{p_{\perp}^2}. \quad (3.5)$$

3.2.3 Cherenkov Ring Imaging Detector

The identification of charged particles is performed with the Cherenkov Ring Imaging Detector (CRID). When a charged particle travels through a medium faster than the phase velocity of light in the medium, a cone of radiation (Cherenkov radiation) is produced. The principle of the CRID is to deduce the particle velocity by measuring the angle of the Cherenkov cone. The velocity and the momentum of the particle, as measured in the CDC, are combined to determine the mass of the particle.

The schematic of the SLD barrel CRID is shown in figure 25. The barrel CRID is divided into 40 sectors: 20 each in the north and the south end of the SLD detector. Within each sector, there are two quartz-window trays that contain the radiator fluid, two Time Projection Chambers (TPC) for imaging the Cherenkov photons and a set of 10 mirrors to focus the Cherenkov radiation. To identify particles over a large momentum range, two radiators are used in the CRID system: liquid (C_6F_{14}) and gas ($C_5F_{12} + N_2$). The liquid radiator, with an index refraction of 1.2723 at $\lambda=190$ nm [42], is confined in 40 quartz-window trays of 1 cm thickness below the TPC box. The Cherenkov radiation from the liquid radiator is focused directly onto the TPC (referred to as “proximity focus”) as illustrated in figure 25. The main vessel of the detector is filled with a mixture of 85% C_5F_{12} radiator gas and 15% N_2 . This yields an index of refraction of about 1.0017 at $\lambda=190$ nm [43]. The Cherenkov radiation from the gas radiator is focused back to the TPC via a set of 400 UV-reflective spherical mirrors. The spherical mirrors focus Cherenkov light emitted by a track to the same point on the TPC regardless of the origin of the light on the track’s trajectory. The mirrors are needed to focus the gas radiation, otherwise the long path length of the track through the gas radiator would smear

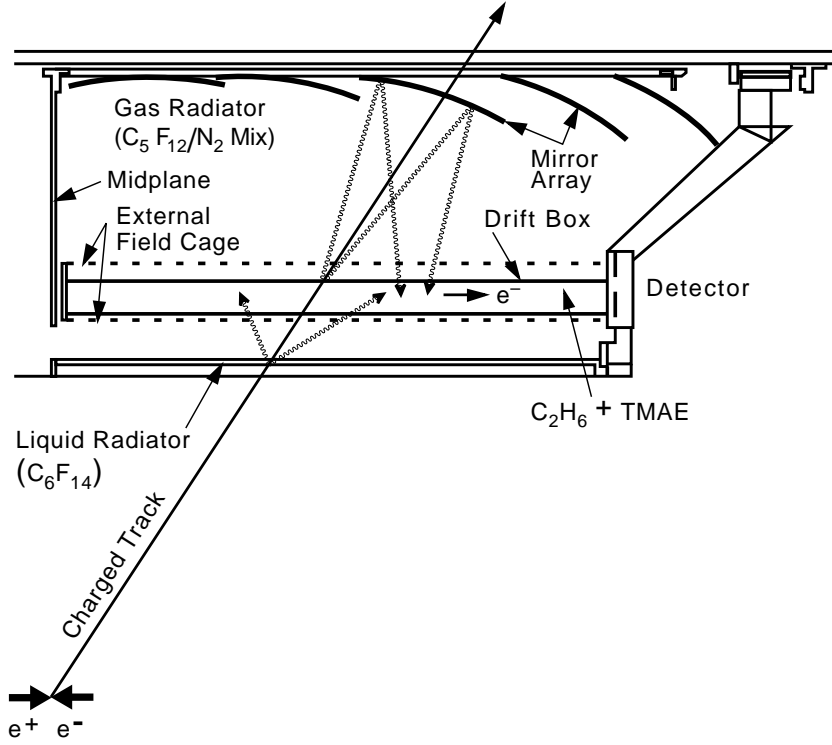


Figure 25: A sectional view of the SLD barrel CRID.

the Cherenkov angle completely.

The Cherenkov photons from the radiators photoionize the C_2H_6 drift gas with TMAE dopant [44] in the TPC. The resulting photoelectron, in the influence of the 400 V/cm electric field, drifts towards the multiwire proportional chamber at the end of the TPC box. The multiwire proportional chamber is composed of a plane of 93 $7\mu m$ carbon filaments oriented in the vertical direction with 3.2 mm separation between filaments. The horizontal position of the photoelectron is determined by the wire number, the vertical position is obtained from using the charge division method and the longitudinal coordinate is calculated from the drift time. With all the hits reconstructed in the TPCs, a maximum likelihood method is then used to fit for the best particle hypothesis (see Appendix A.1).

The use of CRID is important in this analysis. For additional information on the topic, refer to Appendix A and reference [45]

3.2.4 Liquid Argon Calorimeter

The Liquid Argon Calorimeter (LAC) is a sampling calorimeter that measures the energy of charged and neutral particles by sampling the development of showers initiated by incident particles [46]. The basic LAC module consists of a stack of lead plates separated by plastic spacers and immersed in a common bath of liquid argon. The liquid argon is the active medium that becomes ionized by the passing charged particles. The lead plates induce shower developments and also act as the charge collecting electrodes.

The barrel LAC is about 6 meters long with an inner radius of 1.8 meters and an outer radius of 2.9 meters. It is composed of 288 modules mounted inside a large cylindrical cryostat sharing the same liquid argon volume. The barrel LAC is segmented in three main sections along the z (beam) direction and 48 modules in $r\phi$ (azimuth). The calorimeter in the radial direction is further divided into electromagnetic and hadronic towers.

The individual modules consist of alternating planes of large lead sheets and segmented lead tiles. The lead sheets are held at ground potential while the lead tiles are maintained at -2000 V and function as charge pickup electrodes. The pair of an adjacent lead sheet and a lead tile is referred to as a cell (see figure 26).

The geometry of the LAC modules is shown in figure 27. The lead sheets and tiles for the electromagnetic modules are both 2 mm thick, with a 2.75 mm gap for the liquid argon to soak through. There are two readout channels: EM1 and EM2, where EM1 corresponds to the energy deposition in the first 6 radiation

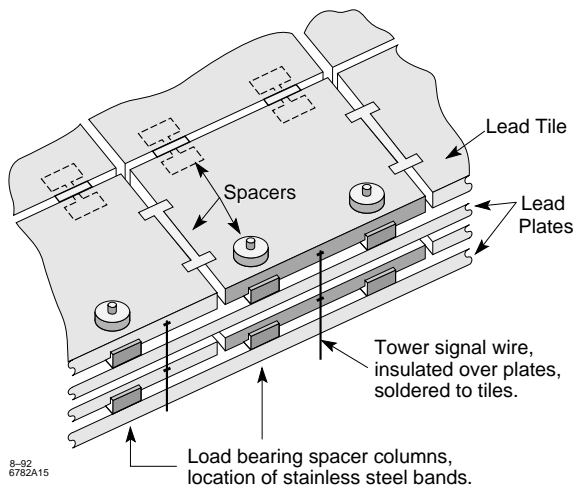


Figure 26: The figure shows a portion of the cell structure of a LAC module. The wiring configuration for the tiles is also shown in the figure.

lengths while EM2 corresponds to the readout for the latter part of the module (the remaining 15 radiation lengths of lead). The electromagnetic module with 21 radiation lengths is sufficient to contain 45 GeV electrons, with energy leakage of 1-2%.

For the hadronic modules, the thickness of the lead plates and tiles are both increased to 6 mm, with the same plate separation of 2.75 mm. There are also two readout channels for the hadronic modules, HAD1 and HAD2, each with 1 interaction length of lead.

The parameters of the Liquid Argon Calorimeter are given in table 3. The energy resolution for electromagnetic module is $\sigma/E \approx 15\%/\sqrt{E}$ and for the hadronic module is $\sigma/E \approx 60\%/\sqrt{E}$.

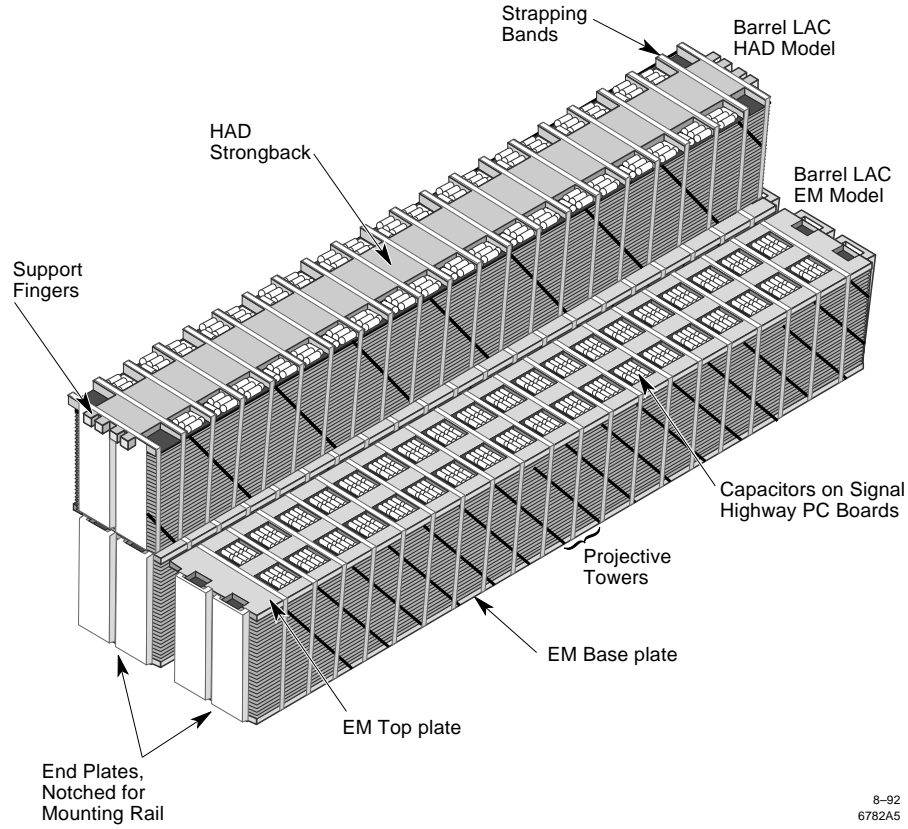


Figure 27: Schematic of LAC modules. The module in the foreground is the electromagnetic module (EM1+EM2). In the background, the hadronic module is stacked on top of the electromagnetic tower. There are total of 288 modules: 48 arranged in the azimuthal direction and 3 along the beam direction.

3.2.5 Magnet

The SLD magnet coil provides a uniform axial magnetic field of 0.6 Tesla in the central detector. The field in the tracking chamber has been determined to be uniform to within 3%. The coil has a diameter of 5.9 meters, a thickness of 29 cm and a length of 6.5 meters. The cylinder is formed by winding a 10 kilometer long rectangular aluminum conductor (5 cm by 8 cm) in four 127-turn layers. The nominal current required is 6600 amps and the resulting power dissipation in the coil is 5.0 MW.

	EM1	EM2	HAD1	HAD2
Lead Thickness (mm)	2.0	2.0	6.0	6.0
Argon Gap (mm)	2.75	2.75	2.75	2.75
Cell Count	8	20	13	13
Radiation Lengths	6.0	15.0	13.9	13.9
Interaction Lengths	0.24	0.60	1.0	1.0
Energy Resolution σ/\sqrt{E}	15%	15%	60%	60%

Table 3: Liquid Argon Calorimeter parameters.

3.2.6 Warm Iron Calorimeter

The outermost subdetector is the Warm Iron Calorimeter (WIC) [47]. The primary roles of the WIC are to perform muon identification and to act as the magnetic return flux for the solenoidal magnet. Since most charged particles other than muons are stopped in the LAC, a track seen in the WIC is likely to be a muon. It was also originally designed to provide calorimetry information to catch the energy leakage from the LAC. However, the energy resolution was very poor and the efforts were eventually abandoned.

The structure of the WIC is shown in figure 28. It consists of 18 layers of Iarocci (limited-streamer) tubes [48] sandwiched between 5 mm thick steel plates. An Iarocci tube consists of eight high voltage 100 μm wires suspended in individual compartments. The tube is filled with 88% CO_2 , 9.5% isobutane and 2.5% argon. The operating voltage of the Iarocci tube in the limited streamer mode is 4.75 KV. The wires inside the tube are not connected to any readout electronics. Instead, the inner surface of the tube is coated with a layer of slightly conductive graphite paint to allow electrodes mounted on the outer surface of the Iarocci tube to pick up the streamer discharge signal inside the tube. The signal from the electrodes (strips or pads) are recorded in binary (hit or no hit).

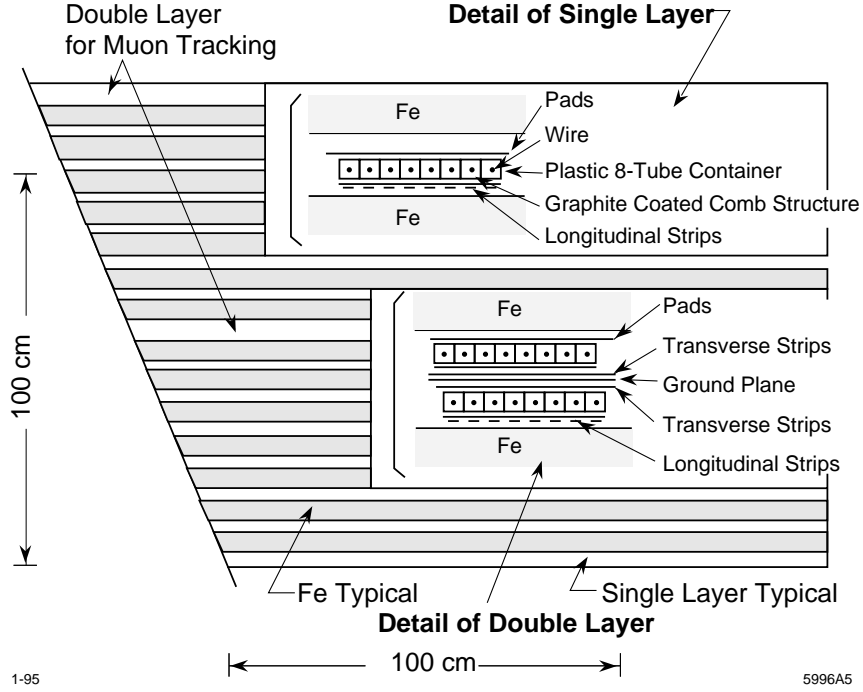


Figure 28: The schematic of the WIC and the layout of the Iarocci tubes. Most of the air gaps are instrumented with a single layer of Iarocci tubes, except the top layer of each “coffin” is instrumented with double layers.

The barrel WIC provides muon coverage up to $\cos \theta$ of 0.6 with an efficiency of about 85% for muons above 2.5 GeV.

3.2.7 Luminosity Monitor

The Luminosity Monitors (LUM) [49] are finely segmented silicon-tungsten calorimeters for measuring small angle Bhabha scatterings. The detectors are mounted around the beampipe about one meter downstream of the interaction point (see figure 29). The two detectors, Luminosity Monitor and Small-Angle Tagger (LM-SAT) and Medium-Angle-Silicon Calorimeter (MASC), each covers different angular regions. LM-SAT covers between 28 and 68 mrad while MASC

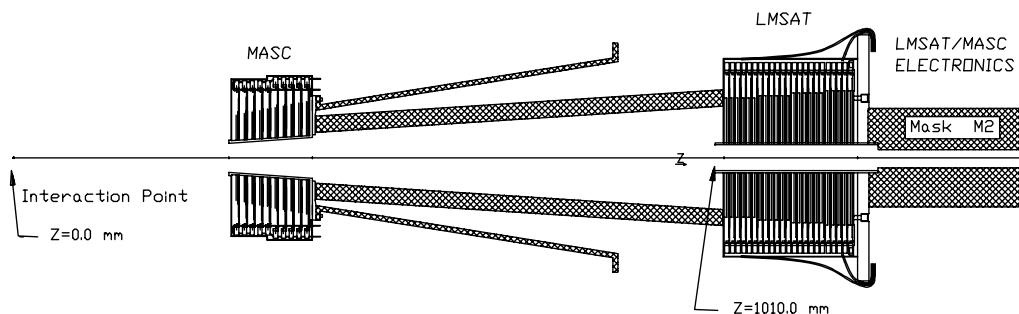


Figure 29: Luminosity monitor.

covers the 68-190 mrad region. The MASC detector was removed from the beamline in 1996 to accommodate the space requirement of the new vertex detector (VXD3). As the name suggests, the primary purpose of the luminosity monitor is to obtain the absolute integrated luminosity by precisely measuring the low angle Bhabha scattering cross section. The precision on the absolute luminosity measurement is on the order of 3%.

3.3 Data Acquisition and Trigger

The long time (1/120 sec) between beam crossings at the SLC is a blessing from the side of data acquisition and triggering. It makes the task of data acquisition and triggering relatively straightforward at SLD.

The SLD data acquisition system is located above the SLD detector. It consists of 18 FASTBUS crates. The task of assembling events from the various detectors is performed using the ALEPH Event Builder (AEB) modules [50].

The task of triggering is controlled by a dedicated trigger AEB. There are various conditions that may trigger a complete readout of the detector. For hadronic events, the three trigger conditions are: 1) a minimum energy sum trigger from

the LAC, 2) at least two tracks with large angles with respect to each other or 3) one track in the CDC with a lower LAC energy threshold requirement. In addition to the hadronic trigger, there are triggers for flagging Bhabhas and di-muon events and a random trigger that writes out the whole detector about every 20 seconds. The average trigger rate is about 0.2 HZ during good low-background running conditions.

CHAPTER 4

MONTE CARLO SIMULATION

High energy physics experiments make extensive use of simulations, commonly referred to as Monte Carlo simulations. Monte Carlo simulation is not only used to aid the design of experimental apparatus, it is also heavily used to guide physics analyses. The Monte Carlo data, which are essentially identical to the real data, are particularly useful in physics analyses for tuning selection criteria and estimating physics input parameters that cannot be easily obtained otherwise. The generation of Monte Carlo data proceeds in two steps. First, the underlying physics processes are generated and then the detector responses are simulated.

4.1 Physics Modeling

The first step in the Monte Carlo simulation is to generate the underlying physics. The package adopted at SLD to generate the physics events is JETSET 7.4 [51]. At the Z^0 pole, the physics process is $e^+e^- \rightarrow Z^0 \rightarrow f\bar{f} \rightarrow$ final state particles. Figure 30 illustrates the different stages of the event generation. The process begins with the production of the Z^0 boson by the annihilation of an electron and a positron. The Z^0 boson subsequently decays to a fermion and

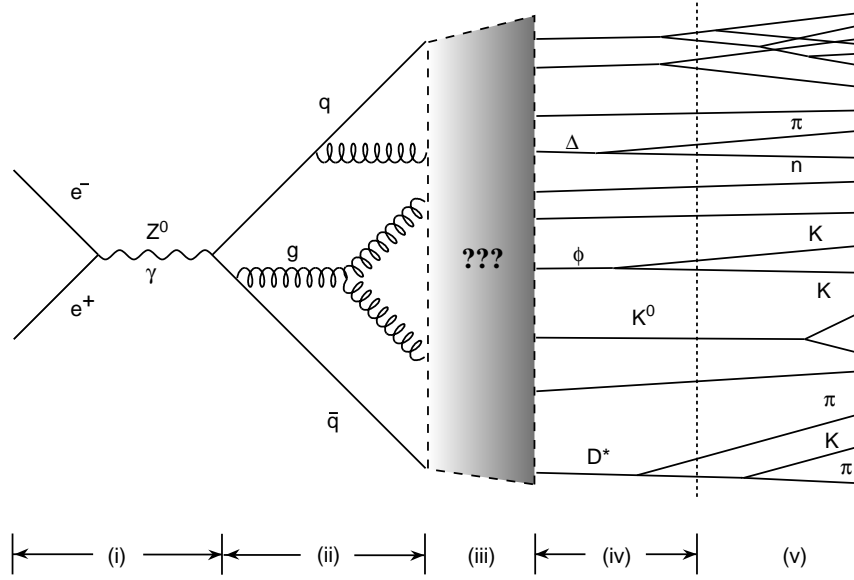


Figure 30: The figure shows the different stages of the underlying physics process. Region (i) shows the production and decay of Z^0 or photon from e^+e^- annihilation to $q\bar{q}$ pair. This process is fully described by the electroweak theory. Region (ii) shows the hard processes of gluon radiations. This QCD process can be calculated perturbatively. The shaded box in region (iii) is where the fragmentation process takes place. The process is intrinsically non-perturbative and can only be described by phenomenological models. The decays of short-lived and semistable particles are shown in regions (iv) and (v).

antifermion pair. This chain process, illustrated in region (i) of figure 30, is very well understood and can be calculated in the context of the electroweak theory.

The second stage (region ii) involves gluon and photon radiation. The basic processes are:

- $l \rightarrow l\gamma$ and $q \rightarrow q\gamma$ (photo radiation),
- $q \rightarrow qg$ (gluon radiation),
- $g \rightarrow q\bar{q}$ (gluon splitting) and
- $g \rightarrow gg$ (gluon self-coupling).

These processes are simulated in JETSET using the parton shower model. The parton shower model is an approximation to the direct matrix element calculation. Each process is characterized by a splitting kernel $P_{a \rightarrow bc}(z)$, which is the probability for the reaction to occur. The branching rate is proportional to the integral $\int P_{a \rightarrow bc}(z) dz$, where z is the fraction of energy carried away by daughter b . The daughters b and c can then branch off to form more particles, and so on. The parton showering process continues until the energy of the partons fall below a certain cutoff. Strictly speaking, leptons (l) are not partons, however, the same phenomenology is applicable to quarks and leptons. Instead of treating the leptonic events separately, for simplicity, JETSET treats leptons as “parton-like”.

The next stage of the development is hadronization or fragmentation. At this step, colored partons are transformed into colorless hadrons. As implied by the shaded region in figure 30, this part of the process is not very well understood. The strong coupling at this stage becomes large and perturbative QCD calculation breaks down. To describe this part of the physics development, phenomenological models are used. In particular, JETSET uses the string fragmentation model [52]. This model assumes linear confinement of the quark and antiquark with a constant potential of ≈ 1 GeV/fm. As the quark and antiquark moves apart from their common production point, a color flux tube, with a transverse dimensions comparable to the typical hadron size (≈ 1 fm), is stretched between the two quarks. A new quark and antiquark pair may be formed, when the potential energy exceeds the mass of the new quark pair. The production of quark pairs continues until only on-shell colorless hadrons are left. The string model is illustrated in figure 31. The energy of the resulting hadron is described by the fragmentation function, $D_Q^h(z)$, which is the probability that the hadron h carries a fraction z of the energy of the heavy quark Q . The default JETSET uses the “LUND symmetric” fragmenta-

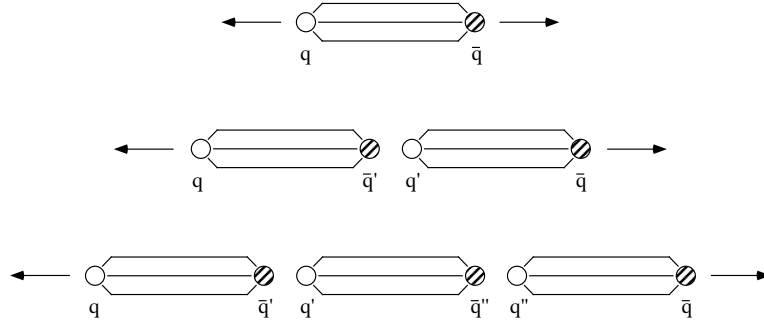


Figure 31: The figure shows the evolution of quark pair production in the string fragmentation model. As the quarks are moving part, the color flux tube is stretched until a new $q\bar{q}$ pair is produced. The same process repeats for the successive daughter quarks.

tion function for light quarks (u , d and s). The Peterson function [53] is used for hadronization processes involving charm and bottom quarks.

The next physics phase (region iv) involves the decay of the unstable particles. In JETSET, lifetime and branching ratio information for the various hadrons is used to simulate the decay process. Unfortunately, a large fraction of the hadron decay properties have not been experimentally measured and therefore, some theoretical assumptions have to be made (e.g. factorization and strong isospin symmetry). In the SLD Monte Carlo, the B_s^0 , B_d^0 and B^\pm decay properties are governed by the CLEO B decay model, which are found to be in better agreement with the data from the CLEO and ARGUS experiments. The semi-leptonic B decays are handled by the scheme of Isgur, Scora, Grinstein and Wise (ISGW) [55] in the CLEO B decay model. The remaining short-lived particles, including b -baryons, decay according to the default JETSET. The long lived particles (e.g. K_s^0 , Σ^- , Λ and Ω^-), however, decay according to the detector simulation (to be described in the next section) to account for possible interactions with the detector material.

4.2 Detector Modelling

The next stage of the simulation is to produce simulated data that resembles real data. This requires good modelling of particle interactions in the detector volume and the response of the various subdetectors. The SLD uses GEANT 3.21 [56] to simulate the detector interactions. The GEANT simulation includes a detailed description of the geometry of the SLD detector and the associated construction materials. The magnetic field map in the detector is also provided in the simulation. The GEANT simulation starts with a list of particles output from JETSET and traces each particle's trajectory to the boundaries of the detector elements, at which point the interaction probabilities with the detector elements are calculated. The electromagnetic interactions are simulated using the EGS4 [57] package and hadronic interactions are modelled using the GHEISHA hadron generator. The full GEANT simulation includes the effect of multiple scattering, radiation loss due to ionization, Bremsstrahlung, photoelectric effect, δ ray production, e^+e^- pair production, Compton scattering and nuclear interactions.

To simulate the background conditions for the different data collection periods, raw detector hits from the data runs are overlayed onto the GEANT generated hits. These data hits are collected roughly every 20 sec throughout the run (using a random trigger) and are presumably all from detector noise or accelerator background.

The raw outputs from the detector simulation are reconstructed and the results are stored in a format similar to the real data. The main difference of the two formats is that Monte Carlo data also includes the truth information (particle type, location of the production and decay vertices, energy, momentum etc...) of each particle.

4.3 Monte Carlo Tuning

The Monte Carlo simulation generally models the data well. However, there are some discrepancies that must be corrected. The two main effects have to do with tracking efficiency and tracking resolution modelling.

It was found that the average track multiplicity from the selected B decay events is slightly higher in the Monte Carlo than data. This is an indication that the track reconstruction efficiency may be over estimated in the Monte Carlo. The remedy is to randomly remove tracks from the Monte Carlo events. The rate at which tracks are removed is determined by comparing the reconstructed B vertex charge distribution in data and Monte Carlo. The result indicates that by removing $\approx 1.5\%$ of the Monte Carlo tracks will yield a good agreement between data and Monte Carlo.

The second effect is the track resolution. Based on the study of track impact parameter (distance of the closest approach of the track to the e^+e^- interaction point) distributions between data and Monte Carlo, it was determined that additional smearing is needed in the Monte Carlo. The discrepancy is corrected by smearing the CCD positions in the detector. It was also discovered that the impact parameter distributions in the data exhibit systematic shifts as a function of $\cos\theta$ and ϕ , which are not accounted for in the Monte Carlo [70]. The systematic biases are shown in figure 32. The offsets are modelled in the Monte Carlo by shifting the track positions to match the observed shifts. The corrections are made in four $\cos\theta$ and forty ϕ bins. The means of the xy and z impact parameter distributions are shown in figures 33 and 34 for data and the shifted Monte Carlo. The agreement is good after the corrections.

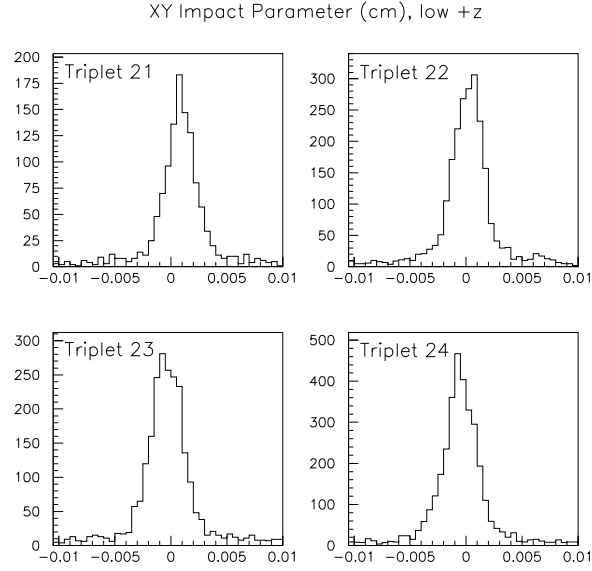


Figure 32: The track Z impact parameter distributions in different VXD3 ϕ regions for data. The distributions reveal the systematic offsets that need to be modelled in the Monte Carlo.

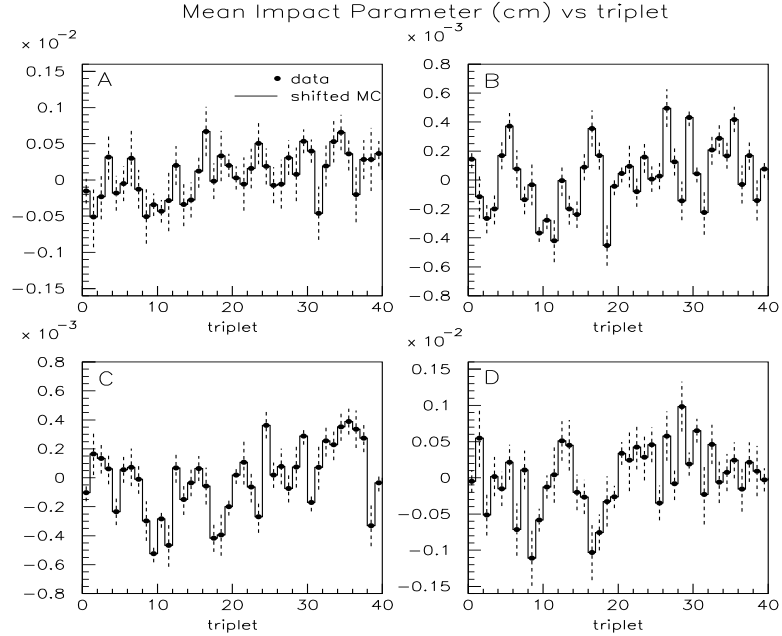


Figure 33: Track xy impact parameter means (cm) in 4 regions of $\cos \theta$ and 40 regions of ϕ . Dots are data and solid line is Monte Carlo after corrections. Plot (a) is for $\cos \theta < -0.65$, (b) $-0.65 < \cos \theta < 0$, (c) $0 < \cos \theta < 0.65$ and (d) $\cos \theta > 0.65$.

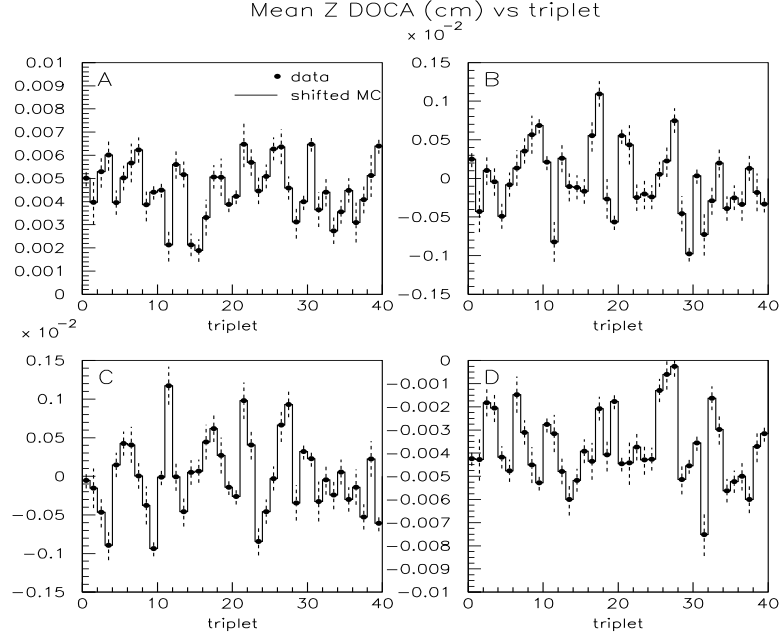


Figure 34: Track z impact parameter means (cm) in 4 regions of $\cos \theta$ and 40 regions of ϕ . Dots are data and solid line is Monte Carlo after corrections. The $\cos \theta$ ranges for plots (a) - (d) are defined in figure 33.

C H A P T E R 5

DATA REDUCTION

The data set used in this analysis consists of roughly 400,000 hadronic Z^0 decays collected by the SLD experiment during the 1996-1998 runs. One of the first steps in analyzing the data is to reduce the data sample to a more manageable size. This is accomplished through a series of filtering procedures that remove the unwanted background events. For this analysis (which will be described in detail in later chapters), the events of interest are $Z^0 \rightarrow b\bar{b}$ decays. Therefore, it is important to design a data reduction scheme that retains $b\bar{b}$ events while rejecting all other non $b\bar{b}$ events. These and other relevant issues are discussed in the following chapter.

5.1 Physics Event Filter

Events that pass the SLD hardware trigger requirements include hadronic events ($Z^0 \rightarrow q\bar{q}$), the leptonic events ($Z^0 \rightarrow e^+e^-$, $\mu^+\mu^-$, and $\tau^+\tau^-$), 2-photon events, beam related backgrounds and cosmic ray events. A software filter is used to further reduce the contributions of beam related backgrounds. The filter requires either one high momentum track in the drift chamber or energy deposition in the calorimeter that is inconsistent with beam-gas or beam-wall interactions. The specific energy deposition requirements are:

- $\text{NEMHI} \geq 10$
- $\text{EHI} > 15 \text{ GeV min-I}$
- $\text{ELO} < 140 \text{ GeV min-I}$
- $\text{EHI} > 1.5 \times (\text{ELO}-70)$
- $\text{NEMHI} > 0$ for both north and south side of the detector

NEMHI is defined as the number of LAC electromagnetic towers with more than 60 ADC counts ($\approx 250 \text{ MeV}$ for minimum ionizing particles, min-I). EHI is the high-threshold energy sum, which is the sum of energy deposited in the electromagnetic towers with ADC count > 60 and the hadronic towers with ADC count > 120 (equivalent to 1.3 GeV min-I). ELO is the lower-threshold energy sum, which is the sum of energy deposited in the electromagnetic towers with ADC count > 8 (equivalent to 33 MeV min-I) and the hadronic towers with ADC count > 12 (equivalent to 130 MeV min-I). The cuts on NEMHI and EHI are similar to the ones imposed at the trigger level. The purpose for the requirement on ELO is to reject beam backgrounds (mostly SLC muons) that tend to produce many low energy calorimeter hits. All events that pass the physics filter are reconstructed using the full SLD event reconstruction code and then written out to the data summary tape (DST). At this stage, the data consists of all the important reconstructed event parameters and is ready for physics analysis.

5.2 Hadronic Event Selection and $b\bar{b}$ Tagging

Further data reduction is achieved at the physics analysis level. It consists of two steps: selecting hadronic events and tagging $b\bar{b}$ decays. We start the discussion

by describing the reconstruction of the e^+e^- interaction point (IP), which is needed in the hadronic event selection and $b\bar{b}$ tagging algorithms.

5.2.1 Interaction Point Determination

The Z^0 decay tracks are expected to point back to the primary interaction point. This knowledge is used to reconstruct the IP position. One possible algorithm to find the IP location would be to simply fit all tracks in a given event to a common vertex. At SLD, the motion of electron and positron beams near the collision point in the transverse plane ($r - \phi$) is estimated to be stable within $7 \mu m$ for ≈ 30 sequential hadronic events. This allows us to average many events to obtain a more precise determination of the IP position. However, the averaging scheme is not applicable in the longitudinal direction due to the long beam size ($\approx 700 \mu m$) and therefore the Z position is determined on an event by event basis.

The IP position is determined in the $r - \phi$ direction using an iterative algorithm [58]. An initial IP position is first chosen and all tracks from ≈ 30 sequential events with vertex detector hits and less than 3σ from the initial IP position are fitted to a common vertex. The 3σ requirement is imposed to reject tracks from secondary vertices that do not point back to the primary interaction point. The newly found vertex is then taken as the best estimate of the IP location and the fitting procedure is repeated. The procedure is iterated until a good vertex fit probability is achieved ($\chi^2/d.o.f. < 1.3$).

The IP position along the beamline direction is given by the median of the Z_{poca} distribution of the selected tracks in a given event. Z_{poca} is defined as the distance along the IP axis (parallel to the beam pipe) from the IP to the point of the closest approach of the track to the beam axis. A track is selected in the Z calculation

if the $r - \phi$ impact parameter with respect to the IP is less than $500 \mu m$ and the $r - \phi$ distance of closest approach (DOCA) of the track is within 3σ of the IP.

The IP resolution is measured directly from the data using $Z^0 \rightarrow \mu^+ \mu^-$ events. Assuming μ^\pm track impact parameter resolution with respect to the fitted IP position (from the ≈ 30 hadronic events) is the quadrature sum of the true IP resolution and the μ pair track error (from the μ pair miss distance), the IP resolution in the $r - \phi$ plane is measured to be $\approx 4 \mu m$. The resolution in Z is taken from the Monte Carlo and is estimated to be $\approx 17 \mu m$ for $b\bar{b}$ events [59].

5.2.2 Hadronic Event Selection

The purpose of the hadronic event selection is to remove the di-lepton events ($Z^0 \rightarrow l^+ l^-$). This is a fairly trivial task since di-lepton events have a much lower track multiplicity than hadronic events. $Z^0 \rightarrow e^+ e^-, \mu^+ \mu^-$ decays have typically two tracks per event and $\tau^+ \tau^-$ decays can produce up to 6 tracks. Therefore, a requirement of at least 7 or more charged tracks removes essentially all the leptonic Z^0 decays. A track is included in the total track count if the transverse momentum with respect to the beamline is greater than $200 \text{ MeV}/c$ and the DOCA to the IP is less than 5 cm . A requirement is also imposed on the angle of the thrust axis, \vec{T} , to ensure that the event is well contained in the active region of the detector. The thrust axis points along the direction of the energy flow and is determined based on the calorimeter cluster hits. Specifically, it is obtained by maximizing the function

$$T = \frac{\sum_i |\vec{T} \cdot \vec{E}_i|}{\sum_i |\vec{E}_i|}, \quad (5.1)$$

where E_i is the energy and direction of i th calorimeter cluster. The complete set of cuts to select the hadronic events is listed below:

- Number of tracks ≥ 7
- $\cos(\vec{T}) < 0.85$
- Number of tracks with VXD3 hits ≥ 3
- Total charge track energy > 18 GeV

After the hadronic event selection, about 310K events are left in the data sample with $q\bar{q}$ purity of over 99.9%.

5.2.3 $b\bar{b}$ Event Selection

The next filtering step is to extract $b\bar{b}$ events from the hadronic sample. This is accomplished by taking advantage of two features of the B meson decay topology. At the Z^0 pole, the average energy of a B meson is 32 GeV and the average decay length is approximately 3 mm, as illustrated in figure 35. With the pixel-based CCD vertex detector, the secondary vertices can be easily resolved using an inclusive topological technique developed at SLD. The large separation between the secondary and primary vertices is used to identify the weak decays of heavy quarks. Furthermore, the invariant mass of the secondary vertices can be used to differentiate heavy B meson from lighter meson (e.g. D^0, D^\pm, K_s^0) decays. The topological vertex finding algorithm and the vertex mass determination are discussed in the next two sections.

5.2.3.1 Topological Vertex Reconstruction

There are different approaches to search for secondary decay vertices. One method is to fit all track combinations to a common vertex to find the vertices. This

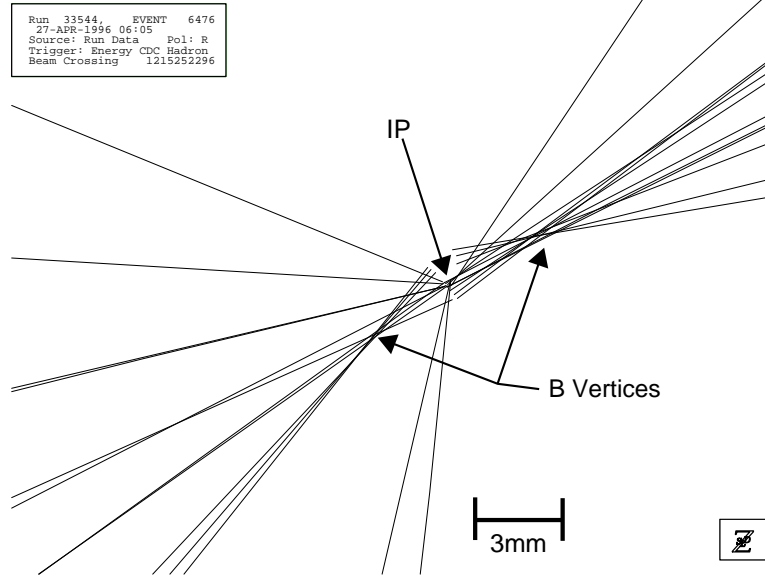


Figure 35: A $Z^0 \rightarrow b\bar{b}$ event from the 1996 data.

approach is effective, but it is extremely computationally intensive and therefore impracticable for high track multiplicity events. An inclusive technique was developed at SLD that searches for vertices in the 3-D coordinate space [60]. In this method, each track is parameterized by a Gaussian “probability density tube” in 3-D. The width of the tube is given by the track error at the point of the closest approach (POCA) to the IP. The regions of space where the probability density tubes overlap are significant are the vertex candidates. A parabolic approximation to a helical track is used to represent the Gaussian tube and the functional form for a given track i is defined as:

$$f_i(\vec{r}) = \exp \left\{ -\frac{1}{2} \left[\left(\frac{x' - (x'_0 + \kappa y'^2)}{\sigma_T} \right)^2 + \left(\frac{z' - (z'_0 + \tan(\lambda) y')}{\sigma_L} \right)^2 \right] \right\}, \quad (5.2)$$

where the positive y' axis points in the track momentum direction in the xy plane at the POCA to the IP. The parameter κ is the curvature and λ is the dip angle of the track. The parameters σ_T and σ_L are the track errors at the POCA to the IP. A graphical representation of the Gaussian tube is illustrated in figure 36 with the

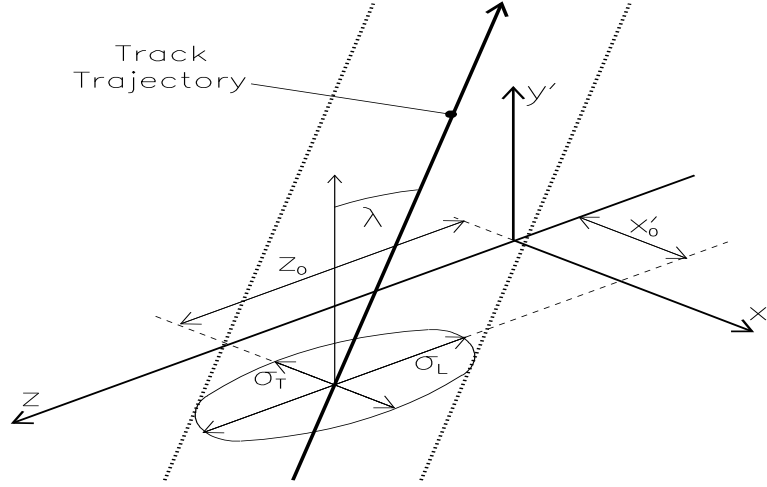


Figure 36: The Gaussian probability tube for a track.

1σ edge shown in dotted lines. The vertices are found by maximizing the function:

$$V(\vec{r}) = \sum_{i=0}^N f_i(\vec{r}) - \frac{\sum_{i=0}^N f_i^2(\vec{r})}{\sum_{i=0}^N f_i(\vec{r})}, \quad (5.3)$$

where $f_0(\vec{r})$ describes the IP location and uncertainty. It is parameterized as a 3-D Gaussian ellipsoid centered on the IP with $\sigma_{xy} = 4 \mu m$ and $\sigma_z = 17 \mu m$. The second term in equation 5.3 is introduced to ensure that $V(\vec{r})$ is non-zero in regions of space where there are at least two overlapping tracks and that $V(\vec{r})$ is approximately 0 at regions where there is only 1 track or the IP function. The track probability tubes and the function $V(\vec{r})$ from a Monte Carlo $Z^0 \rightarrow b\bar{b}$ event are shown in figure 37. Two vertices that correspond to the IP and the secondary decay vertex are clearly resolved in figure 37(b). The topological vertex finding algorithm searches for local maxima of $V(\vec{r})$ only in the overlapping region of two tracks. This significantly reduces the amount of computation needed. In a hemisphere with N tracks, we expect $\frac{1}{2}N(N+1)$ number of local maxima. This number is reduced by requiring the corresponding χ^2 of the two tracks or track-IP fit to be below a certain threshold. A pair of local maxima $(V(\vec{r}_1), V(\vec{r}_2))$ are considered resolved if

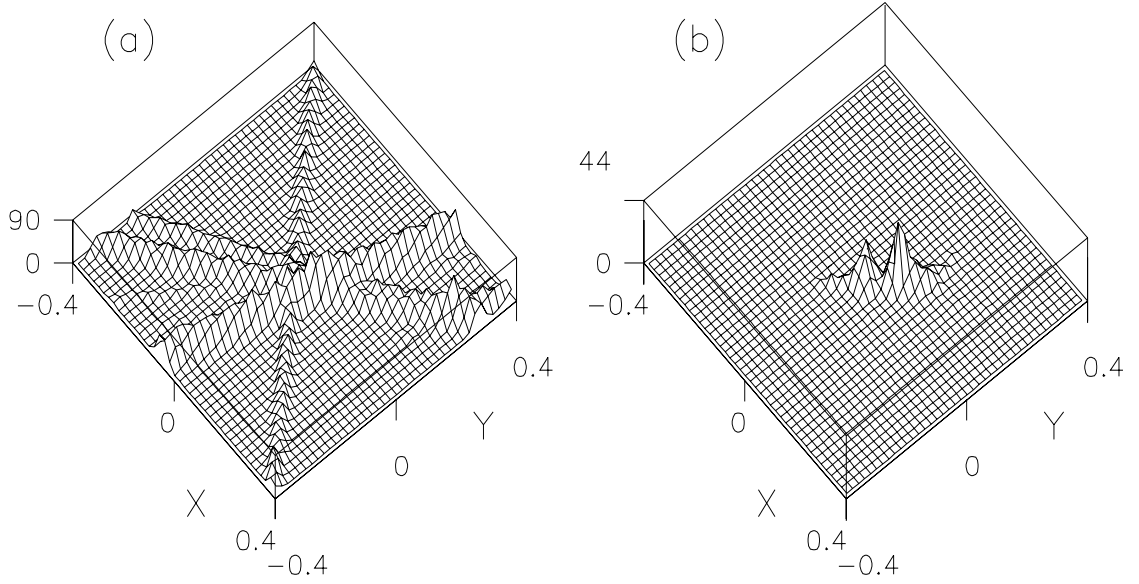


Figure 37: (a)Plot of Gaussian probability density tubes projected on the x-y plane. (b)Plot of $V(\vec{r})$ projected on the x-y plane. The two maxima correspond to the location of the IP(left peak) and the secondary decay vertex(right peak).

the ratio of the minimum of $V(\vec{r})$ along the straight line joining \vec{r}_1 and \vec{r}_2 to the lower of $V(\vec{r}_1)$ and $V(\vec{r}_2)$ is below the tunable parameter R_0 .

$$\frac{\min\{V(\vec{r}) : \vec{r} \in \vec{r}_1 + \alpha(\vec{r}_2 - \vec{r}_1), 0 \leq \alpha \leq 1\}}{\min\{V(\vec{r}_1), V(\vec{r}_2)\}} < R_0 \quad (5.4)$$

Two adjacent minima are merged to a single cluster if the above condition is not satisfied. This merging procedure is repeated until all clusters are resolved. The remaining resolved clusters are the vertex candidates. The precise vertex position is found by fitting all tracks associated with the cluster to a common point. If the χ^2 contribution to the vertex fit of a particular track exceeds the parameter χ_0^2 , the track is removed and the vertex is refitted.

5.2.3.2 Identifying B Vertices

The next step after locating secondary decay vertices is to determine whether these vertices are from B or other hadron decays. The invariant mass of the vertex is used as the discriminating variable. To achieve the optimal resolution on the invariant mass calculation, a pair of neural networks are used to enhance vertex purity and to identify potential B decay tracks not attached to any vertices. The list of vertices from the topological vertexing algorithm are processed by the first neural network to suppress fake vertices [61]. The inputs to the neural network include: the distance between the primary and secondary vertices (D), D divided by the estimated error and the angle between the vertex axis (from the IP to the secondary vertex) and the momentum vector of the vertex. Tracks that are associated with the vertices that fail the neural network cut are tagged as un-associated tracks. At this point, tracks in the hemisphere that are not assigned to any vertex may still be coming from the B decays. A second neural network is used to determine whether these tracks can be re-attached to the good vertices. The attachment neural network uses the angle between the vertex axis and the track momentum and the normalized 3-D impact parameter of the track to the IP as two of the inputs. The remaining three input parameters are the DOCA of the track to the vertex axis (T), the distance from the IP to the POCA of the track on the vertex axis (L) and the ratio L/D . The definitions of the parameters are illustrated in figure 38.

After the re-attachment, all the secondary decay tracks in the same hemisphere are fitted to a common vertex. This new position is used to define the B vertex axis (line between IP and vertex positions). The invariant mass of the vertex, m_{vtx} , is calculated assuming pion mass for the attached tracks. The missing transverse

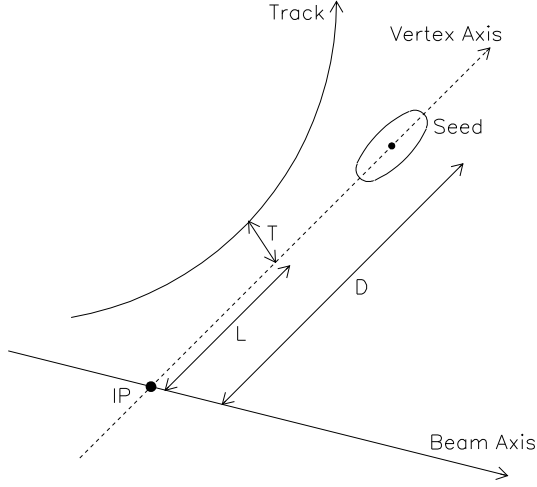


Figure 38: This diagram defines the track attachment parameters L , D and T .

momentum (p_t) with respect to the vertex axis is included in the invariant mass calculation to partially account for neutral particles that should be associated with the B decay. The transverse momentum used in this calculation is the minimum value calculated by allowing the vertex axis to move freely within the 1σ contour of the IP and the secondary vertex error. The minimum p_t is used to suppress the long tail in the vertex mass distribution from charm and light quarks (u , d and s) events. The p_t corrected vertex mass is obtained using the expression:

$$m_{p_t} = \sqrt{m_{vtx}^2 + p_t^2} + |p_t|. \quad (5.5)$$

The m_{p_t} distribution for data and Monte Carlo are shown in figure 39. A minimum cut of 2 GeV (in at least one of the hemispheres) is used in the analysis which yields an event sample with b hadron purity of about 97% and single hemisphere b tagging efficiency of 54%.

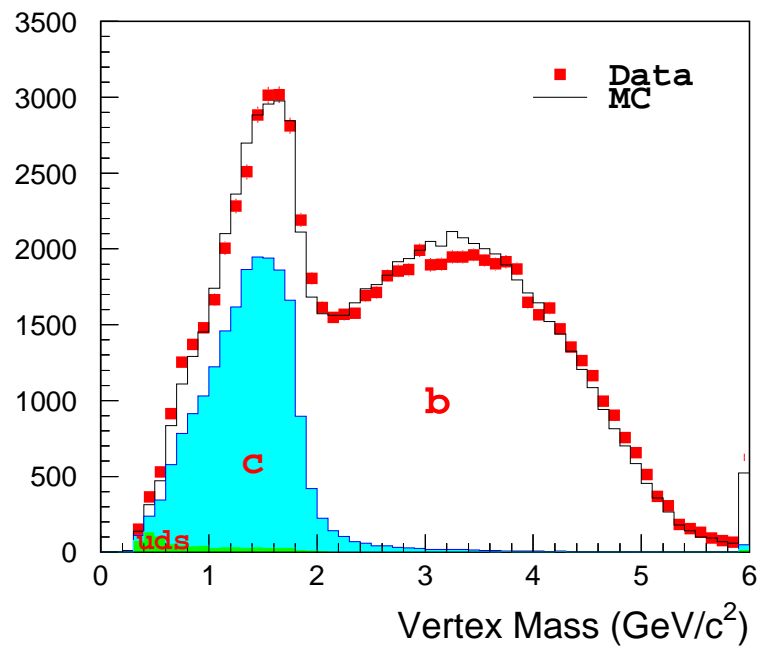


Figure 39: The p_t corrected vertex mass distributions.

CHAPTER 6

EVENT RECONSTRUCTION

As mentioned in the introduction, a time dependent measurement of $B_s^0 - \bar{B}_s^0$ oscillations requires three basic ingredients: 1.) a sample enriched in B_s^0 decays, 2.) determination of the B flavor at production and decay vertices, and 3.) reconstruction of the B_s^0 proper decay time. In an unbiased b -hadron sample, the intrinsic B_s^0 production fraction is roughly 10%. The remaining events are mostly B_d^0 , B^\pm and a small contribution from b -baryons. The charged B hadrons can be suppressed by requiring the charge of the reconstructed hadron to be zero. However, B_d^0 mesons and neutral b -baryons are not easily distinguishable from B_s^0 mesons. A clean method to identify B_s^0 decays is to fully reconstruct the B_s^0 decay chain. Unfortunately, this approach is not feasible at SLD due to the limited size of the data sample. In this analysis, we take the alternative method to obtain a high purity sample of B_s^0 decays by performing a partial reconstruction of B_s^0 . Specifically, we look for decays of the type $B_s^0 \rightarrow D_s^- X$ (and charge conjugate mode), where X denotes any decay products. As shown in the Feynman diagrams in figure 40, the presence of a D_s^- in a B hemisphere is a strong indication that the parent B particle is a B_s^0 . This knowledge is exploited to enhance the B_s^0 fraction in the data sample. In this analysis, the D_s^- is fully reconstructed via the decay channels: $D_s^- \rightarrow \phi\pi^-$, $K^{*0}K^- \rightarrow K^+K^-\pi^-$. The expected branching fraction for the entire

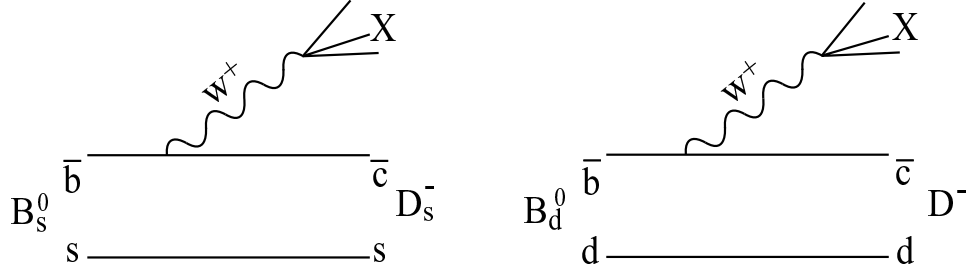


Figure 40: The Feynman diagrams for B_s^0 and B_d^0 decays. The dominant B_s^0 decay mode yields a D_s in the final state while B_d^0 decays into a D^+ .

B_s^0 decay chain is only of the order of a few percent. Therefore, it is important to maintain high efficiency at each stage of event reconstruction. Furthermore, it is important to have good proper time resolution and good flavor tagging in order to resolve the rapid oscillations of the B_s^0 mesons. All these topics are discussed in the remaining part of this chapter. We start by describing the flavor tagging techniques used in the analysis.

6.1 Flavor Tagging

For a given event, we need to know the flavor of the B_s^0 at production (i.e. whether it was produced as a B_s^0 or \bar{B}_s^0) and decay in order to determine whether the event is mixed ($B_s^0 \rightarrow \bar{B}_s^0$) or unmixed ($B_s^0 \rightarrow B_s^0$). The final state determination is based on the charge of the D_s . We assume the D_s comes from the direct $b \rightarrow c$ transition. In this scenario, a D_s^+ would imply that the parent B meson at the decay vertex is a \bar{B}_s^0 , while a D_s^- would imply that the parent is a B_s^0 . As illustrated in figure 41, the final state is misidentified if the D_s comes from the W decay. The wrong sign D_s production ($W \rightarrow D_s$) rate is about 10% [62]. The determination of the initial state is much more involved than the final state. A total of six different

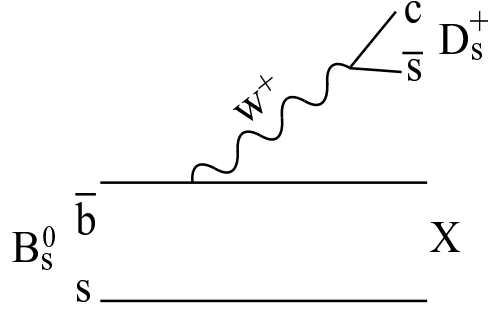


Figure 41: The Feynman diagram for the wrong-sign B_s^0 decay. This is the source of the final state mistag for the B_s^0 events.

tags are used- each with a different efficiency and analyzing power. These tags are: polarized forward-backward asymmetry, jet charge, vertex charge, dipole charge, lepton charge and kaon charge. A graphic summary of the initial state tags is shown in figure 42.

6.1.1 Polarized Forward-Backward Asymmetry

The most powerful initial state tag, unique to SLD, is the polarization tag. As discussed in chapter 2, the differential cross section for the polarized $e^+e_{L,R}^- \rightarrow Z^0 \rightarrow b\bar{b}$ exhibits a large forward-backward asymmetry. For a polarized Z^0 decay, the outgoing quark is produced preferentially along the direction opposite to the spin of the Z^0 boson. Therefore by knowing the helicity of the electron beam and the direction of the jet, the flavor of the primary quark in the jet can be inferred. The correct tag probability of this method is highly dependent on the polar angle of the jet with respect to the beam axis and the electron beam polarization. The probability that the jet is a b quark jet is

$$P(b) = \frac{1 + A_{FB}}{2}, \quad (6.1)$$

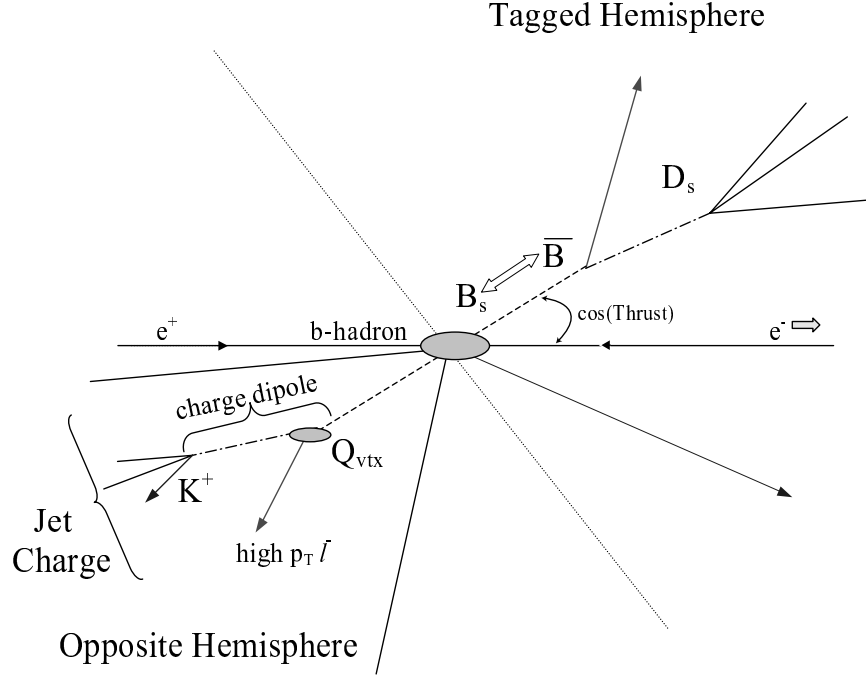


Figure 42: The drawing gives an overview of the initial state tags. The available tag consists of polarization, jet charge, vertex charge, charge dipole, high p_t lepton and kaon tags.

where A_{FB} is the polarized forward-backward asymmetry, defined as,

$$A_{FB} = 2A_b \left(\frac{A_e - P_e}{1 - A_e P_e} \right) \left(\frac{\cos \theta_{\vec{T}}}{1 + \cos^2 \theta_{\vec{T}}} \right), \quad (6.2)$$

with A_b and A_e (defined in chapter 2.3) assumed to have the Standard Model values of 0.935 and 0.150, respectively. The polar angle θ_T in equation (6.2) is defined as the angle between the thrust axis (signed to point in the hemisphere of interest) and the electron beam direction. P_e is the electron beam polarization ($P_e > 0$ for right handed and < 0 for left handed electron beam). The polarization tag is 100% efficient and the average correct tag probability is about 73%.

6.1.2 Jet Charge

In addition to polarization, charge information in the hemisphere opposite to the reconstructed B_s^0 can be used to determine the initial quark flavor. One such tag is the momentum-weighted jet charge. The jet charge method exploits the fact that the charged tracks from the B decays carry information about the flavor of the primary quark. In general, B decay products have higher momentum than fragmentation tracks. Therefore, to emphasize the contribution of B decay tracks to the jet charge, each track in the hemisphere is weighted by its momentum parallel to the thrust axis. The momentum-weighted jet charge, Q_{jet} , is defined as:

$$Q_{jet} = \sum_i^{trks} q_i \left| \vec{p}_i \cdot \vec{T} \right|^\kappa, \quad (6.3)$$

where q_i and \vec{p}_i are the charge and momentum vector of track i . The vector, \vec{T} , is the thrust axis and κ (equal to 0.5) is a parameter determined from Monte Carlo that maximizes the jet charge separation between b and \bar{b} jets. The Q_{jet} distribution for data and Monte Carlo are shown in figure 43. The Monte Carlo histograms show the separation between b and \bar{b} quarks. A positive (negative) opposite hemisphere Q_{jet} value tags the event hemisphere as \bar{b} (b). The average correct tag fraction is about 65%.

6.1.3 Opposite Hemisphere Topological Tags

The remaining initial state tags used in the analysis all require the presence of topologically reconstructed vertices. The requirement of a topologically reconstructed vertex in the opposite hemisphere reduces the efficiency of the tag. However, they provide additional initial state information (when available) and therefore are included to enhance the overall tagging purity.

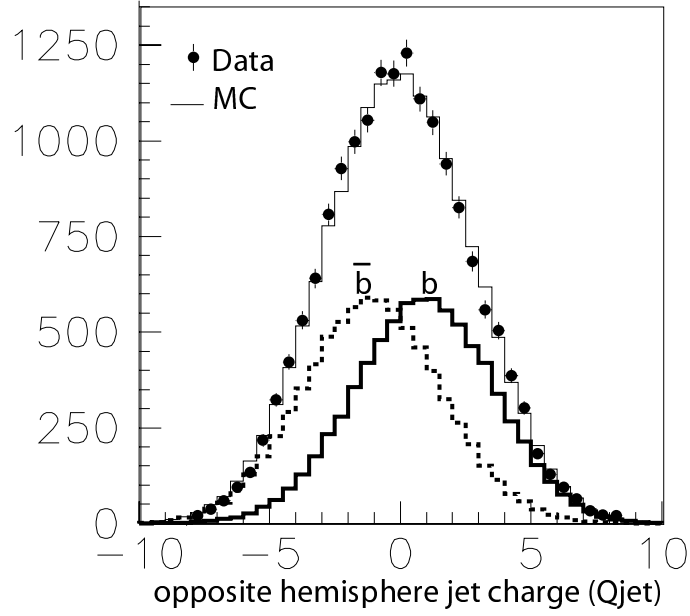


Figure 43: Momentum-weighted jet charge distributions for data and Monte Carlo.

6.1.3.1 Vertex Charge

The vertex charge tag requires the topological vertex to be charged. The sign of the charge gives information on the flavor of the parent quark in the hemisphere. For a vertex charge greater than zero (less than zero), it is likely that the hadron is a B^+ (B^-), which implies that the parent quark is a \bar{b} (b). To maximize the vertex charge purity, VXD-alone vectors (to be discussed in section 6.2.5) are included in the vertex charge determination.

6.1.3.2 Dipole Charge

Unlike the vertex charge tag, the dipole tag does not explicitly require the topological vertex to be charged. This tag exploits the cascade decay ($b \rightarrow c$) structure to infer the flavor of the parent quark. The dipole algorithm separates secondary decay tracks into two categories: B or D decay tracks. The charge

dipole is defined as the product of the sign of the charge difference and the distance between the B and the D vertices:

$$\delta q = \text{sign}(Q_D - Q_B) \cdot L_{B-D}. \quad (6.4)$$

For a decay containing a b (\bar{b}) quark, δq is likely to be greater than zero (less than zero).

6.1.3.3 High p_t Leptons/Secondary Kaons

The presence of leptons or secondary kaons provide additional information on the initial state. A positive charge lepton from a B vertex would indicate that the parent quark in the hemisphere is \bar{b} ($\bar{b} \rightarrow W^+ \rightarrow l^+$). In the case of kaons, the dominant production mode is from the $b \rightarrow c \rightarrow s$ decay chain. For this decay mode, the charge of the kaon and the parent b quark have the same sign. If more than one kaon is attached to the B or D vertex, the sum of the kaon charges is used. The lepton and the kaon tags are available in 18% and 15% of the events, respectively.

6.1.4 Combination Using Neural Networks

A series of neural networks is used to combine all the opposite hemisphere charged tags [63]. A neural network is extremely effective at maximizing all the available information as well as handling correlations between tags. Three separate neural networks are trained for the following tags: 1.) vertex charge, 2.) charge dipole and 3.) lepton/kaon/jet charge.

The purity of the reconstructed vertex charge strongly depends on the invariant mass of the vertex. A low mass vertex would suggest that a significant number of

tracks (either neutral or charged) are not accounted for. Therefore, the p_t corrected mass is included as one of the inputs to the vertex charge neural net. The remaining inputs are: vertex charge, vertex decay length and the number of VXD-alone vectors. The average vertex charge tagging purity using the neural net is about 74% with an efficiency of 52%.

The charge dipole neural net contains similar inputs as the vertex charge neural net. These are: δq , p_t corrected vertex mass, vertex decay length and vertex charge. The tagging purity using the neural net is about 68% with an efficiency of 29%.

Due to the low efficiency of lepton and kaons tags, lepton and kaon information are combined with jet charge into a single neural net. The inputs to the third neural net are: Q_{jet} , charge of the lepton weighted by its transverse momentum (if available), sum of the kaon charges weighted by the total momentum of the kaons (if available), vertex charge and vertex decay length. The average tagging purity is about 67%.

A fourth neural net is trained to combine the results of the three charge tag neural nets and to return the b quark probability as the output. Finally, the result of the fourth neural net is analytically combined with the b quark probability from the polarization tag to obtain the overall initial state tag probability. The overall tagging purity is about 77%. The b quark probability distribution using the combined neural net tag for both data and Monte Carlo are shown in figure 44.

6.2 B_s^0 Candidate Selection

The next step of the analysis after the initial state determination is to search for the signal events ($B_s^0 \rightarrow D_s^- X$). Figure 45 is an illustration of the signal decay topology. On average the B_s^0 decay vertex is about 3mm from the IP while the

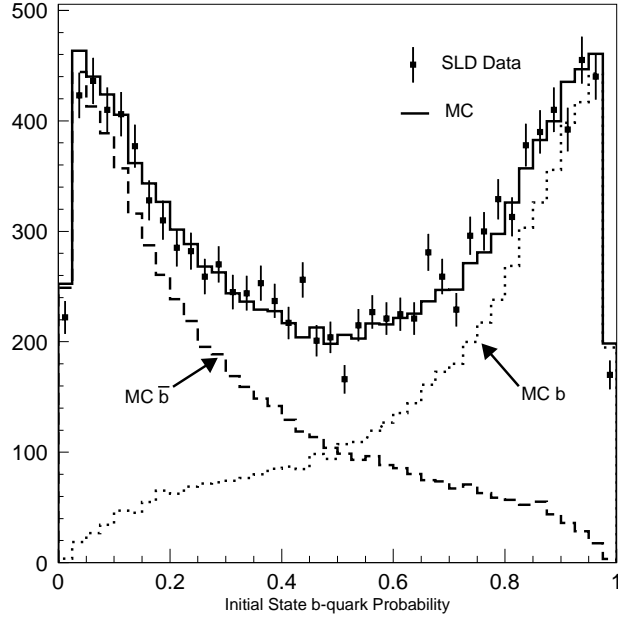


Figure 44: The initial state b quark probability distribution for data and Monte Carlo using the combined neural net tag.

D_s is about 1mm from the B_s^0 decay vertex. The B_s^0 decays to a D_s^- and an odd number of charged tracks (typically only one track). The D_s^- decays downstream of the B_s^0 to a pair of kaons and a pion. The reconstruction of the B_s^0 candidate is divided up into three main steps: 1.) reconstruct D_s^- candidates, 2.) locate the B_s^0 decay vertex and 3.) determine the boost of the B_s^0 . The latter two quantities are needed to compute the proper decay time of the B_s^0 .

6.2.1 D_s Reconstruction

The two D_s decay modes used in the analysis are: $D_s^- \rightarrow \phi\pi^-$ ($\phi \rightarrow K^+K^-$) and $K^{*0}K^-$ ($K^{*0} \rightarrow K^+\pi^-$). D_s^- candidates are reconstructed by first pairing oppositely charged tracks to form a ϕ (K^{*0}) candidate for the $\phi\pi^-$ ($K^{*0}K^-$) mode. A third track is then attached to form a D_s candidate. Charged tracks used in the

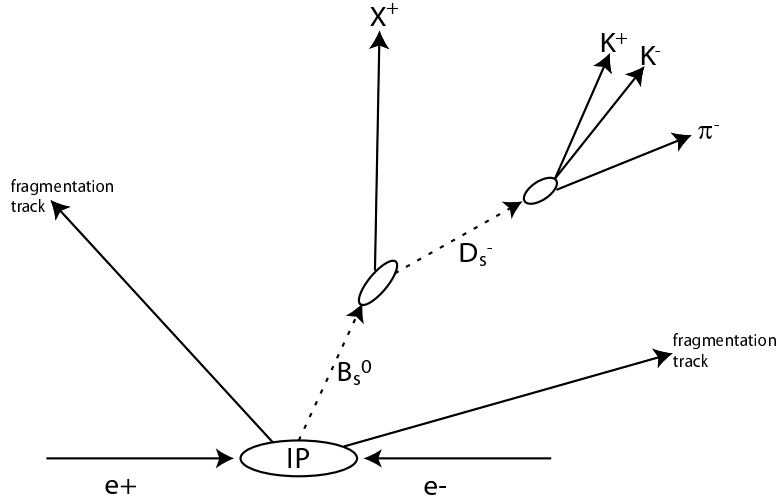


Figure 45: $B_s^0 \rightarrow D_s^- X$ event topology.

combination are required to satisfy three quality cuts to ensure that the tracks are well reconstructed. The tracks used in the analysis are required to have:

- at least 23 CDC hits (out of 80 possible hits);
- at least 2 vertex detector hits;
- combined $\chi^2/\text{d.o.f.}$ for the CDC+VXD3 fit of less than 8.

To maximize the discrimination between true D_s decays and combinatorial background, kinematical information for the D_s candidate is fed into a neural net. The neural net inputs for the $\phi\pi$ ($K^{*0}K$) mode include: K^+K^- ($K^+\pi^-$) invariant mass, fitted vertex probability of the D_s , total momentum of the D_s , helicity angle θ^* (angle between the ϕ (K^{*0}) and the D_s flight direction in the D_s rest frame), helicity angle λ^* (angle between the charged daughter of the D_s and the K^+ from ϕ (K^{*0}) decay in the rest frame of the neutral meson), and particle ID information for the three tracks. The complete list of neural net inputs is shown in table 4. The neural net is trained on a sample of $Z^0 \rightarrow b\bar{b}$ Monte Carlo events. The neural

$\phi\pi$ Mode	$K^{*0}K$ Mode
D_s vertex χ^2 prob	D_s vertex χ^2 prob
$P_{tot}(D_s)$	$P_{tot}(D_s)$
KK opening angle	$K\pi$ (from K^{*0}) opening angle
D_s decay length (in σ)	D_s decay length (in σ)
helicity angle λ^*	helicity angle λ^*
helicity angle θ^*	helicity angle θ^*
particle ID of three tracks	particle ID of three tracks
	Average Normalized 3-D impact parameter of $KK\pi$ tracks

Table 4: D_s Neural net inputs. Left column is for $\phi\pi$ and right column is for $K^{*0}K$

net outputs are shown in figure 46. The data and Monte Carlo distributions are in good agreement.

The optimal neural net cut that maximizes the sensitivity of the analysis to B_s^0 mixing is determined separately for each of the two D_s decay modes. The minimum cut for the $\phi\pi$ mode is determined to be at 0.9 and for the $K^{*0}K$ mode, at 0.8. Furthermore, for the $K^{*0}K$ mode, the kaon from the K^{*0} decay is required to be identified by the CRID in order to suppress combinatorial and other non- D_s backgrounds (e.g. D^+ reflection).

The $KK\pi$ invariant mass spectra are shown in Figures 47 and 48. The D_s mass peak is fitted separately for events with loose and hard kaon ID and for $Q=0$ and $Q=\pm 1$ events, where Q is defined as the total charge of all tracks associated with the B decay. For the $\phi\pi$ mode, both the neutral B candidates ($Q=0$) and the charged candidates ($Q=\pm 1$) are used in the analysis. The charged sample is heavily contaminated with B^\pm events, however, it still contains a significant fraction of B_s^0 events and therefore is not discarded in the analysis. For the $K^{*0}K$ mode, only the neutral candidates are included in the final event sample. The definition of the

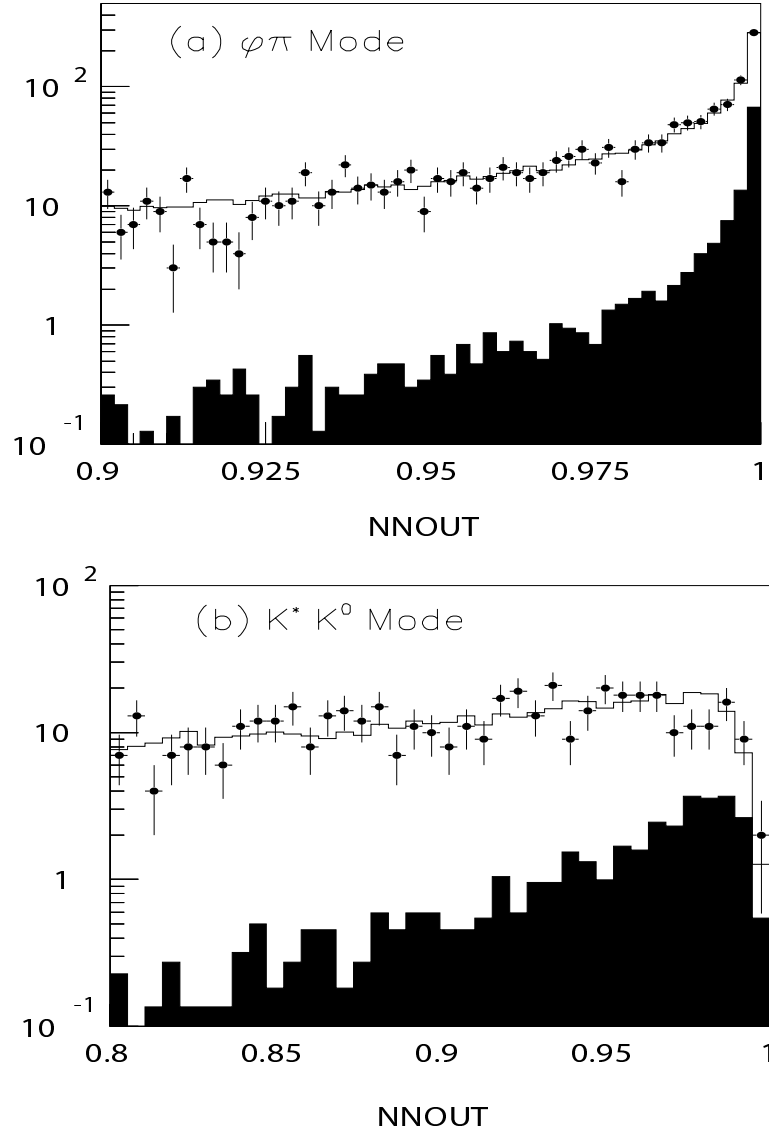


Figure 46: D_s neural net output distributions for (a) $\phi\pi$ and (b) $K^* K^0$ modes. Dots are data, open histograms are Monte Carlo and solid black histograms represent MC simulation of true D_s events.

loose kaon ID for the $\phi\pi$ mode is that all assumed particle types are consistent with the available CRID information (i.e. the kaon candidates are not tagged as definite pion or proton and the pion candidate is not tagged as definite kaon or proton). The hard kaon ID requires at least one kaon candidate to be identified as a kaon. The loose kaon ID for the $K^{*0}K$ mode requires at least one positively identified kaon and the hard kaon ID requires both kaon candidates to be tagged as definite kaons by the CRID. The estimated numbers of D_s candidates and combinatorial fractions are given in tables 5 and 6. The details of the B vertex charge reconstruction and the $m_{KK\pi}$ mass fits are described in section 6.2.5. A candidate event of the B_s^0 semileptonic decay from the 1998 data is shown in figure 49.

	No Definite Kaon ID		With Definite Kaon ID	
	Q=0	Q= ± 1	Q=0	Q= ± 1
# of hadronic candidates	100	56	54	39
# of semileptonic candidates	9	7	12	3
Combinatorial fraction	42.3 \pm 2.1%	53.8 \pm 2.7%	21.7 \pm 2.2%	14.1 \pm 1.4%

Table 5: Number of $D_s \rightarrow \phi\pi$ candidates within ± 40 MeV of the nominal D_s mass and the estimated average combinatorial background fractions.

	1 Kaon ID	2 Kaons ID
	Q=0	Q=0
# of hadronic candidates	40	30
# of semileptonic candidates	6	5
Combinatorial fraction	32.9 \pm 3.3%	22.3 \pm 2.2%

Table 6: Number of $D_s \rightarrow K^{*0}K$ candidates within ± 40 MeV of the nominal mass and the estimated average combinatorial background fractions.

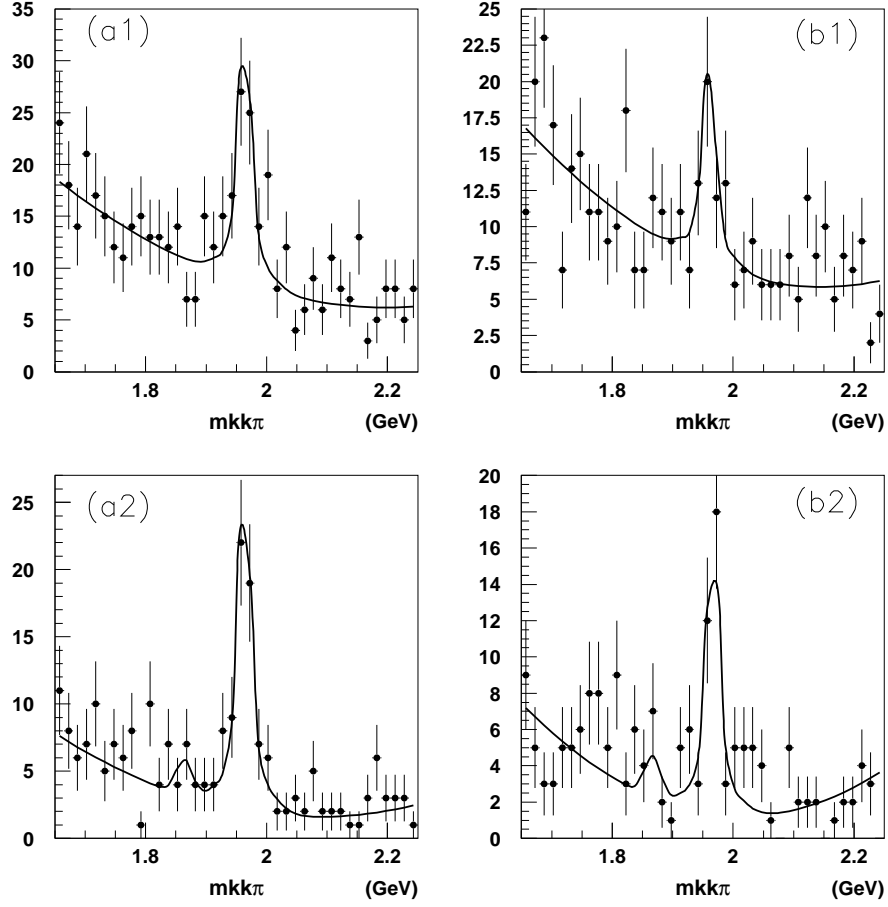


Figure 47: Distributions of the $KK\pi$ invariant mass for the $\phi\pi$ mode. Plots in the left column (a1,a2) are for the B_s^0 candidates with reconstructed vertex charge = 0 and plots in the right column (b1,b2) are for the B_s^0 candidates with reconstructed vertex charge = ± 1 . The $\phi\pi$ sample is further subdivided into events with loose kaon ID (a1,b1) and events with hard kaon ID (a2,b2). The lower peak at about 1.87 GeV is the D^+ mass peak.

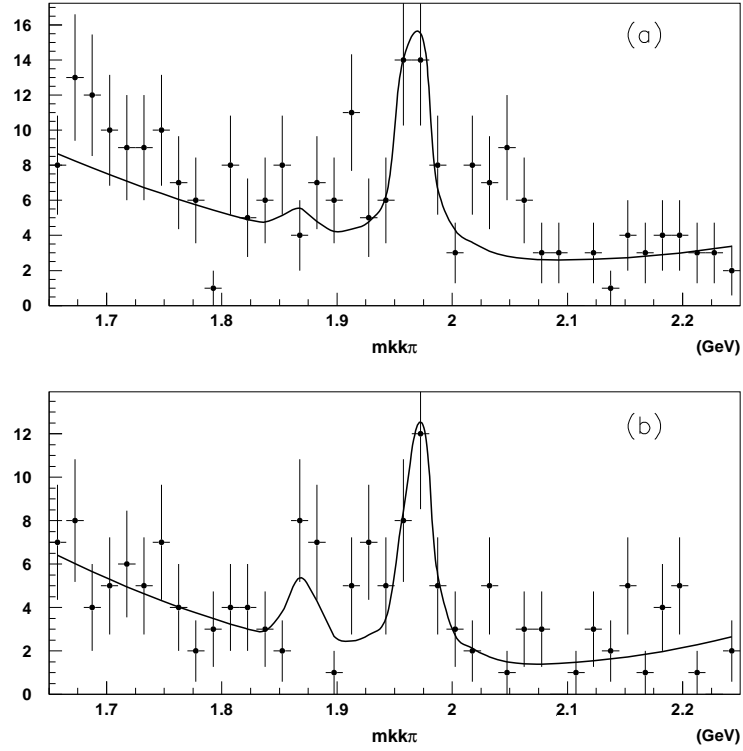


Figure 48: Distributions of the $KK\pi$ invariant mass for the K^*K^0 mode. (a) for events with loose kaon ID and (b) for events with hard kaon ID. The lower peak at about 1.87 GeV is the D^+ mass peak.

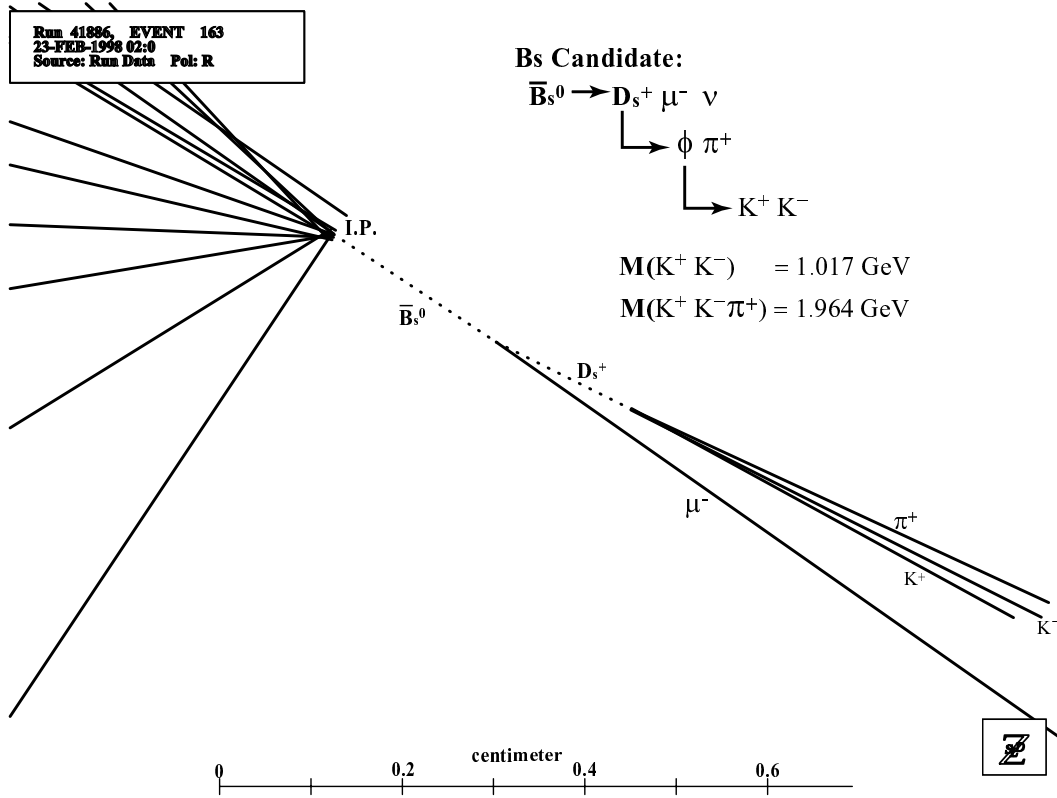


Figure 49: Candidate B_s^0 semileptonic decay event. All tracks in the event (K^+, K^-, π^+ and μ^-) have been identified by the particle ID system. The three hadronic tracks are consistent with coming from the D_s decay. The D_s is vertexed upstream with a μ^- track to form the \bar{B}_s^0 candidate.

6.2.2 B Decay Length Reconstruction

We now move on to discuss the reconstruction of the B decay length. The decay length of the B_s^0 is defined as the distance between the IP and the B_s^0 decay vertex. The algorithm to determine the IP position has already been discussed in the previous chapter. The B_s^0 decay vertex is found by vertexing the D_s track with other B decay tracks in the hemisphere. To improve the decay length resolution, a “virtual” D_s track is first constructed using the D_s daughter tracks. A detailed description of the “virtual” D_s track reconstruction is included in Appendix B. From this point on, we will refer to the “virtual” D_s track as simply the D_s track.

The B vertex reconstruction algorithm consists of two steps. The first step involves the selection of the seed vertex (preliminary estimate of the B_s^0 decay vertex). To find the seed, the D_s track is individually vertexed with each quality track (excluding D_s daughters) in the same hemisphere, and the vertex that is farthest from the IP and upstream (or consistent with being upstream within 5σ) of the D_s and has a vertex fit χ^2 of less than 5 is chosen as the seed. The definition of a quality track is given in section 6.2.1. Step two involves the separation of tracks into secondary decay and fragmentation tracks. The discriminating variable used is the L/D parameter, as defined in figure 38. A track is chosen as a secondary B decay track if it satisfies the following two conditions: 1.) the track L/D is greater than 0.5 and 2.) the track forms a good vertex with the D_s track (fit $\chi^2 \leq 5$). The latter condition is imposed to reject B daughter tracks (from double charm decays) that do not point back to the B vertex. Finally, the selected tracks are then vertexed together with the D_s to obtain the best estimate of the B decay position. The average number of tracks attached to the B vertex is about 2.5. The resulting B decay length resolution is highly dependent on the decay topology. The decay

length and the residual plots for various B species are shown in Figures 50 and 51, respectively. The list of decay length resolutions estimated from Monte Carlo for the various decay categories is shown in table 7. The resolution is parameterized by the sum of two Gaussians with core fraction fixed to 60%.

Decay Category	Q=0		Q= ± 1	
	Core σ_L (μm)	Tail σ_L (μm)	Core σ_L (μm)	Tail σ_L (μm)
$B_s^0 \rightarrow D_s^- X$ (right-sign)	50 ± 1	151 ± 4	59 ± 2	224 ± 10
$B_s^0 \rightarrow D_s^+ X$ (wrong-sign)	85 ± 5	281 ± 22	85 ± 5	281 ± 22
$B_d^0 \rightarrow D_s^\pm X$	80 ± 3	312 ± 13	96 ± 6	341 ± 20
$B^\pm \rightarrow D_s^\pm X$	105 ± 8	398 ± 72	79 ± 3	292 ± 11
$b - Baryon \rightarrow D_s^\pm X$	83 ± 5	222 ± 17	83 ± 5	222 ± 17

Table 7: Decay length resolutions for various decay topologies. Resolutions are parameterized separately for neutral and charged B events except for wrong-sign B_s^0 and b -Baryon events.

6.2.3 B Boost Reconstruction

The next major aspect of B_s^0 reconstruction is to determine the boost:

$$\beta\gamma = |\vec{P}_B|/m_B = \frac{\sqrt{E_B^2 - m_B^2}}{m_B}, \quad (6.5)$$

where \vec{P}_B is the momentum vector, E_B is the total energy and m_B is the mass of the B hadron. As shown in equation 6.5, the task of boost reconstruction is to estimate the total B hadron energy. The total B energy can be expressed as the sum of energy of charged and neutral tracks from the B decay,

$$E_B = E_B^{ch} + E_B^0. \quad (6.6)$$

The contribution from charged tracks is calculated by summing the energy of tracks attached to the B vertex, including D_s daughters. If the mass of the charged

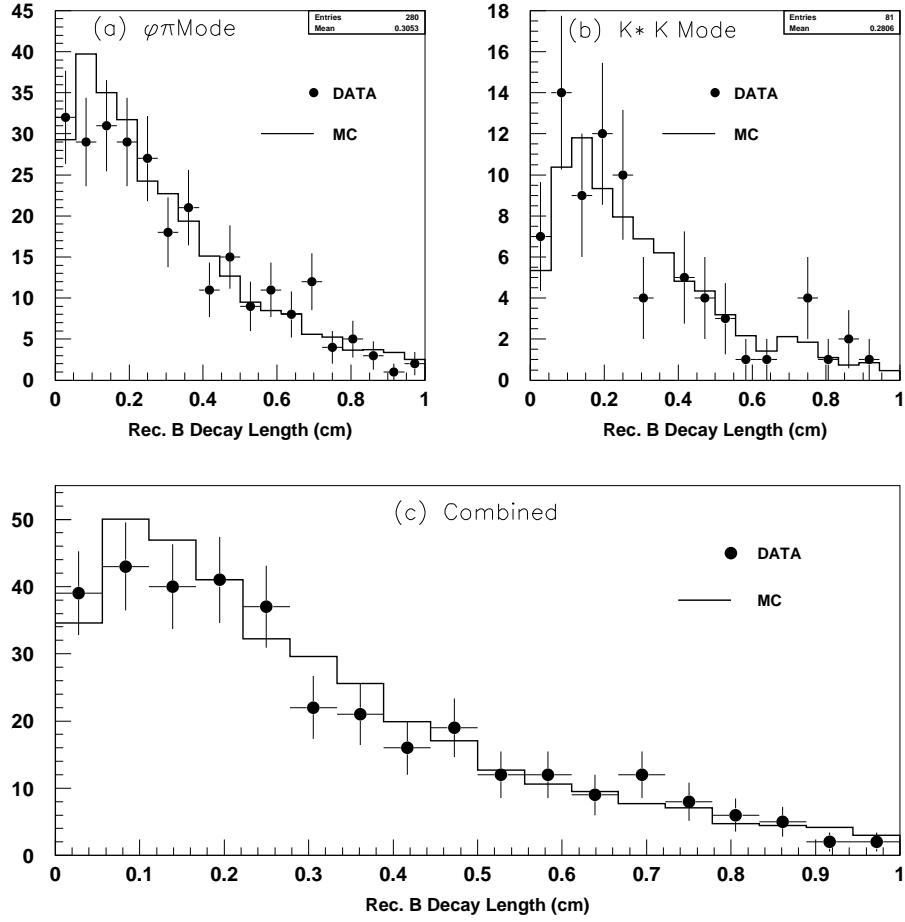


Figure 50: Decay length distributions for data and Monte Carlo. Plot (a) is for $\phi\pi$ mode, (b) is for $K^{*0}K$ and (c) is for both modes combined.

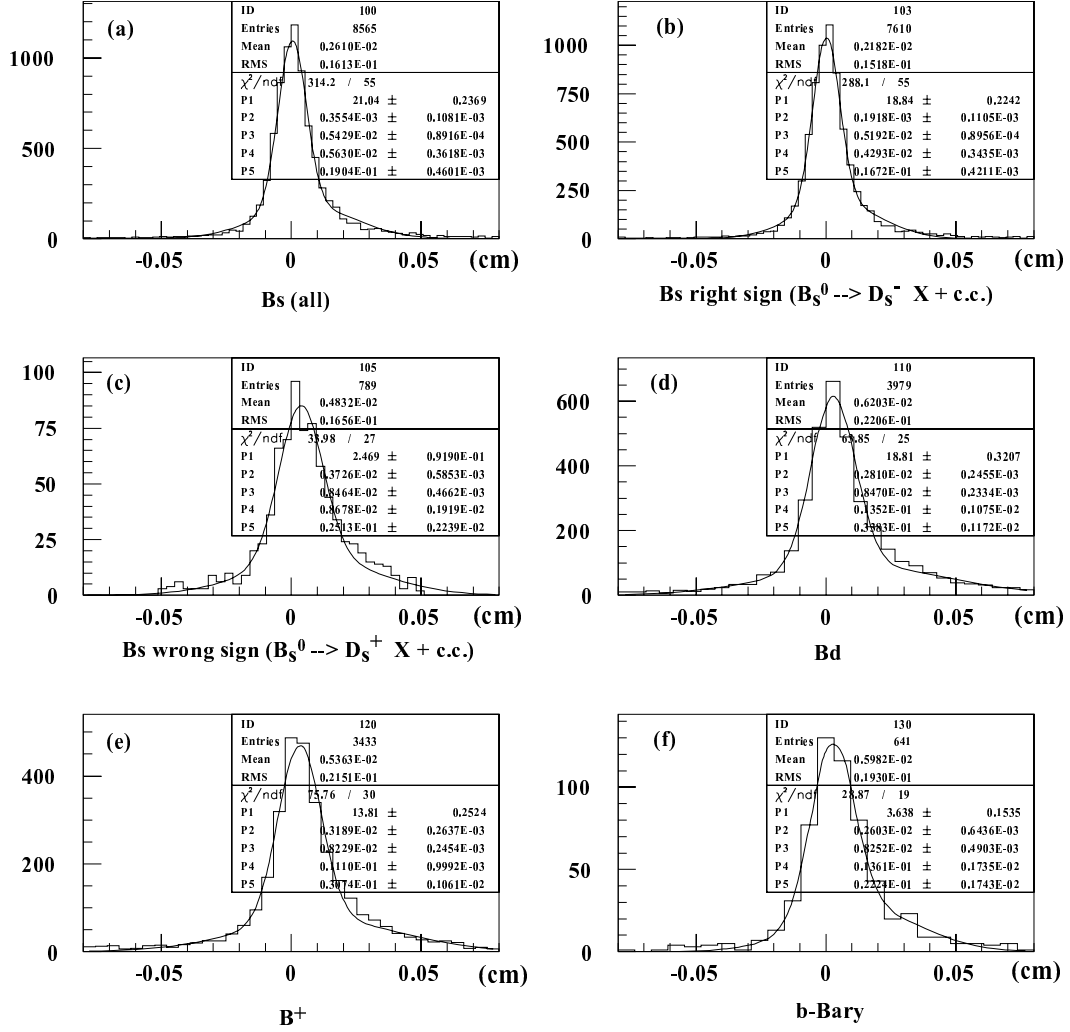


Figure 51: Decay length residual ($L_{reconstructed} - L_{true}$) plots for (a) B_s^0 inclusive, (b) B_s^0 right-sign, (c) B_s^0 wrong-sign, (d) B_d^0 , (e) B^+ and (f) b -baryons events. The plots include both neutral ($Q=0$) and charged ($Q=\pm 1$) events. The fitting function used to fit the residual plots is the sum of two Gaussians with the core fraction fixed to 60%. The parameter P1 is the normalization, P2 (P5) is the mean of the core (tail) Gaussian and P3 (P4) is the width of the core (tail) Gaussian.

particle associated with the B vertex is not known, the pion mass is assumed in the energy calculation. The track attachment algorithm for the boost reconstruction is slightly more inclusive than the one used for the decay length reconstruction. The attachment requirements are loosened to improve the efficiency of attaching true B decay tracks to the vertex. A track is attached to the vertex if the following conditions are satisfied:

- a quality track (as defined in section 6.2.1);
- angle between track and $D_s < 90$ degrees;
- $L/D > 0.3$;
- $T < 0.1$.

The parameters L , D and T are defined in chapter 5.2.3.2. The calculation of the neutral B energy (E_B^0) involves four different algorithms: fragmentation, mass, maximum missing mass and thrust angle methods. The first two algorithms use calorimeter information while the last two methods rely solely on the reconstructed charged tracks and the kinematics of the B decay to estimate the neutral energy.

6.2.3.1 Fragmentation Method

The fragmentation method [64] is based on the idea that the energy of the B hadron is the difference between the total energy in the hemisphere (E_h) and the energy carried away by the fragmentation particles (E_f),

$$E_B = E_h - E_f. \quad (6.7)$$

The total energy in the hemisphere is equal to the nominal beam energy of 45.6 GeV. Similar to the B energy, the fragmentation energy has both charged and neutral

contributions ($E_f = E_f^{ch} + E_f^0$). The charged fragmentation energy is simply the energy of all the charged tracks in the hemisphere minus the energy of the tracks attached to the B vertex,

$$E_f^{ch} = E_h^{ch} - E_B^{ch}. \quad (6.8)$$

The tracks used in the E_h^{ch} calculation include not only the quality tracks but also the “Okay” tracks. The “Okay” tracks are tracks without vertex detector hits but are otherwise well reconstructed tracks with good momentum information from the drift chamber. A Monte Carlo study indicates that the inclusion of “Okay” tracks improves the calculation of E_h^{ch} .

The last remaining quantity to be determined is the neutral fragmentation energy. To compute this quantity, we sum up energy in the electromagnetic calorimeter that is not associated with any charged track in the hemisphere. The un-associated hits in the hadronic towers contain large contamination from the low momentum π^\pm tracks and therefore are not used in the neutral energy sum. The un-associated electromagnetic calorimeter hits are presumably coming from neutral particles from the fragmentation process as well as the B decay. To disentangle the two contributions, we parameterize using Monte Carlo, E_f^0 as a function of the total un-associated electromagnetic calorimeter energy. Figure 52 shows the parameterization obtained from a sample of Monte Carlo $B_s^0 \rightarrow D_s^- X$ events. The parameterization allows us to estimate the true neutral fragmentation energy from the measured un-associated electromagnetic energy. Finally, having determined both E_f^{ch} and E_f^0 , equation 6.7 can be used to estimate the total B energy.

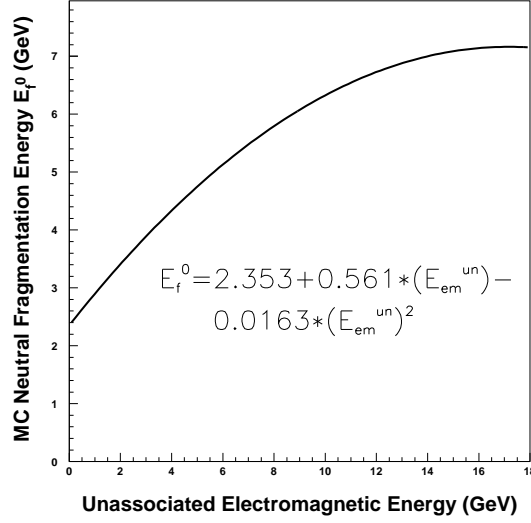


Figure 52: Functional dependence between the average un-associated electromagnetic energy and the average neutral fragmentation energy.

6.2.3.2 Mass Method

The mass method, as the name implies, uses the mass of the B hadron as a constraint to obtain the total B energy. In this method, the four-momentum vector of the B hadron (P_B^μ) is calculated using the charged tracks attached to the B vertex and the missing energy in the hemisphere. The missing energy is added to account for the neutrinos. The missing energy component is given by:

$$E_{miss} = E_h - (E_h^{ch} + E_{em}^{un}), \quad (6.9)$$

where the variable E_{em}^{un} is the total un-associated electromagnetic energy. If the invariant mass of the charged and missing energy system is below the nominal B hadron mass, the un-associated electromagnetic clusters are added to the system one at the time. The cluster nearest to the B vertex axis is added in first, followed by the next nearest clusters until the invariant mass of the system reaches the nominal B mass. The invariant mass is allowed to exceed the nominal B mass

provided the addition of the new cluster brings the invariant mass closer to the nominal B mass. On rare occasions when there are high energy un-associated clusters (>3 GeV clusters), those clusters are used in the invariant mass calculation first before using the clusters nearest the vertex axis, since high energy clusters are more likely to be coming from the B than the fragmentation process. Finally, the B hadron energy is simply the sum of E_B^{ch} , E_{miss} and the energy of the attached calorimeter clusters.

6.2.3.3 Maximum Missing Mass Method

The maximum missing mass method is a novel technique originally developed at SLD for the B fragmentation measurement [65]. It exploits the kinematics of the B decay to estimate the neutral B energy. The outline of the technique is given below.

The neutral B energy can be expressed as:

$$(E_B^0)^2 = M_0^2 + P_t^2 + (P_B^{0L})^2, \quad (6.10)$$

where p_t is the measured transverse momentum of all B tracks with respect to the B vertex axis, M_0 is the missing mass and P_B^{0L} is the missing longitudinal momentum (along the vertex axis) of the neutral B decay tracks. One of the three unknown variables in equation 6.10 can be eliminated using the B mass constraint:

$$\begin{aligned} m_B^2 &= E_B^2 - (P_B^{chL} + P_B^{0L})^2 \\ &= (E_B^{ch} + E_B^0)^2 - (P_B^{chL} + P_B^{0L})^2 \\ &= \left[E_B^{ch} + \sqrt{M_0^2 + P_t^2 + (P_B^{0L})^2} \right]^2 - (P_B^{chL} + P_B^{0L})^2, \end{aligned} \quad (6.11)$$

where P_B^{chL} is the longitudinal momentum of the charged B decay tracks with respect to the vertex axis. The remaining two unknowns in equation 6.11 are M_0

and P_B^{0L} . If the missing mass is known, P_B^{0L} can be solved and hence the total neutral B energy can be calculated.

The missing mass for a given decay has a kinematic upper bound (M_{0max}) that is given by the expression:

$$M_{0max}^2 = m_B^2 - 2m_B\sqrt{M_{ch}^2 + p_t^2} + M_{ch}^2, \quad (6.12)$$

where M_{ch} is the invariant mass of the charged B decay tracks. The true missing mass (M_0) is the maximum missing mass (M_{0max}) when the momentum of the decaying charged tracks (\vec{P}_B^{ch}) in the B rest frame is perpendicular to the B boost direction. It was found, based on Monte Carlo study, that the true missing mass tends to cluster near the maximum missing mass. For this reason, we set M_0 equal to M_{0max} . If the calculated M_{0max} is less than zero, we constrain the value of M_0 to zero. We can now calculate P_B^{0L} by solving equation 6.11 and then the total B energy.

6.2.3.4 Thrust Angle Method

The last boost reconstruction algorithm makes an assumption that the sum of momenta from the B decay and the fragmentation tracks should point along the direction of the thrust axis, as shown in figure 53. Given this assumption, we can write a series of constraints:

1. $|P_B| \cos(\theta) + |P_f| \cos(\phi) = |P_h|$
2. $|P_B| \sin(\theta) = |P_f| \sin(\phi)$
3. $E_B + E_f = E_h$
4. $E_B^2 = m_B^2 + P_B^2$

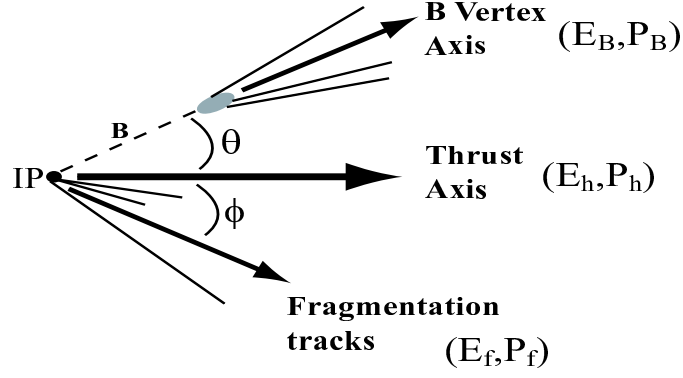


Figure 53: Schematic diagram showing the variables used in the thrust angle method.

$$5. E_f^2 = m_f^2 + P_f^2$$

$$6. E_h^2 = m_h^2 + P_h^2$$

The variables P_B (E_B), P_f (E_f) and P_h (E_h) are the total B , fragmentation and hemisphere momentum (energy), respectively. The angle θ (ϕ) is the angle between the B (fragmentation) flight direction and the thrust axis. The parameters m_f and m_h are fragmentation and hemisphere invariant masses. Constraints (1) and (2) can be combined to eliminate the ϕ dependence. The resulting equation is then substituted into constraint (4) to solve for E_B . We write E_B as a function of θ , E_h , m_h and m_f :

$$E_B = \frac{E_h M_x^2 \pm P_h \cos(\theta) \sqrt{M_x^4 - 4m_B^2(m_h^2 + P_h^2(1 - \cos^2(\theta)))}}{2m_h^2 + P_h^2(1 - \cos^2(\theta))}, \quad (6.13)$$

where $M_x^2 = m_b^2 + m_h^2 - m_f^2$. To resolve the two-fold ambiguity for E_B in equation 6.13, some assumptions are made and the positive solution is chosen. The hemisphere and fragmentation mass are estimated from the charged tracks in the event using Monte Carlo parameterizations [66].

6.2.3.5 Averaging the Boost Algorithms

The results of the four boost algorithms are combined, taking correlations into account, to obtain the most optimal estimate of the B boost [67]. The average is performed in bins of charged track momentum (P_B^{ch}) and missing mass (M_0). Figure 54 compares the boost distributions between data and Monte Carlo. The agreement is good for $\phi\pi$ and $K^{*0}K$ as well as for the combined distributions. The relative boost residual ($\frac{boost_{rec}-boost_{MC}}{boost_{MC}}$) distributions for the different B species are shown in figure 55. The summary of the relative boost resolution is given in table 8.

Decay Category	Q=0		Q= ± 1	
	Core $\sigma_{\beta\gamma}$ (%)	Tail $\sigma_{\beta\gamma}$ (%)	Core $\sigma_{\beta\gamma}$ (%)	Tail $\sigma_{\beta\gamma}$ (%)
$B_s^0 \rightarrow D_s^- X$ (right-sign)	7.6 ± 0.2	19.1 ± 0.4	10.9 ± 0.4	23.8 ± 0.8
$B_s^0 \rightarrow D_s^+ X$ (wrong-sign)	8.2 ± 0.2	20.6 ± 1.1	10.6 ± 1.0	24.6 ± 2.6
$B_d^0 \rightarrow D_s^\pm X$	8.5 ± 0.2	21.1 ± 0.6	11.9 ± 0.6	23.2 ± 1.0
$B^+ \rightarrow D_s^\pm X$	11.1 ± 0.7	23.0 ± 1.3	8.8 ± 0.3	22.8 ± 0.6
$b - Baryon \rightarrow D_s^\pm X$	9.7 ± 0.9	23.1 ± 1.5	11.7 ± 1.0	27.6 ± 3.9

Table 8: Relative boost resolutions for various decay topologies. The resolution is parameterized by the sum of two Gaussians with core fraction fixed to 60%.

6.2.4 B_s^0 Proper Time

Having reconstructed the decay length (L) and the boost ($\beta\gamma$) of the B_s^0 , we can now calculate the proper decay time. The proper decay time is given as:

$$\tau = L/(\gamma\beta c). \quad (6.14)$$

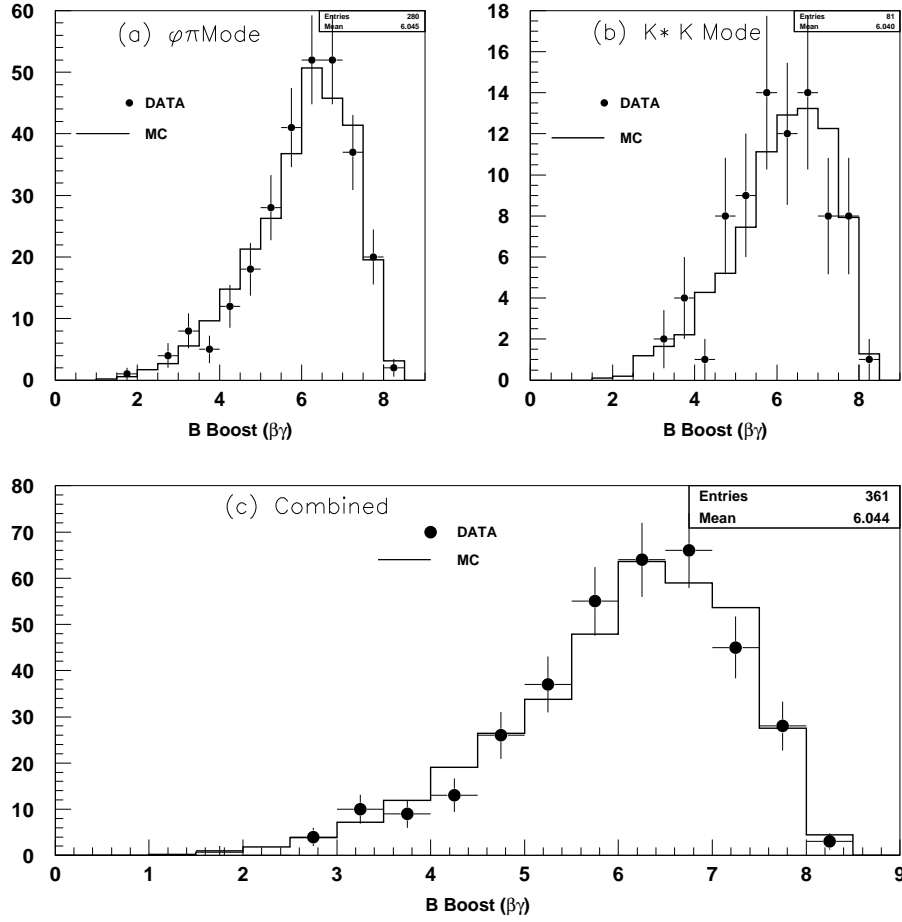


Figure 54: Reconstructed boost distributions for (a) $\phi\pi$ mode, (b) $K^{*0}K$ mode and (c) combined.

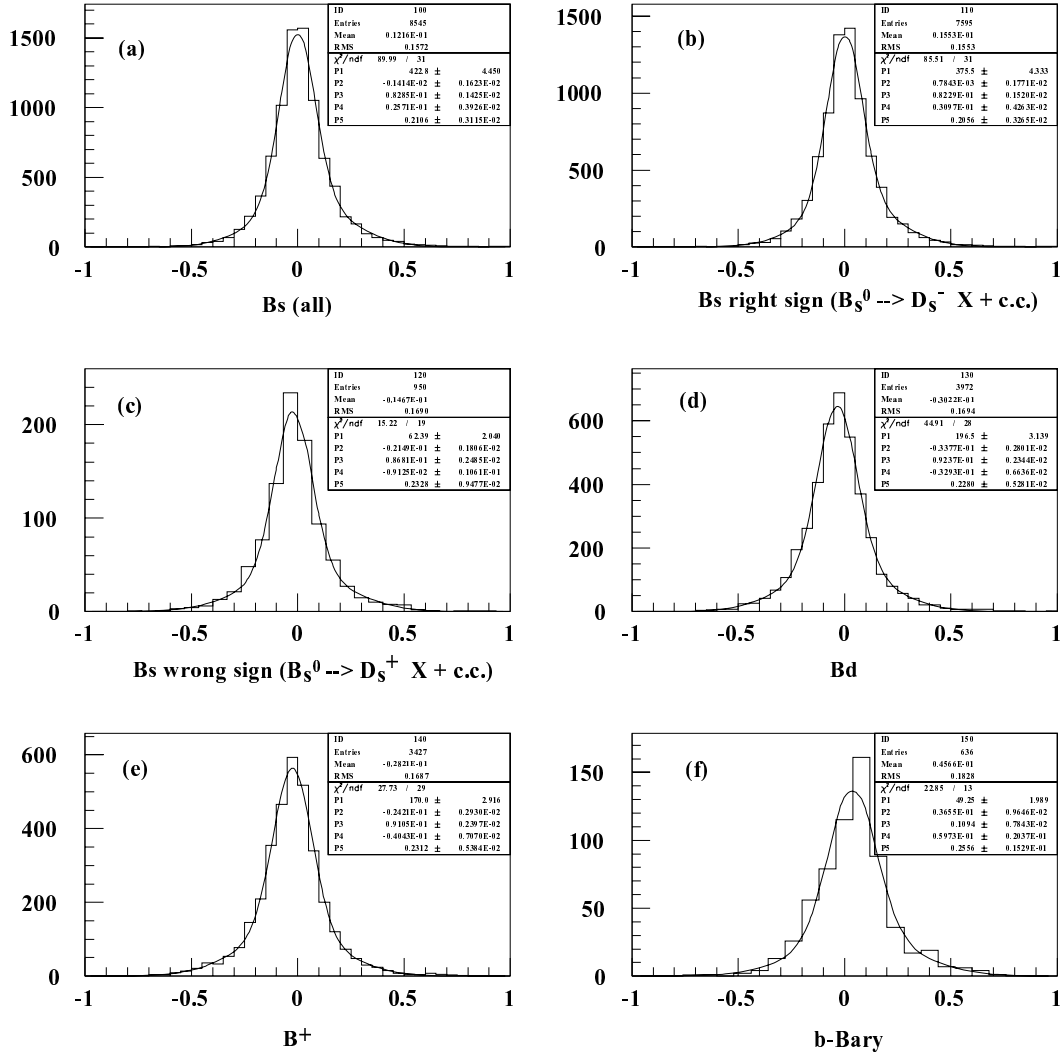


Figure 55: Relative boost residuals for (a) B_s^0 inclusive, (b) B_s^0 right-sign, (c) B_s^0 wrong-sign, (d) B_d^0 , (e) B^+ and (f) b -baryon events. The plots include both neutral ($Q=0$) and charged ($Q=\pm 1$) events. The fitting function used to fit the residual plots is the sum of two Gaussians with the core fraction fixed to 60%. The parameter P1 is the normalization, P2 (P5) is the mean of the core (tail) Gaussian and P3 (P4) is the width of the core (tail) Gaussian.

The proper decay time distributions for data and Monte Carlo are shown in figure 56. The plots show some events with negative reconstructed proper time. These are events where the reconstructed B decay vertex is behind the IP. The negative proper time events do not contribute to the analysis and therefore, for simplicity, are removed from the final data sample.

6.2.5 B Vertex Charge Reconstruction

We conclude the chapter on event reconstruction with a discussion on the determination of the charge of the B vertex. Nominally, the charge of the B hadron is the sum of the charge of the quality tracks associated with the B decay. To improve charge purity, tracks with only VXD3 hits (VXD-alone vectors) that are not used in the decay vertex and momentum reconstruction are also included in the B charge determination [61]. The VXD-alone vectors are required to have hits in all three layers of the vertex detector. This requirement is necessary for two reasons: it suppresses fake vectors from random hits and improves track curvature determination. A neural net is used to decide whether a vector is consistent with a track coming from a B decay. The inputs to the vector neural net are similar to the ones for quality track attachment. The inputs are: T , L , L/D (as defined in chapter 5.2.3.2) and the angle between the VXD-alone vector and the vertex axis. If a vector is attached to a secondary vertex, the helix fit is repeated with the secondary vertex as an additional constraint to improve the curvature/charge determination. Monte Carlo studies indicate that the charge is correctly signed for about 85% of the VXD-alone vectors. The B vertex charge, Q , is given by the sum of the charge of quality tracks (from the neural net attachment as described in chapter 5.2.3.2) and VXD-alone vectors attached to the vertex. The neural net

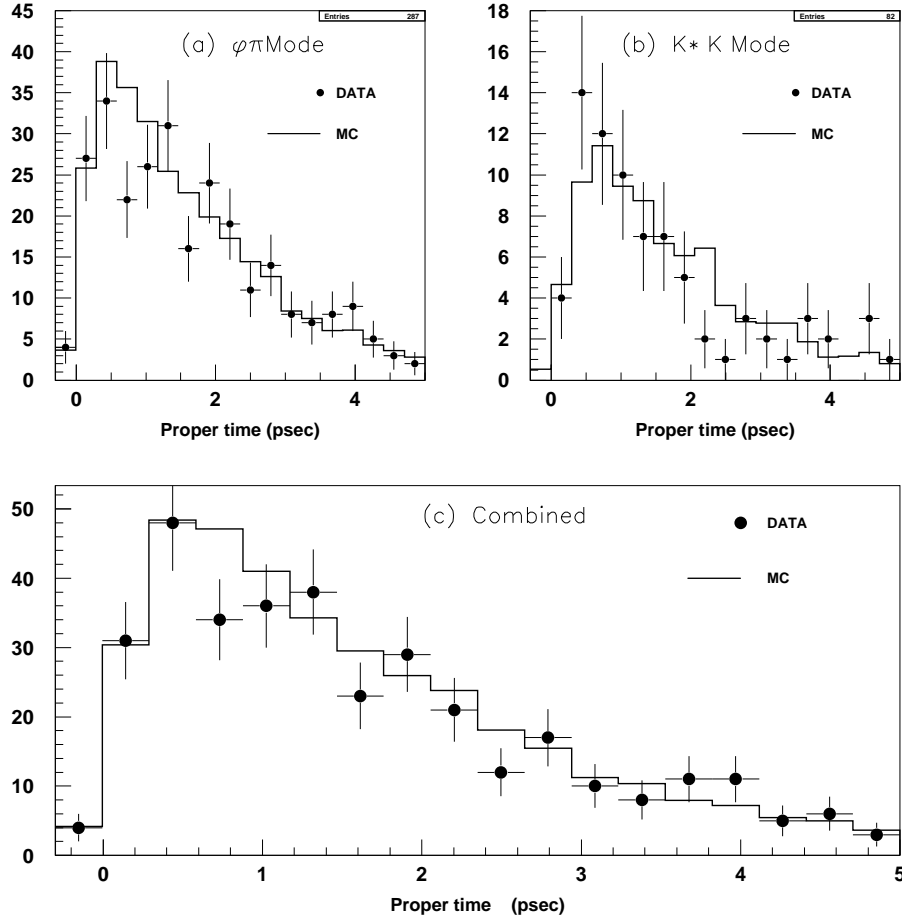


Figure 56: Reconstructed proper decay time distributions for (a) $\phi\pi$ mode, (b) $K^{*0}K$ mode and (c) combined.

based vertex charge reconstruction requires the B_s^0 candidate hemisphere to contain a topological vertex. For events with no topological vertices found, which occurs in data $4\pm 1\%$ (in Monte Carlo $5.0\pm 0.3\%$) of the time, the charge of the B vertex is taken as the sum of the charge of quality tracks attached to the candidate vertex from the boost reconstruction algorithm. The reconstructed vertex charge distributions for data and Monte Carlo are shown in figure 57. For the $\phi\pi$ mode, the cut on the vertex charge (Q) is shown on the plot. For the $K^{*0}K$ mode, Q is required to be zero.

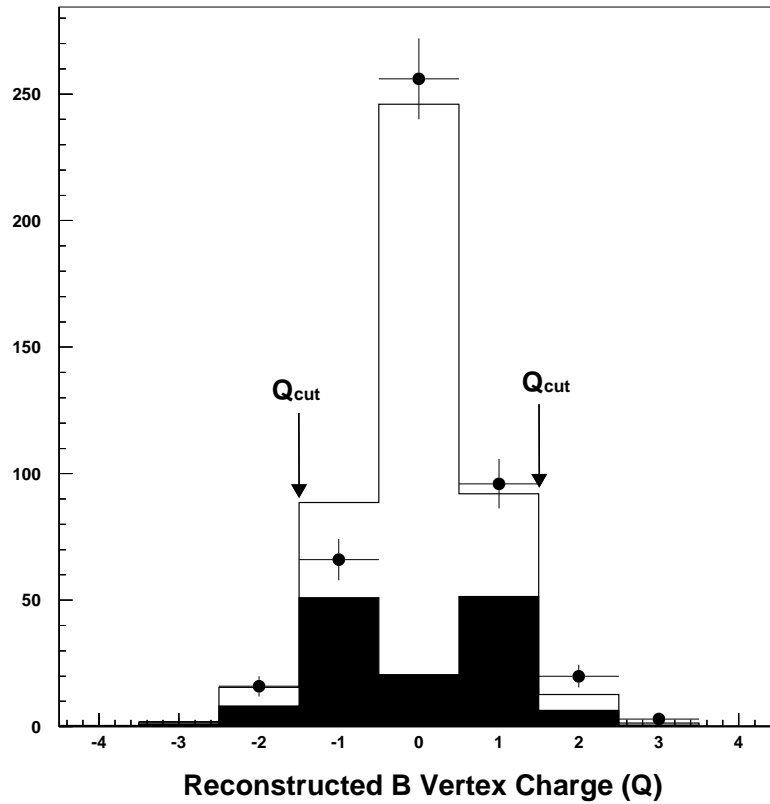


Figure 57: Reconstructed B vertex charge distribution for data (dots), M.C. neutral B events (open histogram), and M.C. charged B events (solid histogram). The distribution is for $\phi\pi$ and $K^{*0}K$ modes combined.

CHAPTER 7

B_s^0 OSCILLATION STUDIES

In this chapter, we discuss the method used to extract the oscillation frequency of the B_s^0 meson from the data. In particular, we use the unbinned maximum likelihood approach to search for the oscillation signal. The construction of the likelihood function is the main topic of this chapter. In addition, a new method of fitting, the Amplitude fit [68], which incorporates the convenience of the likelihood method and the power of Fourier analysis, will be introduced in the last section.

7.1 Likelihood Function

The likelihood function in a time dependent mixing analysis describes the proper time distribution of the data. Unfortunately, in a real world, we do not have a pure sample of B_s^0 nor do we have a perfect detector to reconstruct the B_s^0 candidate events. Therefore, the proper time probability distributions for the mixed and unmixed events in equation 2.36 have to be modified to account for the background sources as well as detector effects. We will illustrate in this section, the approach we use to construct a likelihood function that properly describes the data.

The events in the data sample can be divided into seven main sources, each with its own proper time distribution function, F_x . The seven physics sources are:

1. $F_{B_s}^{rs} = B_s^0 \rightarrow D_s^- X$ right-sign decays + c.c.
2. $F_{B_s}^{ws} = B_s^0 \rightarrow D_s^+ X$ wrong-sign decays + c.c.
3. $F_{B_d} = B_d^0 \rightarrow D_s^\pm X$ + c.c.
4. $F_{B^+} = B^+ \rightarrow D_s^\pm X$ + c.c.
5. $F_{BB} = \text{B Baryon} \rightarrow D_s^\pm X$ + c.c.
6. $F_{cc} = \text{primary charm quark} \rightarrow D_s^\pm X$ + c.c.
7. $F_{comb} = \text{combinatorial events}$

The right-sign and wrong-sign B_s^0 events are treated separately in the likelihood function because their proper time resolutions are found to be significantly different. The proper time distribution of the data is the sum of the seven physics functions with the contribution from each source weighted by its fraction in the sample and the appropriate normalization constant. The resulting probability distribution function for events tagged as mixed (opposite initial and final state flavor) is:

$$\begin{aligned}
P_{mixed}(\tau_{rec}) = & f_{D_s}(m_{KK\pi}) \left[\frac{f_{B_s}^{rs}}{N_1} F_{B_s}^{rs}(\tau_{rec}, mixed) + \frac{f_{B_s}^{ws}}{N_2} F_{B_s}^{ws}(\tau_{rec}, mixed) + \right. \\
& \frac{f_{B_d}}{N_3} F_{B_d}(\tau_{rec}, mixed) + \frac{f_{B^+}}{N_4} F_{B^+}(\tau_{rec}, mixed) + \\
& \left. \frac{f_{BB}}{N_5} F_{BB}(\tau_{rec}, mixed) + \frac{f_{cc}}{N_6} F_{cc}(\tau_{rec}, mixed) \right] + \\
& [1 - f_{D_s}(m_{KK\pi})] \cdot F_{comb}(\tau_{rec}) , \tag{7.1}
\end{aligned}$$

where τ_{rec} is the reconstructed proper time, f_{D_s} is the fraction of D_s in the sample, f_x is the fraction of category x in the D_s signal peak (e.g. $f_{B_d} = \frac{\text{total \# of } B_d \rightarrow D_s^\pm X}{\text{total \# of true } D_s \text{ events}}$), and N_i is the normalization constant for category i . A similar expression for $P_{unmixed}(\tau_{rec})$ is obtained by replacing mixed with unmixed physics functions.

The right-sign B_s^0 decays are the golden events that contribute to the mixing signal. To construct their time distribution, we start with the ideal situation. We mentioned earlier, the perfect time distribution has the form, for the mixed events:

$$P_{mixed}(\tau) = \frac{e^{-\tau/\tau_{B_s}}}{2\tau_{B_s}}(1 - \cos(\Delta m_s \tau)), \quad (7.2)$$

where τ_{B_s} is the B_s^0 lifetime and Δm_s is the mass difference between the mass eigenstates. To account for the fraction of truly unmixed events that are tagged as mixed due to imperfect flavor tag, we introduce the initial state mistag rate (η_i) to the above equation. The new time distribution has the form:

$$P_{mixed,\eta}(\tau) = \frac{e^{-\tau/\tau_{B_s}}}{2\tau_{B_s}} [(1 - \eta_i)(1 - \cos(\Delta m_s \tau)) + \eta_i(1 + \cos(\Delta m_s \tau))]. \quad (7.3)$$

The final state mistag rate is zero by construction for the right-sign B_s^0 decays; if the final state tag is wrong, the distribution is described by the wrong-sign contribution. The next term to include is the vertex reconstruction efficiency function, $\epsilon_{B_s}(\tau)$. This term is needed to correct the drop in efficiency for reconstructing B vertices near the IP. The proper time distribution with the efficiency function is shown below,

$$P_{mixed,\eta,\epsilon}(\tau) = \frac{e^{-\tau/\tau_{B_s}}}{2\tau_{B_s}} \cdot \epsilon_{B_s}(\tau) \cdot [(1 - \eta_i)(1 - \cos(\Delta m_s \tau)) + \eta_i(1 + \cos(\Delta m_s \tau))]. \quad (7.4)$$

Finally, we convolute the above equation with a proper time resolution function, $G_{B_s}^{rs}(\tau, \tau_{rec})$, to model the uncertainty in reconstructing the proper decay time.

$$F_{B_s}^{rs}(\tau_{rec}, mixed) = \int_0^\infty \frac{e^{-\tau/\tau_{B_s}}}{2\tau_{B_s}} [(1 - \eta_i)(1 - \cos(\Delta m_s \tau)) + \eta_i(1 + \cos(\Delta m_s \tau))] \cdot \epsilon_{B_s}(\tau) \cdot G_{B_s}^{rs}(\tau, \tau_{rec}) d\tau. \quad (7.5)$$

The convolution integral in equation 7.5 effectively transforms the time distribution in true proper time (τ) to the measured reconstructed proper time (τ_{rec}). We

now have a complete proper time distribution function for the right-sign mixed B_s^0 events. The distribution for events tagged as unmixed is obtained by simply replacing η_i with $(1 - \eta_i)$.

The physics function for the wrong-sign B_s^0 events has the same form as the right-sign events. The principal difference is the final state mistag rate which is equal to one in this case. Equation 7.5 can be converted to describe the wrong-sign events by replacing η_i with $(1 - \eta_i)$. In addition, the decay length and boost resolutions for the wrong-sign events are found to be slightly worse than the right-sign events. Therefore, a separate proper time resolution function, $G_{B_s}^{ws}(\tau, \tau_{rec})$, is used.

The neutral B_d^0 meson also exhibits oscillation behavior with the mass difference Δm_d as its characteristic oscillation frequency. Since we do not separate B_d^0 events into right-sign and wrong-sign decays, the final state mistag rate has to be explicitly accounted for in the proper time distribution. The overall mistag rate is a combination of initial and final state mistag rates:

$$\eta_{B_d} = \eta_i(1 - \eta_{f,B_d}) + (1 - \eta_i)\eta_{f,B_d}, \quad (7.6)$$

where η_{f,B_d} is the final state mistag rate for the B_d events. The physics function for the B_d^0 events is given below:

$$F_{B_d}(\tau_{rec, mixed}) = \int_0^\infty \frac{e^{-\tau/\tau_{B_d}}}{2\tau_{B_d}} [(1 - \eta_{B_d})(1 \mp \cos(\Delta m_d \tau)) + \eta_{B_d}(1 \pm \cos(\Delta m_d \tau))] \cdot \epsilon_{B_d}(\tau) \cdot G_{B_d}(\tau, \tau_{rec}) d\tau, \quad (7.7)$$

where ϵ_{B_d} and G_{B_d} are the vertex efficiency and proper time resolution functions for the B_d^0 events, respectively.

The B^+ and b -baryon proper time distributions can be described by a simple exponential, convoluted with the vertex efficiency and proper time resolution functions. The B^+ and b -baryons do not oscillate, however, it is still possible to tag

those events as mixed due to flavor mistag. Of course, if both the initial and final states are wrong, the event would still be correctly classified as unmixed. The physics functions for B^+ and b -baryons are given below:

$$F_{B^+}(\tau_{rec}, mixed) = \int_0^\infty \frac{e^{-\tau/\tau_{B^+}}}{2\tau_{B^+}} \cdot \eta_{B^+} \cdot \epsilon_{B^+}(\tau) \cdot G_{B^+}(\tau, \tau_{rec}) d\tau, \quad (7.8)$$

$$F_{BB}(\tau_{rec}, mixed) = \int_0^\infty \frac{e^{-\tau/\tau_{BB}}}{2\tau_{BB}} \cdot \eta_{BB} \cdot \epsilon_{BB}(\tau) \cdot G_{BB}(\tau, \tau_{rec}) d\tau, \quad (7.9)$$

where η_{B^+} (η_{BB}) is the overall flavor mistag rate and G_{B^+} (G_{BB}) is the proper time resolution function for B^+ (b -baryon) events. Once again, the distributions for the unmixed events can be obtained by replacing η_{B^+} (η_{BB}) with $(1 - \eta_{B^+}(\eta_{BB}))$.

The next physics source is the prompt D_s from $Z^0 \rightarrow c\bar{c}$ decays. Although Monte Carlo study suggests that only about 1% of the events in the data are prompt D_s , we include this contribution in the likelihood function for completeness. In a prompt D_s event, the D_s is produced at the IP and therefore the reconstructed time distribution is not well defined. The apparent time distribution comes from mis-assigning fragmentation tracks to the D_s as secondary B decay tracks. The proper time distribution for the prompt D_s is taken from a sample of $Z^0 \rightarrow c\bar{c}$ Monte Carlo events. The fitted distribution normalized to 1/2 has the form:

$$F_{cc}(\tau_{rec}) = \frac{1}{2}(5.47e^{-\tau_{rec}/0.21}) \cdot erf(18.35 \cdot \tau_{rec}), \quad (7.10)$$

where erf is the error function. The same distribution is used for events tagged as either mixed or unmixed.

The last physics source that we need to consider is combinatorial D_s . These are B candidates that contain a fake D_s . The fake D_s comes from three random tracks that pass all the D_s selection criteria. In the $m_{KK\pi}$ invariant mass plots (see figures 47 and 48), they show up as a monotonic background underneath the D_s mass peak. The B hadron composition of the combinatorial candidates has

been estimated from the $Z^0 \rightarrow b\bar{b}$ Monte Carlo. The results are listed in table 9. The values in the table are obtained using the default $D_s \rightarrow \phi\pi, K^{*0}K$ neural net cuts (varying the D_s neural net cuts did not result in any significant change in the B hadron composition). The final state mistag rate has also been studied. The

B_s^0	B_d^0	B^\pm	b -baryons
$(18 \pm 2)\%$	$(38 \pm 2)\%$	$(37 \pm 2)\%$	$(7 \pm 1)\%$

Table 9: B hadron fractions for the D_s combinatorial events within ± 40 MeV of the nominal D_s mass. The results listed are for the default values of D_s neural net cuts.

mistag rate is consistent with 50% which suggests that the combinatorial events do not induce any mixing signal. This important fact allows us to parameterize the proper time distribution of the combinatorial events directly from the data using events outside the D_s mass peak (D_s sidebands). These events are presumably all combinatorial events. The sideband regions are defined as: $1.7 < m_{KK\pi} < 1.8$ GeV (lower sideband) and $2.05 < m_{KK\pi} < 2.2$ GeV (upper sideband). A series of detailed Monte Carlo studies has been performed to verify that the B hadron composition and proper time distributions for the combinatorial and sideband events are consistent. Since no significant difference is found between the mixed and unmixed combinatorial events, the two samples are combined. The plot of the sideband combinatorial events from the data and the result of the fit are shown in figure 58. The proper time distribution for either tagged mixed or unmixed combinatorial events normalized to 1/2 is:

$$F_{comb}(\tau_{rec}) = \frac{1}{2} \left[1.98 e^{-\tau_{rec}/1.12} \cdot \text{erf}(0.38 \cdot \tau_{rec} + 0.078) \right]. \quad (7.11)$$

We can now combine the seven physics functions to obtain the overall proper time distribution, as shown in equation 7.1. The expressions for $P_{mixed}(\tau_{rec})$ and

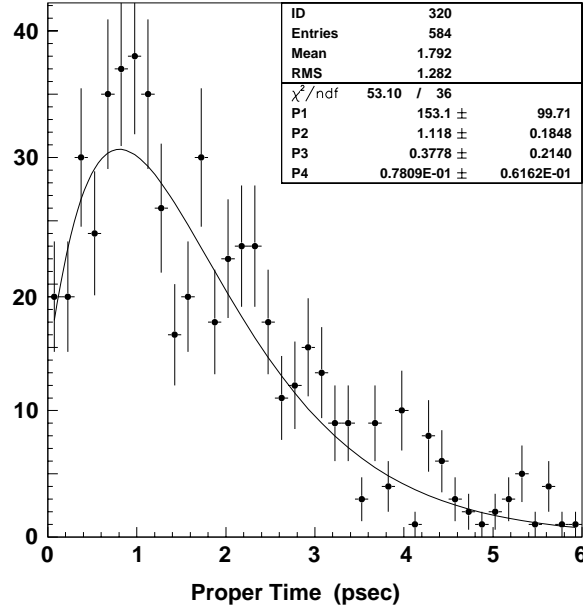


Figure 58: The proper time distribution of the combinatorial D_s events in the data sidebands. The fitting function is: $f(\tau) = P1 \cdot e^{-\tau/P2} \cdot \text{erf}(P3 \cdot \tau + P4)$.

$P_{unmixed}(\tau_{rec})$ are explicitly written out in Appendix B. Finally, the unbinned likelihood function is defined as the product of the probability of the mixed and unmixed events,

$$L = \prod_i^{mixed} P_{mixed}(\tau_{rec}) \prod_j^{unmixed} P_{unmixed}(\tau_{rec}). \quad (7.12)$$

7.2 Likelihood Function Parameterizations

In the previous section, we described the functional form of the likelihood function. Here, we discuss the individual parameters in the likelihood function in detail.

7.2.1 Data Composition

The D_s fraction (f_{D_s}) in equation 7.1, as mentioned earlier, is the fraction of true D_s in the sample. The fraction depends strongly on the reconstructed $KK\pi$ mass. For $m_{KK\pi}$ far from the nominal D_s mass, f_{D_s} is approximately zero. The D_s fraction can reach as high as 90% for events with $m_{KK\pi}$ mass near the nominal D_s mass of 1.97 GeV. The relative fraction of true and combinatorial D_s as a function of $m_{KK\pi}$ is obtained directly from the data by performing a fit to the $m_{KK\pi}$ mass distributions. The fit is done separately for $\phi\pi$ and $K^{*0}K$ modes, for candidates with loose and hard kaon information and for candidates with $Q=0$ and $Q=\pm 1$. The fitting function consists of background and D_s signal terms. The fitting function for the D_s signal peak is the sum of two Gaussians with the same mean and the core fraction fixed to 60%. The widths of the core and tail Gaussians used in the individual mass fits are constrained to be 10.8 MeV and 35.0 MeV respectively, which are obtained from the combined ($\phi\pi$ and $K^{*0}K$) D_s mass fit. The fitting function has the form:

$$f_{signal}(X) = P1 \left\{ \frac{0.6}{\sqrt{2\pi} \cdot 0.0108} \exp \left[-(X - P2)^2 / (2 \cdot 0.0108^2) \right] + \frac{0.4}{\sqrt{2\pi} \cdot 0.035} \exp \left[-(X - P2)^2 / (2 \cdot 0.035^2) \right] \right\}, \quad (7.13)$$

where $P1$ and $P2$ are the two floating parameters. The background shape is modelled by a second order polynomial (for combinatorial events) and a Gaussian function (for $D^+ \rightarrow \phi\pi$ events). The amplitude of the D^+ Gaussian is allowed to float while the mean is constrained to be 99.2 MeV below the fitted D_s mass peak (which corresponds to the world average value of D_s and D^+ mass difference [19]) and the width is fixed to the Monte Carlo value of 13.3 MeV. The background

fitting function has the form:

$$f_{bkg}(X) = P3 + P4 \cdot X + P5 \cdot X^2 + P6 \cdot \exp \left[-(X - P2 + 0.0992)^2 / (2 \cdot 0.0133^2) \right]. \quad (7.14)$$

The results of the fits are shown in tables 10 and 11. Given the background and

Decay Mode	Category	P1	P2
$\phi\pi$	Q0K0	0.55 ± 0.03	1.965 ± 0.003
	Q0K1	0.72 ± 0.13	1.964 ± 0.003
	Q1K0	0.47 ± 0.11	1.959 ± 0.004
	Q1K1	0.48 ± 0.10	1.966 ± 0.002
$K^{*0}K$	K0	0.49 ± 0.11	1.967 ± 0.004
	K1	0.36 ± 0.08	1.971 ± 0.003

Table 10: Fit results for the D_s signal peak. Category Q0 (Q1) denotes Q=0 (Q= ± 1) events. K0 (K1) denotes events with loose kaon (hard kaon) information. The parameter P1 is the normalization of the two Gaussians and P2 is the fitted D_s mass peak (in GeV).

Decay Mode	Category	P3	P4	P5	P6
$\phi\pi$	Q0K0	200.6 ± 3.9	-180.2 ± 3.3	41.5 ± 1.1	$8.2 \times 10^{-7} \pm 0.4$
	Q0K1	149.3 ± 2.5	-139.6 ± 1.9	32.9 ± 0.7	1.6 ± 1.9
	Q1K0	195.3 ± 7.0	-180.7 ± 7.6	42.9 ± 2.1	$5.0 \times 10^{-3} \pm 0.5$
	Q1K1	190.2 ± 1.8	-188.7 ± 0.3	47.0 ± 0.4	2.8 ± 1.8
$K^{*0}K$	K0	144.6 ± 2.8	-136.3 ± 2.4	32.6 ± 0.8	1.7 ± 1.8
	K1	141.0 ± 1.9	-138.1 ± 0.3	34.1 ± 0.4	3.0 ± 1.9

Table 11: Fit results for the background shape. Category Q0 (Q1) denotes Q=0 (Q= ± 1) events. K0 (K1) denotes events with loose kaon (hard kaon) information.

signal shapes, the D_s fraction can be calculated on an event by event basis,

$$f_{D_s}(m_{KK\pi}) = \frac{f_{signal}(m_{KK\pi})}{f_{signal}(m_{KK\pi}) + f_{bkg}(m_{KK\pi})}. \quad (7.15)$$

The remaining fractions in equation 7.1 ($f_{B_s}^{rs}$, $f_{B_s}^{ws}$, f_{B_d} , f_{B^+} , f_{BB} and f_{cc}) are obtained from the Monte Carlo. These parameters are defined as the fraction of each physics source in the D_s mass peak (not including combinatorial events). Monte Carlo studies indicate that the fraction of each source is not correlated with the reconstructed mass of the D_s . Therefore, there is no need to parameterize those fractions as a function of $m_{KK\pi}$. We can simply use the average values within a certain D_s mass window (e.g. ± 40 MeV of the nominal D_s mass). However, the sample composition does depend strongly on the vertex charge (Q) and lepton ID. Naturally, the neutral vertex sample would have a higher B_s^0 fraction than the charged sample, and an identified lepton in the B vertex would suppress the wrong-sign D_s that comes predominantly from B_d^0 and B^+ decays. The fractions obtained from the Monte Carlo are given in table 12. The values listed have been corrected for the differences between the various branching ratios in the SLD Monte Carlo and the world averages [62].

Decay Mode		$f_{B_s}^{rs}$ (%)	$f_{B_s}^{ws}$ (%)	f_{B_d} (%)	f_{B^+} (%)	f_{BB} (%)	f_{cc} (%)
$\phi\pi$	Q0L0	53.3 \pm 0.9	6.1 \pm 0.1	26.7 \pm 0.8	5.5 \pm 0.4	7.0 \pm 0.1	1.4 \pm 0.04
	Q0L1	80.9 \pm 1.0	3.5 \pm 0.04	11.4 \pm 0.8	2.3 \pm 1.1	0.8 \pm 0.4	1.1 \pm 0.03
	Q1L0	30.4 \pm 1.4	3.5 \pm 0.2	16.9 \pm 1.3	42.7 \pm 0.6	5.2 \pm 0.3	1.4 \pm 0.04
	Q1L1	49.5 \pm 3.3	2.1 \pm 0.1	12.1 \pm 2.2	34.0 \pm 3.2	1.1 \pm 0.6	1.1 \pm 0.03
$K^{*0}K$	L0	55.4 \pm 1.4	6.3 \pm 0.2	26.9 \pm 1.3	4.8 \pm 0.7	5.0 \pm 0.5	1.6 \pm 0.05
	L1	81.9 \pm 2.2	3.5 \pm 0.09	10.1 \pm 1.9	1.7 \pm 0.8	2.7 \pm 0.8	0 \pm 0.05

Table 12: Data composition in the D_s mass peak (within ± 40 MeV). Category Q0 (Q1) denotes Q=0 (Q= ± 1) event sample. L0 (L1) denotes event sample without (with) an identified lepton in the B vertex. The errors given in the table are Monte Carlo statistical errors.

7.2.2 Final State Mistag

Since the initial state tag has been discussed in detail in section 6.1.4, we will only focus on the final state mistag rates in this section. The final state mistag rate for B_s^0 events is effectively accounted for in the relative ratio between the right-sign ($f_{B_s}^{rs}$) and the wrong-sign $f_{B_s}^{ws}$ B_s^0 fractions. The final state mistag rates for B_d^0 , B^+ and b -baryons are taken from the Monte Carlo. The rates are adjusted to correct for the different B_d^0 and B^\pm right-sign to wrong-sign branching ratios used in the SLD Monte Carlo and the world measurements. The list of final state mistag rates assumed in the likelihood function is given in table 13. The rates are parameterized separately for events with and without an identified lepton in the B vertex. The B_s^0 candidate sample with an identified lepton is enriched with semileptonic B decays and therefore contains significantly lower fraction of wrong-sign D_s .

	$f_{B_s}^{ws} / (f_{B_s}^{rs} + f_{B_s}^{ws})$ (%)	η_{f,B_d} (%)	η_{f,B^+} (%)	$\eta_{f,BB}$ (%)
No Lepton ID	10.3 ± 0.6	79.2 ± 0.9	76.0 ± 1.0	92.2 ± 2.0
With Lepton ID	4.1 ± 0.7	89.4 ± 2.0	93.3 ± 1.0	91.7 ± 8.0

Table 13: Effective final state mistag rates. The errors given in the table are Monte Carlo statistical errors.

7.2.3 Vertex Reconstruction Efficiency

The efficiency function is defined as the fraction of events that pass all the selection cuts as a function of true proper decay time of the B hadron. The function accounts for the biases in the proper time distribution that maybe introduced by the analysis cuts. In particular, it is known that the topological vertex reconstruction

algorithm performs poorly in identifying vertices near the IP. This is due to the fact that near the IP, the secondary vertices are not well resolved from the IP. This effect introduces a dip in the proper time distribution that must be accounted for, in this case, by the efficiency function. The efficiency function is parameterized separately for different B hadrons. The plots of vertex efficiency versus true proper time are shown in figure 59. The fitting function for B_s^0 , B_d^0 and B^+ fits is:

$$\epsilon(\tau) = P1 \frac{1 - e^{P2 \cdot \tau}}{1 + e^{P2 \cdot \tau}} + P3 + P4 \cdot e^{P5 \cdot \tau}. \quad (7.16)$$

The last exponential term ($P4e^{P5 \cdot \tau}$) in equation 7.16 is introduced to model the drop in efficiency at large proper time. The drop is particularly significant for charged B events. The parameters $P4$ and $P5$ are fixed to zero for the b -baryon efficiency function.

7.2.4 Proper Time Resolution Functions

The proper time resolution can be expressed in terms of the decay length and boost resolutions ($\sigma_L, \sigma_{\gamma\beta}$) as in:

$$\sigma_\tau(\tau, i, j) = \left[\left(\frac{\sigma_L^i}{\gamma\beta c} \right)^2 + \left(\tau \frac{\sigma_{\gamma\beta}^j}{\gamma\beta} \right)^2 \right]^{1/2}, \quad (7.17)$$

where the indices $i, j = 1$ for core and 2 for tail. The proper time resolution contains a constant term that depends on σ_L and a term that rises linearly with proper time that depends on $\sigma_{\gamma\beta}$. This behavior is illustrated in Figure 60 for the B_s^0 events.

In practice, there are four σ_τ distributions given by the various σ_L and $\sigma_{\gamma\beta}$ core-tail combinations. The resolution function is obtained by summing all four contributions:

$$G(\tau, \tau_{rec}) = f_c^2 G_{cc} + f_c f_t (G_{ct} + G_{tc}) + f_t^2 G_{tt}, \quad (7.18)$$

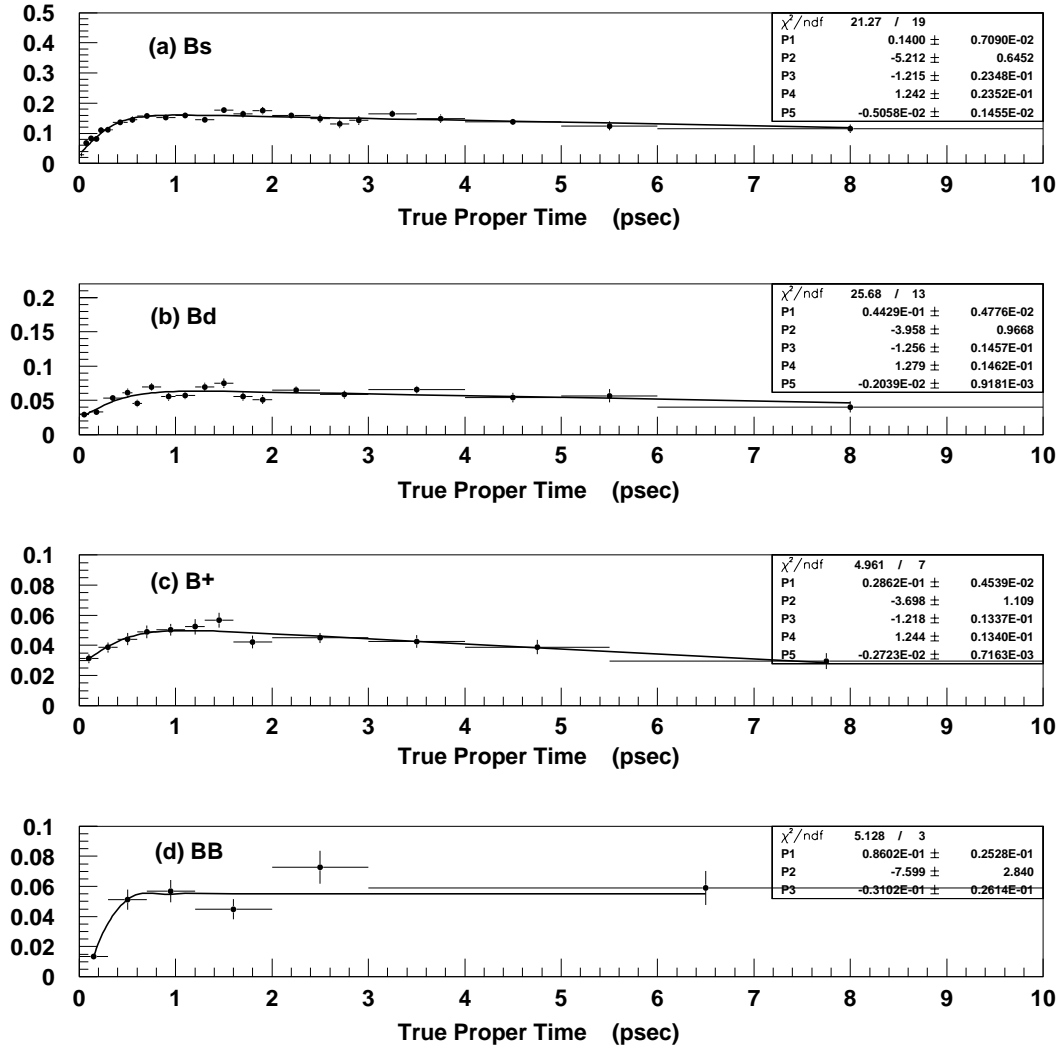


Figure 59: Vertex efficiency functions for (a) B_s^0 , (b) B_d^0 , (c) B^+ and b -baryon events.

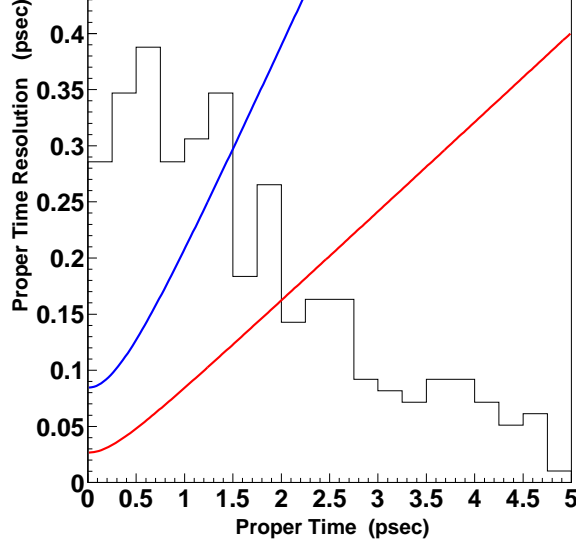


Figure 60: σ_τ distributions for $B_s^0 \rightarrow D_s^- X$ events. The lower red curve is calculated using $\sigma_L(core)$ and $\sigma_{\gamma\beta}(core)$. The upper blue curve is calculated using $\sigma_L(tail)$ and $\sigma_{\gamma\beta}(tail)$. The background histogram is the proper time distribution of the data events.

with $f_c=0.6$, $f_t=0.4$, and $G_{i,j}$ defined as:

$$G_{i,j} = \frac{1}{\sqrt{2\pi}\sigma_\tau(\tau, i, j)} \exp \left[-(\tau - \tau_{rec})^2 / 2\sigma_\tau^2(\tau, i, j) \right]. \quad (7.19)$$

7.2.4.1 Event by Event Decay Length Resolution

Instead of using the average decay length resolution (see table 7) to parameterize the proper time resolution, we can gain more sensitivity to mixing by estimating the decay length resolution on an event by event basis, thereby assigning more weight to events with good decay length resolution. We take advantage of the fitted B vertex error to estimate the decay length uncertainty σ_L^{rec} for each event. The uncertainty is the quadrature sum of IP and fitted B vertex errors along the vertex axis direction. The normalized decay length residual plots, $(L_{rec} - L_{MC})/\sigma_L^{rec}$, are

generated for different B species. If the B vertex error estimate is unbiased, we would expect the width of the normalized residual plot to be equal to one. The deviation from one corresponds to the correction factor that we need to apply to convert the estimated decay length error to the true decay length error. The true decay length error (σ_L^{true}) is given by,

$$\sigma_L^{true} = N_{\sigma_L} \times \sigma_L^{rec}, \quad (7.20)$$

where N_{σ_L} is the width of the normalized decay length residual distribution. In practice, we fit the normalized residual plot to the sum of two Gaussians. Consequently, we have the core and tail correction factors for each B decay type. The complete list of correction factors is given in table 14.

Decay Category	Q=0		Q=±1	
	Core N_{σ_L}	Tail N_{σ_L}	Core N_{σ_L}	Tail N_{σ_L}
$B_s^0 \rightarrow D_s^- X$ (right-sign)	1.07±0.02	2.16±0.05	1.11±0.06	2.18±0.10
$B_s^0 \rightarrow D_s^+ X$ (wrong-sign)	1.39±0.09	3.65±0.32	1.30±0.31	4.13±0.84
$B_d^0 \rightarrow D_s^\pm X$	1.23±0.03	3.68±0.15	1.26±0.07	3.77±0.26
$B^+ \rightarrow D_s^\pm X$	1.41±0.02	4.26±0.31	1.39±0.05	3.93±0.17
$b - Baryon \rightarrow D_s^\pm X$	1.24±0.08	2.93±0.22	1.24±0.08	2.93±0.22

Table 14: Decay length resolution correction factors.

7.2.4.2 Event by Event Relative Boost Resolution

Additional improvement on the sensitivity of B mixing can be achieved by estimating the boost resolution on an event by event basis. It is expected that the boost resolution is highly dependent on the amount of energy from the charged tracks in the vertex. If a B candidate has large charged track energy (E_B^{ch}), it would imply that very little energy is in the neutral component. Since the estimation of

the neutral energy is fairly imprecise in comparison to the charged energy, we would expect that B events with smaller neutral energy to have significantly better boost resolution. Therefore we parameterize the boost resolution in bins of charged energy. Figure 61 shows the relative boost residual for the right-sign B_s^0 events in E_B^{ch} bins. As shown in the plots, the core and the tail widths exhibit strong dependence on E_B^{ch} . The parameterization is performed separately for the different B species and vertex charge sample (except $Q=0$ and $Q=\pm 1$ samples are combined for wrong-sign B_s^0 and b -baryon events to improve statistics). The results of the fits are given in table 15.

7.2.4.3 Proper Time Offsets

Both the reconstructed decay length and boost are found to have some systematic biases. For example, the reconstructed decay length for the double charm decays is slightly shifted towards longer decay length (towards the charm vertex). The proper time biases show up in the residual plot as the Gaussian is not perfectly centered at zero. The shift is very small for most cases, nevertheless, the effect should still be modelled in the likelihood function. The offset of the decay length residual distribution is parameterized as a function of reconstructed decay length. The shift in the boost is parameterized as a function of E_B^{ch} . The offsets are accounted for by introducing a proper time correction for each event. The correction is defined as:

$$(\delta\tau)_{i,j} = \frac{(\delta L)_i}{\beta\gamma c} - \left[\frac{\delta(\beta\gamma)}{\beta\gamma} \right]_j \cdot \tau, \quad (7.21)$$

where i, j are the core/tail indices, δL is the mean of the decay length residual and $\frac{\delta(\beta\gamma)}{\beta\gamma}$ is the mean of the relative boost residual. The correction is included in the resolution function by replacing τ_{rec} with $\tau_{rec} - (\delta\tau)_{i,j}$.

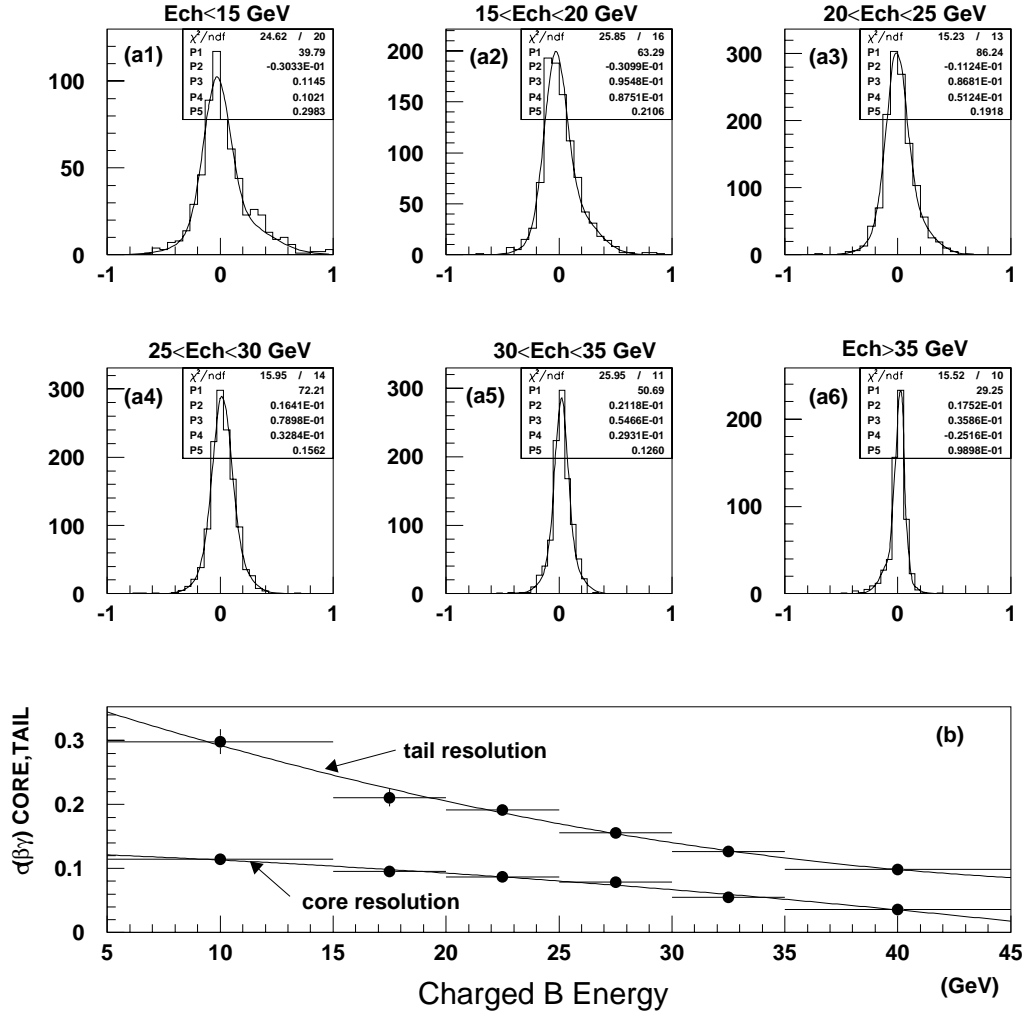


Figure 61: Plots (a1)-(a6) are the relative boost residuals in various bins of charged B energy for the right-sign B_s^0 ($Q=0$) events. Plot (b) shows the resulting core and tail relative boost resolution as a function of charged B energy.

Decay Category	Core Resolution (Q=0)		
	P1	P2	P3
B_s^0 (Q=0)	0.128±0.009	-0.0012±0.0006	-0.000027±0.00001
B_s^0 (Q=0)	0.21±0.03	-0.008±0.002	0.00009±0.00004
B_d^0 (Q=0)	0.20±0.03	-0.007±0.002	0.00009±0.00004
B^+ (Q=0)	0.20±0.02	-0.0036±0.0008	-
$b - Baryon$ (Q=0)	0.13±0.03	0.001±0.002	-0.0001±0.00005
	Tail Resolution (Q=0)		
	P1	P2	P3
Right-Sign B_s^0 (Q=0)	0.40±0.04	-0.01±0.003	0.0001±0.00004
Wrong-Sign B_s^0 (Q=0)	0.7±0.2	-0.03±0.01	0.0005±0.0002
B_d^0 (Q=0)	0.52±0.06	-0.02±0.005	0.00020±0.00009
B^+ (Q=0)	0.27±0.06	0.003±0.002	-
$b - Baryon$ (Q=0)	1.1±0.2	-0.07±0.01	0.001±0.0002
Decay Category	Core Resolution (Q=±1)		
	P1	P2	P3
Right-Sign B_s^0 (Q=±1)	0.26±0.05	-0.009±0.004	0.00011±0.00007
Wrong-Sign B_s^0 (Q=±1)	0.21±0.03	-0.008±0.002	0.00009±0.00004
B_d^0 (Q=±1)	0.24±0.02	-0.0043±0.0008	-
B^+ (Q=±1)	0.48±0.09	-0.016±0.007	0.0002±0.0001
$b - Baryon$ (Q=±1)	0.13±0.03	0.001±0.002	-0.0001±0.00005
	Tail Resolution (Q=±1)		
	P1	P2	P3
Right-Sign B_s^0 (Q=±1)	0.54±0.08	-0.024±0.006	0.0004±0.0001
Wrong-Sign B_s^0 (Q=±1)	0.7±0.2	-0.03±0.01	0.0005±0.0002
B_d^0 (Q=±1)	0.35±0.05	-0.006±0.002	-
B^+ (Q=±1)	0.48±0.09	-0.016±0.007	0.0002±0.0001
$b - Baryon$ (Q=±1)	1.1±0.2	-0.07±0.01	0.001±0.0002

Table 15: The event by event relative boost resolution parameterizations for the various categories. The function used in the fit is: $\sigma_{\beta\gamma}(E_B^{ch}) = P1 + P2 \cdot E_B^{ch} + P3 \cdot (E_B^{ch})^2$.

A check of the resolution function has been performed on the Monte Carlo. Figure 62 shows the proper time residual distributions for right-sign B_s^0 events in bins of true proper time with the calculated event by event resolution function. The same comparison has also been performed for the other B hadrons, and in all cases, the agreement is good.

7.2.5 Normalizations

The last issue on the likelihood function that needs to be addressed is the normalization. The complete likelihood function is normalized by dividing each physics term by a normalization constant. The normalization is required to ensure that the weight of each physics source in the likelihood function is not biased by the efficiency and the proper time resolution of the event. The normalization constant (N_i) is calculated for category i by integrating the sum of the mixed and unmixed physics functions for source i over all reconstructed proper times,

$$N_i = \int_0^{+\infty} (F_i^{mixed} + F_i^{unmixed}) d\tau_{rec}. \quad (7.22)$$

In practice, the integration is performed from 0 to 10 *psec*. Since the oscillation terms cancel in the sum, the normalization constant does not depend on Δm_s .

7.3 Likelihood Fit

We now have the final likelihood function that we can use to fit the data. To verify that the likelihood function correctly models the proper time distribution, a comparison between the likelihood function and the mixed fraction (# of events tagged as mixed / total # of events) distribution is performed. Figure 63 shows

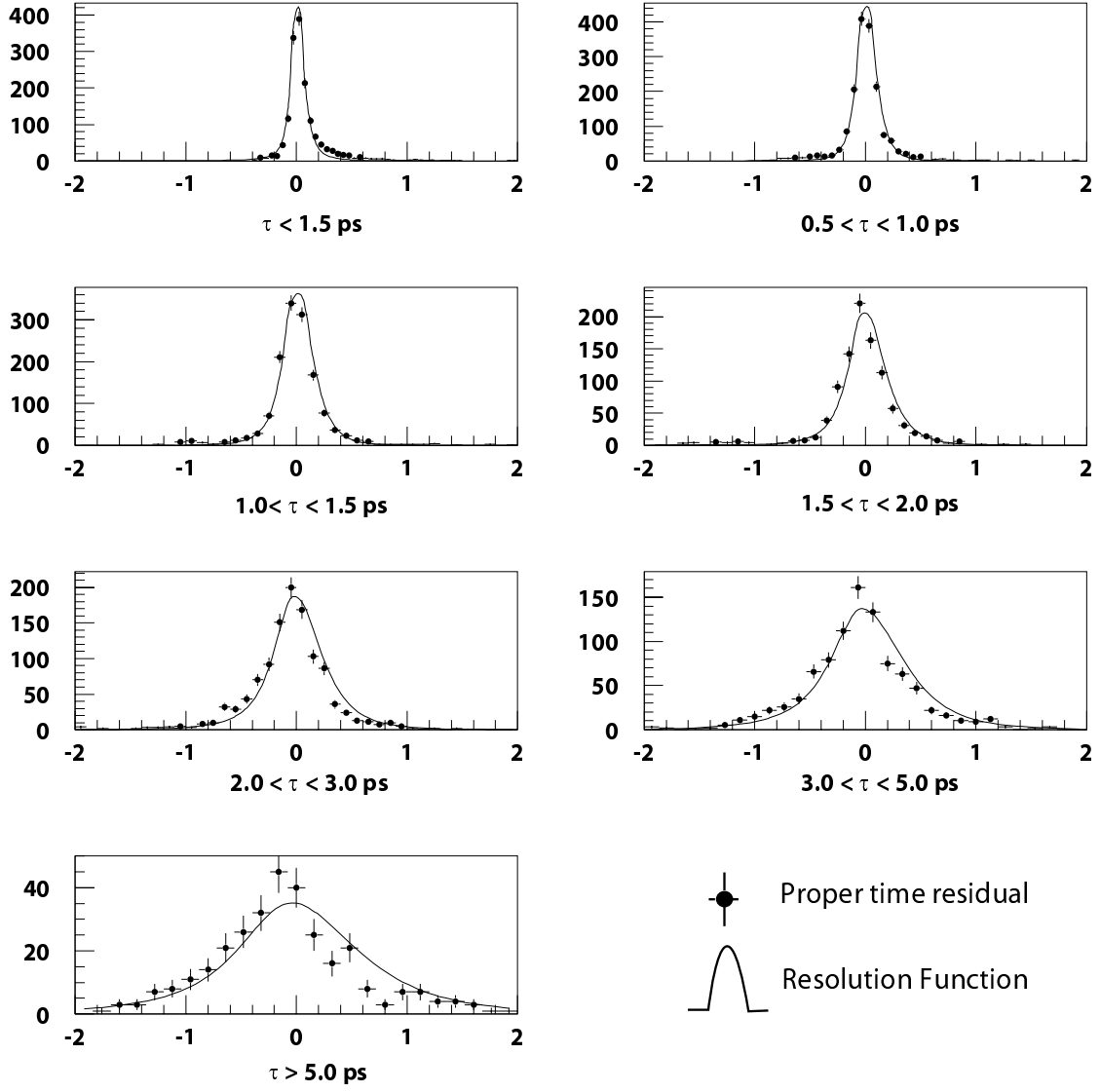


Figure 62: Proper time residual distributions (dots) in bins of true proper time for the right-sign B_s^0 ($Q=0$) events. The residual distributions are overlaid with the calculated proper time resolution functions.

good agreement between the mixed fraction distributions for the Monte Carlo events and the corresponding likelihood functions.

The likelihood fit results are shown in figures 64 and 65. Figure 64 shows the mixed fraction plot and the likelihood function for data. The $-\log(\text{likelihood})$

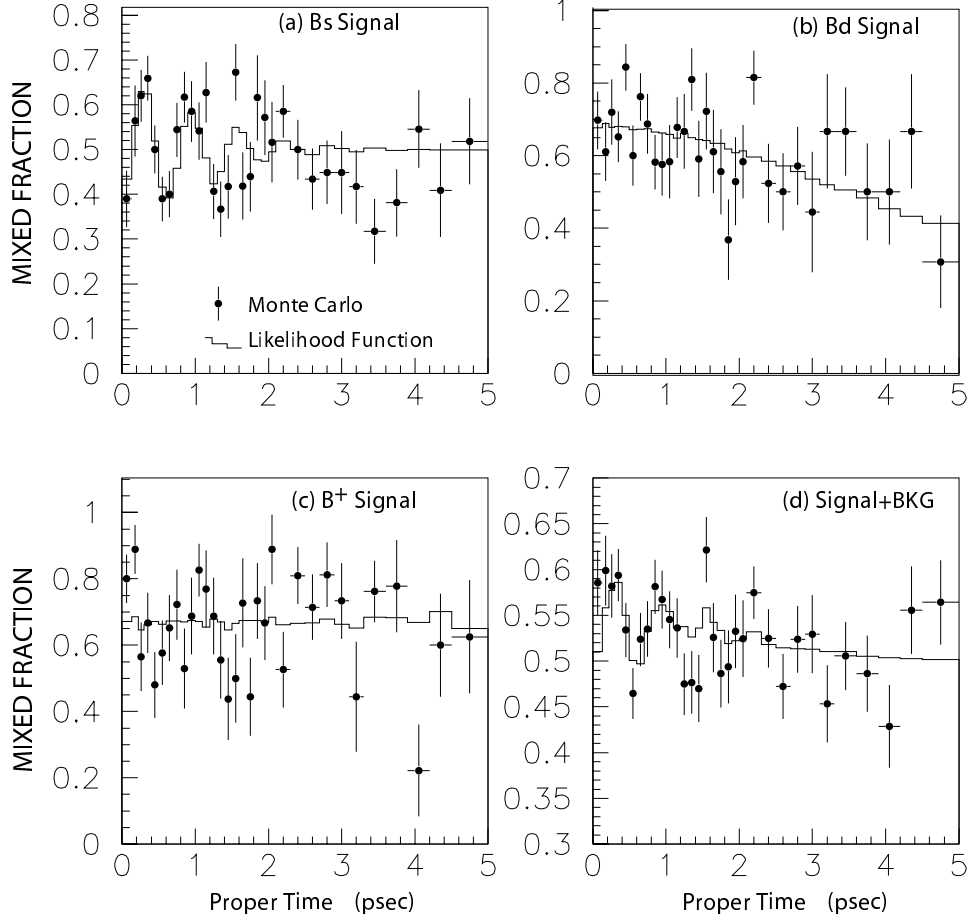


Figure 63: Mixed fraction distributions (dots) for (a) $B_s^0 \rightarrow D_s^\pm X$, (b) $B_d^0 \rightarrow D_s^\pm X$, (c) $B^+ \rightarrow D_s^\pm X$ and (d) all events. The histograms are the likelihood functions for the respective category. The generated Δm_s value is 10 psec^{-1} .

versus Δm_s distribution for data is shown in figure 65. The likelihood function is calculated with B hadron lifetimes and Δm_d fixed to the world averages. No significant minimum is seen in the Δm_s range between 0 and 25 psec^{-1} . In the

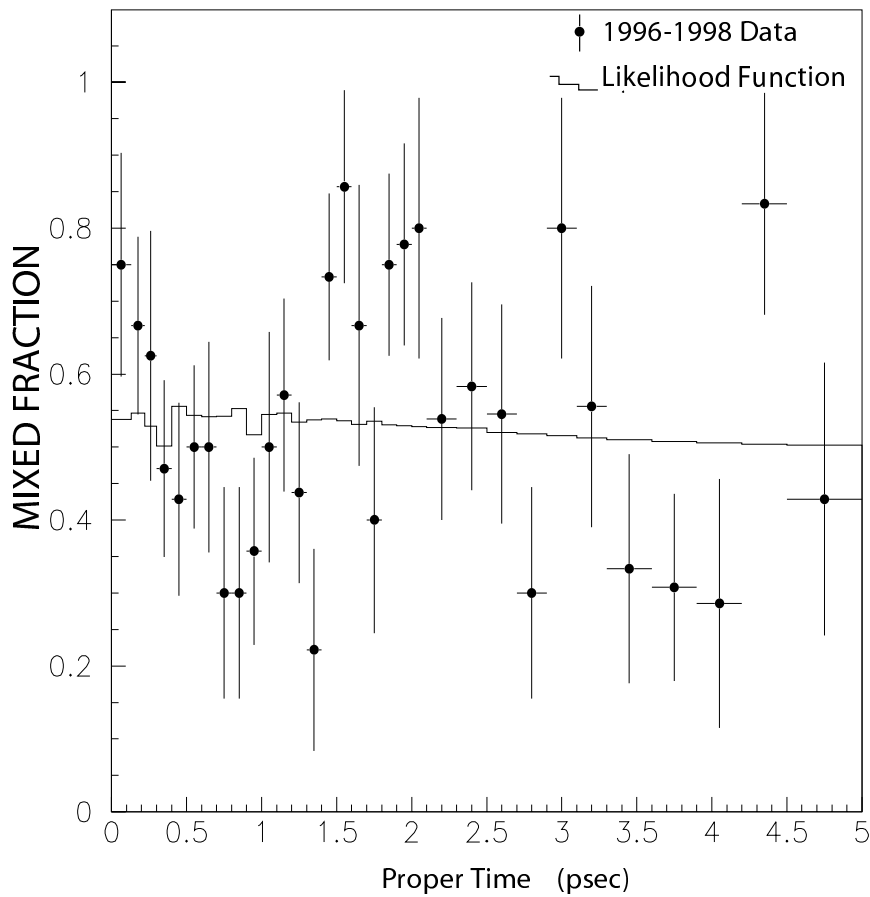


Figure 64: Mixed fraction distribution (dots) and the likelihood function (histogram) for data.

absence of a signal, setting a limit using the traditional likelihood approach is not straightforward. Furthermore, it is extremely cumbersome to combine the likelihood function of different analyses, not to mention, different experiments. These are the primary motivations for introducing a new fitting scheme that could circumvent the problems mentioned. We discuss this new method in the next section.

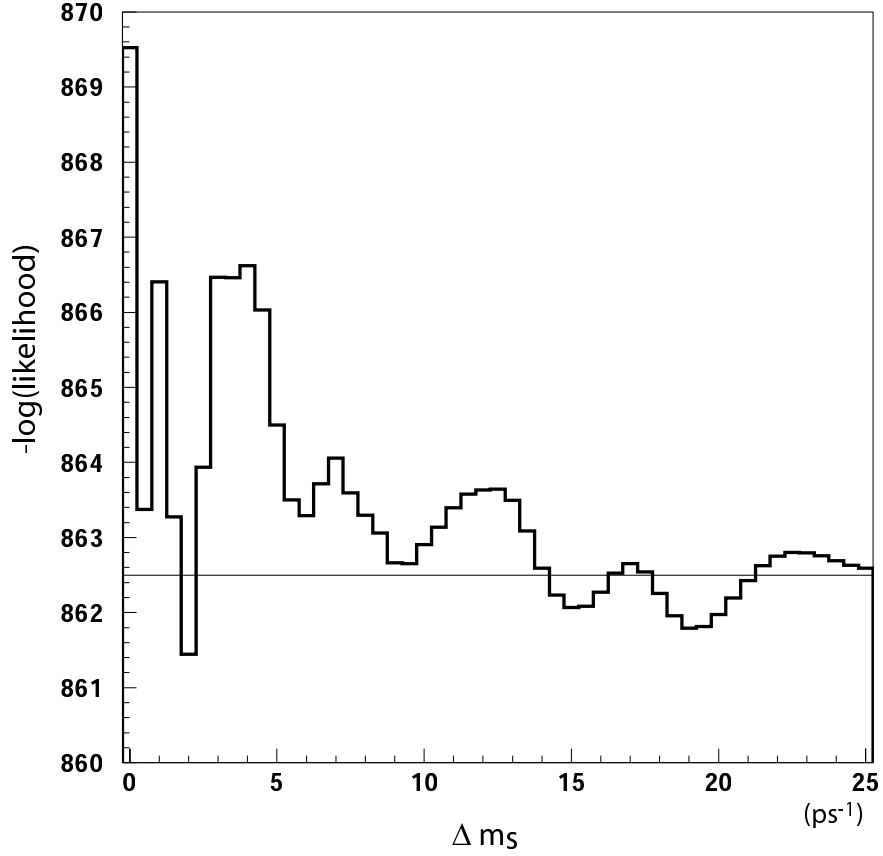


Figure 65: Distribution of $-\log(\text{likelihood})$ versus Δm_s for data. The horizontal line is the reference *likelihood* value at $\Delta m_s = \infty$.

7.4 Amplitude Fit

The amplitude method is introduced to the B_s^0 mixing community as a solution to many of the complications associated with the standard likelihood analysis. The method, in essence, transforms the traditional likelihood fit into a “Fourier-like” analysis. Fourier analysis is a powerful approach to search for periodic signals, therefore, it is particularly suited for the B_s^0 analysis. In an amplitude fit, the likelihood function is modified by introducing a term \mathbf{A} , the amplitude, in front of the B_s^0 cosine terms ($\cos(\Delta m_s) \rightarrow \mathbf{A} \cos(\Delta m_s)$). For this analysis, the physics

functions $F_{B_s}^{rs}(\tau_{rec})$ and $F_{B_s}^{ws}(\tau_{rec})$ now have the forms:

$$\begin{aligned}
F_{B_s}^{rs}(\tau_{rec}, mixed) &= \int_0^\infty \frac{e^{-\tau/\tau_{B_s}}}{2\tau_{B_s}} [(1 - \eta_i) (1 - \mathbf{A} \cdot \cos(\Delta m_s \tau)) + \eta_i (1 + \mathbf{A} \cdot \cos(\Delta m_s \tau))] \cdot \epsilon_{B_s}(\tau) \cdot G_{B_s}^{rs}(\tau, \tau_{rec}) d\tau. \\
F_{B_s}^{ws}(\tau_{rec}, mixed) &= \int_0^\infty \frac{e^{-\tau/\tau_{B_s}}}{2\tau_{B_s}} [(1 - \eta_i) (1 + \mathbf{A} \cdot \cos(\Delta m_s \tau)) + \eta_i (1 - \mathbf{A} \cdot \cos(\Delta m_s \tau))] \cdot \epsilon_{B_s}(\tau) \cdot G_{B_s}^{ws}(\tau, \tau_{rec}) d\tau.
\end{aligned} \tag{7.23}$$

Instead of fitting directly for Δm_s , as in the case of the standard likelihood method, Δm_s is fixed to a particular value and the amplitude \mathbf{A} is determined by the fit. The fit for \mathbf{A} is repeated for a range of Δm_s values to produce the amplitude plot. The amplitude plot is effectively a normalized frequency spectrum of the proper time distribution. The amplitude is expected to be consistent with zero for values of Δm_s far from Δm_s^{true} and to reach unity at the true mass difference value. If the oscillation frequency is large and no signal is observed, the range of Δm_s for which $\mathbf{A} + 1.645\sigma_A \leq 1$ can be excluded at the 95% confidence level (C.L.). The 95% C.L. sensitivity is defined as the value of Δm_s at which $1.645\sigma_A = 1$. The sensitivity value corresponds to the average limit that the analysis is expected to set. Of course, an analysis can be lucky (amplitude values fluctuate low near the sensitivity) and obtain a higher than expected limit. Conversely, an analysis can be unlucky (amplitude values fluctuate high) and set a lower than expected limit.

For illustration, the amplitude fit result using a pure sample of Monte Carlo $B_s^0 \rightarrow D_s^\pm X$ events is shown in figure 66. The signal peak at the generated Δm_s of 10 psec^{-1} is clearly seen in the amplitude plot. The sensitivity is the Δm_s value at the intersection of the sensitivity curve and the horizontal line of $A=1$. In this illustration, the sensitivity is beyond 25 psec^{-1} . The slope of the sensitivity curve increases as σ_t increases. For analysis with excellent proper time resolution, the sensitivity curve tends to be fairly shallow.

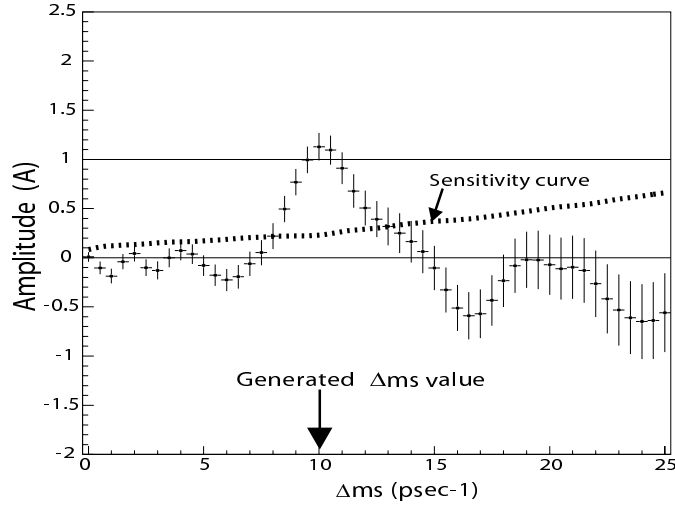


Figure 66: Amplitude fit plot for Monte Carlo B_s^0 events. A signal peak is seen at the Monte Carlo generated value of 10 psec^{-1} . The error bar on the amplitude corresponds to 1σ . The amplitude error grows as a function of Δm_s due to proper time resolution effect.

Figure 67 shows the amplitude test results using a sample of $b\bar{b}$ Monte Carlo which corresponds to roughly 20 times the data size. The amplitude fit is performed for four different values of input Δm_s . A signal peak is clearly seen for input Δm_s values of 4 and 10 psec^{-1} . A slight enhancement in the signal region is also observed for generated Δm_s of 17 psec^{-1} . Figure 67d illustrates the scenario when the true Δm_s value is far beyond the sensitivity of the analysis. In this case, the sensitivity at the 95% confidence level is about 22 psec^{-1} and the generated Δm_s is 270 psec^{-1} . The amplitude plot shows that all data points are consistent with amplitude of zero and no signal peak is observed. In this example, the values of Δm_s less than 20.5 psec^{-1} can be excluded at the 95% confidence level.

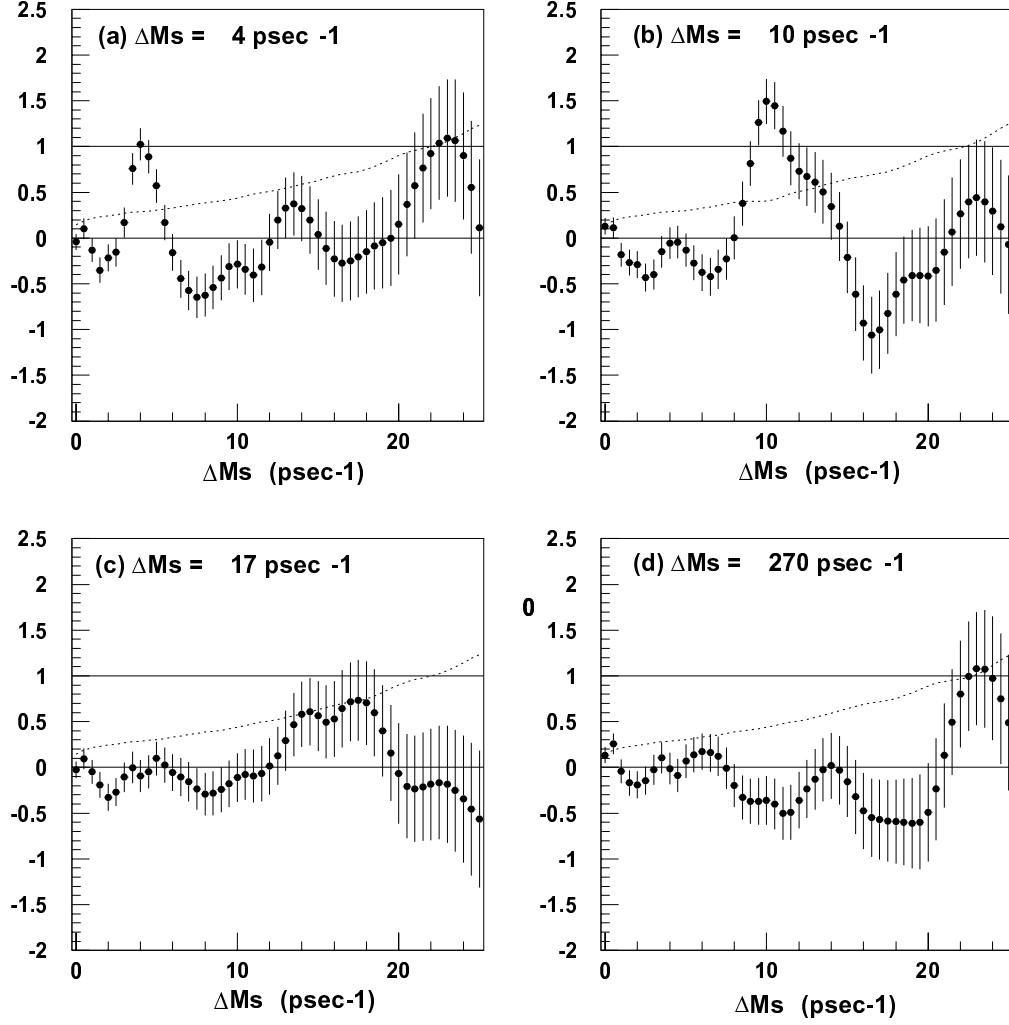


Figure 67: Amplitude fit result using full Monte Carlo simulation including background events with input Δm_s of (a) 4, (b) 10, (c) 17 and (d) 270 psec⁻¹.

CHAPTER 8

RESULTS AND CONCLUSIONS

In this chapter we first present the amplitude fit result for the $B_s^0 - \bar{B}_s^0$ mixing analysis. We then discuss the issue of systematic uncertainties associated with the amplitude fit. We conclude this chapter with some general remarks on the world average as well as on the future B_s^0 mixing measurements.

8.1 $D_s + Tracks$ Result

The amplitude plot for the “ D_s +Tracks” analysis is shown in figure 68 (for the experts who wish to combine this analysis with other results, the data file that conforms to the COMBOS averaging algorithm developed by the LEP B Oscillations Working Group is included in Appendix D). The D_s +Tracks result excludes the following values of the $B_s^0 - \bar{B}_s^0$ mixing oscillation frequency: $\Delta m_s < 1.4 \text{ } psec^{-1}$ and $2.5 < \Delta m_s < 5.3 \text{ } psec^{-1}$ at the 95% confidence level. The sensitivity of the analysis is at $3.3 \text{ } psec^{-1}$. Since the limit is much higher than the sensitivity of the analysis, it is essential that we study the probability for this analysis to exclude Δm_s values considerably beyond the sensitivity. The exclusion probability for a given Δm_s is defined as:

$$P_{exclude}(\sigma_A, \Delta m_s) = \int_{-\infty}^{1-1.645\sigma_A} \frac{1}{\sqrt{2\pi}\sigma_A} e^{-0.5(A/\sigma_A)^2} dA. \quad (8.1)$$

The integrand is a normalized Gaussian centered at $A = 0$ (the expected value of A for no signal) with a width that is given by the uncertainty in the amplitude at the particular Δm_s value. The exclusion probability distribution is shown in figure 69. The probability for excluding Δm_s of 5.3 psec^{-1} is about 45%. Therefore the excluded regions obtained in this analysis are reasonable, assuming Gaussian statistics.

One important feature to note about the result is the shallow slope of the sensitivity curve. This analysis has achieved an excellent proper time resolution. Consequently, the amplitude error grows fairly slowly as a function of Δm_s . At high Δm_s , this fact allows the analysis to be competitive with other B_s^0 mixing analyses with larger data sample. The effect of including this analysis in the SLD and world averages will be discussed in later sections.

As mentioned earlier, the analysis is statistically limited. Unfortunately, the SLD data run has officially ended and no additional data will be available. The data collected from the 1992 to 1995 run periods (prior to the installation of VXD3) could provide more statistics. However, studies show that the sensitivity gain from the VXD2 data is marginal due to worse decay length resolution. Alas, the limitation of the data size is the main obstacle in improving the sensitivity of the analysis.

8.2 Systematic Uncertainties

The likelihood function contains many input parameters that are either measured or estimated from the Monte Carlo. Whenever possible, we derive the parameters directly from the data to reduce dependence on the Monte Carlo modelling. However, there are uncertainties associated with each of the input parameters regardless of their origin. The effect of these uncertainties on the amplitude fit are

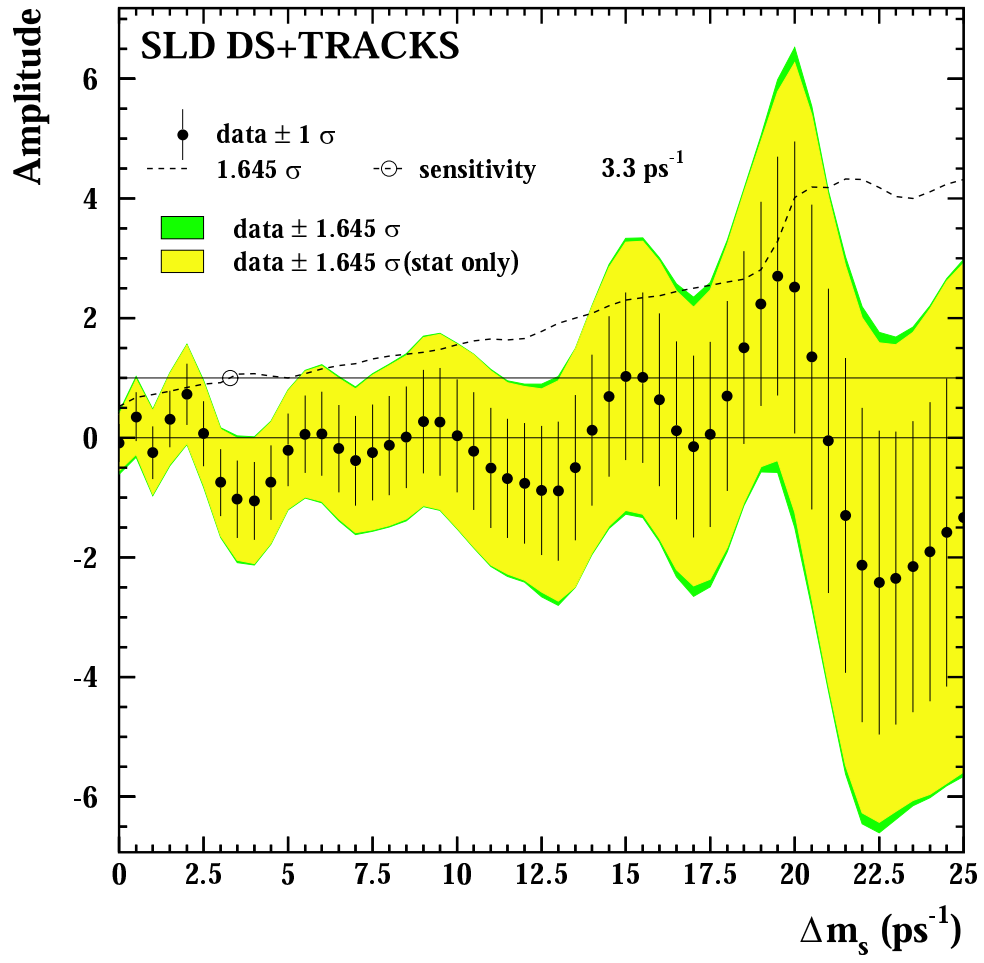


Figure 68: Amplitude plot for D_s +Tracks.

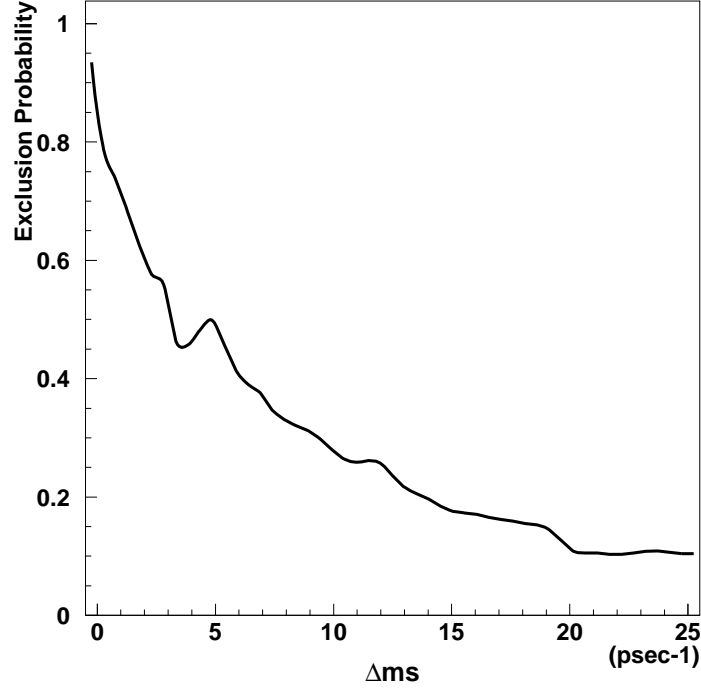


Figure 69: Exclusion probability for the D_s +Tracks analysis.

estimated by varying the parameters in the fit according to their measured or expected uncertainties. The effect of the variation is included in the amplitude plot using the prescription given in reference [68]. The systematic uncertainty on the amplitude due to a particular variation is:

$$\sigma_A^{syst} = (A^{new} - A^{nom}) + (1 - A) \frac{(\sigma_A^{new} - \sigma_A^{nom})}{\sigma_A^{nom}}, \quad (8.2)$$

where A^{new} (A^{nom}) and σ_A^{new} (σ_A^{nom}) are the new (nominal) amplitude and uncertainty. The prescription for calculating the systematic error (equation 8.2) takes into account not only the change in amplitude value but also the change in statistical error of the amplitude. The results of the individual variations are combined to obtain the overall systematic uncertainty. This procedure is performed for each Δm_s data point on the amplitude plot.

In this analysis, we study the systematic error on some of the more significant parameters in the likelihood function. These parameters and their errors are discussed in the next few sections.

8.2.1 B Hadron Lifetimes and Δm_d

The B hadron lifetimes and Δm_d values used in the fit are obtained from the world averages. Table 16 lists the values assumed in the fit and the uncertainties used to determine the systematic error.

Parameter	Value and Error	Ref.
τ_{B_s}	$1.464 \pm 0.057 \text{ ps}$	[62]
τ_{B_d}	$1.562 \pm 0.029 \text{ ps}$	[62]
τ_{B^\pm}	$1.656 \pm 0.025 \text{ ps}$	[62]
$\tau_{BBaryons}$	$1.208 \pm 0.051 \text{ ps}$	[62]
Δm_d	$0.476 \pm 0.016 \text{ ps}^{-1}$	[62]

Table 16: World average values of B lifetimes and Δm_d .

8.2.2 Sample Composition

The uncertainty in the D_s fraction, $f_{D_s}(m_{KK\pi})$, comes from the $m_{KK\pi}$ mass fit. The issue involves how well the combinatorial background level can be determined. A series of studies indicate that the fit for the background level is stable within 5% for the $\phi\pi$ loose kaon ID samples. For the $K^{*0}K$ and hard kaon ID samples, the statistics are significantly lower and the fits vary at the 10% level. Based on these findings, we assign 5% or 10% systematic uncertainty on the D_s fraction on the respective event sample.

As mentioned in section 7.2.1, the fractions $f_{B_s}^{rs}$, $f_{B_s}^{ws}$, f_{B_d} , f_{B^+} , f_{BB} and f_{cc} used in the likelihood fit are derived from Monte Carlo and world average branching ratios. Assuming that the Monte Carlo models the detector efficiency and acceptance well, the principal uncertainties in the sample fractions are from the uncertainties in the branching ratio measurements. The list of branching ratios assumed in the analysis are given in table 17. All the parameters are varied by $\pm 1 \sigma$ to estimate their systematic error contributions.

Parameter	Value and Error	Ref.
$f(\bar{b} \rightarrow B_s^0)$	0.100 ± 0.012	[62]
$f(\bar{b} \rightarrow B_d^0, B^+)$	0.401 ± 0.010	[62]
$f(\bar{b} \rightarrow B \text{ Baryon})$	0.099 ± 0.017	[62]
$R_b \cdot \mathcal{B}(b \rightarrow \bar{B}_s^0) \cdot \mathcal{B}(\bar{B}_s^0 \rightarrow D_s^+ X) \cdot \mathcal{B}(D_s^+ \rightarrow \phi\pi^+)$	$(6.21^{+0.71}_{-0.78}) \times 10^{-4}$	[62, 69]
$\mathcal{B}(b \rightarrow W^- \rightarrow D_s^-) \cdot \mathcal{B}(D_s^- \rightarrow \phi\pi^-)$	$(3.66 \pm 0.45) \times 10^{-3}$	[69]
$\mathcal{B}(B_{d,u} \rightarrow D_s^\pm X) \cdot \mathcal{B}(D_s^\pm \rightarrow \phi\pi^-)$	$(3.71 \pm 0.28) \times 10^{-3}$	[62]
$\mathcal{B}(B_{d,u} \rightarrow D_s^- X) / \mathcal{B}(B_{d,u} \rightarrow D_s^\pm X)$	0.172 ± 0.083	[62]
$\mathcal{B}(\bar{c} \rightarrow D_s^-) \cdot \mathcal{B}(D_s^- \rightarrow \phi\pi^-)$	$(3.4 \pm 0.3) \times 10^{-3}$	[62]

Table 17: B production fractions and various branching ratios assumed in the amplitude fit. The uncertainties for the branching ratios do not include uncertainty from $\text{Br}(D_s \rightarrow \phi\pi)$.

One important parameter that deserves special attention is the branching ratio of right-sign B_s^0 . ALEPH has performed a direct measurement on this quantity [69]. Unfortunately, the error on the measurement is of the order of 30%. The published value is:

$$R_b \cdot \mathcal{B}(b \rightarrow \bar{B}_s^0) \cdot \mathcal{B}(\bar{B}_s^0 \rightarrow D_s^+ X) \cdot \mathcal{B}(D_s^+ \rightarrow \phi\pi^+) = (6.68 \pm 1.99) \times 10^{-4}, \quad (8.3)$$

where the error quoted does not include the error from $B(D_s^+ \rightarrow \phi\pi^+)$. To obtain

a better estimate of the right-sign B_s^0 branching ratio, we assume factorization (i.e. leptonic W decay is independent of the spectator diagram), which implies:

$$B(\overline{B}_s^0 \rightarrow D_s^+ X) = \frac{B(\overline{B}_s^0 \rightarrow D_s^+ l^- \overline{\nu} X)}{B(\overline{B}_s^0 \rightarrow l^- \overline{\nu} X)}, \quad (8.4)$$

where $B(\overline{B}_s^0 \rightarrow l^- \overline{\nu} X)$ is the direct semileptonic branching ratio $B(b \rightarrow l^+ \nu X)$. Equation 8.4 allows us to transform the more precise measurement of the right-sign B_s^0 semileptonic branching ratio [62]:

$$R_b \cdot \mathcal{B}(b \rightarrow \overline{B}_s^0) \cdot \mathcal{B}(\overline{B}_s^0 \rightarrow D_s^+ l^- \nu X) \cdot \mathcal{B}(D_s^+ \rightarrow \phi \pi^+) = (6.49_{-0.89}^{+0.82}) \times 10^{-5}, \quad (8.5)$$

to the inclusive right-sign B_s^0 branching ratio. We then combine the direct (equation 8.3) and the inferred (equation 8.5) measurements using the B semileptonic branching ratio from reference [62] to obtain the value:

$$R_b \cdot \mathcal{B}(b \rightarrow \overline{B}_s^0) \cdot \mathcal{B}(\overline{B}_s^0 \rightarrow D_s^+ X) \cdot \mathcal{B}(D_s^+ \rightarrow \phi \pi^+) = (6.21_{-0.78}^{+0.71}) \times 10^{-4}, \quad (8.6)$$

which has an uncertainty of 12%. The above rate does not include the contribution from wrong-sign B_s^0 decays. For the latter contribution, we assume that the rates are equal for all B mesons:

$$B(B_s^0 \rightarrow D_s^+ X) = B(B_d^0 \rightarrow D_s^+ X) = B(B^+ \rightarrow D_s^+ X). \quad (8.7)$$

8.2.3 Flavor Tagging

The systematic error on the initial state mistag rate (η_i) is comprised of the systematic errors from the six individual tags and the combination procedure. The contributions from the two dominant tags, polarization and jet charge, have been studied in detail [64]. The effect of varying the electron beam polarization and

various other input parameters brings about a spread on the mistag rate of about 1%. The remaining contributions are expected to be relatively small. Therefore, we assign a conservative uncertainty of $\pm 2\%$ (absolute) to the initial state mistag rate.

The final state mistag rates are not explicitly treated in the systematic error analysis. The effects have been accounted for in the systematic uncertainties on the branching ratios of right-sign to wrong-sign B decays as listed in table 17.

8.2.4 Proper Time Resolution and Offsets

The decay length and boost uncertainties are the dominant contributions to the proper time resolution systematic error. The effect from the decay length resolution has been studied using $Z^0 \rightarrow \tau^+\tau^-$ events [70]. The estimated decay length resolutions in data and Monte Carlo obtained from the negative tail of the τ decay length distributions are consistent within the errors of the fit, and the observed difference is less than 5%. To cover any unknown effects not accounted for, we assign $\pm 10\%$ systematic error on decay length resolution.

A comparison of the neutral electromagnetic energy distribution associated with B decay between data and Monte Carlo suggests that the uncertainty due to calorimetry is about 3%. Unfortunately, no additional study has been performed to constraint the boost uncertainty. Therefore we place a very conservative value of $\pm 20\%$ on the boost resolution.

Finally, we obtain the systematic error of proper time offset corrections by studying the change before and after the inclusion of corrections. We assign the systematic error equal to the total offset.

8.2.5 Systematic Error Table

The list of systematic errors and nominal amplitude values are given in table 18 for a few values of Δm_s . As the table indicates, the analysis is statistically limited. The statistical error is the main uncertainty on the amplitude values and the total systematic error is almost negligible by comparison.

8.3 SLD Average

In addition to D_s +Tracks, there are two more B_s^0 analyses at SLD: Lepton+D and Charge Dipole. All three B_s^0 mixing analyses use the same initial state tag and similar boost reconstruction algorithms. The main differences are the methods of selecting B_s^0 candidates and tagging the final B_s^0 flavor. The Lepton+D analysis takes a more inclusive approach than D_s +Tracks at selecting events. It requires a lepton and a topologically reconstructed vertex consistent with a charm meson. A neural net is implemented in the analysis to suppress wrong-sign lepton from $b \rightarrow c$ decays. The charge of the lepton is used to determine the final flavor of the B_s^0 . The average correct tag probability of the lepton tag is about 95%. The Lepton+D has more statistics than the D_s +Tracks analysis. However, it has slightly poorer proper time resolution and B_s^0 purity.

The Charge Dipole is the most inclusive analysis at SLD. It requires events to have a topologically reconstructed vertex consistent with a B decay. The final state tag is determined by exploiting the charge structure of the $b \rightarrow c$ transition. The tagging algorithm is identical to the opposite hemisphere charge dipole method used for the initial state tag. The only difference is that the dipole charge is calculated for the event hemisphere as opposed to the opposite hemisphere. The average final

Δm_s	5 ps ⁻¹	10 ps ⁻¹	15 ps ⁻¹	20 ps ⁻¹
Measured amplitude A	-0.203	0.029	1.027	2.513
Statistical uncertainty (σ_A^{stat})	± 0.599	± 0.933	± 1.361	± 2.283
Total systematic uncertainty (σ_A^{syst})	+0.119 -0.102	+0.145 -0.129	+0.326 -0.339	+0.840 -0.882
τ_{B_s}	+0.016 -0.017	+0.008 -0.008	+0.020 -0.021	+0.017 -0.019
τ_{B_d}	-0.0009 +0.0006	-0.0006 +0.0006	-0.002 +0.002	+0.00009 -0.00004
τ_{B^\pm}	-0.0006 +0.0006	-0.0006 +0.0006	-0.0005 +0.0005	-0.007 +0.007
$\tau_{B \text{ baryons}}$	+0.0001 -0.0002	+0.0001 -0.0002	+0.0002 -0.0001	+0.002 -0.002
Δm_d	-0.0002 +0.0002	-0.001 +0.001	+0.0004 -0.0004	+0.0008 -0.0008
$f(\bar{b} \rightarrow B_s^0)$	+0.018 -0.017	+0.012 -0.012	+0.021 -0.022	+0.010 -0.011
$f(\bar{b} \rightarrow B \text{ Baryon})$	+0.005 -0.005	+0.004 -0.004	+0.0009 -0.0010	-0.019 +0.019
$(R_b \cdot \mathcal{B}(b \rightarrow \bar{B}_s^0) \cdot$	-0.044 +0.061	-0.032 +0.043	-0.040 +0.048	-0.068 +0.068
$\mathcal{B}(\bar{B}_s^0 \rightarrow D_s^+ X) \cdot \mathcal{B}(D_s^+ \rightarrow \phi \pi^+)$				
$\mathcal{B}(b \rightarrow W^- \rightarrow D_s^-) \cdot \mathcal{B}(D_s^- \rightarrow \phi \pi^-)$	+0.018 -0.018	+0.013 -0.012	+0.022 -0.022	+0.010 -0.012
$\mathcal{B}(B_{d,u} \rightarrow D_s^\pm X) \cdot \mathcal{B}(D_s^- \rightarrow \phi \pi^-)$	+0.018 -0.019	+0.013 -0.014	+0.013 -0.014	+0.042 -0.047
$\mathcal{B}(B_{d,u} \rightarrow D_s^- X) / \mathcal{B}(B_{d,u} \rightarrow D_s^\pm X)$	+0.016 -0.016	+0.012 -0.013	+0.058 -0.060	+0.153 -0.156
$\mathcal{B}(\bar{c} \rightarrow D_s^-) \cdot \mathcal{B}(D_s^- \rightarrow \phi \pi^-)$	+0.002 -0.002	+0.003 -0.003	+0.007 -0.007	+0.011 -0.011
Decay length resolution	+0.017 -0.017	+0.048 -0.053	+0.021 -0.021	+0.038 -0.062
Boost resolution	-0.016 +0.031	+0.099 -0.094	-0.110 +0.061	-0.316 +0.298
f_{D_s}	+0.048 -0.046	+0.019 -0.018	+0.096 -0.096	-0.090 +0.076
Initial state tag	-0.066 +0.074	-0.054 +0.078	-0.094 +0.089	-0.430 +0.358
Proper time offset	+0.006 -0.006	+0.007 -0.007	+0.278 -0.278	+0.671 -0.671

Table 18: Table of statistical and systematic uncertainties for several Δm_s values.

state correct tag probability is about 78%. This value is higher than the dipole charge initial state tag since charge dipole as a final state tag is not diluted by B^0 mixing. The Charge Dipole analysis has over 11,000 reconstructed B_s^0 candidate events with an average B_s^0 purity of about 16%.

The three analyses have been combined at SLD using the latest D_s +Tracks result presented here and the results released at the 2001 summer conferences for the Lepton+D and Charge Dipole analyses [71]. To ensure the analyses are statistically independent, data used in one analysis is excluded from the rest. This is accomplished by ordering the three analyses based on sensitivity per event. Each analysis is required to remove events already selected by the more sensitive analyses. The D_s +Tracks has the highest sensitivity per event, followed by Lepton+D and then Charge Dipole. The same exercise is performed on data and Monte Carlo to avoid introducing biases. Combining the amplitude results of Lepton+D and Charge Dipole yields a sensitivity of 12.1 psec^{-1} at the 95% confidence level. The sensitivity improves to 13.7 psec^{-1} with the inclusion of D_s +Track. The combined SLD amplitude plot is shown in figure 70. The SLD average excludes $B_s^0 - \overline{B}_s^0$ mixing oscillation frequency of $\Delta m_s < 13.7 \text{ psec}^{-1}$ at the 95% confidence level.

8.4 World Scene

The search for B_s^0 oscillations has also been performed by the ALEPH, DELPHI, OPAL, and CDF collaborations. A combined world average is obtained using the COMBOS algorithm developed by the LEP B Oscillations Working Group [72]. The algorithm takes into account correlated systematic errors and different assumed branching ratio values between various experiments. The combined LEP and CDF analyses based on the results released at the 2001 summer conferences yields a

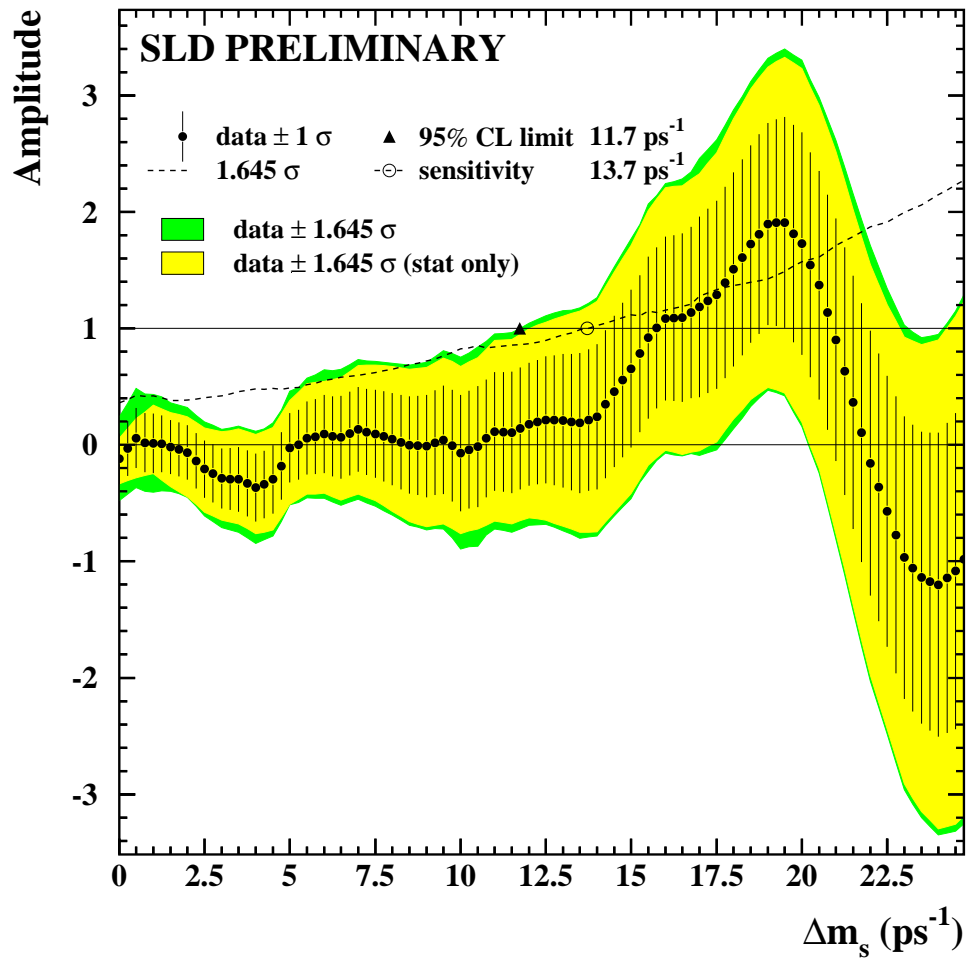


Figure 70: SLD average amplitude plot including the final D_s +Tracks result.

sensitivity of 15.6 psec^{-1} . The addition of the SLD average mentioned in the previous section brings the world average sensitivity to 18.5 psec^{-1} . The result of the world combination is shown in figure 71. The excluded region at the 95% confidence level is $\Delta m_s < 14.6 \text{ psec}^{-1}$. Figure 72 shows the amplitude and error at $\Delta m_s = 15 \text{ psec}^{-1}$ for the individual analyses used in the world average.

The most significant deviation from zero on the amplitude plot occurs at about 17 psec^{-1} . A toy Monte Carlo study was carried out to evaluate the significance of the “bump”. The result indicates that about 3% of the simulated experiments with Δm_s set to a large value have fluctuations similar to the one observed in the data. Therefore the “bump” is not a conclusive signal. Nevertheless, the observed feature is tantalizing, given the fact that the “bump” is within the preferred values of Δm_s from the constraints on the $\rho - \eta$ plane.

The achieved world limit on Δm_s now provides a strong constraint on the apex of the Unitarity Triangle. Figure 73 illustrates the constraints on the $\rho - \eta$ plane using experimental results as of ICHEP-2000, including the previous D_s +Tracks result [24]. The allowed region of $\rho - \eta$ is computed using the Bayesian approach. It is shown on the plot as the two black contour circles. The constraint from the ratio of Δm_s and Δm_d is shown in the dotted curve. As one can see, the curve severely confines the allowed region of the apex. The probability distribution for Δm_s can be extracted from the plot. From the distribution, the preferred value of Δm_s is: $15.6 \leq \Delta m_s \leq 20.5 \text{ psec}^{-1}$ at the 95% confidence level.

8.5 Outlook

The SLD experiment has made significant contributions to the world average on the limit for B_s^0 oscillations. This is an impressive accomplishment given that

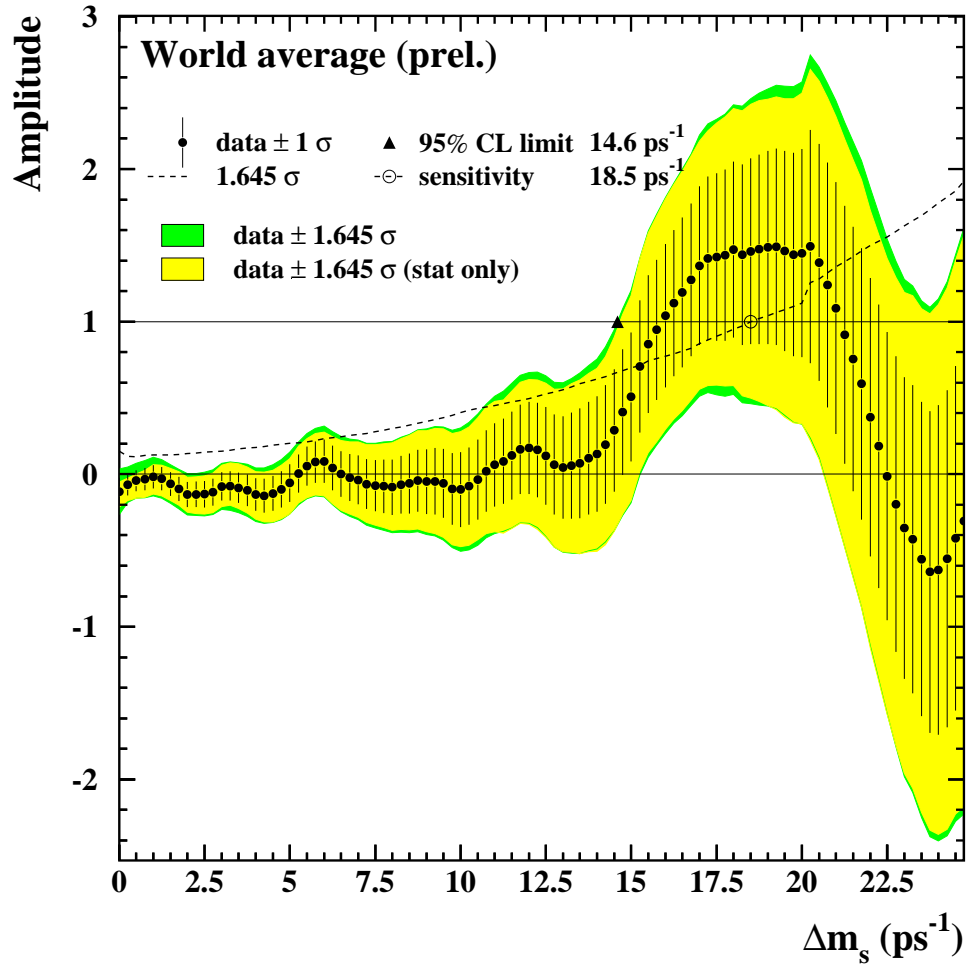


Figure 71: World amplitude plot including the latest D_s +Tracks result.

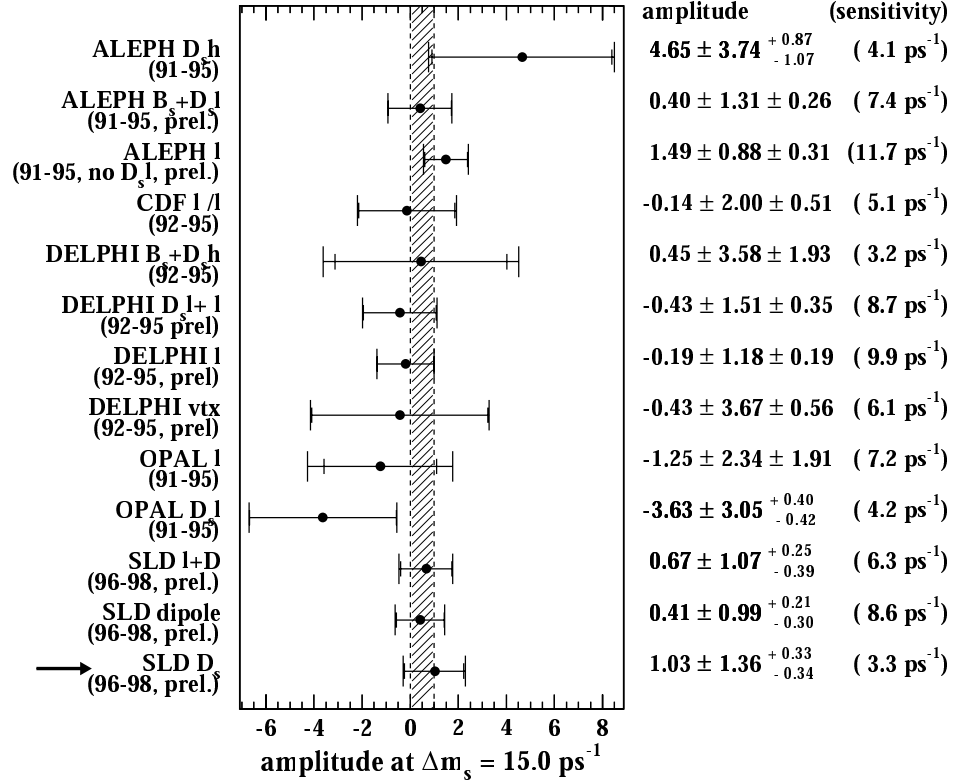


Figure 72: The plot shows the amplitudes and errors at Δm_s of 15 $psec^{-1}$. The arrow points to the data point for the D_s +Tracks analysis.

the SLD data size is about a factor of 10 less than that of the LEP experiments. In the near future, both SLD and LEP are expected to release analysis updates. However, it is unlikely that a definitive signal can be observed using data from the current generation of experiments.

If Δm_s lies in the region suggested by the $\rho - \eta$ plot, the CDF experiment in RUN II will very likely be the first experiment to observe the signal. Figure 74 shows the projected sensitivity for 2 fb^{-1} of data. A 5σ discovery can be achieved up to Δm_s of about 40 $psec^{-1}$.

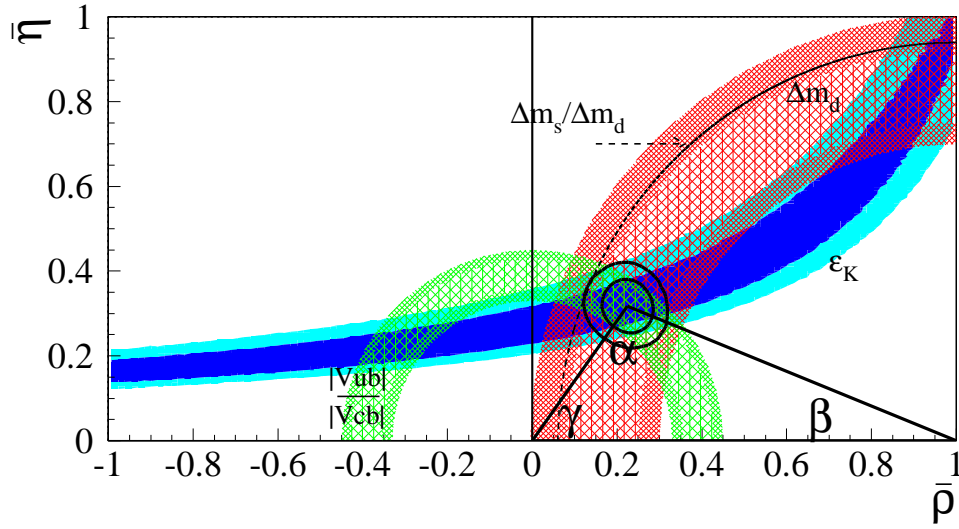


Figure 73: The allowed regions for $\bar{\rho}$ and $\bar{\eta}$ (contours at 68%, 95%) and the various experimental constraints.

The aggressive efforts to search for B_s^0 oscillations have steadily increased the Δm_s limit over the years. With new generation experiments coming on line, such as Tevatron RunII, LHC-B and BTeV, the end of the search is finally within sight. If upcoming experiments fail to make a discovery and push the limit beyond the preferred predicted region, then it would imply that the $|V_{td}|$ leg on the Unitarity Triangle is so short that the triangle cannot be closed. This would be an even more important discovery, a golden signature of physics beyond the Standard Model. In either case, this is only the beginning of an exciting era of B_s^0 physics.

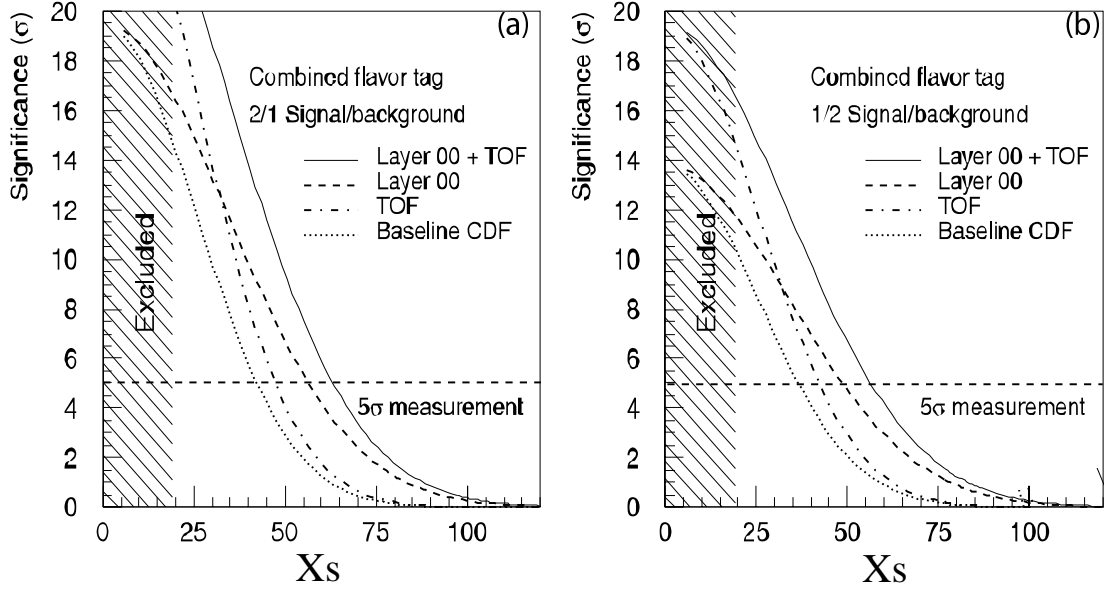


Figure 74: Projections of B_s^0 mixing reach as a function of X_s ($X_s = \Delta m_s / \Gamma_B$) at CDF RUN II. Plot (a) assumes a signal to background ratio of 2:1 while plot (b) assumes a more conservative signal to background ratio of 1:2.

A P P E N D I X A

THE CHERENKOV RING IMAGING DETECTOR

Cherenkov radiation is produced when a charged particle traverses a dielectric medium with a velocity βc greater than the phase velocity of light in the medium. This phenomenon was first discovered by P. A. Cherenkov in 1934 [73]. The angle, θ_c , of the Cherenkov radiation with respect to the particle's flight direction is given by

$$\cos \theta_c = \frac{1}{n(E)\beta}, \quad (\text{A.1})$$

where n is the index of refraction of the medium (generally a function of the energy of the Cherenkov radiation, E). The frequency spectrum of the Cherenkov radiation is given by the Tamm-Frank relation,

$$\frac{dN}{dE} = \left(\frac{\alpha}{\hbar c} \right) Z^2 L \sin^2 \theta_c, \quad (\text{A.2})$$

where dN is the number of photons with energy between E and $E + dE$, α is the fine structure constant, Z is the charge of the particle and L is the path length of the particle through the medium. For a medium with a relatively constant index of refraction, the radiation spectrum rises linearly with E . Therefore, Cherenkov radiation generally peaks in the short wavelengths.

The Cherenkov radiation is widely used as a means to identify particles. More specifically, the information on the angle of the Cherenkov cone and the momentum

of the track (determined from a tracking detector) yields the mass of the particle. A general survey of ring imaging detectors can be found in [74]. The number of photons detected per ring ($N_{det.}$) in a ring imaging detector is one of the important parameters that indicates the performance of the system. In the case where $n(E)$ is flat, the parameter can be approximated by the expression

$$N_{det.} = N_0 Z^2 L \sin^2 \theta_c, \quad (\text{A.3})$$

where N_0 is the parameter that describes the response of the photon detector. This parameter has the following form:

$$N_0 = \left(\frac{\alpha}{\hbar c} \right) \int_{\Delta E} \epsilon(E) dE, \quad (\text{A.4})$$

where the integration is over the detectable range of photon energies and the efficiency function, $\epsilon(E)$, includes the effects of detector quantum efficiency, the transmission efficiency of photon through the detector materials and other losses. The typical N_0 achieved for ring imaging detectors is between 30 to 80 cm^{-1} in the ultraviolet region. The SLD CRID is a dual-radiator system, similar to the RICH detector at the DELPHI experiment [75], designed to perform particle identification over a large momentum range. The achieved N_0 for the SLD CRID is about 52 cm^{-1} (68 cm^{-1}) for the liquid (gas) radiator system [76].

A.1 Maximum Likelihood Method

After the positions of the Cherenkov photons in the TPC have been reconstructed, a maximum likelihood method is used to determine the particle type for each track [77]. For a given track, a set of five likelihood values are computed, each corresponds to a particular particle hypothesis (i.e. electron, muon, pion, kaon

or proton). The likelihood function, \mathcal{L} , is the probability of observing the spatial distribution of photons in the TPC given a set of particle hypotheses, $\{h_k\}$, for the event. The probability of observing n_e number of photoelectrons given the expected value \bar{n}_e for the hypothesis $\{h_k\}$ follows the Poisson distribution

$$P(n_e|\bar{n}_e) = \frac{\bar{n}_e^{n_e}}{n_e!} e^{-\bar{n}_e}. \quad (\text{A.5})$$

The overall likelihood function is defined as,

$$\begin{aligned} \mathcal{L} &= P(n_e|\bar{n}_e)P(\{\vec{x}_i\}) \\ &= \bar{n}_e^{n_e} e^{-\bar{n}_e} \prod_{i=1}^{n_e} P(\vec{x}_i) \\ &= e^{-\bar{n}_e} \prod_{i=1}^{n_e} \rho(\vec{x}_i), \end{aligned} \quad (\text{A.6})$$

where $P(\vec{x})$ is the probability of finding a photoelectron in the differential volume $d^3\vec{x}$, $\rho(\vec{x})$ is the expected number of photoelectrons in $d^3\vec{x}$ ($\rho = \bar{n}_e P$) and the index i runs over all photoelectrons in the TPC. The expression for $\rho(\vec{x})$ can be separated into two terms:

$$\rho(\vec{x}) = B(\vec{x}) + \sum_k \rho_{k,h_k}(\vec{x}), \quad (\text{A.7})$$

where $B(\vec{x})$ models the random hits in the TPC and the second term represents the photoelectrons from the Cherenkov radiation for a given track k and particle hypothesis h_k . This term can be written more conveniently using the following set of coordinates: Cherenkov polar angle (θ_c), photon conversion length in the TPC (l) and Cherenkov azimuthal angle (ϕ_c). In this coordinate system, the density is

$$\rho_{k,h_k}(\vec{x}) = \frac{N_{k,h_k}}{2\pi} \frac{e^{-l/\lambda}}{\lambda} \frac{e^{-(\theta_c - \theta_0)^2/2\sigma_\theta^2}}{\sqrt{2\pi}\sigma_\theta} \frac{1}{\mathcal{J}}, \quad (\text{A.8})$$

where N_{k,h_k} is the number of expected photoelectrons per ring and θ_0 is the expected Cherenkov angle for track k and particle hypothesis h_k . The parameter λ is the photon absorption length in the TPC, θ_c is the measured Cherenkov angle for the

TPC hit assuming the photon originated from track k , σ_θ is the resolution of the measured Cherenkov angle and \mathcal{J} is the coordinate transformation Jacobian.

The likelihood for the five particle hypotheses for track k can be calculated based on equation A.6. The value for hypothesis h_k of track k is given by the set of $\{h_j\}_{j \neq k}$ that maximizes \mathcal{L} . The likelihood function is not explicitly normalized, therefore only the ratios of the likelihoods or the differences of log-likelihoods are useful. In particular, a log-likelihood difference of at least 5 is required for particle identification using the liquid information. For example, a definite pion is required to satisfy the conditions: $\log(\mathcal{L}_\pi) - \log(\mathcal{L}_K) > 5$ and $\log(\mathcal{L}_\pi) - \log(\mathcal{L}_P) > 5$. For the gas system, only a log-likelihood difference of 3 is required. Whenever possible, the liquid and gas information are combined to enhance the efficiency and purity of particle identification.

A.2 Liquid Tray Alignment

Another indicator of the performance of the ring imaging detector, aside from N_0 , is the Cherenkov angle resolution. The measured resolution for the CRID gas system is about 4.5 mrad, which is in good agreement with the Monte Carlo simulation. However, the average CRID liquid Cherenkov angle resolution is about 15 mrad for the data, whereas the Monte Carlo predicts a resolution of approximately 10 mrad. One possible contribution to the degradation seen in the data maybe due to the mis-alignment of the liquid radiator trays. It is conceivable that over time, the trays may be tilted or even warped.

The mis-alignment or distortion of the liquid tray can be quantified by studying the inclusive Cherenkov angle (for $\beta = 1$ particles) along the surface of the liquid tray. For a perfectly aligned tray with no distortions, the asymptotic Cherenkov

angle should be the same regardless of the location of the origin of the Cherenkov cone. In the scenario where some parts of the liquid tray is warped or slanted towards the center of the detector (true position of the tray is further away from the TPC), the reconstructed Cherenkov angle would be smaller than the nominal value. Conversely, the reconstructed angle would be larger if the true position of the tray is closer to the imaging plane of the TPC.

To map the shape of the liquid trays, each tray is divided into four regions along the beam pipe direction and four regions in azimuth (see figure 75). There are 16

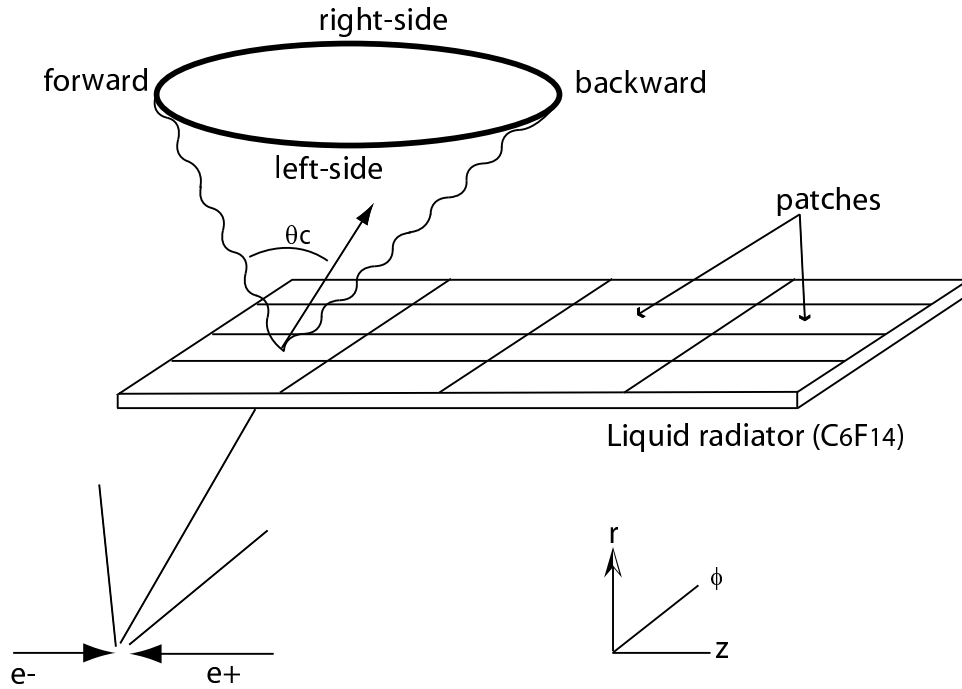


Figure 75: Partitions of the liquid radiator tray.

resulting “patches” for each tray. The inclusive Cherenkov angle distribution for tracks with momentum greater than 3 GeV is filled individually for the 16 patches. The distributions are further sub-divided into four Cherenkov ϕ quadrants (forward, backward, left-side and right-side). These histograms (64 per tray) are used to map out the shape of the liquid trays for the alignment procedure. The liquid tray

alignment is performed in four steps: z -tilt (dr/dz) correction, azimuthal ($dr/d\phi$) rotation, liquid tray z (dz) alignment and lastly, the global radial displacement (dr).

The slope of the tray in z is parameterized by fitting the average inclusive Cherenkov angles along the z direction to a first-order polynomial. The left-side and right-side Cherenkov photons are not used in the fit to avoid complication associated with the mis-alignments of the adjacent trays. To increase the statistics of the fit, the four patches in the azimuthal direction are combined in the same z slice. The resulting slopes for the 40 liquid trays are shown in figure 76.

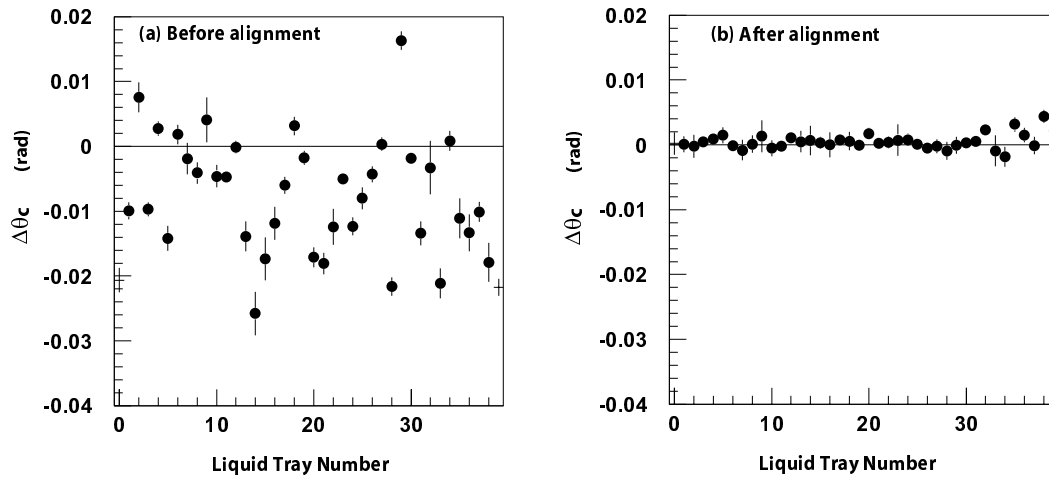


Figure 76: Distribution of $\Delta\theta_c$ ($\theta_c(z = 0) - \theta_c(z = 1.3m.)$) as a function of liquid tray number for the forward Cherenkov photons. Plot (a) shows the distribution before dr/dz alignment and (b) is after dr/dz alignment.

The rotation of the liquid tray along the long axis ($dr/d\phi$) is mapped by fitting the Cherenkov angles along the azimuthal direction to a first-order polynomial. Similar to the dr/dz alignment, only the forward Cherenkov photons are used and patches in z are combined in the same ϕ slice. The distribution of $dr/d\phi$ tilt before and after alignment are shown in figure 77.

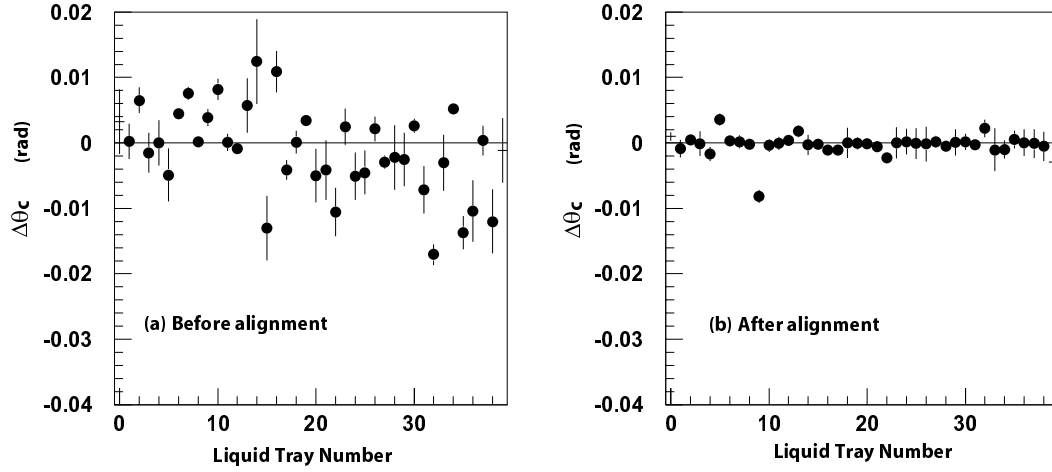


Figure 77: Distribution of $\Delta\theta_c$ ($\theta_c(x = 0) - \theta_c(x = 33\text{cm.})$) as a function of liquid tray number for the forward Cherenkov photons. Plot (a) shows the distribution before $dr/d\phi$ alignment and (b) is after $dr/d\phi$ alignment.

The global dz alignment of the liquid tray is done by iteratively moving the trays along the z axis until the reconstructed inclusive Cherenkov angles for the forward and backward photons agree. Since the backward photons are internally reflected for tracks with large dip angles, the comparison between the forward and backward Cherenkov angles is restricted to the first z slice nearest to the mid-plane of the SLD detector. The resulting distributions are shown in figure 78 before and after global z shifts.

The last alignment procedure entails moving the liquid tray globally in the radial direction to normalize the asymptotic Cherenkov angle for all trays to the assumed nominal value of 672 mrad. The Cherenkov angle distributions before the radial alignment are shown in figure 79 and after the alignment are given in figure 80.

The distribution of the average inclusive liquid Cherenkov angle for the 640 patches before tray alignment shows a spread of about 4 mrad. The liquid angle

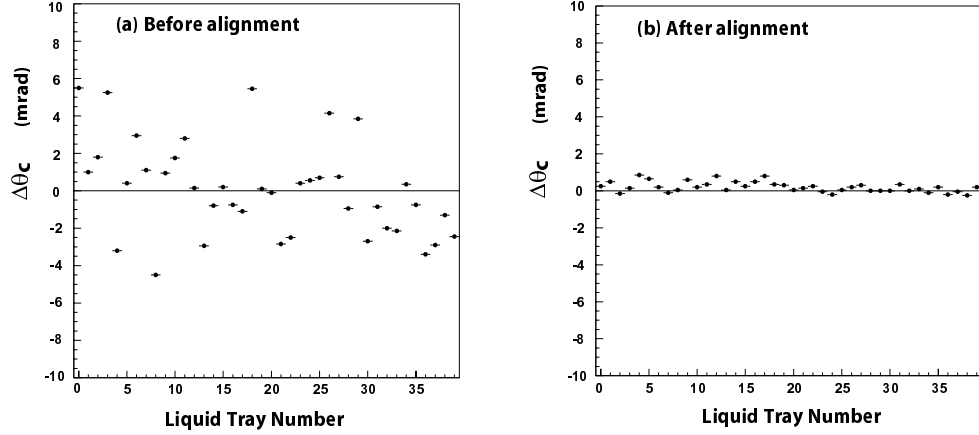


Figure 78: Distribution of the difference between forward and backward inclusive Cherenkov angles for the first z slice nearest to the detector mid-plane as a function of liquid tray number. Plot (a) shows the distribution before global z shift and (b) is after the alignment.

resolutions as a function of track dip angle before and after liquid tray alignments are shown in figures 81 and 82. The results indicate that the liquid tray alignment removed the 4 mrad variation observed due to the tilting of the trays and other similar effects. However, the improvement does not fully account for the large 10 mrad mismatch between data and Monte Carlo resolutions. It appears that there are additional sources of smearing still lurking in the data.

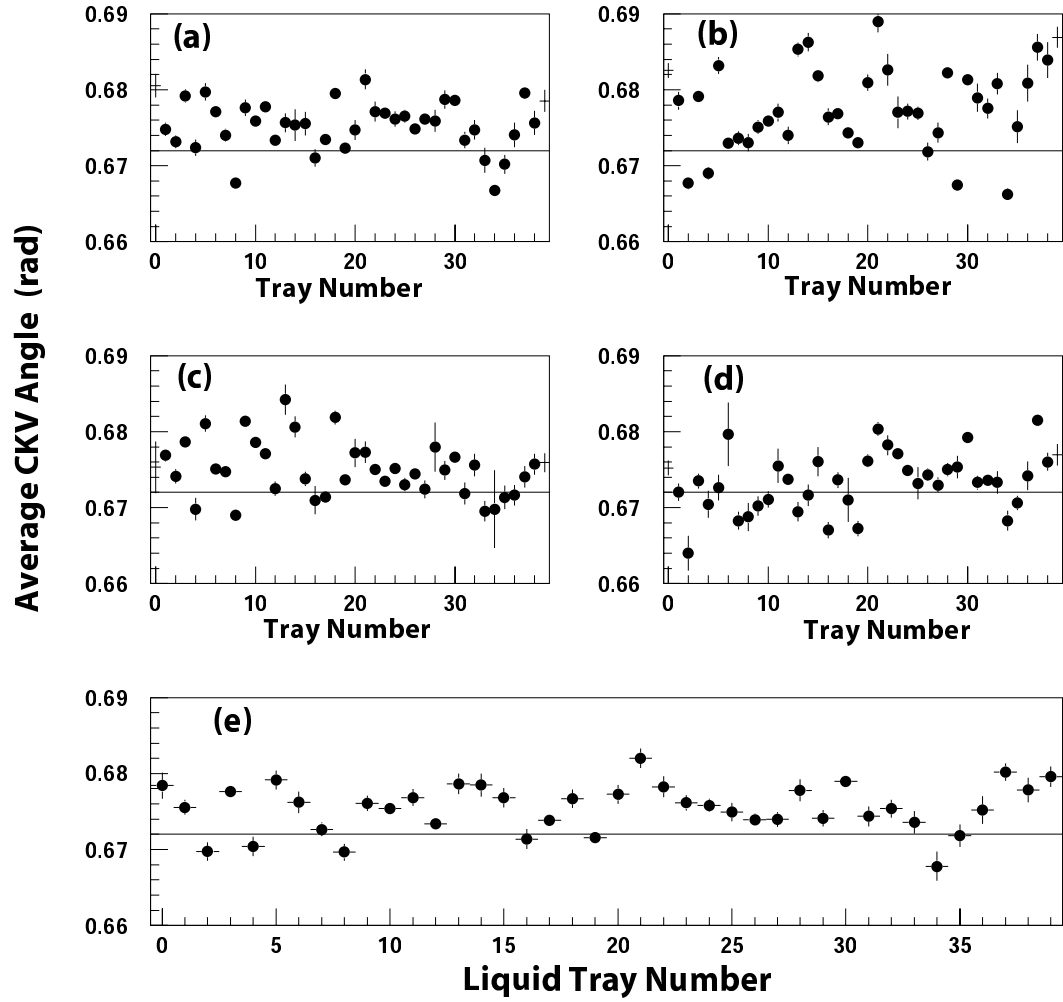


Figure 79: Distribution of the average inclusive Cherenkov angles for (a) forward, (b) backward, (c) right-side, (d) left-side and (e) combined photons as a function of liquid tray number before global radial alignment.

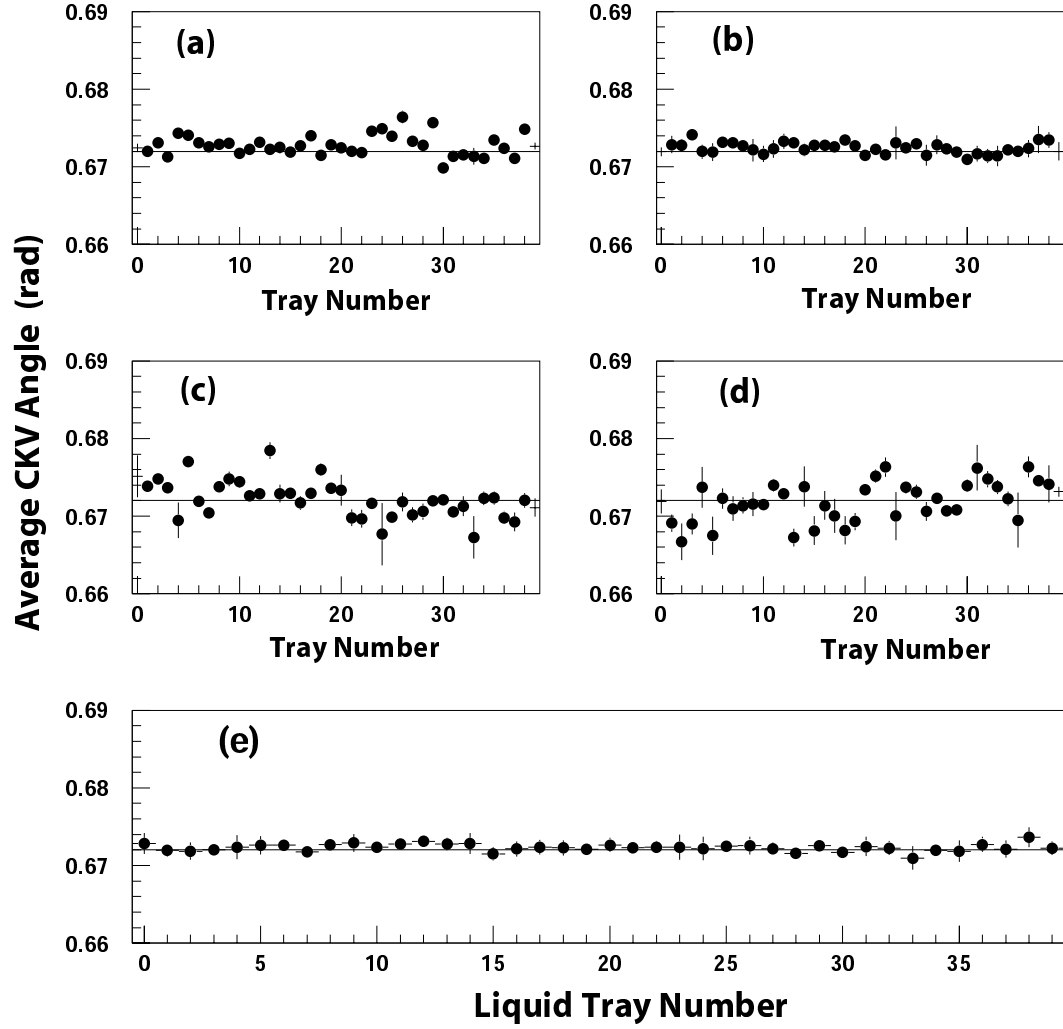


Figure 80: Distribution of the average inclusive Cherenkov angles for (a) forward, (b) backward, (c) right-side, (d) left-side and (e) combined photons as a function of liquid tray number after global radial alignment.

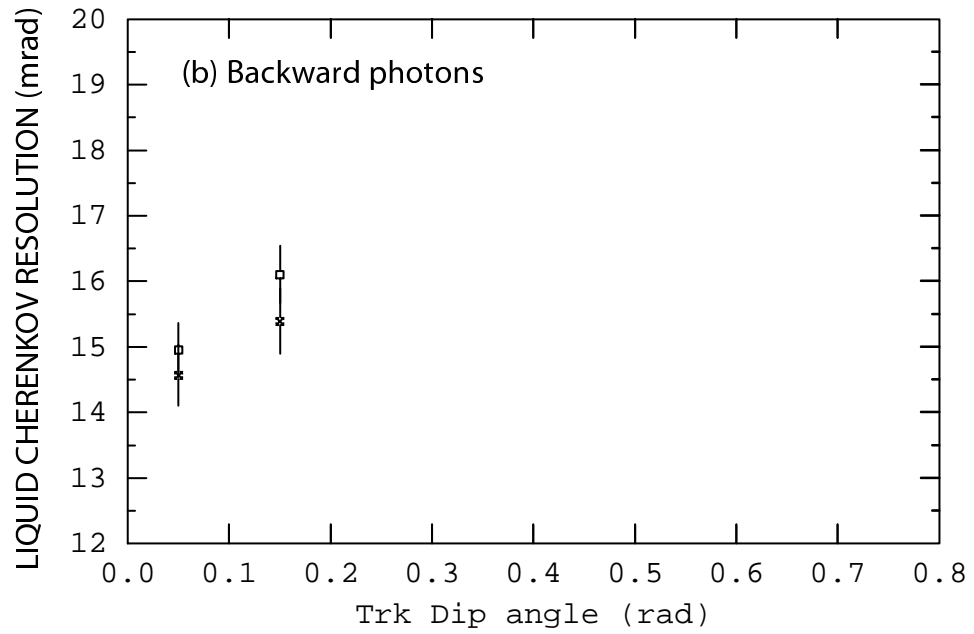
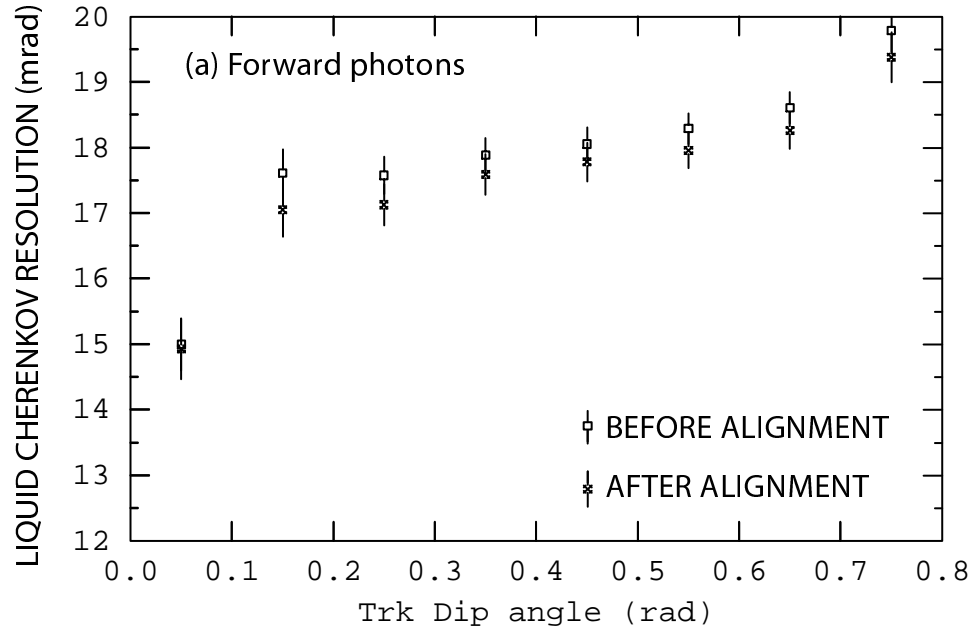


Figure 81: Distributions of liquid Cherenkov resolution as a function of track dip angle before and after liquid tray alignments for (a) forward and (b) backward photons.

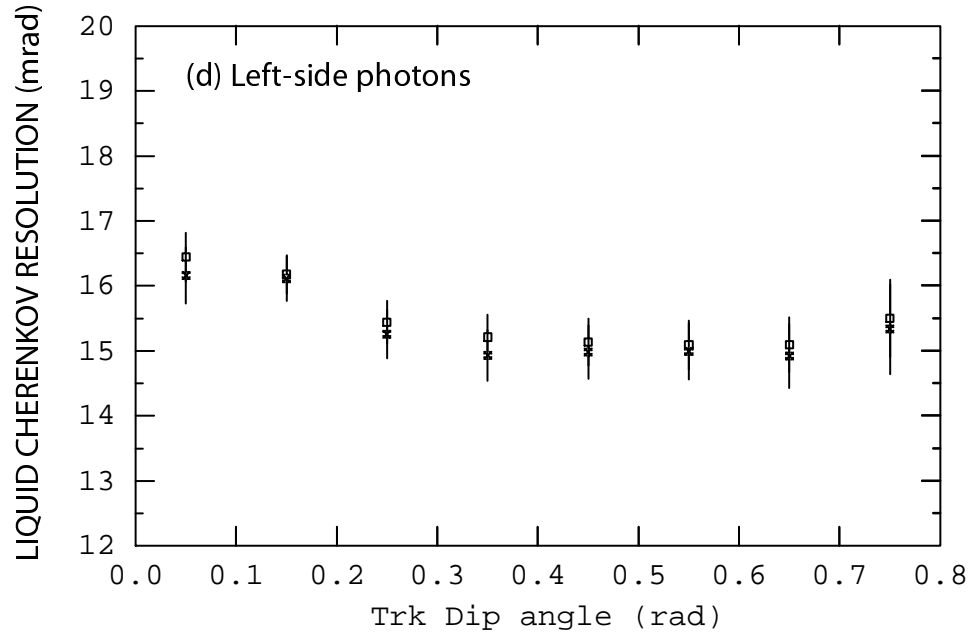
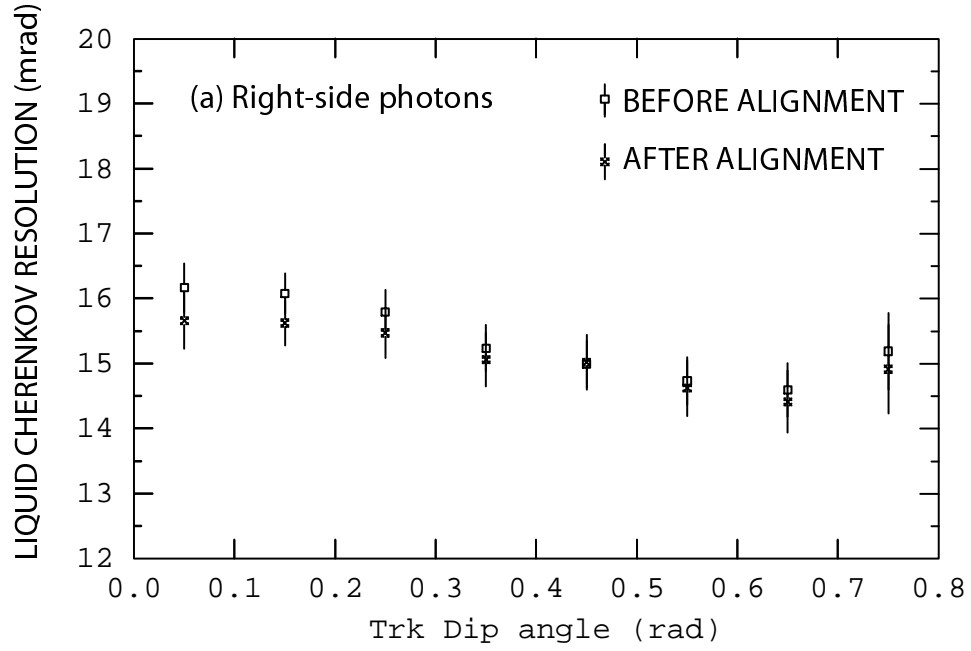


Figure 82: Distributions of liquid Cherenkov resolution as a function of track dip angle before and after liquid tray alignments for (a) right-side and (b) left-side photons.

A P P E N D I X B

VIRTUAL D_s TRACK RECONSTRUCTION

In many SLD physics analyses, the track of interest is often not reconstructed in the detector, either because the track is neutral or the particle decays before reaching the active tracking region. The standard technique to solve this problem is to identify all the daughter tracks and then combine the daughter momenta to form the momentum of the parent track. For most analyses, the parent track reconstruction ends here and only parent momentum information is used for the later stage of the analysis. For B_s^0 mixing analysis, it is important to achieve good decay length resolution in order to resolve the rapid oscillations, which in turn requires a vertex fit of the B_s^0 decay particles. This is the primary motivation to improve the reconstruction of the parent track, so that it can be used in a vertex fit. The goal is to reconstruct a D_s track that contains all the relevant parameters associated with a real track (track helix parameters, track error matrix, 2-D and 3-D normalized impact parameters). This track can later be used to perform a full vertex fit with other B_s^0 decay tracks to obtain a more precise location as well as an estimate of the error of the B_s^0 decay vertex. In this Appendix, we discuss the details of the algorithm to construct the “virtual” D_s track. The discussion applies not only to $D_s \rightarrow KK\pi$ decays but also to decays that include any arbitrary number of daughter tracks.

B.1 Parent Track Calculations

The basic track information consists of the charge, track parameters, and the error matrix of the track. These are the essential input elements to a vertex fitting routine. In this section we will describe how to calculate each parameter.

B.1.1 Parent Track Parameters

The track parameters in helix representation at SLD are given by ϕ , $\frac{1}{P_t}$, $\tan(\lambda)$, and the space-point x , y , z . In helix parameterization, only 2 space-points are needed to uniquely define a track. Therefore, the additional space-point is provided for redundancy. The parameter ϕ is the azimuthal angle, p_t is the transverse momentum and λ is the dip angle of the track. The space-point x,y,z corresponds to the location where the first three track parameters are defined. The parameters ϕ , $\frac{1}{P_t}$ and $\tan(\lambda)$ of the parent track are calculated by combining the daughter track momenta (in cartesian coordinates) at the parent decay vertex and then transforming the information to helix representation. The space-point x , y , z is the decay vertex location of the parent, which will be later summed to the POCA to the beam-line. Lastly, the charge of the parent track is calculated by summing over the charge of the daughters.

B.1.2 Parent Track Error Matrix

The full error matrix for a given track is a 5x5 symmetric matrix with 15 independent elements. In helix parameterization, the matrix is given in the form:

$$\sigma^2 = \begin{pmatrix} \sigma_\phi^2 & \dots & \dots & \dots & \dots \\ \sigma_{\frac{1}{p_t}\phi}^2 & \sigma_{\frac{1}{p_t}}^2 & \dots & \dots & \dots \\ \sigma_{\tan\lambda\phi}^2 & \sigma_{\tan\lambda\frac{1}{p_t}}^2 & \sigma_{\tan\lambda}^2 & \dots & \dots \\ \sigma_{\xi\phi}^2 & \sigma_{\xi\frac{1}{p_t}}^2 & \sigma_{\xi\tan\lambda}^2 & \sigma_\xi^2 & \dots \\ \sigma_{\eta\phi}^2 & \sigma_{\eta\frac{1}{p_t}}^2 & \sigma_{\eta\tan\lambda}^2 & \sigma_{\eta\xi}^2 & \sigma_\eta^2 \end{pmatrix}, \quad (\text{B.1})$$

where σ_ϕ , $\sigma_{(1/p_t)}$, and $\sigma_{\tan\lambda}$ will be subsequently referred to as the directional errors and σ_ξ and σ_η be referred to as the spatial errors of the track. $\hat{\xi}$ and $\hat{\eta}$ are the two orthonormal vectors transverse to the track momentum direction and are defined as:

$$\hat{\xi} = \frac{\hat{P} \times \hat{B}}{|\hat{P} \times \hat{B}|}, \quad (\text{B.2})$$

$$\hat{\eta} = \hat{\xi} \times \hat{P}, \text{ where} \quad (\text{B.3})$$

\hat{P} is the momentum of the track and \vec{B} is the magnetic field.

To simplify the calculation of the error matrix, we made the assumption that there is very little correlation between the directional and the spatial portions of the error matrix. This assumption allows us to decouple the matrix into two parts and calculate each part independently. We have estimated the directional-spatial correlation terms using numerical methods [78], and the results suggest that the approximation we made are valid.

B.1.2.1 Directional Error Matrix

The directional elements of the parent track error matrix are obtained by propagating the directional errors of the daughter tracks. The algebra parameterizing

the parent track errors in terms of the daughter errors is quite cumbersome but can be broken up into several steps.

First we express the directional errors of the parent track in terms of its Cartesian components:

$$\Delta\alpha = \sum_{i=x,y,z} \left(\Delta P^i(prt) \cdot \frac{\partial\alpha}{\partial P^i(prt)} \right), \quad (\text{B.4})$$

where $\Delta\alpha$ is the uncertainty of the parent parameter ϕ , $\frac{1}{p_t}$, or $\tan\lambda$. The letters *prt* are used explicitly to indicate that P^i is the momentum of the parent. The momentum errors of the parent, $\Delta P^i(prt)$, can now be written in terms of the errors of the daughter tracks:

$$\Delta P^i(prt) = \sum_{dtrn=daughter1}^{daughterN} \left(\Delta P^i(dtrn) \right), \quad (\text{B.5})$$

where $P^i(dtrn)$ denotes the momentum of the daughter *n*. We now need to rewrite the errors of the daughter tracks in helix parameterization. This step is required because many of the the SLD tracking codes use the helix parameterization.

$$\Delta P^i(dtrn) = \sum_{\beta=\frac{1}{p_t}, \phi, \tan\lambda} \left(\Delta\beta(dtrn) \cdot \frac{\partial P^i(dtrn)}{\partial\beta(dtrn)} \right), \quad (\text{B.6})$$

where $\beta(dtrn)$ is the helix parameter (ϕ , $\frac{1}{p_t}$, or $\tan\lambda$) of the daughter track *dtrn*.

Combining expressions (B.4) to (B.6) we get:

$$\Delta\alpha = \sum_i \sum_{dtrn} \sum_{\beta} \left(\frac{\partial\alpha}{\partial P^i(prt)} \cdot \frac{\partial P^i(dtrn)}{\partial\beta(dtrn)} \right) \cdot \Delta\beta(dtrn). \quad (\text{B.7})$$

To evaluate the error matrix elements $\sigma_{\alpha\alpha'}^2$, we need to multiply $\Delta\alpha$ by $\Delta\alpha'$ and then take the expectation value:

$$\sigma_{\alpha\alpha'}^2 = \overline{(\Delta\alpha \cdot \Delta\alpha')}. \quad (\text{B.8})$$

The expression can be written more elegantly in matrix form:

$$\sigma_{\alpha\alpha'}^2 = A_{\alpha} \cdot \Gamma \cdot (A_{\alpha'})^{\dagger}, \quad (\text{B.9})$$

where Γ is a $(3 \times N)$ by $(3 \times N)$ symmetric matrix, and N is the number of daughter tracks. The Γ matrix contains the directional portion of the error matrices of the daughter tracks. Most of the off-diagonal elements are zero because we assume that the daughter tracks are not correlated with each other. The matrix is arranged in the following form:

$$\Gamma = \begin{pmatrix} \begin{pmatrix} \sigma_\phi^2 & \sigma_{\phi \frac{1}{p_t}}^2 & \sigma_{\phi \tan \lambda}^2 \\ \sigma_{\frac{1}{p_t} \phi}^2 & \sigma_{\frac{1}{p_t}}^2 & \sigma_{\frac{1}{p_t} \tan \lambda}^2 \\ \sigma_{\tan \lambda \phi}^2 & \sigma_{\tan \lambda \frac{1}{p_t}}^2 & \sigma_{\tan \lambda}^2 \end{pmatrix} & \leftarrow \text{daughter1} \\ \vdots & \begin{pmatrix} 3 \times 3 \\ \text{daughter2} \end{pmatrix} \\ \vdots & \ddots \\ 0 & \dots & \dots & \begin{pmatrix} 3 \times 3 \\ \text{daughterN} \end{pmatrix} \end{pmatrix}. \quad (\text{B.10})$$

A_α is a 1 by $(3 \times N)$ matrix that contains the Jacobian coefficients:

$$A_\alpha = \begin{pmatrix} \Lambda_\alpha^\phi(dtr1) & \Lambda_\alpha^{\frac{1}{p_t}}(dtr1) & \Lambda_\alpha^{\tan \lambda}(dtr1) & \dots \\ \Lambda_\alpha^\phi(dtrN) & \Lambda_\alpha^{\frac{1}{p_t}}(dtrN) & \Lambda_\alpha^{\tan \lambda}(dtrN) & \dots \end{pmatrix}, \quad (\text{B.11})$$

with the coefficients, Λ_α^β , for the daughter track $dtrn$, defined as:

$$\Lambda_\alpha^\beta(dtrn) = \sum_{i=x,y,z} \left(\frac{\partial \alpha(prt)}{\partial P^i(prt)} \cdot \frac{\partial P^i(dtrn)}{\partial \beta(dtrn)} \right) \quad (\text{B.12})$$

The relevant partial derivatives (with letters prt and $dtrn$ suppressed) are :

$$\frac{\partial(\frac{1}{p_t})}{\partial P_x} = -\left(\frac{1}{p_t}\right)^3 \cdot P_x, \quad \frac{\partial(\frac{1}{p_t})}{\partial P_y} = -\left(\frac{1}{p_t}\right)^3 \cdot P_y, \quad \frac{\partial(\frac{1}{p_t})}{\partial P_z} = 0 \quad (\text{B.13})$$

$$\frac{\partial P_x}{\partial(\frac{1}{p_t})} = -p_t^2 \cdot \cos \phi, \quad \frac{\partial P_y}{\partial(\frac{1}{p_t})} = -p_t^2 \cdot \sin \phi, \quad \frac{\partial P_z}{\partial(\frac{1}{p_t})} = -p_t^2 \cdot \tan \lambda \quad (\text{B.14})$$

$$\frac{\partial \phi}{\partial P_x} = \left(\frac{-P_y}{p_t^2}\right), \quad \frac{\partial \phi}{\partial P_y} = \left(\frac{P_x}{p_t^2}\right), \quad \frac{\partial \phi}{\partial P_z} = 0 \quad (\text{B.15})$$

$$\frac{\partial P_x}{\partial \phi} = -p_t \cdot \sin \phi, \quad \frac{\partial P_y}{\partial \phi} = p_t \cdot \cos \phi, \quad \frac{\partial P_z}{\partial \phi} = 0 \quad (\text{B.16})$$

$$\frac{\partial \tan \lambda}{\partial P_x} = \left(\frac{-P_y}{P_x^2}\right), \quad \frac{\partial \tan \lambda}{\partial P_y} = \left(\frac{1}{P_x}\right), \quad \frac{\partial \tan \lambda}{\partial P_z} = 0 \quad (\text{B.17})$$

$$\frac{\partial P_x}{\partial(\tan \lambda)} = 0, \quad \frac{\partial P_y}{\partial(\tan \lambda)} = 0, \quad \frac{\partial P_z}{\partial(\tan \lambda)} = p_t \quad (\text{B.18})$$

Now we have all the essential pieces to calculate the coefficients of $\Lambda_\alpha^\beta(dtrn)$, and hence the elements of the matrix A_α :

For $\alpha = \phi$:

$$\Lambda_\alpha^\phi(dtrn) = P_t^{-2}(prt) \cdot P_t(dtrn) \left[P^y(prt) \sin \phi_{dtrn} + P^x(prt) \cos \phi_{dtrn} \right] \quad (\text{B.19})$$

$$\Lambda_\alpha^{\frac{1}{p_t}}(dtrn) = P_t^{-2}(prt) \cdot P_t^2(dtrn) \left[P^y(prt) \cos \phi_{dtrn} - P^x(prt) \sin \phi_{dtrn} \right] \quad (\text{B.20})$$

$$\Lambda_\alpha^{\tan \lambda}(dtrn) = 0 \quad (\text{B.21})$$

For $\alpha = \frac{1}{p_t}$:

$$\Lambda_\alpha^\phi(dtrn) = P_t^{-3}(prt) \cdot P_t(dtrn) \left[P^x(prt) \sin \phi_{dtrn} - P^y(prt) \cos \phi_{dtrn} \right] \quad (\text{B.22})$$

$$\Lambda_\alpha^{\frac{1}{p_t}}(dtrn) = P_t^{-3}(prt) \cdot P_t^2(dtrn) \left[P^x(prt) \cos \phi_{dtrn} + P^y(prt) \sin \phi_{dtrn} \right] \quad (\text{B.23})$$

$$\Lambda_\alpha^{\tan \lambda}(dtrn) = 0 \quad (\text{B.24})$$

For $\alpha = \tan \lambda$:

$$\Lambda_\alpha^\phi(dtrn) = P_t^{-3}(prt) \cdot P^z(prt) \cdot P_t(dtrn) \left[P^x(prt) \sin \phi_{dtrn} - P^y(prt) \cos \phi_{dtrn} \right] \quad (\text{B.25})$$

$$\begin{aligned} \Lambda_\alpha^{\frac{1}{p_t}}(dtrn) &= \left[\frac{P_t^2(dtrn)}{P_t^3(prt)} \right] \cdot \left[P^z(prt) \cdot P^x(prt) \cos \phi_{dtrn} + \right. \\ &\quad \left. P^z(prt) \cdot P^y(prt) \sin \phi_{dtrn} - P_t^2(prt) \cdot \tan \lambda_{dtrn} \right] \end{aligned} \quad (\text{B.26})$$

$$\Lambda_\alpha^{\tan \lambda}(dtrn) = \left[\frac{P_t(dtrn)}{P_t(prt)} \right] \quad (\text{B.27})$$

B.1.2.2 Spatial Error Matrix

To complete the parent track error matrix we will need to find the spatial elements of the matrix. The error matrix of the vertex fit is 3x3. The SLD track fitter returns the vertex error in the following form:

$$\sigma^2 = \begin{pmatrix} \sigma_x^2 & & \\ \sigma_{xy}^2 & \sigma_y^2 & \\ \sigma_{xz}^2 & \sigma_{yz}^2 & \sigma_z^2 \end{pmatrix}. \quad (\text{B.28})$$

However, for the track error matrix we need the spatial errors in the basis given in ξ , η , and z' . To do that, we take the error matrix from the vertex fit of the daughter tracks and rotate it with respect to the parent track. In helix representation, the local coordinates z' , ξ , and η are defined so that z' is the direction along the parent momentum vector,

$$\hat{\xi} = \frac{\hat{P}(prt) \times \hat{B}}{|\hat{P}(prt) \times \hat{B}|}, \quad \text{where } \vec{B} = \text{magnetic field, and} \quad (\text{B.29})$$

$$\hat{\eta} = \frac{\hat{B} - [\hat{P}(prt) \cdot \hat{B}]\hat{P}(prt)}{\sqrt{1 - (\hat{P}(prt) \cdot \hat{B})^2}} = \hat{\xi} \times \hat{P}(prt). \quad (\text{B.30})$$

We rotate the error matrix (B.28) from x, y, z to ξ , η , z' assuming the magnetic field is aligned with the z axis. The rotated matrix has the form:

$$\sigma^2 = \begin{pmatrix} \sigma_\xi^2 & & \\ \sigma_{\xi\eta}^2 & \sigma_\eta^2 & \\ \sigma_{\xi z'}^2 & \sigma_{\eta z'}^2 & \sigma_{z'}^2 \end{pmatrix}. \quad (\text{B.31})$$

The upper left 2 x 2 matrix (transverse components) is the spatial track error matrix. We now have the complete track error matrix for the parent track.

B.2 Performance

The track error matrix constructed using the method described in this appendix has been checked extensively. The test results are consistent with our expectations. Our algorithm has made the assumption that the spatial-directional correlations for the D_s track are small. To check the validity of the assumption, we have compared the vertexing results using our algorithm with the results from Kalman filtering [79]. Kalman filtering algorithm is more computational intensive, however, the algorithm estimates the spatial-directional correlations. The two methods yield comparable results. The ultimate figure of merit is the B_s^0 decay length resolution. In this case, our vertexing scheme gives a slightly better resolution. Based on the “virtual” D_s track vertexing scheme, the B_s^0 decay length resolution obtained is on the order of $50\ \mu m$ for the 60% core and about $150\ \mu m$ for the tail Gaussian. This is the best resolution achieved of any B_s mixing analysis to date.

A P P E N D I X C

PROPER TIME DISTRIBUTION FUNCTIONS

The complete proper time distribution function for events tagged as mixed is:

$$\begin{aligned}
P_{mixed}(\tau_{rec}) &= f_{D_s}(m_{KK\pi}) \left[\frac{f_{B_s}^{rs}}{N_1} F_{B_s}^{rs}(mixed) + \frac{f_{B_s}^{ws}}{N_2} F_{B_s}^{ws}(mixed) + \right. \\
&\quad \frac{f_{B_d}}{N_3} F_{B_d}(mixed) + \frac{f_{B^+}}{N_4} F_{B^+}(mixed) + \frac{f_{BB}}{N_5} F_{BB}(mixed) + \\
&\quad \left. \frac{f_{cc}}{N_6} F_{cc}(mixed) \right] + [1 - f_{D_s}(m_{KK\pi})] \cdot F_{comb} \tag{C.1} \\
&= f_{D_s}(m_{KK\pi}) \left\{ \frac{f_{B_s}^{rs}}{N_1} \int_0^\infty \left\{ \frac{e^{-\tau/\tau_{B_s}}}{2\tau_{B_s}} [(1 - \eta_i)(1 - \cos(\Delta m_s \tau)) + \right. \right. \\
&\quad \left. \left. \eta_i(1 + \cos(\Delta m_s \tau))] \cdot \epsilon_{B_s}(\tau) \cdot G_{B_s}^{rs}(\tau, \tau_{rec}) \right\} d\tau + \right. \\
&\quad \frac{f_{B_s}^{ws}}{N_2} \int_0^\infty \left\{ \frac{e^{-\tau/\tau_{B_s}}}{2\tau_{B_s}} [(1 - \eta_i)(1 + \cos(\Delta m_s \tau)) + \right. \\
&\quad \left. \left. \eta_i(1 - \cos(\Delta m_s \tau))] \cdot \epsilon_{B_s}(\tau) \cdot G_{B_s}^{ws}(\tau, \tau_{rec}) \right\} d\tau + \right. \\
&\quad \frac{f_{B_d}}{N_3} \int_0^\infty \left\{ \frac{e^{-\tau/\tau_{B_d}}}{2\tau_{B_d}} [(1 - \eta_{B_d})(1 - \cos(\Delta m_d \tau)) + \right. \\
&\quad \left. \left. \eta_{B_d}(1 + \cos(\Delta m_d \tau))] \cdot \epsilon_{B_d}(\tau) \cdot G_{B_d}(\tau, \tau_{rec}) \right\} d\tau + \right. \\
&\quad \frac{f_{B^+}}{N_4} \int_0^\infty \frac{e^{-\tau/\tau_{B^+}}}{2\tau_{B^+}} \cdot \eta_{B^+} \cdot \epsilon_{B^+}(\tau) \cdot G_{B_d}(\tau, \tau_{rec}) d\tau + \\
&\quad \frac{f_{BB}}{N_5} \int_0^\infty \frac{e^{-\tau/\tau_{BB}}}{2\tau_{BB}} \cdot \eta_{BB} \cdot \epsilon_{BB}(\tau) \cdot G_{BB}(\tau, \tau_{rec}) d\tau + \\
&\quad \left. \frac{f_{cc}}{N_6} [5.47 e^{-\tau_{rec}/0.21} \cdot erf(18.35 \cdot \tau_{rec})] \right\} + \\
&\quad [1 - f_{D_s}(m_{KK\pi})] [1.98 e^{-\tau_{rec}/1.12} \cdot erf(0.38 \cdot \tau_{rec} + 0.078)].
\end{aligned}$$

For events tagged as unmixed:

$$\begin{aligned}
P_{unmixed}(\tau_{rec}) &= f_{D_s}(m_{KK\pi}) \left[\frac{f_{B_s}^{rs}}{N_1} F_{B_s}^{rs}(unmixed) + \frac{f_{B_s}^{ws}}{N_2} F_{B_s}^{ws}(unmixed) + \right. \\
&\quad \frac{f_{B_d}}{N_3} F_{B_d}(unmixed) + \frac{f_{B^+}}{N_4} F_{B^+}(unmixed) + \frac{f_{BB}}{N_5} F_{BB}(unmixed) + \\
&\quad \left. \frac{f_{cc}}{N_6} F_{cc}(unmixed) \right] + [1 - f_{D_s}(m_{KK\pi})] \cdot F_{comb} \quad (C.2) \\
&= f_{D_s}(m_{KK\pi}) \left\{ \frac{f_{B_s}^{rs}}{N_1} \int_0^\infty \left\{ \frac{e^{-\tau/\tau_{B_s}}}{2\tau_{B_s}} [(1 - \eta_i)(1 + \cos(\Delta m_s \tau)) + \right. \right. \\
&\quad \left. \left. \eta_i(1 - \cos(\Delta m_s \tau))] \cdot \epsilon_{B_s}(\tau) \cdot G_{B_s}^{rs}(\tau, \tau_{rec}) \right\} d\tau + \right. \\
&\quad \frac{f_{B_s}^{ws}}{N_2} \int_0^\infty \left\{ \frac{e^{-\tau/\tau_{B_s}}}{2\tau_{B_s}} [(1 - \eta_i)(1 - \cos(\Delta m_s \tau)) + \right. \\
&\quad \left. \eta_i(1 + \cos(\Delta m_s \tau))] \cdot \epsilon_{B_s}(\tau) \cdot G_{B_s}^{ws}(\tau, \tau_{rec}) \right\} d\tau + \\
&\quad \frac{f_{B_d}}{N_3} \int_0^\infty \left\{ \frac{e^{-\tau/\tau_{B_d}}}{2\tau_{B_d}} [(1 - \eta_{B_d})(1 + \cos(\Delta m_d \tau)) + \right. \\
&\quad \left. \eta_{B_d}(1 - \cos(\Delta m_d \tau))] \cdot \epsilon_{B_d}(\tau) \cdot G_{B_d}(\tau, \tau_{rec}) \right\} d\tau + \\
&\quad \frac{f_{B^+}}{N_4} \int_0^\infty \frac{e^{-\tau/\tau_{B^+}}}{2\tau_{B^+}} \cdot (1 - \eta_{B^+}) \cdot \epsilon_{B^+}(\tau) \cdot G_{B^+}(\tau, \tau_{rec}) d\tau + \\
&\quad \frac{f_{BB}}{N_5} \int_0^\infty \frac{e^{-\tau/\tau_{BB}}}{2\tau_{BB}} \cdot (1 - \eta_{BB}) \cdot \epsilon_{BB}(\tau) \cdot G_{BB}(\tau, \tau_{rec}) d\tau + \\
&\quad \left. \frac{f_{cc}}{N_6} [5.47 e^{-\tau_{rec}/0.21} \cdot erf(18.35 \cdot \tau_{rec})] \right\} + \\
&\quad [1 - f_{D_s}(m_{KK\pi})] [1.98 e^{-\tau_{rec}/1.12} \cdot erf(0.38 \cdot \tau_{rec} + 0.078)].
\end{aligned}$$

APPENDIX D

COMBOS INPUT DATA FILE

```
*****
BEGIN          SLD          DS+TRKS/COMB
                PRELIMINARY ICHEP2000
```

MEASUREMENT STEP	AMPLITUDE DMS		STAT	SYST
PARAMETERS	FBS	0.100	+0.012	-0.012
	FLAMB	0.099	+0.017	-0.017
	DMD	0.476	+0.016	-0.016
	TAUBS	1.464	+0.057	-0.057
	TAUBD	1.562	+0.029	-0.029
	TAUBU	1.656	+0.025	-0.025
	TAULAMB	1.208	+0.051	-0.051

* SYSTEMATIC UNCERTAINTIES:

```
*
* VARIATION OF PARAMETERS AS ABOVE, AS WELL AS:
* SLD_SIGL: +/- 10% VARIATION OF DECAY LENGTH SIGMA
* SLD_SIGB: +/- 20% VARIATION OF RELATIVE BOOST SIGMA
* FBSRS : Rb*FBS*(Bs-->Ds- X)*(Ds-->Phi Pi)
*         = (6.36 +0.73 -0.78)*10^-4
* FBSWS : (b-->W- -->Ds-)*(Ds-->Phi Pi)
*         =(3.66 +/- 0.45)*10^-3
* FBDU2DS : (Bd,u-->Ds+- X)*(Ds-->Phi Pi)
*         =(3.71 +/- 0.28)*10^-3
* FBDURS : (Bd,u-->Ds- X)/(Bd,u-->Ds+- X)
*         =0.172 +/- 0.083
* SLD_UDSC: (cc -->Ds X)*(DS-->Phi Pi)
*         =(3.4+/-0.3)*10^-3
* SLD_DSFIT: Ds Combinatorial fraction (+/- 5-10%)
* SLD_ISTAG: +/- 0.02 (absolute) for initial state tag
* SLD_OFSET: Proper time offset corrections
*
```

```
DATA
DMS  AMPLITUDE      STAT      SYST+      SYST-
0.0  -0.08983  0.28484  0.14759 -0.12937
1.0  -0.24812  0.42585  0.11648 -0.09797
2.0   0.72599  0.49897  0.10243 -0.10418
```

3.0	-0.74818	0.54194	0.14253	-0.12226
4.0	-1.05575	0.63726	0.14400	-0.12423
5.0	-0.20250	0.59923	0.11921	-0.10192
6.0	0.06735	0.68691	0.14341	-0.13160
7.0	-0.38524	0.73134	0.18125	-0.16510
8.0	-0.12972	0.81365	0.16192	-0.13968
9.0	0.27227	0.85409	0.14964	-0.13209
10.0	0.02867	0.93261	0.14528	-0.12910
11.0	-0.50460	0.98735	0.18533	-0.16552
12.0	-0.76017	0.98532	0.21933	-0.19618
13.0	-0.89035	1.12032	0.30870	-0.31191
14.0	0.12659	1.25201	0.21403	-0.14546
15.0	1.02670	1.36117	0.32557	-0.33881
16.0	0.63393	1.40749	0.29512	-0.31978
17.0	-0.14967	1.41646	0.50585	-0.58878
18.0	0.69754	1.53765	0.37331	-0.38621
19.0	2.23626	1.65454	0.40883	-0.43966
20.0	2.51304	2.28322	0.83972	-0.88240
21.0	-0.05093	2.48494	0.49087	-0.57082
22.0	-2.12932	2.51601	0.77282	-0.73393
23.0	-2.34666	2.36970	0.71395	-0.51842
24.0	-1.90356	2.46725	0.47258	-0.29018
25.0	-1.33749	2.58624	0.49504	-0.39524

DMS	SLD_SIGL+	SLD_SIGL-	SLD_SIGB+	SLD_SIGB-	DMD+	DMD-
0.0	-0.00086	0.00061	-0.00215	0.00105	-0.00549	0.00559
1.0	-0.00028	0.00026	0.03421	-0.02920	0.00451	-0.00440
2.0	0.00262	-0.00227	0.04231	-0.04761	0.00170	-0.00163
3.0	0.01448	-0.01518	0.05932	-0.04575	-0.00040	0.00043
4.0	0.02793	-0.02919	0.05194	-0.04804	0.00061	-0.00062
5.0	0.01726	-0.01651	-0.01598	0.03087	-0.00015	0.00015
6.0	0.01162	-0.01043	0.02957	-0.04211	-0.00021	0.00021
7.0	0.00848	-0.00746	0.12032	-0.11872	0.00085	-0.00083
8.0	0.01318	-0.01353	0.06227	-0.05913	0.00055	-0.00052
9.0	0.03007	-0.03277	0.05072	-0.03726	0.00041	-0.00041
10.0	0.04795	-0.05260	0.09895	-0.09404	-0.00103	0.00102
11.0	0.07795	-0.08029	0.13826	-0.12712	0.00034	-0.00034
12.0	0.08446	-0.08472	0.18972	-0.16791	0.00041	-0.00040
13.0	0.07019	-0.05751	0.23106	-0.24275	-0.00019	0.00018
14.0	0.06367	-0.05745	-0.09031	0.17632	-0.00049	0.00048
15.0	0.02138	-0.02108	-0.10999	0.06122	0.00044	-0.00043
16.0	-0.01684	0.02050	0.16611	-0.20907	0.00067	-0.00065
17.0	-0.02900	0.04357	0.45490	-0.54802	0.00026	-0.00025
18.0	-0.01104	0.02516	0.18392	-0.19431	0.00008	-0.00008
19.0	0.01661	-0.01936	-0.26411	0.25513	0.00042	-0.00041
20.0	0.03770	-0.06220	-0.31624	0.29762	0.00081	-0.00079
21.0	0.05178	-0.04843	0.28979	-0.36998	0.00048	-0.00046
22.0	0.06615	-0.01689	0.73129	-0.69168	-0.00001	0.00001
23.0	0.14450	-0.07687	0.66618	-0.48156	-0.00060	0.00058
24.0	0.19823	-0.14530	0.32809	-0.08057	-0.00061	0.00059
25.0	0.20077	-0.17919	-0.01621	0.25653	-0.00015	0.00015

DMS	TAUBS+	TAUBS-	TAUBD+	TAUBD-	TAUBU+	TAUBU-
0.0	-0.01295	0.01402	-0.00100	0.00101	0.00062	-0.00064
1.0	-0.01264	0.01366	-0.00043	0.00043	0.00005	-0.00004
2.0	0.01420	-0.01539	-0.00283	0.00292	-0.00102	0.00105
3.0	0.00041	0.00026	0.00077	-0.00080	0.00007	-0.00008

4.0	0.01001	-0.01016	-0.00031	0.00030	-0.00075	0.00076
5.0	0.01629	-0.01699	-0.00087	0.00089	-0.00063	0.00064
6.0	0.01292	-0.01337	-0.00128	0.00132	-0.00029	0.00029
7.0	0.00708	-0.00694	-0.00008	0.00007	-0.00030	0.00031
8.0	0.00874	-0.00880	-0.00051	0.00051	-0.00026	0.00027
9.0	0.01451	-0.01489	-0.00110	0.00113	-0.00055	0.00055
10.0	0.00760	-0.00758	-0.00059	0.00062	-0.00056	0.00057
11.0	0.00504	-0.00479	-0.00067	0.00070	-0.00038	0.00038
12.0	0.00592	-0.00566	-0.00084	0.00087	0.00000	0.00000
13.0	0.00256	-0.00197	-0.00005	0.00003	0.00037	-0.00038
14.0	0.01436	-0.01480	-0.00105	0.00107	0.00014	-0.00014
15.0	0.02035	-0.02140	-0.00165	0.00172	-0.00048	0.00049
16.0	0.01310	-0.01353	-0.00092	0.00096	-0.00102	0.00104
17.0	-0.00036	0.00102	0.00091	-0.00097	-0.00144	0.00147
18.0	0.01217	-0.01244	0.00006	-0.00008	-0.00259	0.00263
19.0	0.02561	-0.02720	-0.00110	0.00115	-0.00454	0.00464
20.0	0.01701	-0.01866	0.00009	-0.00004	-0.00672	0.00687
21.0	0.00325	-0.00278	0.00111	-0.00111	-0.00416	0.00426
22.0	0.00983	-0.00849	-0.00091	0.00094	-0.00232	0.00238
23.0	0.02753	-0.02681	-0.00378	0.00387	-0.00110	0.00114
24.0	0.04035	-0.04023	-0.00565	0.00581	-0.00062	0.00065
25.0	0.04918	-0.04987	-0.00671	0.00695	-0.00028	0.00031

DMS	TAULAMB+	TAULAMB-	FBSRS+	FBSRS-	FBSWS+	FBSWS-
0.0	0.00134	-0.00139	-0.07419	0.09955	0.01859	-0.01804
1.0	-0.00122	0.00143	-0.06814	0.09149	0.01860	-0.01802
2.0	-0.00142	0.00161	-0.04033	0.04979	0.01739	-0.01759
3.0	0.00136	-0.00142	-0.03586	0.05340	0.01131	-0.01073
4.0	0.00010	-0.00014	-0.04231	0.06543	0.01520	-0.01442
5.0	0.00012	-0.00015	-0.04386	0.06081	0.01805	-0.01766
6.0	0.00013	-0.00015	-0.05036	0.06849	0.02189	-0.02160
7.0	0.00079	-0.00086	-0.03761	0.05587	0.02194	-0.02148
8.0	0.00078	-0.00086	-0.05216	0.07172	0.02762	-0.02730
9.0	-0.00030	0.00029	-0.04655	0.06044	0.02331	-0.02324
10.0	0.00012	-0.00015	-0.03217	0.04276	0.01264	-0.01248
11.0	-0.00030	0.00031	-0.01365	0.02317	0.00516	-0.00478
12.0	-0.00022	0.00022	-0.00630	0.00999	0.00124	-0.00504
13.0	0.00027	-0.00037	-0.01384	0.02764	0.00819	-0.00746
14.0	-0.00008	0.00003	-0.03050	0.04206	0.01665	-0.01651
15.0	0.00016	-0.00014	-0.03954	0.04829	0.02196	-0.02222
16.0	0.00082	-0.00087	-0.03440	0.04423	0.01781	-0.01795
17.0	0.00186	-0.00207	-0.04983	0.06769	0.01763	-0.01744
18.0	0.00133	-0.00150	-0.07260	0.09211	0.02747	-0.02746
19.0	0.00090	-0.00094	-0.08390	0.09826	0.03375	-0.03439
20.0	0.00175	-0.00176	-0.06792	0.06755	0.01015	-0.01160
21.0	0.00129	-0.00129	-0.00881	0.00929	-0.01869	0.01870
22.0	-0.00142	0.00153	-0.04041	0.06387	-0.01310	0.01367
23.0	-0.00450	0.00477	-0.09166	0.13434	0.00634	-0.00544
24.0	-0.00666	0.00713	-0.11241	0.16267	0.01970	-0.01851
25.0	-0.00751	0.00813	-0.10408	0.14886	0.02609	-0.02498

DMS	FBDU2DS+	FBDU2DS-	FBDURS+	FBDURS-	SLD_UDSC+	SLD_UDSC-
0.0	0.03146	-0.03243	-0.06898	0.06925	0.00062	-0.00062
1.0	0.03104	-0.03183	-0.04021	0.03864	0.00100	-0.00100
2.0	0.01477	-0.01561	0.00467	-0.00629	0.00193	-0.00195
3.0	0.01873	-0.01874	0.00996	-0.01088	0.00087	-0.00088
4.0	0.02173	-0.02131	0.02033	-0.02238	0.00110	-0.00111

5.0	0.01840	-0.01865	0.01574	-0.01572	0.00162	-0.00162
6.0	0.02117	-0.02167	0.03206	-0.03449	0.00256	-0.00257
7.0	0.01483	-0.01449	0.05310	-0.05221	0.00239	-0.00240
8.0	0.01968	-0.02004	0.05160	-0.05339	0.00325	-0.00326
9.0	0.01706	-0.01792	0.02418	-0.02594	0.00354	-0.00356
10.0	0.01316	-0.01371	0.01190	-0.01322	0.00315	-0.00317
11.0	0.00751	-0.00723	0.00800	-0.00950	0.00226	-0.00228
12.0	-0.00094	-0.00207	0.00849	-0.01701	0.00175	-0.00177
13.0	0.00479	-0.00368	0.00611	-0.00732	0.00180	-0.00182
14.0	0.00899	-0.00885	0.01234	-0.01399	0.00375	-0.00379
15.0	0.01275	-0.01355	0.05849	-0.06044	0.00653	-0.00659
16.0	0.01425	-0.01488	0.07899	-0.08093	0.00496	-0.00501
17.0	0.02480	-0.02550	0.07386	-0.07613	0.00308	-0.00312
18.0	0.03252	-0.03439	0.08943	-0.09378	0.00453	-0.00459
19.0	0.03703	-0.04039	0.13205	-0.13929	0.00796	-0.00804
20.0	0.04201	-0.04715	0.15344	-0.15586	0.01060	-0.01072
21.0	0.02225	-0.02413	0.08296	-0.08516	0.00501	-0.00508
22.0	0.03507	-0.03462	0.01205	-0.01073	0.00216	-0.00217
23.0	0.05078	-0.04984	-0.04764	0.05069	0.00111	-0.00110
24.0	0.05364	-0.05258	-0.07390	0.07629	0.00114	-0.00111
25.0	0.04430	-0.04340	-0.06251	0.06344	0.00122	-0.00118

DMS	FBS+	FBS-	FLAMB+	FLAMB-	SLD_DSFIT+	SLD_DSFIT-
0.0	0.01813	-0.01761	0.02285	-0.02228	0.01336	-0.01106
1.0	0.01815	-0.01759	0.01327	-0.01344	0.01541	-0.01462
2.0	0.01697	-0.01717	0.00408	-0.00414	0.03443	-0.03567
3.0	0.01104	-0.01048	0.00283	-0.00269	0.03845	-0.03581
4.0	0.01483	-0.01408	0.00341	-0.00320	0.06515	-0.05983
5.0	0.01761	-0.01724	0.00494	-0.00497	0.04793	-0.04564
6.0	0.02136	-0.02108	0.00298	-0.00299	0.06145	-0.05962
7.0	0.02141	-0.02097	0.00014	0.00003	0.06297	-0.06006
8.0	0.02696	-0.02665	0.00196	-0.00189	0.05937	-0.05716
9.0	0.02275	-0.02269	0.00205	-0.00211	0.02421	-0.02381
10.0	0.01233	-0.01219	0.00370	-0.00381	0.01853	-0.01751
11.0	0.00503	-0.00467	0.00078	-0.00075	0.00943	-0.00748
12.0	0.00112	-0.00492	0.00089	-0.00085	0.01445	-0.01650
13.0	0.00798	-0.00729	0.00635	-0.00642	0.03940	-0.03639
14.0	0.01625	-0.01611	0.00646	-0.00665	0.05571	-0.05475
15.0	0.02144	-0.02169	0.00088	-0.00096	0.09644	-0.09642
16.0	0.01738	-0.01751	-0.00329	0.00342	0.07394	-0.07407
17.0	0.01721	-0.01702	-0.00045	0.00061	0.02851	-0.02931
18.0	0.02681	-0.02680	0.00049	-0.00046	-0.02181	0.01715
19.0	0.03295	-0.03356	-0.00698	0.00702	-0.06388	0.05299
20.0	0.00992	-0.01130	-0.01855	0.01877	-0.08973	0.07611
21.0	-0.01825	0.01825	-0.01371	0.01419	-0.03214	0.02840
22.0	-0.01279	0.01334	0.00997	-0.00983	0.02713	-0.02320
23.0	0.00618	-0.00532	0.03166	-0.03199	0.04280	-0.03562
24.0	0.01922	-0.01808	0.04061	-0.04109	0.07504	-0.06421
25.0	0.02545	-0.02439	0.03788	-0.03831	0.11017	-0.09765

DMS	SLD_ISTAG+	SLD_ISTAG-	SLD_OFFSET+	SLD_OFFSET-
0.0	-0.03056	0.03809	-0.05503	0.05503
1.0	-0.01617	0.01643	0.00118	-0.00118
2.0	-0.06663	0.06227	-0.00915	0.00915
3.0	-0.09611	0.10692	0.01068	-0.01068
4.0	-0.07220	0.08407	-0.01464	0.01464
5.0	-0.06556	0.07361	-0.00569	0.00569

6.0	-0.08043	0.09155	0.01061	-0.01061
7.0	-0.06442	0.08445	-0.00665	0.00665
8.0	-0.06755	0.09158	0.02190	-0.02190
9.0	-0.05307	0.07325	-0.08453	0.08453
10.0	-0.05399	0.07802	0.00697	-0.00697
11.0	-0.05757	0.08546	-0.03193	0.03193
12.0	-0.04900	0.06732	0.00477	-0.00477
13.0	-0.02771	0.04332	0.18040	-0.18040
14.0	-0.02193	0.02348	-0.06487	0.06487
15.0	-0.09407	0.08909	-0.27791	0.27791
16.0	-0.16748	0.16870	-0.12620	0.12620
17.0	-0.18566	0.18533	-0.02484	0.02484
18.0	-0.21123	0.19011	-0.22198	0.22198
19.0	-0.28857	0.25085	0.06753	-0.06753
20.0	-0.42950	0.35844	0.67081	-0.67081
21.0	-0.32693	0.27428	0.26430	-0.26430
22.0	-0.20312	0.19142	0.12118	-0.12118
23.0	-0.11125	0.12584	0.04803	-0.04803
24.0	-0.04964	0.07992	0.15842	-0.15842
25.0	0.02374	0.01976	0.30399	-0.30399

END

A P P E N D I X E

SLD COLLABORATION

Kenji Abe,⁽¹⁵⁾ Koya Abe,⁽²⁴⁾ T. Abe,⁽²¹⁾ I. Adam,⁽²¹⁾ H. Akimoto,⁽²¹⁾ D. Aston,⁽²¹⁾
K.G. Baird,⁽¹¹⁾ C. Baltay,⁽³⁰⁾ H.R. Band,⁽²⁹⁾ T.L. Barklow,⁽²¹⁾ J.M. Bauer,⁽¹²⁾
G. Bellodi,⁽¹⁷⁾ R. Berger,⁽²¹⁾ G. Blaylock,⁽¹¹⁾ J.R. Bogart,⁽²¹⁾ G.R. Bower,⁽²¹⁾
J.E. Brau,⁽¹⁶⁾ M. Breidenbach,⁽²¹⁾ W.M. Bugg,⁽²³⁾ D. Burke,⁽²¹⁾ T.H. Burnett,⁽²⁸⁾
P.N. Burrows,⁽¹⁷⁾ A. Calcaterra,⁽⁸⁾ R. Cassell,⁽²¹⁾ A. Chou,⁽²¹⁾ H.O. Cohn,⁽²³⁾
J.A. Coller,⁽⁴⁾ M.R. Convery,⁽²¹⁾ V. Cook,⁽²⁸⁾ R.F. Cowan,⁽¹³⁾ G. Crawford,⁽²¹⁾
C.J.S. Damerell,⁽¹⁹⁾ M. Daoudi,⁽²¹⁾ S. Dasu,⁽²⁹⁾ N. de Groot,⁽²⁾ R. de Sangro,⁽⁸⁾
D.N. Dong,⁽²¹⁾ M. Doser,⁽²¹⁾ R. Dubois,⁽²¹⁾ I. Erofeeva,⁽¹⁴⁾ V. Eschenburg,⁽¹²⁾
S. Fahey,⁽⁵⁾ D. Falciari,⁽⁸⁾ J.P. Fernandez,⁽²⁶⁾ K. Flood,⁽¹¹⁾ R. Frey,⁽¹⁶⁾
E.L. Hart,⁽²³⁾ K. Hasuko,⁽²⁴⁾ S.S. Hertzbach,⁽¹¹⁾ M.E. Huffer,⁽²¹⁾ X. Huynh,⁽²¹⁾
M. Iwasaki,⁽¹⁶⁾ D.J. Jackson,⁽¹⁹⁾ P. Jacques,⁽²⁰⁾ J.A. Jaros,⁽²¹⁾ Z.Y. Jiang,⁽²¹⁾
A.S. Johnson,⁽²¹⁾ J.R. Johnson,⁽²⁹⁾ R. Kajikawa,⁽¹⁵⁾ M. Kalelkar,⁽²⁰⁾ H.J. Kang,⁽²⁰⁾
R.R. Kofler,⁽¹¹⁾ R.S. Kroeger,⁽¹²⁾ M. Langston,⁽¹⁶⁾ D.W.G. Leith,⁽²¹⁾ V. Lia,⁽¹³⁾
C. Lin,⁽¹¹⁾ G. Mancinelli,⁽²⁰⁾ S. Manly,⁽³⁰⁾ G. Mantovani,⁽¹⁸⁾ T.W. Markiewicz,⁽²¹⁾
T. Maruyama,⁽²¹⁾ A.K. McKemey,⁽³⁾ R. Messner,⁽²¹⁾ K.C. Moffeit,⁽²¹⁾
T.B. Moore,⁽³⁰⁾ M. Morii,⁽²¹⁾ D. Muller,⁽²¹⁾ V. Murzin,⁽¹⁴⁾ S. Narita,⁽²⁴⁾
U. Nauenberg,⁽⁵⁾ H. Neal,⁽³⁰⁾ G. Nesom,⁽¹⁷⁾ N. Oishi,⁽¹⁵⁾ D. Onoprienko,⁽²³⁾
L.S. Osborne,⁽¹³⁾ R.S. Panvini,⁽²⁷⁾ C.H. Park,⁽²²⁾ I. Peruzzi,⁽⁸⁾ M. Piccolo,⁽⁸⁾
L. Piemontese,⁽⁷⁾ R.J. Plano,⁽²⁰⁾ R. Prepost,⁽²⁹⁾ C.Y. Prescott,⁽²¹⁾
B.N. Ratcliff,⁽²¹⁾ J. Reidy,⁽¹²⁾ P.L. Reinertsen,⁽²⁶⁾ L.S. Rochester,⁽²¹⁾
P.C. Rowson,⁽²¹⁾ J.J. Russell,⁽²¹⁾ O.H. Saxton,⁽²¹⁾ T. Schalk,⁽²⁶⁾ B.A. Schumm,⁽²⁶⁾
J. Schwiening,⁽²¹⁾ V.V. Serbo,⁽²¹⁾ G. Shapiro,⁽¹⁰⁾ N.B. Sinev,⁽¹⁶⁾ J.A. Snyder,⁽³⁰⁾
H. Staengle,⁽⁶⁾ A. Stahl,⁽²¹⁾ P. Stamer,⁽²⁰⁾ H. Steiner,⁽¹⁰⁾ D. Su,⁽²¹⁾ F. Suekane,⁽²⁴⁾

A. Sugiyama,⁽¹⁵⁾ S. Suzuki,⁽¹⁵⁾ M. Swartz,⁽⁹⁾ F.E. Taylor,⁽¹³⁾ J. Thom,⁽²¹⁾
 E. Torrence,⁽¹³⁾ T. Usher,⁽²¹⁾ J. Va'vra,⁽²¹⁾ R. Verdier,⁽¹³⁾ D.L. Wagner,⁽⁵⁾
 A.P. Waite,⁽²¹⁾ S. Walston,⁽¹⁶⁾ A.W. Weidemann,⁽²³⁾ E.R. Weiss,⁽²⁸⁾
 J.S. Whitaker,⁽⁴⁾ S.H. Williams,⁽²¹⁾ S. Willocq,⁽¹¹⁾ R.J. Wilson,⁽⁶⁾
 W.J. Wisniewski,⁽²¹⁾ J.L. Wittlin,⁽¹¹⁾ M. Woods,⁽²¹⁾ T.R. Wright,⁽²⁹⁾
 R.K. Yamamoto,⁽¹³⁾ J. Yashima,⁽²⁴⁾ S.J. Yellin,⁽²⁵⁾ C.C. Young,⁽²¹⁾ H. Yuta.⁽¹⁾

(The SLD Collaboration)

- ⁽¹⁾ *Aomori University, Aomori , 030 Japan,*
⁽²⁾ *University of Bristol, Bristol, United Kingdom,*
⁽³⁾ *Brunel University, Uxbridge, Middlesex, UB8 3PH United Kingdom,*
⁽⁴⁾ *Boston University, Boston, Massachusetts 02215,*
⁽⁵⁾ *University of Colorado, Boulder, Colorado 80309,*
⁽⁶⁾ *Colorado State University, Ft. Collins, Colorado 80523,*
⁽⁷⁾ *INFN Sezione di Ferrara and Universita di Ferrara, I-44100 Ferrara, Italy,*
⁽⁸⁾ *INFN Lab. Nazionali di Frascati, I-00044 Frascati, Italy,*
⁽⁹⁾ *Johns Hopkins University, Baltimore, Maryland 21218-2686,*
⁽¹⁰⁾ *Lawrence Berkeley Laboratory, University of California, Berkeley, California*
94720,
⁽¹¹⁾ *University of Massachusetts, Amherst, Massachusetts 01003,*
⁽¹²⁾ *University of Mississippi, University, Mississippi 38677,*
⁽¹³⁾ *Massachusetts Institute of Technology, Cambridge, Massachusetts 02139,*
⁽¹⁴⁾ *Institute of Nuclear Physics, Moscow State University, 119899, Moscow*
Russia,
⁽¹⁵⁾ *Nagoya University, Chikusa-ku, Nagoya, 464 Japan,*
⁽¹⁶⁾ *University of Oregon, Eugene, Oregon 97403,*
⁽¹⁷⁾ *Oxford University, Oxford, OX1 3RH, United Kingdom,*
⁽¹⁸⁾ *INFN Sezione di Perugia and Universita di Perugia, I-06100 Perugia, Italy,*

- ⁽¹⁹⁾ *Rutherford Appleton Laboratory, Chilton, Didcot, Oxon OX11 0QX United Kingdom,*
- ⁽²⁰⁾ *Rutgers University, Piscataway, New Jersey 08855,*
- ⁽²¹⁾ *Stanford Linear Accelerator Center, Stanford University, Stanford, California 94309,*
- ⁽²²⁾ *Soongsil University, Seoul, Korea 156-743,*
- ⁽²³⁾ *University of Tennessee, Knoxville, Tennessee 37996,*
- ⁽²⁴⁾ *Tohoku University, Sendai 980, Japan,*
- ⁽²⁵⁾ *University of California at Santa Barbara, Santa Barbara, California 93106,*
- ⁽²⁶⁾ *University of California at Santa Cruz, Santa Cruz, California 95064,*
- ⁽²⁷⁾ *Vanderbilt University, Nashville, Tennessee 37235,*
- ⁽²⁸⁾ *University of Washington, Seattle, Washington 98105,*
- ⁽²⁹⁾ *University of Wisconsin, Madison, Wisconsin 53706,*
- ⁽³⁰⁾ *Yale University, New Haven, Connecticut 06511.*

BIBLIOGRAPHY

- [1] J. Christenson, J. Cronin, V. Fitch and R. Turlay, *Evidence for the 2π decay of the K_2^0 meson*, Phys. Rev. Lett. **13**, 138 (1964).
- [2] S.L. Glashow, *Partial symmetries of weak interactions*, Nuclear Physics **22**, 579 (1961);
S. Weinberg, *A model of leptons*, Phys. Rev. Lett. **19**, 1264 (1967);
A. Salam, *Elementary Particle Theory*, Ed. N. Svartholm, Almquist and Wiksell (1968).
- [3] G. Arnison *et al.* [UA1 Collaboration], *Experimental observation of isolated large transverse energy electrons with associated missing energy at $\sqrt{S} = 540$ GeV*, Phys. Lett. B **122**, 103 (1983);
M. Banner *et al.* [UA2 Collaboration], *Observation of single isolated electrons of high transverse momentum in events with missing transverse energy at the CERN $p\bar{p}$ collider*, Phys. Lett. B **122**, 476 (1983);
G. Arnison *et al.* [UA1 Collaboration], *Experimental observation of leptons pairs of invariant mass around 95 GeV/c² at the CERN SPS collider*, Phys. Lett. B **129**, 130 (1983).
- [4] G. Altarelli, *The Standard Model and beyond*, hep-ph/9809532.
- [5] H. Brown *et al.* [Muon g-2 Collaboration], *Precise measurement of the positive muon anomalous magnetic moment*, Phys. Rev. Lett. **86**, 2227 (2001).
- [6] S. Fukuda *et al.* [SuperKamiokande Collaboration], *Tau neutrinos favored over sterile neutrinos in atmospheric muon neutrino oscillations*, Phys. Rev. Lett. **85**, 3999 (2000).
- [7] Q. Ahmad *et al.* [SNO Collaboration], *Measurement of the charged current interactions produced by B-8 solar neutrinos at the Sudbury Neutrino Observatory*, nucl-ex/0106015.
- [8] M. Turner and J. Tyson, *Cosmology at the millennium*, Rev. Mod. Phys. **71**, S145 (1999);
B. Sadoulet, *Deciphering the nature of dark matter*, Rev. Mod. Phys. **71**, S197 (1999).

- [9] A. Sakharov, *Violation of CP invariance, C asymmetry, and baryon asymmetry of the universe*, JETP Lett. **5**, 24 (1967);
A. Sakharov, *Baryon asymmetry of the universe*, Sov. Phys. Usp. **35**, 417 (1991).
- [10] A. Cohen, D. Kaplan and A. Nelson, *Progress in electroweak baryogenesis*, Ann. Rev. Nucl. Part. Sci. **43**, 27 (1993).
- [11] F. Halzen and A. Martin, **Quarks & Leptons: an Introductory Course in Modern Particle Physics**, John Wiley and Sons (1984);
D. Griffiths, **Introduction to Elementary Particles**, John Wiley and Sons (1987).
- [12] LEP Electroweak Working Group, *A Combination of Preliminary Electroweak Measurements and Constraints on the Standard Model*, CERN-EP/2001-021.
- [13] P. Higgs, *Broken symmetries and the masses of gauge bosons*, Phys. Rev. Lett. **13**, 508 (1964).
- [14] V. Barger and J. Roger, **Collider Physics**, Addison-Wesley (1987).
- [15] A. Kronfeld and P. Mackenzie, *Progress in QCD using Lattice Gauge theory*, Ann. Rev. Nucl. Part. Sci. **43**, 793 (1993).
- [16] P. Burchat, *Physics at an asymmetric energy B meson factory*, SCIPP-91-11
Invited lectures presented at the Lake Louise Winter Institute: Particle Physics - the Factory Era, Lake Louise, Canada, Feb 17-23, 1991.
- [17] M. Kobayashi and T. Maskawa, *CP violation in the renormalizable theory of weak interaction*, Prog. Theor. Phys. **49**, 652 (1973).
- [18] L. Wolfenstein, *Parameterization of the Kobayashi-Maskawa Matrix*, Phys. Rev. Lett. **51**, 1945 (1983).
- [19] D. Groom *et al.* [Particle Data Group Collaboration], *Review of particle physics*, Eur. Phys. J. C **15**, 1 (2000).
- [20] A. Buras *et al.*, *B^0 - \bar{B}^0 mixing, CP violation and the B-meson decay*, Nucl. Phys. B **245**, 369 (1984).
- [21] G. Altarelli and P. Franzini, *B^0 - \bar{B}^0 mixing within and beyond the Standard Model*, Z. Phys. **C37**, 271 (1988).
- [22] B. Aubert *et al.* [BaBar Collaboration], *Observation of CP violation in the B^0 meson system*, hep-ex/0107013;
K. Abe *et al.* [Belle Collaboration], *Observation of large CP violation in the neutral B meson system*, hep-ex/0107061.

- [23] P. Harrison *et al.* [BaBar Collaboration], **The BaBar Physics Book: Physics at an Asymmetric B Factory**, SLAC-R-0504 (1998).
- [24] M. Ciuchini *et al.*, *2000 CKM Triangle Analysis: A Critical Review with Updated Experimental Inputs and Theoretical Parameters*, hep-ph/0012308.
- [25] SLAC Linear Collider Design Report, SLAC-R-229 (1980), and revisions.
- [26] SLD Design Report, SLAC-R-273 (1984), and revisions.
- [27] R. Fernow, **Introduction to experimental particle physics**, Cambridge University Press (1986).
- [28] Zeroth Order Design Report For The Next Linear Collider, SLAC-R-0474 (1996);
TESLA Technical Design Report Part I: Executive Summary, hep-ph/0106314;
JLC Design Study, KEK Report 97-1 (1997).
- [29] M. Breidenbach, *SLC and SLD- experimental experience with a linear collider*, SLAC-PUB-6313 (1993).
- [30] M. Woods, *The polarized electron beam for the SLAC Linear Collider*, SLAC-PUB-7320 (1996).
- [31] E. Reuter *et al.*, Mechanical design and development of a high power target system for the SLC positron source, SLAC-PUB-5369 (1991).
- [32] R. Koontz, T. Lee, C. Pearson and A. Vlieks, *Recent performance, lifetime and failure modes of the 5045 klystron population at SLAC*, SLAC-PUB-5890 (1992).
- [33] T. Limberg, P. Emma and R. Rossmanith, *The north arc of the SLC as a spin rotator*, SLAC-PUB-6210 (1993).
- [34] G. Blaylock, *The WISRD beam energy measurement*, SLD-PHYSICS-NOTE-22 (1993).
- [35] P. Rowson *et al.*, *Calibration of the WISRD energy spectrometer via a Z-peak scan*, SLD-NOTE-264 (1999).
- [36] M. Woods, *The scanning Compton polarimeter for the SLD experiment*, SLAC-PUB-7319 (1996).
- [37] F. Taylor, *A first order calculation of compton scattering asymmetry*, SLD-PHYSICS-NOTE-26 (1995).
- [38] K. Abe *et al.* [SLD Collaboration], *Design and performance of the SLD vertex detector, a 307 Mpixel tracking system*, Nucl. Instrum. Methods A **400**, 287 (1997).

- [39] D. Dong, Ph.D. Dissertation, MIT, SLAC-R-550(1999).
- [40] M. Hildreth *et al.*, Performance of the SLD Central Drift Chamber, SLAC-PUB-6659 (1994).
- [41] J. Venuti and G. Chadwick, *Radiation aging studies of CO₂ hydrocarbon mixtures for the SLD drift chamber*, IEEE Trans. on Nucl. Sci. NS-36, 595 (1989).
- [42] T. Ypsilantis and J. Sequinot, *Theory of ring imaging cerenkov counters*, Nucl. Instrum. Methods A **343**, 30 (1994).
- [43] H. Hawahara and J. Va'vra, SLD CRID Internal Note 78 (1993).
- [44] D. Anderson, Nucl. Instrum. Methods **178**, 125 (1980).
- [45] T. Pavel, Ph.D. Dissertation, Stanford University, SLAC-R-491 (1997).
- [46] D. Axen *et al.*, *The lead-liquid Argon sampling calorimeter of the SLD detector*, Nucl. Instrum. Methods A **328**, 472 (1993).
- [47] A. Benvenuti *et al.*, *The iron calorimeter and muon identifier for SLD*, Nucl. Instrum. Methods A **276**, 94 (1989).
- [48] E. Iarocci, *Platic streamer tubes and their applications in high-energy physics*, Nucl. Instrum. Methods **217**, 30 (1983).
- [49] S. Berridge *et al.*, First results from the SLD silicon calorimeters, IEEE Trans. Nucl. Sci. **39**, 1242 (1992).
- [50] A. Marchioro *et al.*, *the ALEPH event builder*, IEEE Trans. Nucl. Sci. **34**, 133 (1987).
- [51] T. Sjostrand, *High-energy physics event generation with PYTHIA 5.7 and JETSET 7.4*, Comput. Phys. Communi. **82**, 74 (1994).
- [52] X. Artru and G. Mennessier, *String model and multiproduction*, Nucl. Phys. B **70**, 93 (1974).
- [53] C. Peterson, D. Schlatter, I. Schmitt and P. Zerwas, *Scaling violations in inclusive $e^+ e^-$ annihilation spectra*, Phys. Rev. D **27**, 105 (1983).
- [54] P. Kim, private communication.
- [55] N. Isgur, D. Scora, B. Grinstein and M. Wise, *Semileptonic B and D decays in the quark model*, Phys. Rev. D **39**, 799 (1989).
- [56] R. Brun, R. Hagelberg, M. Hansroul and J. C. Lassalle, *Geant: Simulation program for particle physics experiments. User guide and reference manual*, CERN-DD-78-2-REV (1978); CERN Application Software Group, *GEANT 3.21 Program*, CERN Program Library (1994).

- [57] W. Nelson, H. Hirayama and D. Rogers, *The EGS4 code system*, SLAC-R-265 (1985).
- [58] K. Abe *et al.* [SLD Collaboration], *Measurements of R_b with impact parameters and displaced vertices*, Phys. Rev. D **53**, 1023 (1996).
- [59] D. Su, private communication.
- [60] D. J. Jackson, *A topological vertex reconstruction algorithm for hadronic jets*, Nucl. Instrum. Methods A **388**, 247 (1997).
- [61] K. Abe *et al.* [SLD Collaboration], *Direct Measurement of A_b using Charged Vertices*, SLAC-PUB-8542 (2000).
- [62] ALEPH, DELPHI, L3, OPAL, CDF, and SLD Collaborations, *Combined results on b -hadron production rates, lifetimes, oscillations and semileptonic decays*, CERN-EP-2000, SLAC-PUB-8492, hep-ex/0009052.
- [63] T. Moore, private communication.
- [64] T. Moore, Ph.D. Dissertation, Yale (2000).
- [65] K. Abe *et al.* [SLD Collaboration], *Precise measurement of the b -quark fragmentation function in Z^0 boson decays*, Phys. Rev. Lett. **84**, 4300 (2000).
- [66] D. Jackson, private communication.
- [67] D. Dong, private communication.
- [68] H.G. Moser and A. Roussarie, *Mathematical methods for $B^0\bar{B}^0$ oscillation analyses*, Nucl. Instrum. Methods A **384**, 491 (1997).
- [69] D. Buskulic *et al.* [ALEPH Collaboration], *Measurement of D_s^+ meson production in Z decays and of the \bar{B}_s^0 lifetime*, Z. Phys. C **69**, 585 (1996).
- [70] A. Chou, Ph.D. Dissertation, Stanford (2001).
- [71] K. Abe *et al.* [SLD Collaboration], *Time Dependent $B_s^0 - \bar{B}_s^0$ Mixing Using Inclusive and Semileptonic B Decays at SLD*, SLAC-PUB-8568 (2000).
- [72] LEP B Oscillations Working Group, <http://lepbosec.web.cern.ch/LEPBOSC>.
- [73] P. Cerenkov, *Visible radiation produced by electrons moving in a medium with velocities exceeding that of light*, Phys. Rev. **52**, 378 (1937).
- [74] J. Seguinot and T. Ypsilantis, *A historical survey of ring imaging Cerenkov counters*, Nucl. Instrum. Meth. A **343**, 1 (1994).
- [75] DELPHI Technical Proposal, LEPC 83-3 (1983).

- [76] D. Aston, private communication.
- [77] K. Abe *et al.*, *Obtaining physics results from the SLD CRID*, Nucl. Instrum. Meth. A **371**, 195 (1996).
- [78] C. Young, private communication.
- [79] R. Luchsinger and C. Grab, *Vertex reconstruction by means of the method of Kalman filtering*, Computer Physics Communications **76**, 263 (1993).